

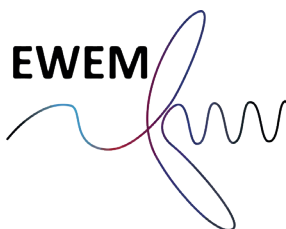


Fault Detection of Drive Trains in 10 MW Offshore Wind Turbines using Non-Traditional Methods

Maarten Johan Gerben van der Drift



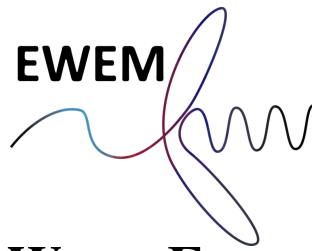
EWEM



 NTNU

 TU Delft

This page intentionally left blank.



**EUROPEAN WIND ENERGY MASTER
OFFSHORE ENGINEERING**

**Fault Detection of Drive Trains in 10 MW Offshore
Wind Turbines using Non-Traditional Methods**

**Master of Science Thesis
Thesis defence at the 2nd of September 2020**

Maarten Johan Gerben van der Drift
August 26, 2020

In partial fulfillment of the requirements for the degrees of



**NORWEGIAN UNIVERSITY OF
SCIENCE AND TECHNOLOGY**

Department of Marine Technology
Master of Science
Technology - Wind Energy



**DELFT UNIVERSITY OF
TECHNOLOGY**

Faculty of 3mE
Master of Science
Offshore Engineering

Student number

517532

4384180

Supervisors

A.R. Nejad
Prof. Z. Gao

S.J. Watson
P. van der Male

De molen draait niet met de wind die voorbij is
Dutch expression about wind

Abstract

One of the world's biggest concerns is global warming, a solution to this can be wind energy. Offshore wind energy has advantages over onshore wind energy, however, the levelized cost of energy is higher. The maintenance costs are a major cost contributor. To lower these costs, research is performed on faults and its detection. Currently, little is known about fault detectability and vibration propagation in a drive train of an offshore wind turbine. Fault detection and vibration propagation in a drive train of a 10 MW floating offshore wind turbine is therefore investigated to get an insight about the effect of faults on the vibration monitoring data of a drive train. Three different faults with five different degradation levels are applied one by one on the bearings of a 10 MW drive train model. These faults are radial and axial damage in the main shaft front bearing and radial damage in the high speed shaft rear bearing. One traditional, two non-traditional and two novel fault detection methods are used to detect faults and their vibration propagation.

One common and one novel fault detection method are deployed in the time domain: the Velocity Root-Mean-Square (RMS) Threshold Method and the Peeters' Anomaly Detection Method. The Velocity RMS Threshold Method compares the RMS of the vibration velocity of non-rotating parts with a threshold proposed by ISO 10816-21. The latter method makes use of statistical indicators and is tailored for this study. Although changes after fault introduction were observable, the methods can not be used and need to be altered for usage in the wind industry.

The non-traditional Angular Velocity Error Energy Method is deployed in the frequency domain. It makes use of the angular velocity measurements from the drive train's shafts and compares the normalized energy of its spectra with a threshold. This method inspired the development of novel fault detection methods introduced in this study, being the Bearing Velocity Energy Method (making use of bearing velocity measurements and also based on the Velocity Root-Mean-Square Threshold Method) and the Shaft Vibration Energy Method (making use of the velocity and acceleration of shafts). Both methods compare the normalized energy of the spectra with a threshold. Radial damage in the main shaft front bearing could be detected using the Angular Velocity Error Energy Method, the Bearing Velocity Energy Method and the Shaft Vibration Energy Method. Damage was detectable from 15% degradation onwards. Next to a change in vibration in the main shaft and its bearings, a different vibration behaviour was observed at the planet carrier front and rear bearing, intermediate speed shaft front bearing and on the low speed shaft. Axial damage in the main shaft front bearing could only be detected using the Shaft Vibration Energy Method. It was shown that this kind of damage was detectable by monitoring the main shaft's vibration from 50% degradation and higher. Radial damage in the high speed shaft rear bearing could be detected using the Bearing Velocity Error Method and the Shaft Vibration Energy Method. Damage could only be detected for degradation higher than 70%, by monitoring the high speed shaft and its bearings. Next to the typical measurement locations, it is recommended to place extra sensors measuring velocity on the first stage planet carrier front and rear bearing housings, intermediate speed shaft front bearing housings and on the low speed shaft.

The outcome of this study contributes to the understanding of vibration propagation and fault detection in a drive train. The fault detection methods can be implemented in maintenance and monitoring methods for offshore wind turbines. Maintenance engineers can use the detected vibration propagation to check the affected gearbox components and replace them before they fail.

Preface

In front of you lies my thesis "*Fault Detection of Drive Trains in 10 MW Offshore Wind Turbines using Non-Traditional Methods.*" This report serves as the final deliverable to graduate from and finish the master European Wind Energy Master (EWEM) - Offshore Engineering.

However, considered to be impossible three years ago, I managed to complete a master programme. It has been a pleasure writing on this thesis. I am proud on it. Although, sometimes difficult and tiring, writing the report gave me a better understanding of myself. In a way, it made me realize what my abilities and disabilities were and how I can use them to make the world a better place.

My father inspired me to take a look into wind energy. When he was in his mid-20s he built a wind turbine himself. With very primitive tools and a construction manual by Fons de Beer [de Beer, 1982], he constructed a wind turbine in the countryside. My father proved that everybody can build a wind turbine. The pictures showing my father working on the wind turbine inspired me to set up a wind energy project for my high school research paper. I want to thank my Dad Fred for the effort he put in motivating and inspiring me and keeping me sharp with his questions.



My Dad, working on the gearbox of his own wind turbine

Next to my Dad, I would like to thank my Mum Anne for the frequent phone consultations. As no one else she could advise me what to do. This was really helpful for me.

I want to thank Zhen Gao and Amir Nejad from NTNU in Trondheim for their criticism, information supply and their (bi-)weekly guiding. Also, I would like to thank Pim van der Male and Simon Watson for keeping me sharp. Shuai Wang deserves a mention as well. He was always available for some quick questions regarding his drive train model.

Finally, I would like to thank my friends. Thanks to my friends in The Netherlands for the long phone calls. Especially thanks to Shanna, who also designed my cover page. And I also would like to thank my friends in Trondheim for the great time we spent together. Especially Lukas, for the discussions on sustainability, comments on this thesis and the dumpster dive and outdoor adventures, Guillem for the regular cross-country ski tours and the others of the penthouse of Herman Krag's veg 24. You guys made corona time a pleasure! Without them, I would not be able to write a thesis like this.

Maarten Johan Gerben van der Drift
Schiedam, August 26, 2020

Contents

Abstract	ii
Preface	iii
List of Figures	vii
List of Tables	xi
List of Symbols	xiii
List of Subscripts	xvii
List of Abbreviations	xx
Terminology	xxiv
1 Introduction	1
1.1 Problem Statement	4
1.2 Research Aim	4
1.3 Research Objective	4
1.4 Research Questions	6
1.5 Thesis Structure	6
2 Theoretical Background	7
2.1 Drive Train	7
2.1.1 Gearboxes	8
2.1.2 Bearings	10
2.1.3 Electrical Generator Basic Characteristics	12
2.1.4 10 MW Drive Train Model	12
2.2 Multibody System Modelling	13
2.3 Floating Wind Turbine	14
2.4 Maintenance	15
2.4.1 Fault Statistics	17
2.4.2 Drive Train Failure	17
2.5 Monitoring	18
2.5.1 Supervisory Control and Data Acquisition Data	18
2.5.2 Condition Monitoring	19
2.5.3 Health Monitoring	22
2.6 Loads	22
2.6.1 Aerodynamic Loads	22
2.6.2 Hydrodynamic Loads	25
2.7 Global Response Analysis	27
2.7.1 Rigid Body	27
2.7.2 Modal Analysis	28

2.8	Damage	28
2.8.1	Damage Definition	28
2.8.2	Fatigue Damage	29
2.8.3	Modelling Damage	30
3	Methodology	32
3.1	Decoupled Analysis	32
3.2	Design Load Case	33
3.3	Fault Cases	34
3.4	Natural Frequencies	35
3.4.1	Shafts Rotational Frequencies	35
3.4.2	Mesh Frequencies	36
3.4.3	Shafts Natural Frequencies	36
3.5	Fault Detection	36
3.5.1	Time Domain Analysis	36
3.5.2	Frequency Domain Analysis	41
4	Results	46
4.1	Natural Frequencies	46
4.1.1	DTU 10 MW Wind Turbine Natural Frequencies	46
4.1.2	Spar Natural Frequencies	46
4.1.3	Shafts Rotational Frequencies	47
4.1.4	Mesh Frequencies	47
4.1.5	Shafts Natural Frequencies	48
4.1.6	Non-Rotating Bearings Natural Frequencies	48
4.2	Time Series Analysis	50
4.2.1	Filtering Transient & Abnormal Behaviour	50
4.2.2	Velocity Root-Mean-Square Threshold Method	51
4.2.3	Peeters' Anomaly Detection Method	57
4.3	Frequency Domain Analysis	63
4.3.1	Angular Velocity Error Energy Method	63
4.3.2	Bearing Velocity Energy Method	66
4.3.3	Shaft Vibration Energy Method	77
4.4	Comparison Measurement Locations with ISO Standard	86
5	Discussion, Conclusion & Recommendations	89
5.1	Discussion	89
5.2	Conclusion	90
5.3	Recommendations	92
6	List of References	93
7	Bibliography	100
Appendix A	Model Specifications	106
A.1	DTU 10 MW Reference Wind Turbine Specifications	106
A.2	Spar Specifications	107
A.3	Drive Train Specifications	108

Appendix B	Natural Frequencies of Shafts & Non-Rotating Bearings	111
B.1	Shafts Natural Frequencies	111
B.2	Non-Rotating Bearings Natural Frequencies	114
Appendix C	Angular Velocity Error Energy Method Figures	120
C.1	Angular Velocity Error Function Time Series	120
C.1.1	MBR	120
C.1.2	MBX	121
C.1.3	HSBR	121
C.2	Angular Velocity Error Function Spectra	122
C.2.1	MBR	122
C.2.2	MBX	122
C.2.3	HSBR	123
Appendix D	Bearing Velocity Energy Method Figures	124
D.1	Bearing Velocity Time Series	124
D.1.1	MBR	124
D.1.2	HSBR	126
D.2	Bearing Velocity Spectra	127
D.2.1	MBR	127
D.2.2	HSBR	130
Appendix E	Shaft Vibration Energy Method Figures	131
E.1	Shaft Vibration Time Series	131
E.1.1	MBR	131
E.1.2	MBX	132
E.1.3	HSBR	133
E.2	Shaft Vibration Spectra	133
E.2.1	MBR	133
E.2.2	MBX	134
E.2.3	HSBR	135

List of Figures

1	Reference axis system	xxiv
2	Schematic layout of Wang’s 10 MW drive train model to indicate the terminology of shafts	xxv
3	Terminology of bearings	xxv
1.1	Annual global temperature anomaly	1
1.2	Total installed capacity of offshore wind farms in Europe	2
1.3	Levelized cost of energy for onshore and offshore wind energy	3
1.4	Schematic overview of the methodology followed in this study	5
2.1	Composition of a typical drive train of modern wind turbines	8
2.2	Composition of a tapered roller bearing	11
2.3	Composition of a cylindrical roller bearing	11
2.4	10 MW drive train model with two planetary stages and one parallel stage	12
2.5	Multibody system model of the 10 MW drive train model	13
2.6	Degrees of freedom of a rigid body	14
2.7	Three main floating concepts	15
2.8	Comparison of traditional maintenance methods	16
2.9	Annual failure rate and downtime per failure of wind turbines	17
2.10	Typical measurement positions of a wind turbine with two main bearings as recommended by ISO 10816-21	20
2.11	2D aerofoil basic sketch and conventions	24
2.12	Relation between drag coefficient and Reynolds number	25
2.13	Figurative explanation of modal analysis	28
2.14	Representative volume element of a material	29
2.15	Typical stress-cycle curve for fatigue analysis	30
3.1	Decoupled analysis approach for drive train data generation	32
3.2	Schematic overview of the 10 MW wind turbine drive train model	34
3.3	Typical values for the zone boundaries of the velocity root mean square of non-rotating parts as proposed by ISO 20816-1	37
3.4	Typical values for the zone boundaries of the velocity root mean square of non-rotating parts as proposed by ISO 2018-21	38
3.5	Standard normal distribution	40
3.6	Spectrum folding around the Nyquist frequency	41
4.1	Time series of low speed shaft planet carrier front bearing velocity in x -direction with MBR damage	51
4.2	Velocity root-mean-square development of critical bearings with MBR damage	52
4.3	Map showing where MBR damage is detectable using the Velocity Root-Mean-Square Threshold Method	52
4.4	Velocity in x -direction root-mean-square development of main shaft front and rear bearings with MBX damage	53
4.5	Velocity root-mean-square development of critical bearings with MBX damage	54

4.6	Map showing where MBX damage is detectable using the Velocity Root-Mean-Square Threshold Method	54
4.7	Velocity root-mean-square development of critical bearings with HSBR damage .	55
4.8	Map showing where HSBR damage is detectable using the Velocity Root-Mean-Square Threshold Method	55
4.9	Doubtful velocity root-mean-square development with MBR damage	56
4.10	β time series of velocity with HSBR damage	58
4.11	β time series of acceleration with HSBR damage	59
4.12	Doubtful β time series of velocity and acceleration with HSBR damage	60
4.13	Sensitivity analysis of fused period versus total number of baseline time series with a share of $\beta \geq 2$ higher than 4.6% for gearbox components' acceleration . .	61
4.14	Normal distributions of doubtful β time series of velocity and acceleration with HSBR damage	62
4.15	Zooms of spectra showing two angular velocity error functions with MBR damage	64
4.16	Map showing where MBR damage is detectable using the Angular Velocity Error Energy Method	65
4.17	Zooms of spectra showing two angular velocity error functions with HSBR damage	65
4.18	Zooms of spectrum showing of main shaft front bearing velocity y -direction with MBR damage	67
4.19	Zooms of spectrum showing main shaft front bearing velocity z -direction with MBR damage	67
4.20	Zooms of spectrum showing main shaft rear bearing velocity y -direction with MBR damage	68
4.21	Zooms of spectrum showing main shaft rear bearing velocity z -direction with MBR damage	69
4.22	Zooms of spectra showing low speed shaft planet carrier front bearing velocity x - and z -direction with MBR damage	70
4.23	Zooms of spectra showing low speed shaft planet carrier rear bearing velocity x - and z -direction with MBR damage	70
4.24	Zoom of spectrum showing intermediate speed shaft front bearing velocity y -direction with MBR damage	71
4.25	Zooms of spectra showing of high speed shaft front bearing velocity y - and z -direction with MBR damage	72
4.26	Zooms of spectra showing high speed shaft rear bearing velocity y - and z -direction with MBR damage	72
4.27	Map showing where MBR damage is detectable using the Bearing Velocity Energy Method	73
4.28	Zooms of spectrum showing high speed shaft front bearing velocity in y -direction with HSBR damage	74
4.29	Zooms of spectrum showing high speed shaft front bearing velocity in z -direction with HSBR damage	74
4.30	Zooms of spectrum showing high speed shaft rear bearing velocity y -direction with HSBR damage	76
4.31	Zooms of spectrum showing high speed shaft rear bearing velocity z -direction with HSBR damage	76
4.32	Map showing where HSBR damage is detectable using the Bearing Velocity Energy Method	77
4.33	Zooms of spectra showing main shaft velocity in y - and z -direction with MBR damage	78

4.34	Zooms of spectra showing main shaft acceleration in y - and z -direction with MBR damage	78
4.35	Zooms of spectra showing low speed shaft velocity in y - and z -direction with MBR damage	80
4.36	Map showing where MBR damage is detectable using the Shaft Vibration Energy Method	81
4.38	Zooms of spectrum showing main shaft acceleration in x -direction with MBX damage	82
4.37	Zooms of spectrum showing main shaft velocity in x -direction with MBX damage	82
4.39	Map showing where MBX damage is detectable using the Shaft Vibration Energy Method	83
4.41	Zooms of spectrum showing high speed shaft z -velocity with HSBR damage	84
4.40	Zooms of spectrum showing high speed shaft y -velocity with HSBR damage	84
4.42	Map showing where HSBR damage is detectable using the Bearing Velocity Energy Method	85
4.43	Concluding map showing where MBR damage is detectable	86
4.44	Concluding map showing where MBX damage is detectable	87
4.45	Concluding map showing where HSBR damage is detectable	87
A.1	Topological diagram of the 10 MW wind turbine drive train model	108
B.1	Spectra of main shaft's acceleration	111
B.2	Spectra of low speed shaft's acceleration	112
B.3	Spectra of intermediate speed shaft's acceleration	113
B.4	Spectra of high speed shaft's acceleration	113
B.5	Spectra of main shaft front bearing's velocity	114
B.6	Spectra of main shaft rear bearing's velocity	115
B.7	Spectra of the low speed shaft planet carrier front bearing's velocity	115
B.8	Spectra of the low speed shaft planet carrier rear bearing's velocity	116
B.9	Spectra of the intermediate speed shaft planet carrier front bearing's velocity	117
B.10	Spectra of the intermediate speed shaft rear bearing's velocity	117
B.11	Spectra of the high speed shaft front bearing's velocity	118
B.12	Spectra of the high speed shaft rear bearing's velocity	119
C.1	Angular velocity error functions with MBR damage	120
C.2	Angular velocity error functions with MBX damage	121
C.3	Angular velocity error functions with HSBR damage	121
C.4	Angular velocity error spectra with MBR damage	122
C.5	Angular velocity error spectra with MBX damage	123
C.6	Angular velocity error spectra with HSBR damage	123
D.1	Main shaft front bearing velocity with MBR damage time series	124
D.2	Main shaft rear bearing velocity with MBR damage time series	124
D.3	Low speed shaft front bearing velocity with MBR damage time series	125
D.4	Low speed shaft rear bearing velocity with MBR damage time series	125
D.5	Intermediate speed front bearing velocity with MBR damage time series	125
D.6	High speed shaft front bearing velocity with MBR damage time series	126
D.7	High speed shaft rear bearing velocity with MBR damage time series	126
D.8	High speed shaft front bearing velocity with HSBR damage time series	126
D.9	High speed shaft rear bearing velocity with HSBR damage time series	127

D.10	Main shaft front bearing velocity with MBR damage spectra	127
D.11	Main shaft rear bearing velocity with MBR damage spectra	128
D.12	Low speed shaft planet carrier front bearing velocity with MBR damage spectra .	128
D.13	Low speed shaft planet carrier rear bearing velocity with MBR damage spectra .	128
D.14	Intermediate speed front bearing velocity with MBR damage spectra	129
D.15	High speed shaft front bearing velocity with MBR damage spectra	129
D.16	High speed shaft rear bearing velocity with MBR damage spectra	129
D.17	High speed shaft front bearing velocity with HSBR damage spectra	130
D.18	High speed shaft rear bearing velocity with HSBR damage spectra	130
E.1	Main shaft velocity with MBR damage time series	131
E.2	Main shaft acceleration with MBR damage time series	131
E.3	Low speed shaft velocity with MBR damage time series	132
E.4	Main shaft velocity with MBX damage time series	132
E.5	Main shaft acceleration with MBX damage time series	132
E.6	High speed shaft velocity with HSBR damage time series	133
E.7	Main shaft velocity with MBR damage spectra	133
E.8	Main shaft acceleration with MBR damage spectra	134
E.9	Low speed shaft velocity with MBR damage spectra	134
E.10	Main shaft velocity with MBX damage spectra	134
E.11	Main shaft acceleration with MBX damage spectra	135
E.12	High speed shaft velocity with HSBR damage spectra	135

List of Tables

1	Terminology of shafts	xxv
2	Terminology of bearings	xxvi
3	Terminology of damage	xxvi
4	Terminology of fault cases	xxvi
1.1	Overview of increasing wind turbine sizes over the years	2
2.1	Overview of different gearbox configurations and their mass and costs for a 2.5 MW wind turbine	9
2.2	Overview of Supervisory Control and Data Acquisition parameters	19
3.1	Site characteristics Norway 5 area	33
3.2	Environmental conditions for the load case	33
3.3	Main shaft front bearing radial stiffness degradation	35
3.4	Main shaft front bearing axial stiffness degradation	35
3.5	High speed shaft rear bearing radial stiffness degradation	35
3.6	Definition of evaluation zones for vibration	37
3.7	Peeters' definition of alarm level β in colors and the maximum allowed share of β 's in that range	39
3.8	Angular velocity error functions for the different fault cases	43
4.1	Natural frequencies of the isolated DTU 10 MW reference turbine blade	46
4.2	Spar natural frequencies obtained from decay tests	46
4.3	Drive train's minimum shaft rotational frequencies	47
4.4	Drive train's maximum shaft rotational frequencies	47
4.5	Drive train's shaft rotational frequencies for a wind speed of 12 m/s	47
4.6	Drive train's minimum mesh frequencies	47
4.7	Drive train's maximum mesh frequencies	47
4.8	Drive train's mesh frequencies for a wind speed of 12 m/s	48
4.9	Shaft natural frequencies	48
4.10	Main shaft front and rear bearings natural frequencies	49
4.11	Low speed shaft planet carrier front and rear bearings natural frequencies	49
4.12	Intermediate speed shaft planet carrier front and rear bearings natural frequencies	49
4.13	Intermediate speed shaft front and rear bearings natural frequencies	49
4.14	High speed shaft front and rear bearings natural frequencies	50
4.15	Analysed angular frequency intervals for the Angular Velocity Error Energy Method	63
4.16	Normalized energy of angular velocity error function spectra frequency intervals with MBR damage	64
4.17	Normalized energy of angular velocity error function spectra frequency intervals with HSBR damage	66
4.18	Frequency intervals for main shaft front and rear bearing velocity with MBR damage	67
4.19	Normalized energy for main shaft front bearing velocity with MBR damage	68
4.20	Normalized energy for main shaft rear bearing velocity with MBR damage	69
4.21	Frequency intervals for low speed shaft planet carrier front and rear bearing velocity with MBR damage	70

4.22	Normalized energy for low speed shaft planet carrier front and rear bearing velocity with MBR damage	71
4.23	Frequency intervals for intermediate speed shaft front bearing velocity with MBR damage	71
4.24	Normalized energy for intermediate speed shaft front bearing velocity with MBR damage	71
4.25	Frequency intervals for high speed shaft front and rear bearing velocity with MBR damage	72
4.26	Normalized energy for high speed shaft front and rear bearing velocity with MBR damage	73
4.27	Frequency intervals for high speed shaft bearings velocity with HSBR damage	74
4.28	Normalized energy for high speed shaft front bearing velocity with HSBR damage	75
4.29	Normalized energy for high speed shaft rear bearing velocity with HSBR damage	75
4.30	Frequency intervals for main shaft vibration with MBR damage	77
4.31	Normalized energy for main shaft vibration velocity and acceleration with MBR damage	79
4.32	Frequency intervals for low speed shaft vibration velocity with MBR damage	79
4.33	Normalized energy for low speed shaft velocity with MBR damage	80
4.34	Frequency intervals for main shaft vibration with MBR damage	81
4.35	Normalized energy for main shaft velocity and acceleration with MBX damage	82
4.36	Frequency intervals for high speed shaft vibration velocity with HSBR damage	83
4.37	Normalized energy for high speed shaft velocity with HSBR damage	85
A.1	DTU 10 MW reference wind turbine properties	106
A.2	Properties of DTU 10 MW wind turbine's drive train	107
A.3	Spar's platform properties	107
A.4	Spar's mooring system properties	107
A.5	Specifications of 10 MW wind turbine drive train model	108
A.6	Main components' material properties	109
A.7	Gear geometrical specifications	109
A.8	Bearings designation and geometrical specifications	110
A.9	Dynamic model parameters of bearings	110
B.1	Main shaft natural frequencies	112
B.2	Low speed shaft natural frequencies	112
B.3	Intermediate speed shaft natural frequencies	113
B.4	High speed shaft natural frequencies	114
B.5	Main shaft front bearing natural frequencies	114
B.6	Main shaft rear bearing natural frequencies	115
B.7	Low speed shaft planet carrier front bearing natural frequencies	116
B.8	Low speed shaft planet carrier rear bearing natural frequencies	116
B.9	Intermediate speed shaft planet carrier front bearing natural frequencies	117
B.10	Intermediate speed shaft rear bearing natural frequencies	118
B.11	High speed shaft front bearing natural frequencies	118
B.12	High speed shaft rear bearing natural frequencies	119

List of Symbols

Matrices

C	Damping matrix [N s/m] or [Nm s/rad]
F	Force vector [N] or [Nm]
K	Stiffness matrix [N/m] or [Nm/rad]
M	Mass matrix [kg] or [kg m ²]
x	Position vector [m] or [rad]

Symbols

α	Deterministic parameter [-]
α	Gear ratio [-]
β	Alarm level [-]
β	Angle [rad] or [°]
γ	Deterministic parameter [-]
Λ	Height dependent parameter [m]
λ	Wave length [m]
μ	Mean [unit]
ν	Kinematic viscosity ($\approx 1.5 \times 10^{-5}$ m ² /s for air) [m ² /s]
ν	Poisson's ratio [-]
ω	Angular frequency [rad/s]
ω	Deterministic parameter [-]
ω	Shaft rotational speed [rad/s]
ϕ	Angular position [rad]

ϕ	Blade twist [rad] or [$^{\circ}$]
ρ	Density [kg/m ³]
σ	Parameter [unit]
σ	Standard deviation [unit]
σ	Stress [Pa]
τ	Torque [Nm]
θ	Angle [rad] or [$^{\circ}$]
φ	Power spectral density [unit ² /Hz] or [unit ² s/rad]
a	Parameter [-]
C	Damping [N s/m]
c	Chord length [m]
c	Coefficient [-]
c	Crest factor [-]
D	Diameter [m]
d	Lift per unit span [N/m]
E	Energy [unit ²]
E	Young's modulus [Pa]
e	Dynamic transmission error [rad/s]
F	Forcing element [N] or [Nm]
f	Force per length [N/m]
f	Frequency [Hz]
g	Gravitational acceleration (≈ 9.81 m/s ²)
H	Wave amplitude [m]
I	Turbulence intensity [-]

K	Kurtosis [-]
K	Stiffness [N/m]
k	Wave number [m^{-1}]
L	Lag size [unit]
L	Parameter [m]
L	Scale parameter [m/s]
l	Length [m]
l	Lift per unit span [N/m]
N	Number [-]
n	Number of teeth [-]
r	Parameter [-]
Re	Reynolds number [-]
S	Stress level [Pa]
S	Surface area [m^2]
s	Skewness [-]
t	Time [s]
u	Wind speed [m/s]
V	Wind speed [m/s]
v	Local transverse body velocity [m/s]
x	Coordinate [m]
x	Global motion [m] or [rad]
x	Parameter [unit]
y	Coordinate [m]
z	Coordinate [m]

Operators

$E\{\cdot\}$	Expectation operator
$f(\cdot)$	Function
$N(\cdot)$	Normal distribution operator
$V\{\cdot\}$	Variance operator
$y(\cdot)$	Constructed feature
d	Exterior derivative operator
$\text{Re}(\cdot)$	Real part operator

List of Subscripts

<i>0</i>	Initial
<i>1,2,3,...</i>	First, second, third
<i>10</i>	At 10 m altitude
<i>$\alpha\alpha$</i>	Axial
<i>$\beta\beta$</i>	Radial
<i>$\gamma\gamma$</i>	Yaw
<i>ac</i>	Of AC system
<i>acc</i>	Acceleration
<i>air</i>	Of air
<i>BL</i>	Baseline
<i>cut-in</i>	Cut-in
<i>cut-out</i>	Cut-out
<i>D</i>	Drag or damaged
<i>HS-A</i>	High speed shaft front bearing
<i>HS-B</i>	High speed shaft front bearing
<i>HSBR</i>	For high speed shaft rear bearing radial damage
<i>HSS</i>	Of high speed shaft
<i>IMS</i>	Of intermediate speed shaft
<i>IMS-A</i>	Intermediate speed shaft front bearing

<i>INP-A</i>	Main shaft front bearing
<i>INP-B</i>	Main shaft rear bearing
<i>H</i>	Planet carrier
<i>i</i>	Number, gear stage or function
<i>in</i>	Input
<i>J</i>	JONSWAP
<i>j</i>	Number, coordinate or fault case
<i>K</i>	Kaimal
<i>k</i>	Direction
<i>L</i>	Lift
<i>LSS</i>	Of low speed shaft
<i>l</i>	Lower
<i>local</i>	Local
<i>MBR</i>	For main shaft front bearing radial damage
<i>MBR</i>	For main shaft front bearing axial damage
<i>MS</i>	Main shaft
<i>m</i>	Mesh
<i>N</i>	Noise
<i>Nyq</i>	Nyquist
<i>n</i>	Number
<i>out</i>	Output
<i>PLC-A</i>	First stage planet carrier front bearing

<i>PLC-B</i>	First stage planet carrier rear bearing
<i>p</i>	Peak or pitch
<i>rated</i>	Rated
<i>ref</i>	Reference altitude
<i>ring</i>	Of ring gear
<i>RMS</i>	Root-mean-square
<i>S</i>	Significant
<i>s</i>	Sample
<i>sun</i>	Of sun gear
<i>tot</i>	Total
<i>u</i>	Upper
<i>vel</i>	Velocity
<i>wind</i>	Of wind
<i>x</i>	In <i>x</i> -direction
<i>xx</i>	Axial
<i>y</i>	In <i>y</i> -direction
<i>yy</i>	Tangential
<i>zz</i>	Radial
<i>*</i>	Normalized

List of Abbreviations

2D	Two dimensional
3D	Three dimensional
AEP	Annual energy production
AGMA	American Gear Manufacturers Association
AI	Artificial intelligence
BEM	Blade element momentum
BL	Baseline
CBM	Condition-based maintenance
CMS	Condition monitoring systems
CMT	Condition monitoring technique
CM	Condition monitoring
CO₂	Carbon dioxide
COB	Center of buoyancy
COG	Center of gravity
CRB	Cylindrical roller bearing
DNV-GL	Det Norske Veritas Germanischer Lloyd
DOF	Degrees of freedom
DTU	Danmarks Tekniske Universitet

ECN	Energieonderzoek Centrum Nederland
EM	Electromechanical
EOM	Equations of motion
EWEA	European Wind Energy Association
FC	Fault case
FE	Force element
GDW	Generalized dynamic wake
GWEC	Global Wind Energy Council
HSBR	High speed shaft rear bearing radial damage applied on HS-B
HSE	Health, safety and environment
HSS	High speed shaft
HS	High speed shaft bearing
ICRA	International Conference on Robotics and Automation
IEA	International Energy Agency
IEC	International Electrotechnical Commission
IEEE	Institute of Electrical and Electronics Engineers
IMS-PLC	Second stage planet carrier bearing
IMS-PL	Second stage planet bearing
IMS	Intermediate speed shaft (bearing)
INP	Main shaft bearing
IRENA	International Renewable Energy Agency

ISHM	Integrated system health management
IWES	Institute for Wind Energy and Energy System Technology
JONSWAP	Joint North Sea Wave Observation Project
LCOE	Levelized cost of energy
LSS	Low speed shaft
Ltd	Limited company
MBR	Main shaft front bearing radial damage applied on INP-A
MBS	Multibody system
MBX	Main shaft front bearing axial damage applied on INP-A
MS	Main shaft
NASA	National Aeronautics and Space Administration
NREL	National Renewable Energy Laboratory
NTNU	Norges teknisk-naturvitenskapelige universitet
PLC	First stage planet carrier bearing
PL	First stage planet bearing
PM	Pierson-Moskowitz
PP	Pole pairs
PSD	Power spectral density
RMS	Root-mean-square
rel.	Relative
RUL	Remaining useful lifetime
RVE	Representative volume element

SCADA	Supervisory control and data acquisition
SHM	Structural health monitoring
SINTEF	Stiftelsen for industriell og teknisk forskning
SPC	Statistical process control
SWL	Still water level
TE	Transmission error
TRB	Tapered roller bearing
UK	United Kingdom
VMP	Vestas multi processor

Terminology

In this work, damage is applied on bearings of a 10 MW wind turbine drive train model. This model is developed by Wang [Wang et al., 2019] and is later referred to as (Wang's) drive train model. Notations will be used which indicate different gearbox components, different kinds of damage and degradation levels. This section is used to clarify the terminology used.

First, the axis system is introduced. Chosen is for a right handed axis system, as is shown in Figure 1. The x -axis is pointing in the direction of the shafts, depicted in Figure 2.

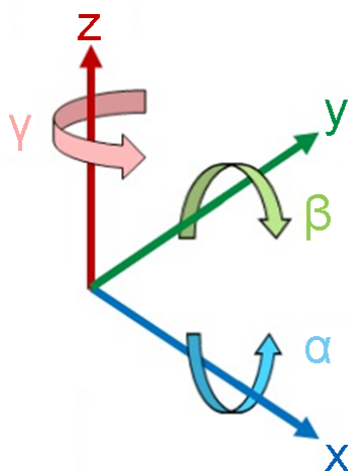


Figure 1: Reference axis system

In Figure 2 one can find a schematic layout of Wang's 10 MW drive train model [Wang et al., 2019], which is used in this study. The name of the shafts are indicated in red. Correspondingly, in Table 1, one can find how it is referred to in this work. Although, Wang's drive train is of a medium speed type, its output end of the drive train is referred to as the high speed end.

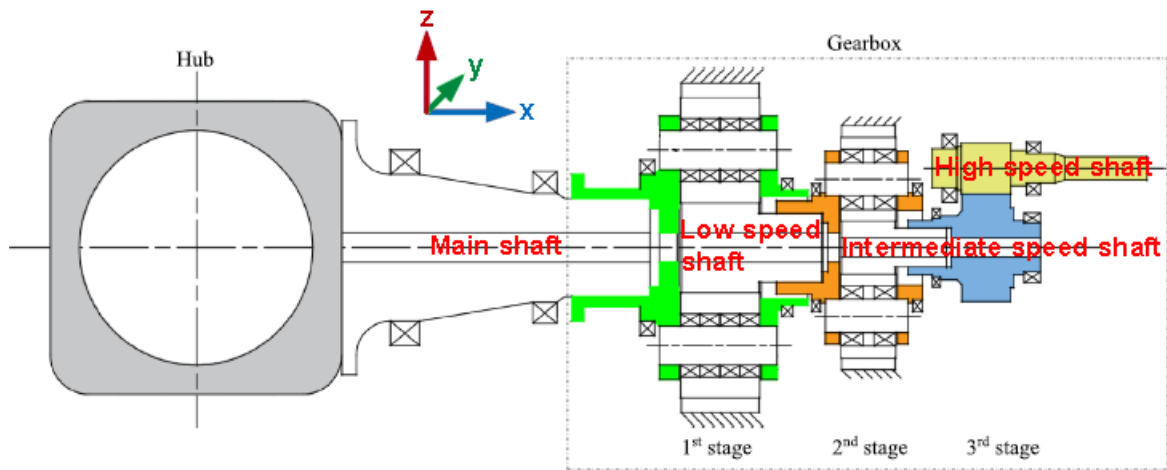


Figure 2: Schematic layout of Wang's 10 MW drive train model to indicate the terminology of shafts [Wang et al., 2019]

Table 1: Terminology of shafts

Shaft no.	Abbreviation	Shaft name
1	MS	Main shaft
2	LSS	Low speed shaft
3	IMS	Intermediate speed shaft
4	HSS	High speed shaft

Another schematic layout of the drive train is depicted in Figure 3. This one serves to display the bearings, splines and gears present in the drive train. In Table 2 the bearing names and abbreviations are depicted, corresponding to the figure below.

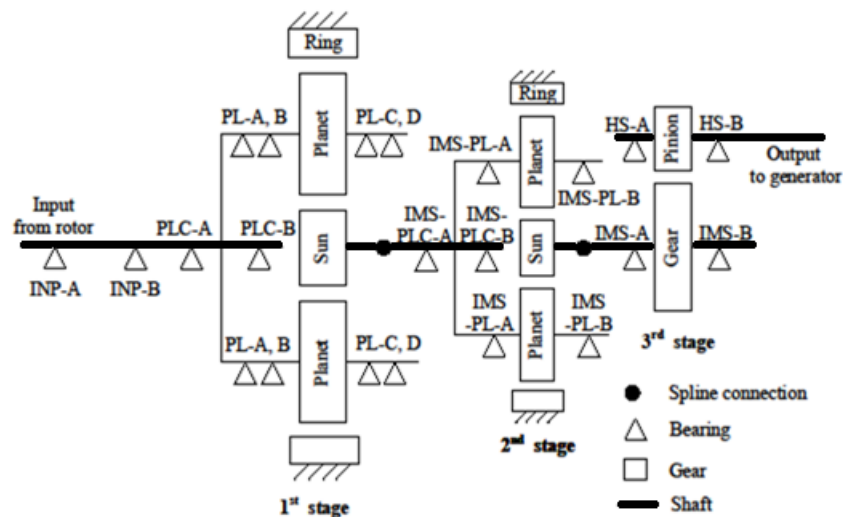


Figure 3: Terminology of bearings

Table 2: Terminology of bearings

Abbreviation	Bearing name	Abbreviation	Bearing name
INP-A	Main shaft front bearing	INP-B	Main shaft rear bearing
PLC-A	First stage planet carrier front bearing	PLC-B	First stage planet carrier rear bearing
PL-A,B	First stage planet front bearings	PL-C,D	First stage planet rear bearings
IMS-PLC-A	Second stage planet carrier front bearing	IMS-PLC-B	Second stage planet carrier rear bearing
IMS-PL-A,B	Second stage planet front bearings	IMS-PL-C,D	Second stage planet rear bearings
IMS-A	Intermediate speed shaft front bearing	IMS-B	Intermediate speed shaft rear bearing
HS-A	High speed shaft front bearing	HS-B	High speed shaft rear bearing

In this study, three types of damage with a certain degradation level are applied on the bearings. The terminology indicating the type of damage is depicted in Table 3. Here, axial damage refers to damage in the x -direction. Radial damage refers to damage in the y - and z -direction. The degradation level is indicated with a fault case, the names of the fault cases are depicted in Table 4. Example: FC1 of MBX would mean main shaft front bearing axial damage applied on INP-A with 15% degradation.

Table 3: Terminology of damage

Abbreviation	Damage type
MBR	Main shaft front bearing radial damage applied on INP-A
MBX	Main shaft front bearing axial damage applied on INP-A
HSBR	High speed shaft rear bearing radial damage applied on HS-B

Table 4: Terminology of fault cases

Abbreviation	Fault case	Degradation level [%]
BL	Baseline	0
FC1	Fault case 1	15
FC2	Fault case 2	30
FC3	Fault case 3	50
FC4	Fault case 4	70
FC5	Fault case 5	90

1 | Introduction

One of the world's biggest concerns is global warming. The concentration of greenhouse gasses is increasing [Ritchie and Roser, 2018] and, as a result, the Earth is warming up more and more [Hansen et al., 2010] as is shown in Figure 1.1. The consequences can be severe and are, amongst others: sea level rise, ice free arctic, more droughts, more wildfires and an increased frequency and duration of storms¹. Solutions should be found in order to decrease these effects.

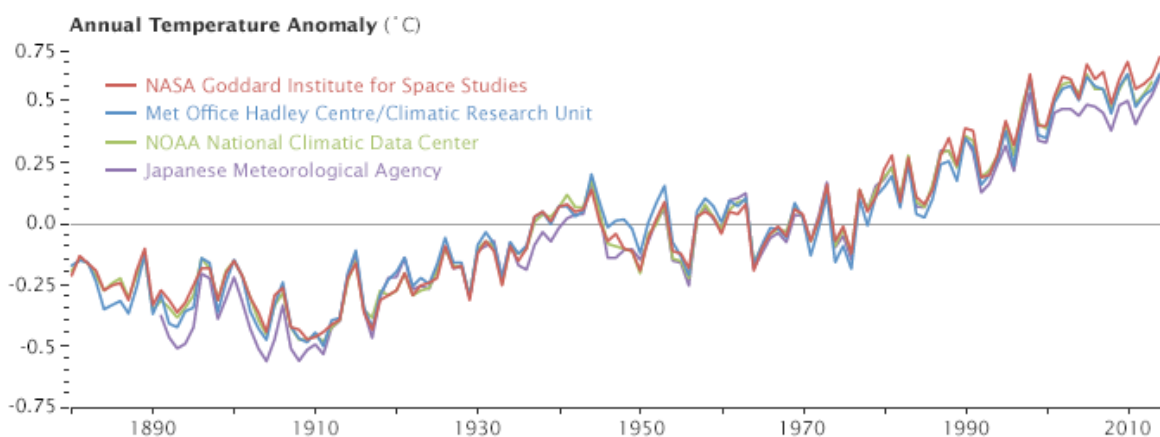


Figure 1.1: Annual global temperature anomaly²

One of the solutions is renewable energy. This is energy obtained from sources that do not deplete³. Examples are wind, solar, geothermal, biomass and hydroelectric energy. However, the levelized cost of energy (LCOE) is higher compared to energy produced from fossil fuels, especially solar and wind power [IRENA, 2019b, p. 12]. To reduce these costs, innovative steps need to be undertaken. One of the concerned areas is the maintenance of offshore wind turbines.

As of the end of 2019, globally a cumulative wind power capacity of 651 GW was reached of which the offshore installations contribute with a capacity of 29 GW. 6.1 GW is installed offshore in 2019 and 54.3 GW is installed on land, adding up to a total of 60.4 GW installed in 2019 [Lee et al., 2020]. That the offshore wind market is rapidly growing is shown in Figure 1.2.

¹<https://climate.nasa.gov/effects/> [Visited on 3rd of December 2019]

²<https://earthobservatory.nasa.gov/world-of-change/DecadalTemp> [Visited on 3rd of December 2019]

³<https://www.studentenergy.org/topics/renewable-energy> [Visited on 3rd of December 2019]

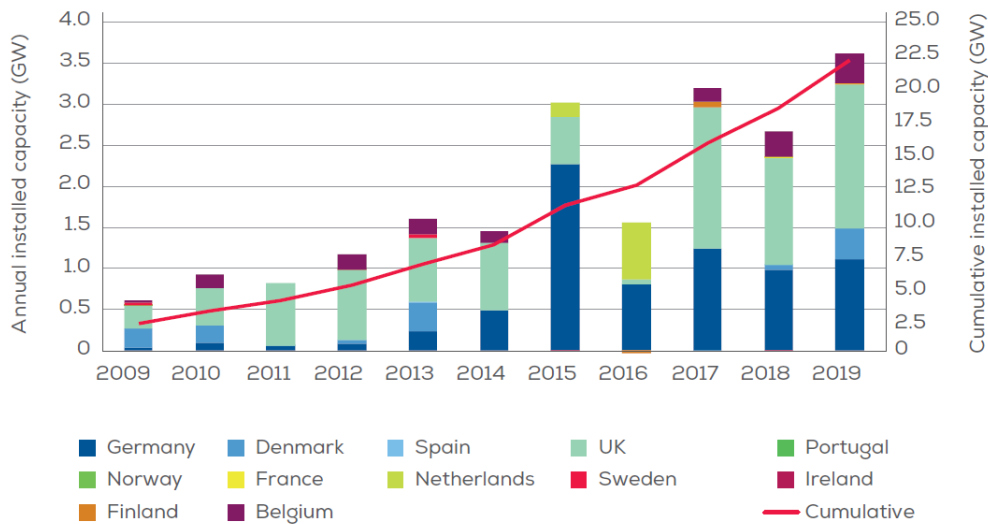


Figure 1.2: Total installed capacity of offshore wind farms in Europe [Ramírez et al., 2020, p. 7]

The growth of the offshore wind industry can be explained, since it has many advantages over on-shore wind. These advantages include: higher wind potential and higher energy demand in coastal areas⁴. Also, since the world’s population is increasing, land is getting scarcer. Land, which is normally used for energy production, can now be used for agriculture and housing. Finally, there are less noise and size restrictions, since the turbines will be placed far away from the shore.

Not only the installed capacity is growing. Due to the innovations in wind energy technology bigger wind turbines can and will be produced, as is shown in Table 1.1. One can see that next to the rated power, the tower height and rotor diameter are increasing. The newly installed 12 MW Haliade-X has a rotor diameter of 220 m and a total height of 260 m⁵. The increasing capacity of wind turbines, caused a demand in knowledge to support bigger wind turbines and to transfer the higher energy rate.

Table 1.1: Overview of increasing wind turbine sizes over the years [Gao, 2019]⁶

Year	Rated power [MW]	Blade length [m]	Blade weight [ton]	Hub height [m]	Nacelle weight [ton]
1989	0.3	5	2	45	3.9
1995	1.3	31	10	68	50
1999	2	44	10	78	75
2005	5	61.5	17	90	240
2016	8	82	35	138	390

Novel and cheaper solutions are continuously developed. These are needed to lower the LCOE, leading to improvements in offshore wind energy. As is shown in Figure 1.3, the LCOE for offshore is decreasing and reducing the gap with the LCOE of onshore wind.

⁴<https://www.americangeosciences.org/critical-issues/faq/what-are-advantages-and-disadvantages-offshore-wind-farms> [Visited on 3rd of December 2019]

⁵<https://www.windpowerengineering.com/vattenfall-and-ge-join-forces-to-deploy-haliade-x-the-worlds-largest-wind-turbine/> [Visited on 1st of June 2020]

⁶<https://en.wind-turbine-models.com/> [Visited on 10th of January 2020]

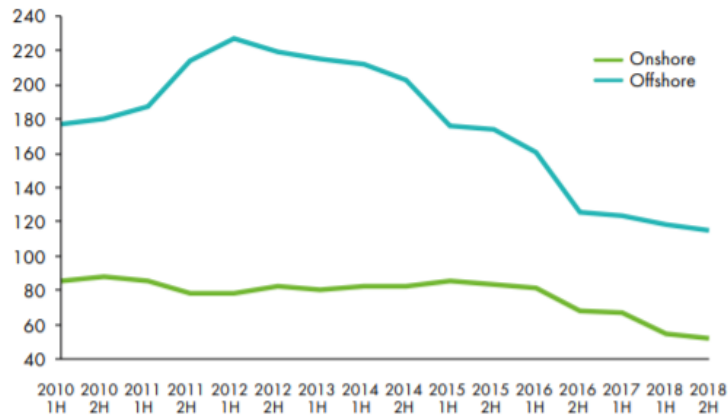


Figure 1.3: LCOE (\$/MWh) for onshore and offshore wind energy [Ohlenforst et al., 2018, p. 17]

By the end of 2019, the following is accomplished in Europe [Ramírez et al., 2020]:

- A total of 5047 offshore wind turbines installed and grid-connected, producing 22072 MW
- 110 wind farms commissioned
- 12 European countries participating
- Average newly-installed offshore wind turbine size is 7.8 MW, 1 MW higher than the average capacity of 2018 [Ramírez et al., 2020]
- 1 full-scale grid-connected floating turbine park

However, the offshore wind industry can not afford to sit back. In order to become competitive with fossil fuels and other renewable energy sources, the LCOE needs to get drastically reduced. Now is the time to come up with more novel and innovative solutions, as stagnation is regression.

Wind energy can have a main role in carbon dioxide (CO₂) emission reductions [IRENA, 2019a], which are imposed by the Paris Agreement. Accelerated wind power deployment could lead to one-quarter (≈ 6.3 gigatonnes) of the annual reductions, covering more than one-third of the global power needs. To fulfill this aim, a capacity of 5000 GW of onshore and 1000 GW of offshore wind needs to get installed quickly. Asia can play a big role to increase the global wind energy capacity to ten times the current capacity. When increasing the scales, electricity costs can drop to 0.03\$/kWh (onshore wind) and 0.07\$/kWh (offshore wind) [IRENA, 2019a].

1.1 Problem Statement

Maintenance of wind turbines which are difficult to access, such as the ones situated offshore, is a costly operation [Rockmann et al., 2017]. Not only the man-hours and downtime are major cost contributors to maintenance costs, also maintenance vessels and helicopters are increasing the costs [Poore and Walford, 2008]. In recent years, numerical tools have been developed for analysing complex aerodynamic and hydrodynamic loads. As a result, its coupling effect, global motion and structural responses of both bottom-fixed and floating wind turbines on aerodynamic and hydrodynamic loads can be predicted. In combination with obtained global responses and high-fidelity models of gearboxes, pitch actuators and yaw mechanisms, it is possible to estimate the loads and responses in these mechanical components and to predict the time when the fatigue failure will occur [Cho, 2019, Nejad et al., 2016b, Wang et al., 2019]. In order to predict the drive train's time until failure, one needs to understand the propagation of vibrations through the system after introduction of a fault. Currently, little is known about fault detectability and vibration propagation in a drive train of an offshore wind turbine.

1.2 Research Aim

Mechanical systems in offshore wind turbines, such as gearboxes, blade pitch actuators and yaw systems, are subject to relatively high failure rates and high downtimes due to complex loadings from turbulent wind [Cho, 2019, Chaaban et al., 2014, Wilkinson and Hendriks, 2010, Rademakers et al., 2011]. In today's industry, a gearbox, for example, is not designed considering specific features of aerodynamic loads for different offshore sites and foundations, such as intermittent forces associated with teetering [Manwell et al., 1999]. The main aim of this research is to get an insight about the effect of faults on the monitoring data of a drive train. Different methods for fault detection in the time and frequency domain are deployed and compared.

1.3 Research Objective

The status of the mechanical systems, particularly the potential failures, needs to be predicted in order to do a timely maintenance before faults occur, of which its occurrence may lead to severe consequences [Coronado and Fischer, 2015]. This can be used in connection with predictive maintenance of these mechanical components. Digital twin models, like Nejad's and Wang's drive train models [Nejad et al., 2016b, Wang et al., 2019] and Cho's pitch model [Cho, 2019], can be run based on the historical environmental data of the offshore site or in real time to predict accumulated damage.

The objective of this thesis is to detect faults and their vibration propagation in an offshore wind turbine's drive train. Therefore, data, generated by a physical model with three simulated faults applied one by one, will be compared with data from a normal functioning wind turbine, to detect deviations in the monitoring data, which may indicate early faults. This is done using fault detection and diagnosis methods. Methods applied will make use of, amongst others, statistical indicators from the time domain [Ghane, 2018, Peeters et al., 2006] and features from the frequency domain. The methodology followed in this study, follows the structure presented in Figure 1.4.

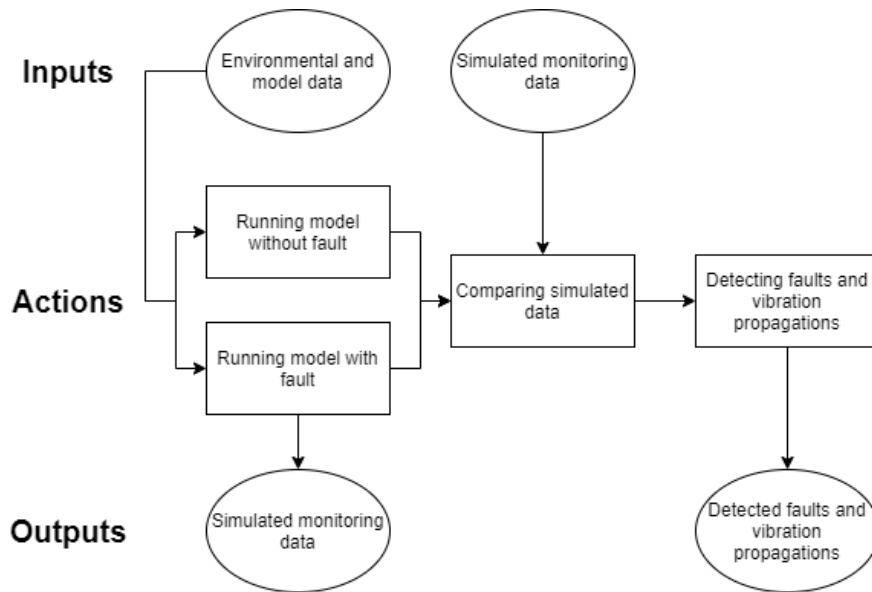


Figure 1.4: Schematic overview of the methodology followed in this study

A 10 MW high fidelity drive train model, developed by Wang [Wang et al., 2019], will be deployed and different fault conditions will be evaluated using one common, two non-traditional and two novel fault detection methods in the time and frequency domain. These are respectively:

1. **Velocity Root-Mean-Square (RMS) Threshold Method.** A common fault detection method in the time domain proposed by ISO [ISO, 2015, ISO, 2016] based on the vibration velocity of non-rotating parts. Its performance is already demonstrated in literature [Ghane et al., 2017, Nejad and Moan, 2017].
2. **Peeters' Anomaly Detection Method.** An interpretation of a fault detection in the time domain proposed in the PhD thesis of Peeters [Peeters et al., 2006]. It makes use of the normal distribution of statistical indicators in the time domain.
3. **Angular Velocity Error Energy Method.** A fault detection method in the frequency domain developed by Nejad [Nejad et al., 2014c]. It makes use of the angular velocity measurements from the drive train's main and high speed shaft, using two additional rotational velocity sensors on the low speed and intermediate speed shafts.
4. **Bearing Velocity Energy Method.** A new method based on the Velocity RMS Threshold Method and the Angular Velocity Error Energy Method. It makes use of bearing velocity measurements in the drive train and compares peaks in its spectra.
5. **Shaft Vibration Energy Method.** A novel method in the frequency domain based on the Angular Velocity Error Energy Method. The peaks of spectra displaying the shafts' vibration velocity and acceleration response are compared.

The outcome will contribute to the understanding of fault detection and vibration propagation in a drive train. It will be a valuable input for research on vibration propagation, since deviation in monitoring data might very well indicate new faults. Moreover, this study's results can be a tool for setting up a framework for predictive maintenance of an offshore wind turbine's drive train.

1.4 Research Questions

The research questions answered are:

1. Is it possible to detect drive train bearing faults using non-traditional fault detection methods?
2. Is vibration propagation caused by bearing faults detectable using non-traditional fault detection methods?
3. From which degradation level are faults and their vibration propagation detectable using non-traditional fault detection methods?

1.5 Thesis Structure

In order to answer these research questions, this thesis is introduced. It is structured as follows. In Chapter 2, relevant theoretical background information is presented. It includes, amongst others, a review on maintenance and monitoring techniques and fault statistics. Also, the drive train and its model is explained in more detail. Aerodynamic and hydrodynamic loads are described and it is explained how the model responds on these loads. Finally, it is explained how damage is modeled in this project.

Then, in Chapter 3 one can find how the research is set up. The research work is set up in two parts: a time domain and a frequency domain analysis. The time domain analysis consists of two fault detection methods: the Bearing Velocity RMS Threshold Method and the Peeters' Anomaly Detection Method. In the frequency domain one non-traditional and two new fault detection methods are deployed. One of these is the Angular Velocity Error Energy Method, developed by Nejad [Nejad et al., 2014c]. Two novel frequency domain fault detection methods are introduced in this project: the Bearing Velocity Energy Method (based on Nejad's method and the Bearing Velocity RMS Threshold Method) and the Shaft Vibration Energy Method (also based on Angular Velocity Error Energy Method).

The outcome of this work is displayed and discussed in Chapter 4. It includes the presentation of the system's natural frequencies, but also the results of the five deployed methods. Some interesting results can be found here. The results are compared with the recommendations of a safety standard [ISO, 2015].

This research work is wrapped up with a discussion, conclusion and some recommendations in Chapter 5. Finally, to support this work, numbers, figures and characteristics of models and results are depicted in the appendices.

2 | Theoretical Background

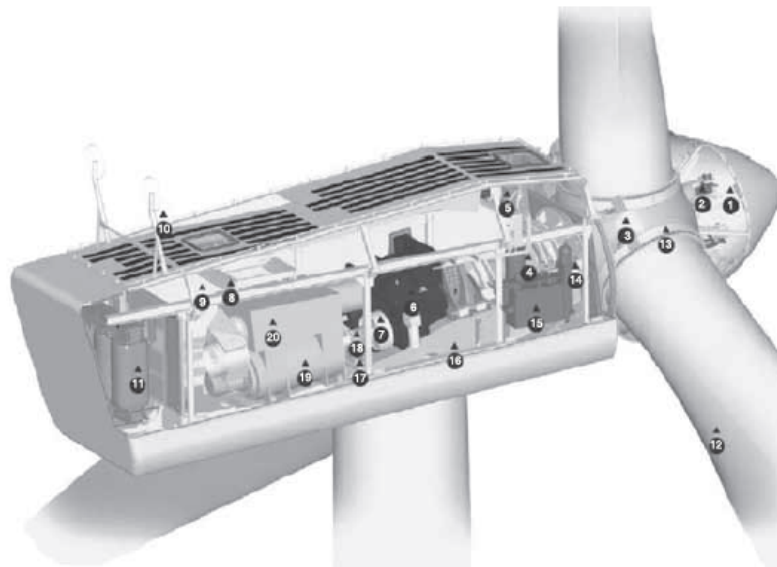
In this chapter, relevant theoretical background information is provided on techniques used in this research work. In the following, the drive train is thoroughly discussed in Section 2.1, since this is this component of interest in this work. The data used for analysis in this thesis is obtained from the response of a 10 MW drive train model. A brief explanation on its layout is presented in Section 2.1.4. The model is created using multibody system (MBS) modelling. Therefore, in Section 2.2, MBS modelling is explained. A new concept in the offshore wind industry is the floating wind turbine. Since, in this work, the wind turbine is placed on a floater for data generation, a short description on floaters is given in Section 2.3. This project serves to provide more insight in maintenance strategies, its state-of-the-art is described in Section 2.4. The data generated should be obtained in real life in order to make the outcome of the project useful. Therefore, one can find an overview on monitoring techniques in Section 2.5. Then, a little insight is given on how loads are generated as an input in Section 2.6. The response on these loads is shown in Section 2.7. Damage is introduced in the healthy drive train model by decreasing bearing stiffness and damping, this is justified by the explanation shown in Section 2.8.

2.1 Drive Train

The main function of a drive train is converting the mechanical energy at the rotor hub of the wind turbine to electrical energy, and to send it to the grid [Chen, 2011]. In typical wind turbine drive trains the power is transmitted from the rotor to the generator through the system composed of the main shaft, friction connection, multiplying gearbox and a flexible coupling [Gawarkiewicz et al., 2015]. The main components include the gearbox, generator and power electronic converters.

A gearbox converts the low speed, high torque power into high speed and low torque power to drive a normal generator. The gearbox is not there if the generator is a direct-drive type which can produce electricity at the low speed side of the wind turbine's rotor [Chen, 2011].

Electricity generation is possible when the wind velocity exceeds the cut-in wind speed V_{cut-in} , but is still below the cut-out wind speed $V_{cut-out}$. The turbine works at 100% capacity with wind speeds higher than the rated wind speed V_{rated} . A small drop of rotational speed results in a significant decrease in the generated power [Gawarkiewicz et al., 2015]. The composition of a typical drive train is presented in Figure 2.1.



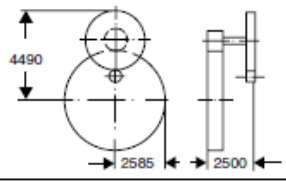
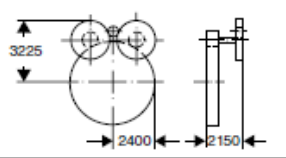
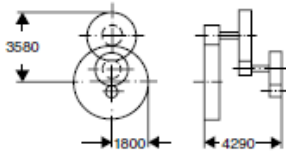
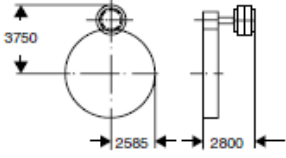
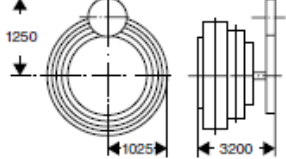
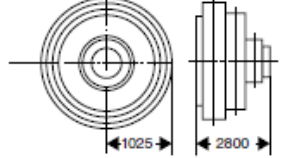
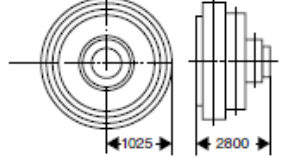
- | | |
|-------------------------------------|----------------------------|
| ① Hub controller | ⑪ High voltage transformer |
| ② Pitch cylinders | ⑫ Blade |
| ③ Blade hub | ⑬ Blade bearing |
| ④ Main shaft | ⑭ Rotor lock system |
| ⑤ Oil cooler | ⑮ Hydraulic unit |
| ⑥ Gearbox | ⑯ Machine foundation |
| ⑦ Mechanical disc brake | ⑰ Yaw gears |
| ⑧ Service crane | ⑱ Composite disc coupling |
| ⑨ VMP-Top controller with converter | ⑲ OptiSpeed® generator |
| ⑩ Ultrasonic wind sensors | ⑳ Air cooler for generator |

Figure 2.1: Composition of a typical drive train of modern wind turbines. VMP controller = Vestas multi processor controller [Chen, 2011]

2.1.1 Gearboxes

Gears are used to transmit power between shafts rotating at different speeds [Chen, 2011]. A combination of gears may be used to increase the low rotational speed of the turbine blades to a high rotational speed for a standard generator [Chen, 2011]. In Table 2.1, one can find an overview of different gearbox configurations and its mass and costs for a 2.5 MW wind turbine.

Table 2.1: Overview of different gearbox configurations and their mass and costs for a 2.5 MW wind turbine [Nejad, 2018, Hau, 2008, Thornblad, 1978]

Configuration:		mass (t)	rel. costs (%)
two stages: parallel		70	180
two stages: parallel with torque splitting		56	164
three stages: parallel		77	192
two stages: one parallel one planetary		41	169
three stages: two planetary one parallel		17	110
three stages: planetary		11	100

The following three gear types are often used and therefore explained in the following [Chen, 2011]:

- **Spur gear (most common):** Teeth are parallel to the rotational axis of the gear. Tooth contact is primarily rolling.
- **Single helical gear:** Cylindrical shaped gear with angled teeth. Designed such that the teeth come in contact with one another with gradually increasing pressure. The load on helical gears is distributed over several teeth, resulting in reduced wear. Helical gears operate with less noise and vibration than spur gears.
- **Double helical gear/Herringbone gear:** May have both left-hand and right-hand helical teeth set in a V-shape.

Gears can be combined in different configurations [Chen, 2011]:

- **Parallel stage:** Two different size gears are fixed on two parallel shafts. The rotational speed ω is inversely proportional to the number of teeth n and the gear diameter D . Equation 2.1 shows its speed-up ratio.

$$\frac{\omega_{HSS}}{\omega_{LSS}} = \frac{n_{LSS}}{n_{HSS}} = \frac{D_{LSS}}{D_{HSS}} \quad (2.1)$$

- **Planetary stage:** The main components of a planetary stage include: an interior toothed gear wheel, two or three smaller toothed gear wheels, a common carrier arm and a centrally placed toothed gear wheel. The ring gear is stationary while the planet carrier is mounted on the turbine rotor shaft rotating with the same speed as the rotor shaft. The planet carrier transmits the driving torque to the planet gears. Planetary gear stages are more compact and produce a higher torque density. Its speed-up ratio is calculated with Equation 2.2.

$$\frac{\omega_{HSS}}{\omega_{LSS}} = 1 + \frac{D_{ring}}{D_{sun}} \quad (2.2)$$

Spur gears and helical gears are used in both parallel gear stages and planetary gear stages.

As power and rotor diameter of a wind turbine increase, the torque and gear ratio also increase [Chen, 2011]. Therefore, multistage gearboxes are required. Typically, three gear stages are used. A planetary stage is designed for a gear ratio up to seven and a parallel stage's ratio usually up to five. The following components are associated with the gearbox and may contribute to its failures [Chen, 2011]:

- **Bearings:** Constrains motion to only the desired motion and reduces friction between moving parts. More on this in Section 2.1.2.
- **Shafts:** Cylindrical elements used to transmit torque.
- **Couplings:** Elements used to connect and transmit torque between two shafts.
- **Mechanical brakes:** Can bring the rotor to a complete stop and halt the turbine blades. The brakes are usually spring or hydraulic operated and designed to work even during electrical power failure. The mechanical brake is built with a fail-safe mechanism. The aerodynamic brake is preferred for stopping as less stress is being placed on the system.
- **Yaw mechanism:** An electric or hydraulic system is used to align the rotor axis with the wind in order to extract as much energy from the wind as possible.

2.1.2 Bearings

Only the torque component is useful for the generator to produce electricity from mechanical energy. The other loading components are transferred towards the tower by means of bearings [Chen, 2011]. Bearings serve to reduce the frictional resistance between two surfaces with relative motion and can be either linear/axial or rotational/radial. Multiple types of bearings are distinguished and include, amongst others: ball bearings, rolling bearings, ball thrust bearings, roller thrust bearings and magnetic bearings¹. In Wang's drive train model (see Section 2.1.4), two types are used: tapered roller bearing (TRB) and cylindrical roller bearing (CRB) [Wang et al., 2019].

¹<https://science.howstuffworks.com/transport/engines-equipment/bearing3.htm> [Visited on 20th of July 2020]

TRBs are able to support large axial and radial loads. They are usually installed in pairs facing opposite directions so that they can handle axial loads in both directions¹, to obtain a large carrying capacity [Yang et al., 2018b] and to achieve a rigid bearing application². A TRB consists of a cup and cone assembly. The outer ring can be found in the cup. The cone assembly is composed of a cage, inner ring and rollers. The TRB provides low friction during operation². A typical composition of a TRB is shown in Figure 2.2.



Figure 2.2: Composition of a tapered roller bearing²

CRBs are able to carry heavy radial loads and cope with high speeds. They accommodate axial displacement and offer high stiffness, low friction and long service life³. CRBs consist of an inner and outer ring, a roller-retaining cage and cylindrical rollers [Timken, 2011]. The cage prevents the rollers from getting into contact with the other roller⁴. Redistribution of the outer load continuously takes place. Less than half of the total number of rollers carry a significant share of the load⁵.

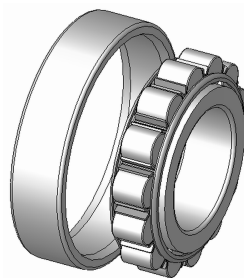


Figure 2.3: Composition of a cylindrical roller bearing⁵

²<https://www.skf.com/group/products/rolling-bearings/roller-bearings/tapered-roller-bearings> [Visited on 20th of July 2020]

³<https://www.skf.com/group/products/rolling-bearings/roller-bearings/cylindrical-roller-bearings> [Visited on 20th of July 2020]

⁴https://www.schaeffler.de/content.schaeffler.de/en/products-and-solutions/industrial/product-portfolio/rolling_and_plain_bearings/cylindrical_roller_bearings/index.jsp [Visited on 20th of July 2020]

⁵https://en.wikipedia.org/wiki/Rolling-element_bearing#Cylindrical_roller [Visited on 20th of July 2020]

2.1.3 Electrical Generator Basic Characteristics

Generator and power electronics integration affects the performance of the wind power systems. A generator consists of a stator and a rotor, with in between the air gap, where a rotating electromagnetic field is produced by three-phase AC current flowing in the machine windings. Its rotating speed is calculated with Equation 2.3 and is related to the synchronous speed ω_s , AC system frequency f_{ac} and number of pole pairs PP [Chen, 2011].

$$\omega_s = \frac{60f_{ac}}{PP} \quad (2.3)$$

There are two types of generators: synchronous and asynchronous/induction generator. The last one operates at a varying speed different from the synchronous speed [Chen, 2011].

2.1.4 10 MW Drive Train Model

The drive train model used in this study is the 10 MW model developed by Wang [Wang et al., 2019], which is designed for the DTU 10 MW wind turbine [Bak et al., 2013]. For the wind turbine's specifications, see Appendix A.1. Wang's drive train is a four-point support drive train configuration with two main bearings and two torque arms having two planetary stages and one parallel stage [Wang et al., 2019]. The layout of the drive train model is presented in Figure 2.4.

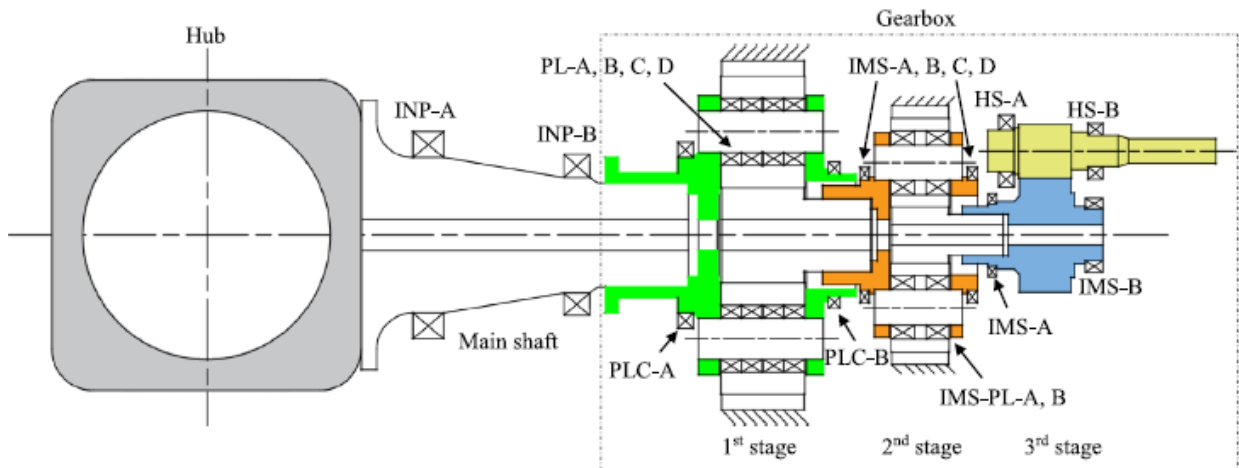


Figure 2.4: 10 MW drive train model with two planetary stages and one parallel stage [Wang et al., 2019]

The drive train is modelled using an MBS approach [Wang et al., 2019], which is explained in Section 2.2. For the drive train dynamics SIMPACK [SIMPACK, 2020] is deployed. Here, the main shaft, transmission shafts and the planet carriers are modelled as flexible bodies. The gears, hub, housing and bed plate are represented by rigid bodies [Wang et al., 2019]. SIMPACK's multibody model is shown in Figure 2.5.

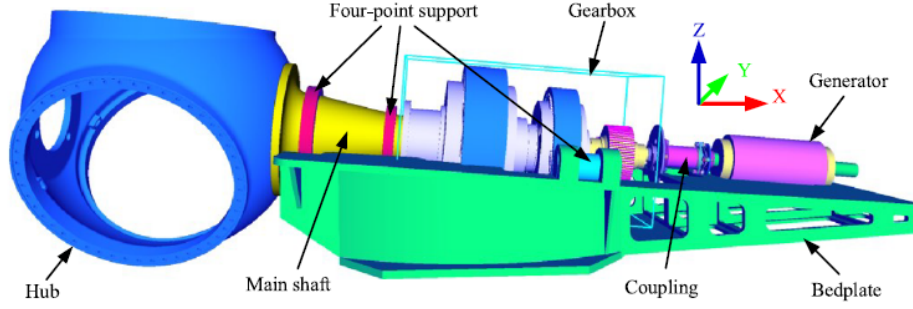


Figure 2.5: MBS model of the 10 MW drive train model [Wang et al., 2019]

The bearings are modelled using a force element (FE) with a linear force-deflection relationship [Wang et al., 2019]. The bearing stiffness is defined with Equation 2.4. Here, K_{xx} , K_{yy} , K_{zz} , $K_{\beta\beta}$ and $K_{\gamma\gamma}$ indicate the axial, tangential, radial stiffness, pitch and yaw stiffness, respectively. $K_{\alpha\alpha}$ is the stiffness in the rotation direction and is therefore 0 [Wang et al., 2019]. The drive train's specifications can be found in Appendix A.3

$$K = \begin{bmatrix} K_{xx} & 0 & 0 & 0 & 0 & 0 \\ 0 & K_{yy} & 0 & 0 & 0 & 0 \\ 0 & 0 & K_{zz} & 0 & 0 & 0 \\ 0 & 0 & 0 & K_{\alpha\alpha} & 0 & 0 \\ 0 & 0 & 0 & 0 & K_{\beta\beta} & 0 \\ 0 & 0 & 0 & 0 & 0 & K_{\gamma\gamma} \end{bmatrix} \quad (2.4)$$

2.2 MBS Modelling

Computer modelling is widely used for determining the dynamic behaviour of a system [Bauer, 2016]. A distinction between finite elements (for analyzing highly sophisticated problems) and multibody system (MBS) (for less accurate but faster computations) modelling is made [Bauer, 2016]. MBS and finite elements can be used independently or they can be combined. For the drive train model (presented in Section 2.1.4) used in this project, MBS modelling is used. Therefore, in the following MBS modelling is briefly explained.

MBS modelling describes the interaction of individual bodies between each other and their environment. This means that loads and movements are simulated [Bauer, 2016, Lehner, 2007]. The modeled bodies, linked through massless joints and kinematic constraints, can be rigid and flexible. The links restrict and allow specific relative motions [Schwertassek and Wallrapp, 1999]. The mass and inertia of a body is placed on its body's center of gravity (COG), where also the bodies' coordinate system is placed. The bodies' exact location in space can be determined by referring to the inertial frame [Bauer, 2016].

A rigid body has 6 degrees of freedom (DOFs), described by independent coordinates. The body can move along and rotate about the x -, y - and z -axis, as is shown in Figure 2.6.

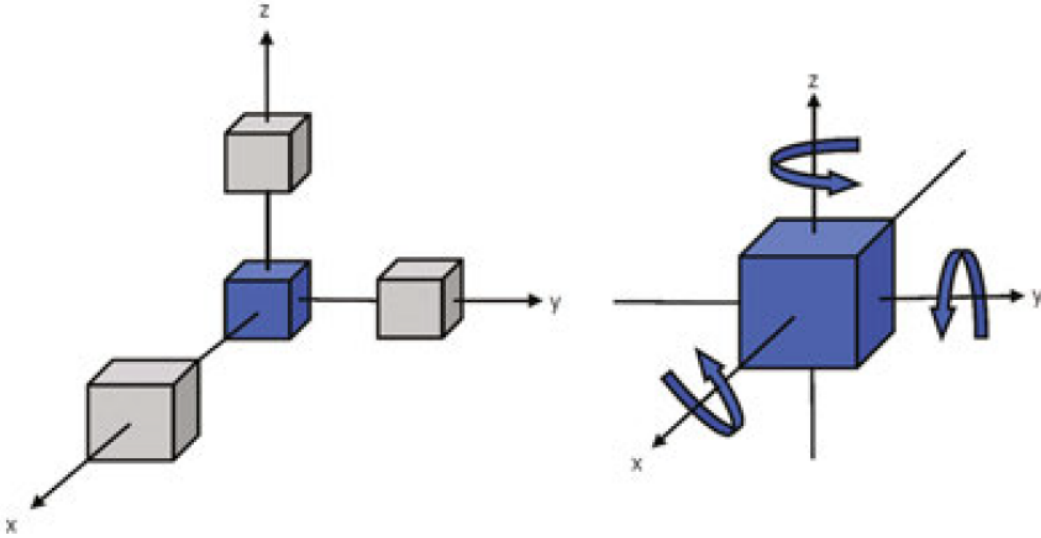


Figure 2.6: DOFs of a rigid body [Bauer, 2016, Juchem, 2009]

Different (massless) joint types can be chosen from to allow for certain translations and rotations. Depending on the joint type, a joint can connect bodies with other bodies or reference frames with no DOF, can provide free movement in all 6 DOF or can apply kinematic excitations to the body [Bauer, 2016]. Loads can be transferred between two body markers by a FE. Its interaction depends on the implemented force law. The bodies' movement is characterized by independent state variables and the inertial properties of its bodies, masses, inertia tensors, and its COGs. The kinematics are defined by multiple coupled equations of motion (EOMs), having a form as is shown in Equation 2.5. Here \mathbf{M} , \mathbf{C} and \mathbf{K} are $N \times N$ matrices representing the inertia, damping and stiffness of the bodies, \mathbf{F} is the $N \times 1$ force vector including torques and moments and the $N \times 1$ displacement, velocity and acceleration vectors are represented by \mathbf{x} , $\dot{\mathbf{x}}$ and $\ddot{\mathbf{x}}$ [Nejad et al., 2014c].

$$\mathbf{M}\ddot{\mathbf{x}} + \mathbf{C}\dot{\mathbf{x}} + \mathbf{K}\mathbf{x} = \mathbf{F} \quad (2.5)$$

The EOMs can be solved by direct (movement is determined by known internal forces or torques, the Newmark method is an example [Newmark, 1959]) and inverse dynamics (reconstruction of the internal forces or torques from movements and external forces) [Bauer, 2016].

2.3 Floating Wind Turbine

A relatively new wind turbine support concept is the floating foundation. This concept is introduced since it gives access to deep-water sites [IRENA, 2016]. Waters deeper than 50 m can be accessed, possibly deploying areas with a strong wind resource near to populated areas [IRENA, 2016]. Also, the installation is way easier and cheaper, since foundations can be standardized on-shore and low-cost readily available vessels can be used [IRENA, 2016]. During installation there is little activity on the seabeds and floaters offer therefore some environmental benefits [IRENA, 2016]. Japan and the United States are possessing few shallow-water sites and are therefore a large potential market [IRENA, 2016].

There are mainly three floating concepts used: a ballast, mooring line and buoyancy stabilized floater, these are depicted in Figure 2.7. These floaters differ in dynamic performance, feasible water depths and ease of installation.

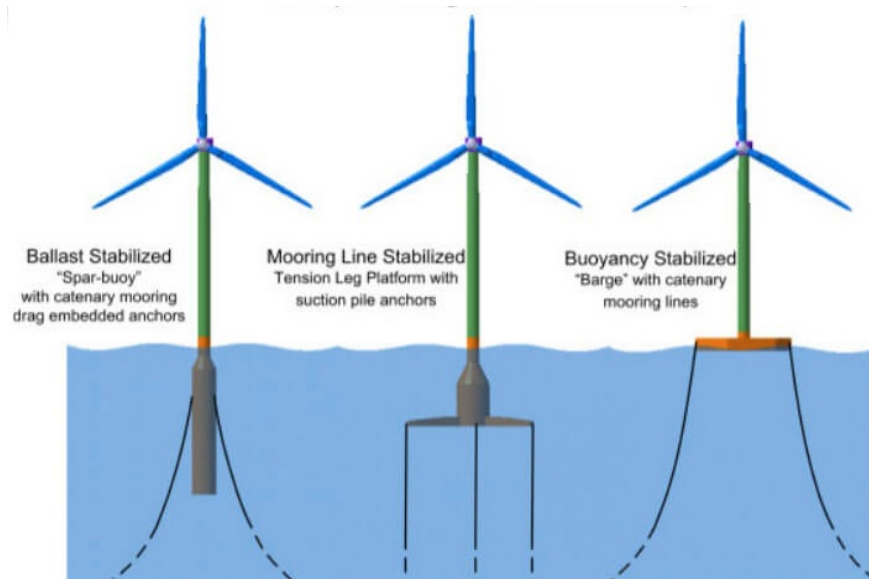


Figure 2.7: Three main floating concepts⁶

The floater used in this study is the spar buoy. This is a cylinder with low water plane area [IRENA, 2016]. It is ballasted such that the center of gravity is kept below the center of buoyancy. The floater's position is maintained by catenary or taut spread mooring lines with drag or suction anchors [IRENA, 2016]. The simple design has lower critical wave-induced motions and allows for lower installed mooring cost than the other floater concepts. Cons are however that heavy-lift vessels are required for offshore operations and it needs deeper water than the other concepts (approximately >100 m) [IRENA, 2016].

2.4 Maintenance

For most of the technical industries, a division in maintenance methods is made. This division is like the following:

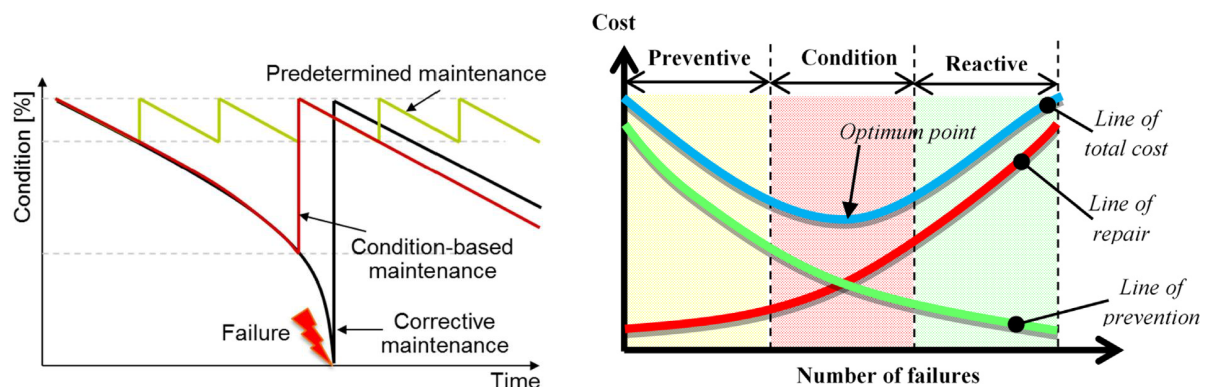
- **Corrective maintenance:** After breakdown or an obvious fault [Rademakers et al., 2011].
 - **Planned maintenance:** Based on the observed degradation of a system.
 - **Unplanned maintenance:** Necessary after an unexpected failure.
- **Preventive maintenance:** Intended to prevent equipment breakdown [Rademakers et al., 2011]
 - **Predetermined maintenance:** Based on fixed time intervals or operating hours
 - **Condition-based maintenance:** Based on the actual health of the system.

⁶<https://www.windpowerengineering.com/new-u-s-patent-granted-for-floating-marine-wind-turbine/> [Visited on 12th of June 2020]

Condition-based preventive maintenance and planned corrective maintenance are based on the observed status or degradation of a system [Rademakers et al., 2011]. The difference is that condition-based maintenance is foreseen in the design and the planned corrective is not. Therefore three types of maintenance are considered: predetermined maintenance, condition-based maintenance and unplanned corrective maintenance [Rademakers et al., 2011].

In Figure 2.8a, one can see the difference and influence between the three different types of maintenance. Usually a combination of maintenance method is used as a maintenance strategy. Figure 2.8b shows the relation between costs and maintenance method. Somewhere there is an optimum point, this point determines the optimum maintenance strategy with a minimized levelized cost of energy (LCOE).

The costs for maintaining an offshore wind farm will be determined by estimating the costs for corrective, preventive and condition-based maintenance [Rademakers et al., 2011]. The usual approach is analyzing the costs and downtime of different O&M scenarios using cost models. First, a baseline scenario (transport by small boats and crane vessels) is selected. If the estimated costs and downtime are high, other transport vessels are chosen. The most cost effective scenario is assessed. The costs for preventive maintenance can be calculated straightforwardly by multiplying the number of visits per year with the costs. Downtime is equal to the time technicians are actually visiting the turbines. For corrective maintenance cost modelling is more complicated [Rademakers et al., 2011].



(a) Influence of maintenance type on asset condition [Cho, 2019, Coronado and Fischer, 2015]

(b) Costs associated with traditional maintenance methods to find an optimum maintenance strategy [González-González and Galar, 2018]

Figure 2.8: Comparison of traditional maintenance methods

For maintenance on offshore wind turbines, the following aspects are relevant:

- **Reliability of turbines:** The reliability of offshore wind turbines is generally higher than onshore turbines. This is achieved by decreasing the number of components and applying automated control systems. The turbine is often designed such that not every single failure will lead to a standstill, assisted by better use of the diagnostics and redundant sensors [Rademakers et al., 2011].
- **Maintainability of turbines:** Offshore wind turbines are designed to make replacements easy.
- **Weather conditions:** When the wind speed and wave height are sufficiently low, maintenance can be carried out. Therefore preventive maintenance is usually planned in the summer.

- **Transportation and access vessels:** Small boats and helicopters (in bad weather) are being used to transfer personnel from the harbour to the farm. Depending on the size of the parts, either small or large (supply) vessels are used.
- **Crane ships and jack-up barges:** For replacing large components, sometimes large crane ships need to be hired.

2.4.1 Fault Statistics

The annual failure rate and downtime for German onshore wind turbines is shown in Figure 2.9. From this figure, it can be observed that the electrical system and electronic control are having the highest failure rate. However, failure of the drive train and gearbox results in the highest downtime, while having (one of the) lowest failure rates.

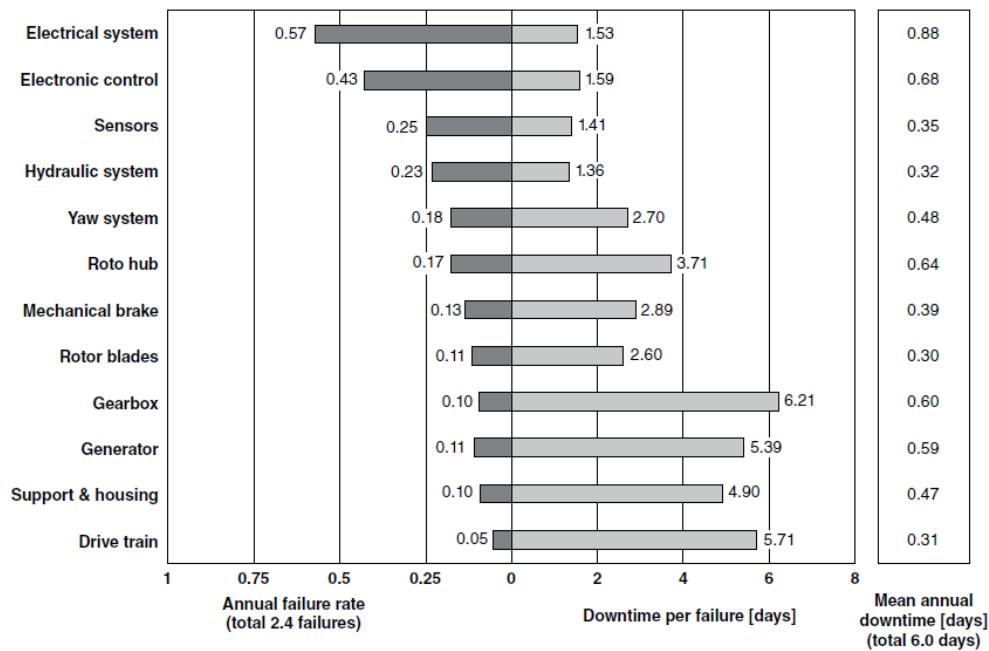


Figure 2.9: Annual failure rate and downtime per failure of wind turbines from German onshore wind turbine failures database [Nejad, 2018, Faulstich et al., 2011]

2.4.2 Drive Train Failure

The least reliable components in a drive train are investigated by an European and a Chinese study. Those are listed in descending order in the following.

European market [Tavner, 2012]:

- Pitch mechanism
- Power electronic converter
- Yaw system
- Control system
- Generator
- Gearbox

Chinese market [Lin et al., 2016]:

- Frequency converter
- Generator
- Pitch system
- Gearbox
- Yaw mechanism

The wind turbine gearbox and bearings could have the following failures [Chen, 2011]:

- Fatigue cracks
- Teeth breakage
- Wear
- Plastic flow
- Scoring (scuffing)
- Surface fatigue
- Spalling

Gearbox failures, resulting in expensive repairs, are mainly caused by excessive loads. Gearboxes are designed to carry a few times the rated torque, preventing damage from unexpected load cases. Often overload clutches are built into the high-speed shaft for protection. Numerical modeling and simulation methods are used to analyze damage and fatigue effects under various situations. Based on such studies, the control strategies could be developed [Chen, 2011].

2.5 Monitoring

Wind turbine monitoring is used for control applications as well as preventive measures. Preventive monitoring is needed to extend the life cycle, schedule maintenance and predict fault conditions. New techniques are being developed to predict possible failures such that the maintenance or repairs can be performed effectively, reducing the costs and the risk of complete failure. The gearbox is problematic and the costs of replacement are high. Two monitoring techniques are commonly used: the use of Supervisory Control and Data Acquisition (SCADA) data and condition monitoring (CM) [Chen, 2011].

2.5.1 SCADA

The use of SCADA data is appealing due to the high costs of vibration measurements using dedicated condition monitoring systems (CMS) [Tautz-Weinert and Watson, 2016]. All big wind turbines have a SCADA system, usually providing 10-minute averaged data of 1 Hz sampled values, measuring the parameters shown in Table 2.2. In recent years, approaches using SCADA data for early failure detection have been developed.

Table 2.2: Overview of SCADA parameters [Tautz-Weinert and Watson, 2016, Yang et al., 2013, Yang et al., 2014]

Environmental parameters	Electrical characteristics	Part temperatures	Control variables
<ul style="list-style-type: none"> • Wind speed • Wind direction • Ambient temperature • Nacelle temperature 	<ul style="list-style-type: none"> • Active power output • Power factor • Generator voltages • Generator phase current • Voltage frequency 	<ul style="list-style-type: none"> • Gearbox bearing • Gearbox lubricant oil • Generator bearing • Rotor and generator shaft • Main bearing • Generator slip ring • Inverter phase • Converter cooling water • Transformer phase • Hub controller • Top controller • Converter controller • Grid busbar 	<ul style="list-style-type: none"> • Pitch angle • Yaw angle • Rotor shaft speed • Number of yaw movements • Fan speed and status • Cooling pump status • Operational status code • Set pitch angle and deviation • Generator speed • Number of starts and stops

Faults of wind turbines can be found using interpretation of trends in SCADA data, given the variability in the operational conditions of wind turbines. A change in the value of a SCADA parameter does not always indicate a fault [Tautz-Weinert and Watson, 2016]. Therefore long term data and (the change in) ratios of SCADA parameters needs to be collected and monitored. This is done using trending methods (using regression lines in scatter diagrams or three-dimensional visualizations). Trending of SCADA parameters can reveal the development of a failure using historical data, where manual interpretation is sometimes required [Tautz-Weinert and Watson, 2016].

2.5.2 Condition Monitoring

Condition monitoring (CM) is a new tool in the wind industry. It can indicate the condition of the system's components [Hameed et al., 2007]. Different measurement techniques can be used for CM, which are amongst others: vibration analysis, oil analysis, acoustic monitoring [Chen, 2011], physical material condition monitoring, thermography and process parameters monitoring [Hameed et al., 2007].

Vibration Analysis

Vibration analysis is a well known technology [Hameed et al., 2007]. It is used to determine the condition of rotating equipment. Various sensors, with different frequency ranges, can be used for different situations and equipment [Chen, 2011]. The sensors return an analog signal proportional to the instantaneous local motion representing a component's health condition [Hameed et al., 2007]. Data can be analysed using, for example, a harmonic analysis [Chen, 2011]. Vibration analysis can be used for monitoring the main bearing, bearings of the generator and the gears, shafts and bearings of the gearbox. This analysis is mostly offered as a complete system, with signal analysis and diagnostics [Hameed et al., 2007].

Sensors

Sensors can be of varying types: position transducers (low frequency, about 1 kHz [Boyce, 2012]), velocity sensors (middle frequency, up to 2 kHz⁷), accelerometers (high frequency) and spectral emitted energy sensors (very high frequencies) [Hameed et al., 2007, Chen, 2011].

The motion sensor converts an object's motion into electrical signals⁸. A linear transducer consists typically of three (1 primary and 2 secondary) selenoid coils. The body, of which the motion is measured, is attached to a ferromagnetic coil and can slide freely⁸. Due to the change of the distance between the selenoid and ferromagnetic coil, an alternating electromagnetic field is caused. The sequence of pulses, transformed by a pulse shaping circuit, can be counted. This serves as a measure of the body's movement [Kursat Yalcin, nd].

Fiber optic sensing is becoming important because it can multiplex thousands of sensors [Xu and Xu, 2017]. A remote wireless sensor architecture is used for retrofitting onto existing turbines. To support the increasing number of diverse sensors, new data systems and processing architecture are required.

ISO 10816-21 [ISO, 2015] recommends measurement positions on a wind turbine's drive train, which is shown in Figure 2.10. In this figure, the characters indicate the following:

Measuring positions on the drive train [ISO, 2015]

- A Rotor main bearing
- B Gearbox planes
- C Generator planes

Measuring positions on the structure [ISO, 2015]

1. In nacelle at main frame close to the main bearing of the rotor
2. On structure above tower flange
3. In rear end of nacelle on one side of generator or main frame

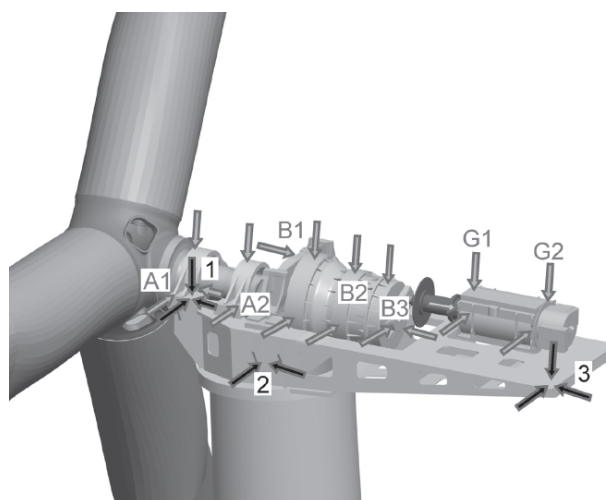


Figure 2.10: Typical measurement positions of a wind turbine with two main bearings as recommended by ISO 10816-21 [ISO, 2015]

⁷<https://www.bkvibro.com/en/products/vibration-sensors.html> [Visited on the 27th of April 2020]

⁸<https://www.positek.com/linear-position-sensor/linear-transducer> [Visited on the 27th of April 2020]

Condition Monitoring Techniques

Condition monitoring (CM) can be performed using different condition monitoring techniques (CMTs), such as [Ghane, 2018]:

- **Offline CM system:** Samples are taken when the wind turbine is shut down and under inspection.
- **Online CM system:** The wind turbine is monitored while running. This system is advantageous for early fault detection.
- **In-line CM system:** Is not dependent on sampling and monitors the whole subsystem.
- **Intrusive or subsystem CM:** Based on related local parameters, requiring a variety of sensors. It makes use of vibration analysis, oil analysis, shock pulse method, physical condition of materials, strain measurement, electrical effects, ultrasonic testing techniques, visual inspection, self-diagnosis sensors, thermography, radiographic inspection and acoustic emission [Ghane, 2018].
- **Non-intrusive or global system CM:** A platform to detect faults using global performance indexes. Some techniques are power curve analyses, performance monitoring, electrical signature and SCADA system data analysis [Ghane, 2018].
- **Model-based approach:** Using mathematical models to describe, control and monitor wind turbines.
- **Signal-based approach:** To predict and analyze states of the system using analyses of the features from measured output signals.

Condition monitoring consists of four stages [Ghane, 2018]:

1. **Data acquisition:** Obtaining relevant data to monitor the system's health.
 - **Event data:** Generally manually filled in in the database and includes information on what happened and what was done.
 - **CM data:** Measured data related to the health condition of the wind turbine's (sub-) component. Usually, only critical parameters are monitored.
2. **Residual generation:** Pre-processing obtained raw data. Data is filtered on out-of-range values, impossible data combinations and missing values. Model- and data-based residual generation methods can be used.
3. **Feature extraction:** Makes from raw data useful data.
4. **Maintenance decision-making:** Suggesting an efficient maintenance policy.
 - **Diagnostic decisions:** Detection, estimation and isolation of faults, intended to detect a fault before it turns into a failure.
 - **Prognostic decisions:** Predicting faults before they occur. Superior to diagnostic decisions, but does not have a 100% accuracy.

The following approaches can be used for fault diagnosis decision making: statistical approaches [Ghane et al., 2016, Ghane et al., 2018], statistical process control (SPC) methods, different cluster analysis [Wenyi et al., 2013] and artificial intelligence (AI) approaches. For fault prognosis, the remaining useful lifetime (RUL) needs to be approximated [Ghane, 2018].

2.5.3 Health Monitoring

In order to increase the production hours and reduce the risk of catastrophes, health monitoring is an important task [Nejad and Moan, 2017]. Structural health monitoring (SHM) systems installed on the aging structure could ensure increased safety and reliability [Giurgiutiu, 2007]. It can replace scheduled maintenance with as-needed maintenance, thus, in the end, saving the cost of unnecessary maintenance and preventing unscheduled maintenance. SHM assesses the state of structural health and predicts the remaining life of the structure, it also allows a wind turbine to be used after its design life. The design paradigm can be changed and savings in cost can be achieved. Most importantly, SHM allows condition-based maintenance (CBM) inspection instead of schedule-driven inspections and that is why health monitoring is addressed in this report [Giurgiutiu, 2007]. It is critical for the integrated system health management (ISHM) system as it provides information to other ISHM functional modules [Xu and Xu, 2017]. Health monitoring systems use both frequency domain and time domain methods [Nejad and Moan, 2017].

SHM can be performed in two ways [Giurgiutiu, 2007]:

1. **Passive:** Measuring various operational parameters and then inferring the state of structural health from these parameters.
2. **Active:** Directly assessing the state of structural health by trying to detect the presence and extent of structural damage.

Damage detection can be performed using wave propagation, frequency response transfer function and electromechanical (EM) impedance. Reliable damage metrics that can assess the state of structural health with confidence and trust are not yet available [Giurgiutiu, 2007]. Damage detection methods can be divided in four levels [Nejad and Moan, 2017, Rytter, 1993]:

Level 1: Damage identification

Level 2: Finding the location of the damage

Level 3: Estimating the severity of the damage

Level 4: Remaining life prediction

Most of the health monitoring methods normally cover up to level 3 [Nejad and Moan, 2017]. Shown is that the reliability of components inside the wind turbine gearbox differ [Nejad and Moan, 2017, Nejad et al., 2014a] and it was also demonstrated that the damage of some components has a big effect on other components of the gearbox [Nejad et al., 2015b].

2.6 Loads

In the following, explanations on simulation of loads are given, which are an input for the global response analysis described in Section 2.7. A division is made between aerodynamic loads (load from wind), described in Section 2.6.1, hydrodynamic (or wave) loads in Section 2.6.2.

2.6.1 Aerodynamic Loads

To obtain the aerodynamic loads on structure, one could use a model. A range of aerodynamic models, from 1D to 3D models, are available. Generally, blade element momentum (BEM) and generalized dynamic wake (GDW) are used, providing computationally efficient solutions [Bachynski, 2014]. The aerodynamic load models have some limitations and thus some effects are not considered. In the following loads from wind are discussed.

Wind Variation

Wind, having longitudinal, lateral and vertical components, has a spatial and temporal variation. The components of the wind speed U at a point in space is shown in Equation 2.6 to be the sum of mean \bar{U} and fluctuating parts u' [Bachynski, 2014].

$$U = \bar{U} + u' \quad (2.6)$$

To describe the fluctuation of the wind, the turbulence intensity I is usually calculated. Its definition is found in Equation 2.7. Here \bar{U} is the mean wind speed at reference altitude and σ_{wind} is the standard deviation of the wind speed.

$$I = \frac{\sigma_{wind}}{\bar{U}_{ref}} \quad (2.7)$$

In order to simulate the wind turbine's response, a 3D wind must be simulated. Three spectra are the most common: Kaimal, von Kármán (both 1D) and Mann (3D) spectra [Bachynski, 2014]. The turbulence for this design load case is modelled using the Kaimal spectrum.

The formula for the Kaimal spectrum φ_K is depicted in Equation 2.8. f is frequency, k indicates the velocity component and \bar{U} is the mean wind speed at hub height [Kaimal et al., 1972].

$$\varphi_K(f) = \sigma_k^2 \frac{4 \frac{L_K}{\bar{U}}}{\left(1 + 6f \frac{L_K}{\bar{U}}\right)^{\frac{5}{3}}} \quad (2.8)$$

σ_k is the standard deviation determined by Equation 2.9 [Kaimal et al., 1972].

$$\begin{aligned} \sigma_x &= I \left(\frac{3}{4} \bar{U} + 5.6 \right) \\ \sigma_y &= 0.8 \sigma_x \end{aligned} \quad (2.9)$$

L_K is the velocity component integral scale parameter defined by Equation 2.10 [Kaimal et al., 1972]. Λ is defined with Equation 2.11 [Kaimal et al., 1972].

$$L_K = 8.1 \Lambda \quad (2.10)$$

$$\Lambda = \begin{cases} 0.7z & \text{if } z \leq 60 \text{ m} \\ 42 \text{ m} & \text{if } z > 60 \text{ m} \end{cases} \quad (2.11)$$

Rotor Loads

When knowing the wind speed, the loads on the blades can be calculated. The simplified formulation of these loads are explained in the following. The basic aerofoil with loads and angles as shown in Figure 2.11 is considered. From basic aerodynamics and geometry, the expressions shown in Equation 2.12 for lift l and drag d force per unit span and angle of attack α are obtained [Hansen, 2008]. Here, c is chord length and ϕ is the blade twist, $\beta(r)$ and θ_p are angles.

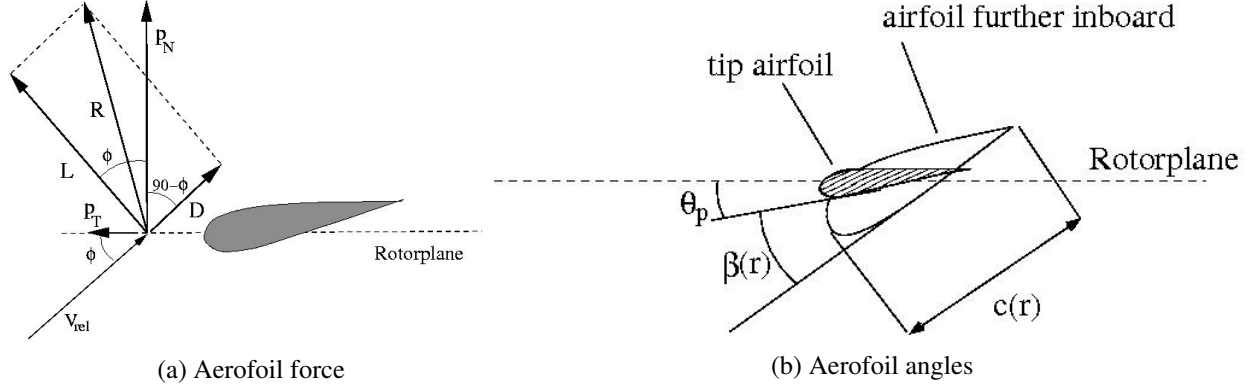


Figure 2.11: 2D aerofoil basic sketch and conventions [Hansen, 2008]

$$\alpha = \phi - \theta(r) = \phi - \beta(r) + \theta_p$$

$$l = \frac{1}{2}\rho V_{rel}^2 c C_l(\alpha)$$

$$d = \frac{1}{2}\rho V_{rel}^2 c C_d(\alpha)$$
(2.12)

Aerodynamic forces on the blade cause an axial rotor torque τ . The torque is described by Equation 2.13 [Burton et al., 2011]. Here, N is the number of blades.

$$\tau = (dL \sin \phi - dD \cos \phi) r = \frac{1}{2}\rho W^2 N c (C_l \sin \phi - C_d \cos \phi) r dr$$
(2.13)

For convenience, Equation 2.14 is introduced [Burton et al., 2011].

$$C_t = C_l \cos \phi + C_d \sin \phi$$

$$C_n = C_l \sin \phi - C_d \cos \phi$$
(2.14)

Tower Drag

The aerodynamic drag force on the tower should also be considered. It is especially important in extreme wind conditions, when the wind turbine is parked and the forces on the rotor are small [Bachynski, 2014]. The local drag force F_{local} , in direction $j = x, y, z$, follows from a quadratic drag model shown in Equation 2.15. D is the local diameter and l the local segment length. Also, V_{local} is the relative wind velocity at the element's center [Bachynski, 2014].

$$F_{local_j} = \frac{1}{2}\rho_{air} D L C_{D_j} V_{local_j} |V_{local_j}|$$
(2.15)

The drag coefficient C_D is highly dependent on the Reynolds number Re . Its relation is shown in Figure 2.12. The calculation of this number is found in Equation 2.16. Here D is the characteristic length (tower diameter in this case), U the mean wind speed and ν the kinematic viscosity ($\approx 1.5 \times 10^{-5}$ for air) [Andersen and Sorensen, 2018].

$$Re = \frac{DU}{\nu} \quad (2.16)$$

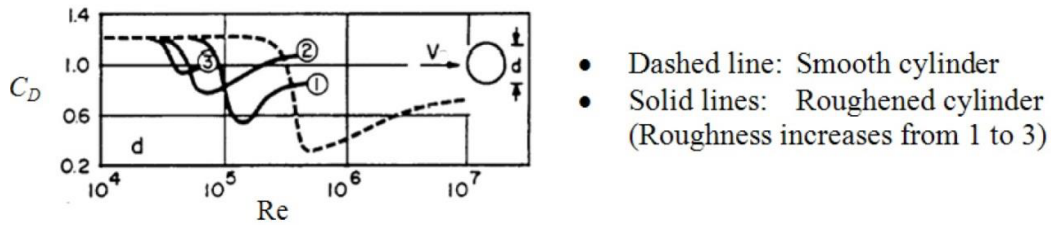


Figure 2.12: Relation between drag coefficient C_D and Reynolds number Re [Andersen and Sorensen, 2018]

2.6.2 Hydrodynamic Loads

Significant loads on the monopiles or floating structures of wind turbines are caused by waves, tidal variations, and current [Bachynski, 2014]. However, in the following only some comments will be given on the hydrostatics, the Morison's equation and the wave spectrum.

Hydrostatics

Hydrostatics relies on the pressure distribution of a fluid at rest. Assumed is that there is no shear stress, the pressure p depends purely on z and the fluid is incompressible. The pressure distribution over the length of a monopile or floater, is depicted in Equation 2.17 [Bachynski, 2014].

$$\frac{dp}{dz} = -\rho g \quad (2.17)$$

The hydrostatic pressure dominates for a floating structure to be stable [Bachynski, 2014]. The hydrostatic analysis results in an output to obtain the \mathbf{K} -matrix of Equation 2.22.

Wave Spectrum

Sea waves consists of random waves of various periods and lengths⁹. Therefore, the waves can be simulated by means of a spectra, describing the wave energy distribution over wave frequencies [Ryabkova et al., 2019]. In the past, multiple wave spectra are developed, such as the Pierson-Moskowitz (PM) [Pierson Jr. and Moskowitz, 1964] and Joint North Sea Wave Observation Project (JONSWAP) [Hasselmann et al., 1973] wave spectra [Ryabkova et al., 2019]. For the simulation of the waves, the JONSWAP spectrum is used.

⁹https://wikiwaves.org/Waves_and_the_Concept_of_a_Wave_Spectrum#Calculating_The_Wave_Spectrum [Visited on 7st of July 2020]

Pierson and Moskowitz [Pierson Jr. and Moskowitz, 1964] assumed that for a steadily blowing long time wind, waves come into equilibrium with the wind [Ryabkova et al., 2019]. The JON-SWAP spectrum is based on the PM spectrum, containing a small modification. It describes the fact that spectral densities at the maximum frequency were higher than the PM spectrum approximations [Ryabkova et al., 2019]. The wave spectrum φ_J , depicted in Equation 2.18, depends on the wind speed. Here, ω is the wave frequency and U_{10} is the wind speed 10 m above the sea.

$$\begin{aligned}\varphi_J(\omega) &= \frac{\alpha g^2}{\omega^5} \exp\left(-\frac{5}{4} \left(\frac{\omega_p}{\omega}\right)^4\right) \gamma^r \\ r &= \exp\left(-\frac{(\omega - \omega_p)^2}{2\sigma^2 \omega_p^2}\right)\end{aligned}\quad (2.18)$$

The deterministic parameters α , ω_p and γ are described in Equation 2.19.

$$\begin{aligned}\alpha &= 0.076 \left(\frac{U_{10}^2}{Fg}\right)^{0.22} \\ \omega_p &= 22 \left(\frac{g^2}{U_{10}F}\right)^{1/3} \\ \gamma &= 3.3\sigma = \begin{cases} 0.07 & \text{when } \omega \leq \omega_p \\ 0.09 & \text{when } \omega > \omega_p \end{cases}\end{aligned}\quad (2.19)$$

Morison's Equation

Morison's equation is often used as an alternative to potential flow theories for slender structures. Using Equation 2.20, the transverse force per length f is calculated. Here $C_a = C_m - 1$ and u and v are the transverse wave particle and local transverse body velocity, respectively [Bachynski, 2014, Morison, 1950]. \dot{u} and \dot{v} are its time derivatives.

$$f = \rho\pi \frac{D^2}{4} \dot{u} + \rho C_a \pi \frac{D^2}{4} (\dot{u} - \dot{v}) + \frac{1}{2} \rho C_D D (u - v) |u - v| \quad (2.20)$$

The three terms represent the Froude-Krylov force, added mass contributions and viscous drag forces, respectively. From the linear wave theory the water particle acceleration is obtained using Equation 2.21. ω is the wave angular frequency, H is the wave amplitude and $k = \frac{2\pi}{\lambda}$ is the wave number [Bachynski, 2014].

$$\dot{u} = \omega^2 H e^{kz} \cos(\omega t - kx) \quad (2.21)$$

2.7 Global Response Analysis

After defining the loads, the response of a wind turbine can be obtained. Therefore, in this section, the global response analysis of a wind turbine is explained, since it is important to know how a model works, before someone makes use of it. After having this knowledge, one can set up a detailed model and afterwards a local load response analysis can be performed for the subcomponents [Nejad, 2018]. The loads and its responses contribute to the fatigue damage of the system.

Global response analysis of a structure can be performed with varying degrees of freedom (DOF), such as a linear rigid body approach (explained in Section 2.7.1), modal methods (see Section 2.7.2), nonlinear beam models and more detailed finite element models considering 2D or 3D elements [Bachynski, 2014].

2.7.1 Rigid Body

A wind turbine can move in 6 DOF. These are for a floating wind turbine: surge (x_1), sway (x_2), heave (x_3), roll (x_4), pitch (x_5) and yaw (x_6). These can be represented by the time dependent motion vector $\mathbf{x}(t) = [x_1(t), x_2(t), x_3(t), x_4(t), x_5(t), x_6(t)]^T$ [Bachynski, 2014]. The equations of motions (EOMs) can then be written as a second order differential equation shown in Equation 2.22. Here, \mathbf{M} is the mass matrix, \mathbf{B} the damping matrix and \mathbf{C} the stiffness matrix. $\ddot{\mathbf{x}}$ and $\dot{\mathbf{x}}$ are the second and first derivative of the motion vector over time. \mathbf{F} is the forcing vector.

$$\mathbf{M}\ddot{\mathbf{x}} + \mathbf{B}\dot{\mathbf{x}} + \mathbf{C}\mathbf{x} = \mathbf{F} \quad (2.22)$$

The problem can be linearized, when neglecting nonlinear excitation terms (such as quadratic damping, or amplitude-dependent higher order terms). The response can be solved in the frequency and time domain. In the frequency domain, the excitation has the form of Equation 2.23, with frequency ω [Bachynski, 2014, Metrikine, 2010].

$$\mathbf{x} = \text{Re} (X_n e^{i\omega t}) \quad (2.23)$$

Then, the EOM becomes as shown in Equation 2.24.

$$(-\omega^2 \mathbf{M}(\omega) + i\omega \mathbf{B}(\omega) + \mathbf{C}) \mathbf{x} = \mathbf{F}(\omega) \quad (2.24)$$

Modification may be necessary in order to include the wind-induced loading and damping [Bachynski, 2014]. For nonlinear load effects in a rigid body model, the EOM should be solved in the time domain. Then, the frequency dependency should be included through a convolution integral or by a state-space representation of the time-dependent coefficients [Bachynski, 2014, Taghipour et al., 2008].

2.7.2 Modal Analysis

The EOM can also be solved for a set of mode shapes. Certain structural deformation patterns are defined as the mode shapes. The time-varying structural deformations are a combination of these mode shapes. Modal analysis can be accurate and computationally efficient [Bachynski, 2014]. Nonlinear loads can be accounted for, but material nonlinearity and geometrical stiffening due to large deformations cannot be considered [Cook et al., 2002, Bachynski, 2014]. A figurative explanation of the modal analysis is shown in Figure 2.13.

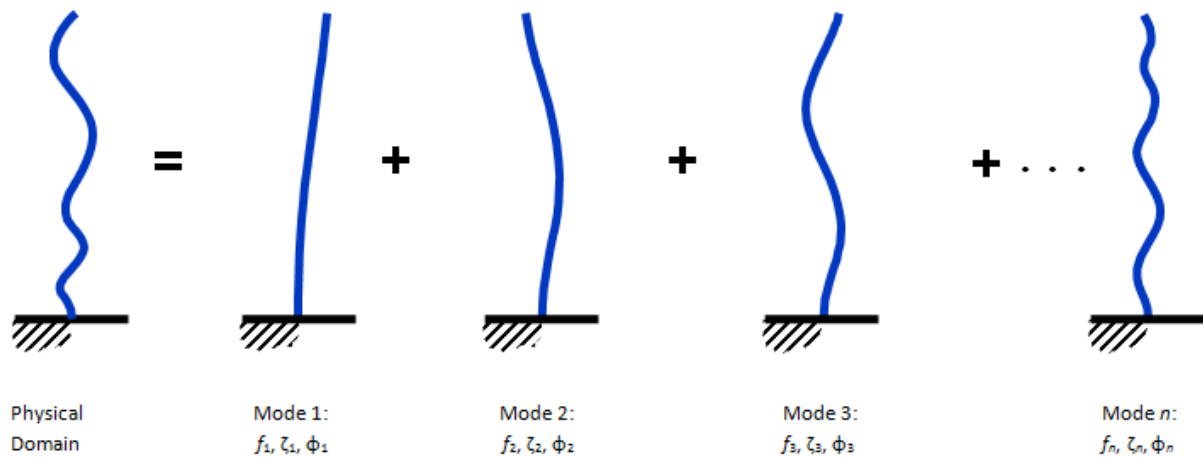


Figure 2.13: Figurative explanation of modal analysis¹⁰

2.8 Damage

This research work investigates fault detectability and vibration propagation in a drive train after simulated damage. It is good to know how damage is defined and how it is simulated. Therefore, the definition of damage is described in Section 2.8.1. Fatigue damage forms a concern in the wind energy industry. This kind of damage is explained in Section 2.8.2. Finally, it is shown how the damage is introduced in Wang's drive train model in Section 2.8.3.

2.8.1 Damage Definition

The material damage is a progressive physical process by which materials break [Lemaitre, 1996]. Many materials have a similar mechanical behaviour, although they have different physical structures. The material properties can therefore be explained by a few energy mechanisms, similar for all these materials [Lemaitre, 1996].

For numerical analysis and experiments, the representative volume element (RVE), depicted in Figure 2.14), is introduced. This is the smallest volume over which measurements can be performed, yielding in a representative value of the whole material [Hill, 1963].

¹⁰http://www.svibs.com/resources/ARTeMIS_Modal_Help_v3/Operational%20Modal%20Analysis.html [Visited on 14th of December 2019]

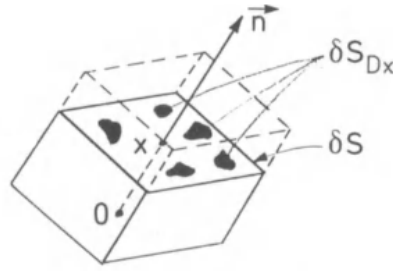


Figure 2.14: Representative volume element (RVE) of a material [Lemaitre, 1996]

On a microscale, the material damage starts when atoms debond, forming microcracks. More microcracks are formed when damage accumulates [Lemaitre, 1996]. Therefore, Figure 2.14 is considered again to define damage. Let S be the area of the RVE plane. S_D is then the effective area of all microcracks or microcavities. Then, damage D can be defined as in Equation 2.25 [Lemaitre, 1996].

$$D = \frac{S_D}{S} \quad (2.25)$$

From this definition it follows that $0 \geq D \geq 1$. $D = 0$ represents undamaged RVE material, whereas $D = 1$ indicates a fully broken RVE [Lemaitre, 1996]. This definition can now also be used on a mesoscale. In the wind energy industry, fatigue damage, a form of damage accumulation, is a concern.

2.8.2 Fatigue Damage

Fatigue damage is caused by cyclic stresses (from the aerodynamic and hydrodynamic loads described in Section 2.6) lower than a structure's yield stress σ_y . Cyclic loading (of which its number of cycles is calculated using rainflow counting [Rychlik, 1987, Bredmose, 2018]) leads to crack propagation. These cracks are initiated by material imperfections. SN diagrams, which are stress-cycle curves, can be obtained from physical testing of metallic materials. These diagrams, of which a typical one is depicted in Figure 2.15, are often (bi-)linear with a logarithmic N -axis. The stress time history at different points on the structure and hot spot stress (estimated by concentration factors) need to be determined, to estimate the fatigue damage and lifetime of a structure.

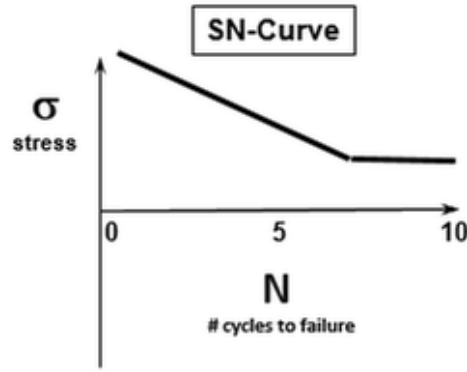


Figure 2.15: Typical *SN* curve for fatigue analysis¹¹

Bearing damage can be in the form of wear or material fatigue [Evans, 2011], which changes bearing properties [Blodt et al., 2008] affecting the load distribution and consequently the bearing stiffness [Harris, 2001].

2.8.3 Modelling Damage

In literature [Lemaitre, 1996, Qiu et al., 2002], it is found that damage and stiffness are correlated, which is also applied in different papers [Nejad and Moan, 2017, Nejad et al., 2014c]. Professor Lemaitre [Lemaitre, 1996] proposes a simple relationship, of which the adapted version is shown in Equation 2.26. Here, K is the system's stiffness for accumulated damage D . K_0 is the initial stiffness, depending on the material's Young's modulus E and the object's length l .

$$\begin{aligned} K &= K_0(1 - D) \\ K_0 &= El \end{aligned} \quad (2.26)$$

Qiu adapted this expression and proposed Equation 2.27. In this equation, $C = K_0/(K_0 - K_f)$. K_f is the system stiffness at the final condition and is generally 0 [Qiu et al., 2002], which would also be the case for this work's fault cases (see Section 3.3). This results in $K = 0$ when $D = 1$ and $K = K_0$ when $D = 0$.

$$\begin{aligned} D &= C \left(1 - \frac{K}{K_0} \right) \\ K &= K_0 \left(1 - \frac{D}{c_1} \right) \\ K &= K_0(1 - D) \end{aligned} \quad (2.27)$$

For dynamic analysis [Bachynski, 2014, Chopra, 1995, Chae and Kim, 2003], Rayleigh damping is normally used. This is an assumption that a system's damping is dependent on its stiffness and mass, shown in Equation 2.28.

$$C = a_1M + a_2K \quad (2.28)$$

¹¹<https://community.sw.siemens.com/s/article/what-is-a-sn-curve> [Visited on 3rd of January 2020]

Mass proportional damping indicates that the system's kinetic energy dissipates due to air friction. However, this energy loss is negligible and unrealistic for rigid body dynamics [Chae and Kim, 2003]. Therefore, the mass proportional damping is dropped and only the stiffness proportional damping remains. This results in Equation 2.29. Here, one can see that the system's damping is inversely proportional to the damage.

$$\begin{aligned} C &= a_2 K \\ C &= a_2 K_0 (1 - D) \end{aligned} \tag{2.29}$$

3 | Methodology

The methodology of this research work is described in this chapter. In order to simulate the data, a decoupled analysis is used. This analysis method is described in Section 3.1. Then, for the global response analysis of the wind turbine, a design load case is set up and presented in Section 3.2. For the local response analysis of the drive train, the faults should be introduced. The introduction of the faults is described in Section 3.3. In Section 3.4, it is explained how the natural frequencies are found. Then and finally, the lion share of this chapter is presented in Section 3.5. This is all about fault detection methods and is split up in two parts: time domain and frequency domain analysis.

3.1 Decoupled Analysis

In order to analyse the response of the system, a decoupled approach is used to generate the loads and responses. The decoupled approach is depicted in Figure 3.1 and explained in more detail below.

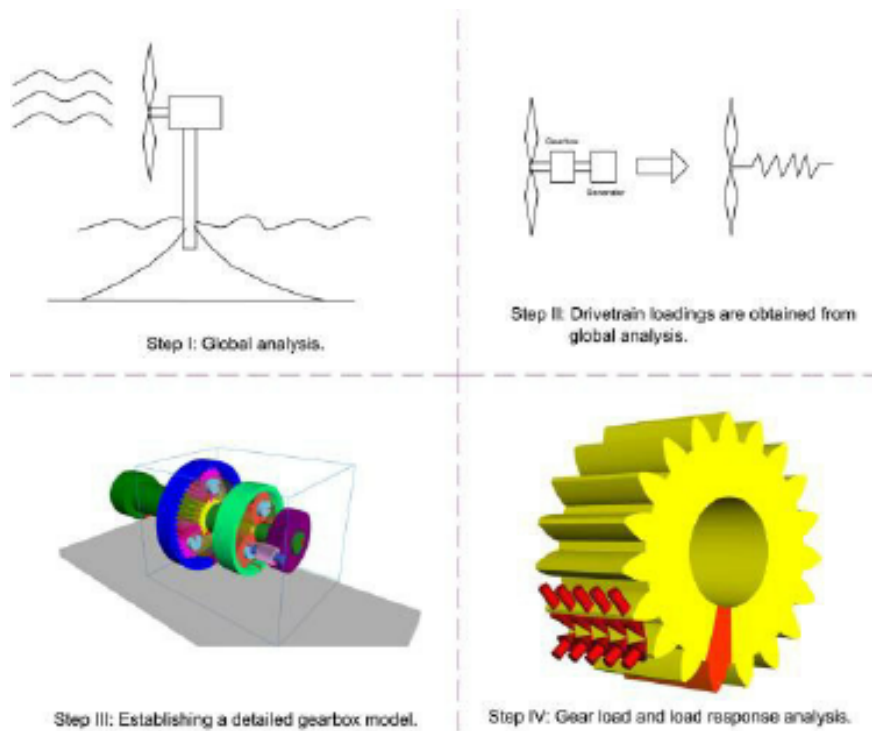


Figure 3.1: Decoupled analysis approach for drive train data generation [Nejad et al., 2015a]

The environmental conditions and its corresponding loads, modelled as is described in Section 3.2, are first applied on the DTU 10 MW [Bak et al., 2013] model (of which its properties are listed in Appendix A.1), which is placed on a floating spar [Hegseth and Bachynski, 2019] (properties in Appendix A.2), to obtain a global response. Afterwards, the output of the global response analysis is applied on Wang’s 10 MW drive train (find the properties in Appendix A.3). The external loads are applied on the main shaft and the motions on the bed plate. This results in the motions which will be discussed in this thesis.

For the global response analysis, SIMA [SIMA, 2019] is used and for the local response analysis of the gearbox, multibody simulation software, called SIMPACK [SIMPACK, 2020], is deployed.

3.2 Design Load Case

For the analysis of the data, there is chosen to do the simulations with one wind speed, so that the data output of the models can be compared easily. Chosen is for a wind speed of 12 m/s, which is approximately the wind turbine’s rated wind speed V_{rated} (=11.4 m/s [Bak et al., 2013]). The reason for this choice is that the rotational speed of the rotor is the highest [Long et al., 2011] and therefore there is a higher occurrence of fatigue damage.

The most probable significant wave height H_S and peak period T_p for the given wind speed are obtained for a site in the Northern North Sea as is described by [Li et al., 2015]. The site characteristics are depicted in Table 3.1.

Table 3.1: Site characteristics Norway 5 area [Li et al., 2015]

Parameter	Value
Water depth [m]	202
Distance to shore [km]	30
Average wind power density at 80 m height [W/m²]	1094.84
Average wave power density [kW/m]	46.43
50-year mean wind speed at 10 m height [m/s]	33.49
50-year significant wave height [m]	10.96
Mean value of T_p [s]	11.06

The environmental conditions, shown in Table 3.2, are found using a long-term joint distribution based on 10 years of hindcast wind and wave data [Li et al., 2015]. The turbulence intensity I is according to IEC 61400-1 [IEC, 2005]. The wind and waves are simulated using the Kaimal and JONSWAP spectra, respectively. A combination of the Morison’s equation and a potential theory formulation is used to calculate the hydrodynamic loads [Bachynski, 2014]. Data is produced at a sampling rate of 600 Hz.

Table 3.2: Environmental conditions for the load case

Parameter	Value
\bar{U} [m/s]	12
H_S [m]	2.5
T_p [s]	10.1
I [-]	0.12

3.3 Fault Cases

The applied damage to the system is modelled by changing the stiffness and damping of the damaged bearings in the MBS model. The stiffness is inversely proportional with the accumulated damage (or degradation), as is explained in Section 2.8. Damping is also reduced when damage accumulates, although understood by the Rayleigh damping, this still is an assumption. Damping might very well increase for increased damage. Wang performed different modelling work and, based on his experience, he found out that the damping of bearings depend on their stiffness.

For this research, the front bearing on the main shaft (INP-A) is damaged in the radial and axial direction and the rear bearing on the high speed shaft (HS-B) is damaged in the radial direction. These kind of faults are in the latter referred to as MBR, MBX and HSBR, respectively. Axial damage refers to damage in the x -direction and radial damage indicates degradation in the y - and z -direction. In Figure 1 one can find how the axis system is defined and in Figure 2 it is shown how this axis system is applied on the drive train. The damaged bearings are indicated in Figure 3.2. These two bearings are chosen since they are most prone to failure [Sheng, 2016].

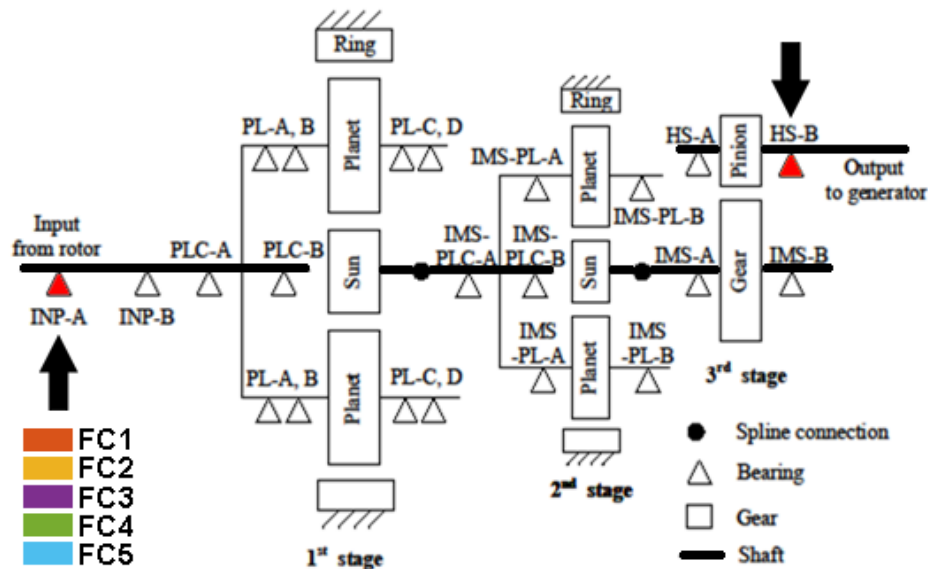


Figure 3.2: Schematic overview of the 10 MW wind turbine drive train model. The damaged bearings are indicated in red and with an arrow [Wang et al., 2019]

The damage or degradation is expressed using Equations 2.27 and 2.29. For example, 90% degradation corresponds to 10% of the healthy bearing stiffness and damping. Five degradation levels are investigated, being 15%, 30%, 50%, 70% and 90%, and are referred to as FC1, FC2, FC3, FC4 and FC5, respectively. The baseline (BL) case refers to 0% degradation. The fault cases (FCs) are displayed in Tables 3.3 to 3.5.

Table 3.3: Main shaft front bearing (INP-A) radial stiffness degradation

MBR								
Fault case	Stiffness	Value	Stiffness	Value	Damping	Value	Damping	Value
		[MN/m]		[MN/m]		[kN s/m]		[kN s/m]
BL	K_{1y}	89.244	K_{1z}	12520	C_{1y}	89.244	C_{1z}	12520
FC1	$0.85K_{1y}$	75.8574	$0.85K_{1z}$	10642	$0.85C_{1y}$	75.8574	$0.85C_{1z}$	10642
FC2	$0.7K_{1y}$	62.4708	$0.7K_{1z}$	8764	$0.7C_{1y}$	62.4708	$0.7C_{1z}$	8764
FC3	$0.5K_{1y}$	44.622	$0.5K_{1z}$	6260	$0.5C_{1y}$	44.622	$0.5C_{1z}$	6260
FC4	$0.3K_{1y}$	26.7732	$0.3K_{1z}$	3756	$0.3C_{1y}$	26.7732	$0.3C_{1z}$	3756
FC5	$0.1K_{1y}$	8.9244	$0.1K_{1z}$	1252	$0.1C_{1y}$	8.9244	$0.1C_{1z}$	1252

Table 3.4: Main shaft front bearing (INP-A) axial stiffness degradation

MBX				
Fault case	Stiffness	Value [MN/m]	Damping	Value [kN s/m]
BL	K_{1x}	3524.5	C_{1x}	3524.5
FC1	$0.85K_{1x}$	2995.825	$0.85C_{1x}$	2995.825
FC2	$0.7K_{1x}$	2467.15	$0.7C_{1x}$	2467.15
FC3	$0.5K_{1x}$	1762.25	$0.5C_{1x}$	1762.25
FC4	$0.3K_{1x}$	1057.35	$0.3C_{1x}$	1057.35
FC5	$0.1K_{1x}$	352.45	$0.1C_{1x}$	352.45

Table 3.5: High speed shaft rear bearing (HS-B) axial stiffness degradation

HSBR								
Fault case	Stiffness	Value	Stiffness	Value	Damping	Value	Damping	Value
		[MN/m]		[MN/m]		[MN s/m]		[MN s/m]
BL	K_{2y}	7419.5	K_{2z}	8542.5	C_{2y}	7419.5	C_{2z}	8542.5
FC1	$0.85K_{2y}$	6306.575	$0.85K_{2z}$	7261.125	$0.85C_{2y}$	6306.575	$0.85C_{2z}$	7261.125
FC2	$0.7K_{2y}$	5193.65	$0.7K_{2z}$	5979.75	$0.7C_{2y}$	5193.65	$0.7C_{2z}$	5979.75
FC3	$0.5K_{2y}$	3709.75	$0.5K_{2z}$	4271.25	$0.5C_{2y}$	3709.75	$0.5C_{2z}$	4271.25
FC4	$0.3K_{2y}$	2225.85	$0.3K_{2z}$	2562.75	$0.3C_{2y}$	2225.85	$0.3C_{2z}$	2562.75
FC5	$0.1K_{2y}$	741.95	$0.1K_{2z}$	854.25	$0.1C_{2y}$	741.95	$0.1C_{2z}$	854.25

3.4 Natural Frequencies

In this section it is explained how the natural frequencies of the drive train are obtained. In Section 3.4.1, the method to find shaft rotational frequencies is described. Then, the mesh frequency determination method is explained in Section 3.4.2. Afterwards, the method to obtain the natural frequencies of the shafts is outlined in Section 3.4.3.

3.4.1 Shafts Rotational Frequencies

The angular velocity repeats over periods of both one revolution and one tooth pitch [Nejad et al., 2014c]. Faults, distributed or local, are likely to be found on either the shafts' rotational frequencies or the gearbox stages' mesh frequencies [Miao and Zhou, 2015]. The shaft rotational frequency is easy to obtain, being the mean of the shaft's rotational velocity.

3.4.2 Mesh Frequencies

For obtaining the mesh frequencies of the stages, one should know that a planetary gearbox' structure and motion are more complex in comparison with the motion of a parallel gearbox [Miao and Zhou, 2015]. Therefore, there is a difference between the mesh frequencies of parallel and planetary gearbox stages. The model used for processing data has two planetary stages and one parallel stage. The mesh frequency of a parallel gearbox stage is calculated with Equation 3.1 [Nejad et al., 2014c]. f_{IMS} and f_{HSS} are the mean rotational frequency of the intermediate speed and high speed shaft respectively and n_{IMS} and n_{HSS} are the number of teeth of the intermediate speed and high speed gear.

$$f_m = f_{IMS}n_{IMS} = f_{HSS}n_{HSS} \quad (3.1)$$

In Equation 3.2, one finds the calculation of a planetary gearbox stage. Here the subscript H , $ring$ and sun represent the planet carrier, ring gear and sun gear respectively [AGMA, 2006, Miao and Zhou, 2015].

$$f_m = f_H n_{ring} = \frac{n_{ring}n_{sun}}{n_{ring} + n_{sun}} f_{sun} \quad (3.2)$$

3.4.3 Shafts Natural Frequencies

The natural frequency of the shafts are obtained by producing spectra from the shafts' acceleration in x -, y - and z -direction. The peaks of the spectra will be considered as the shaft's natural frequencies.

Harmonics occur at multiples of the mesh frequencies f_m , i.e. at mf_m . Sidebands occur at $f_m \pm nf_1$ and $f_m \pm nf_2$ where m and n are integers [Nejad et al., 2012]. These frequencies will thus not be considered as natural frequencies and will be filtered out.

3.5 Fault Detection

The introduced fault needs to be detected. For fault detection one common, two non-traditional and two novel method are deployed. Two of these are methods in the time domain, presented in Section 3.5.1. The three other methods are executed in the frequency domain, described in Section 3.5.2.

3.5.1 Time Domain Analysis

In this section, the fault detection in the time domain is introduced. Starting off with a common method: the Bearing Velocity RMS Threshold Method as proposed by ISO 10816-21 is described in the next section. Afterwards, the Peeters' Anomaly Detection Method is presented and a modification is proposed.

Bearing Velocity RMS Threshold Method

A common method to detect abnormal vibration is the velocity root-mean-square (RMS) threshold for non-rotating parts. In literature, one can find different case studies applying this method [Ghane et al., 2017, Nejad and Moan, 2017]. Therefore, the data obtained from Wang’s 10 MW drive train model will be subject to this method at first.

In ISO standards 20816-1 and 10816-21 [ISO, 2015, ISO, 2016] concerning mechanical vibrations, four evaluation zones are considered as is shown in Table 3.6. In this study it is considered that excessive vibrations can be detected once they get into Zone B.

Table 3.6: Definition of evaluation zones for vibration [ISO, 2015, ISO, 2016]

Zone A	Vibration of new machines
Zone B	Acceptable vibration for long-term operation
Zone C	Unsatisfactory vibration for long-term operation
Zone D	Vibration causing damage to the system

The same ISO standards propose boundaries for these zones using the velocity RMS V_{RMS} of non-rotating parts. The zone boundaries, as proposed by ISO 20816-1, are depicted in Figure 3.3 and are valid for machines of which its International Standard is not yet developed.

Range of typical zone boundary values for non-rotating parts				
r.m.s. vibration velocity				
mm/s				
0,28				0,28
0,45				0,45
0,71				0,71
1,12	Zone boundary A/B 0,71 to 4,5			1,12
1,8				1,8
2,8		Zone boundary B/C 1,8 to 9,3		2,8
4,5				4,5
7,1			Zone boundary C/D 4,5 to 14,7	7,1
9,3				9,3
11,2				11,2
14,7				14,7
18				18
28				28
45				45

NOTE 1 This table only applies to machines for which specific International Standards have not been developed and for which there is no suitable experience available.

NOTE 2 Small machines (e.g. electric motors with power up to 15 kW) tend to lie at the lower end of the range and large machines (e.g. prime movers with flexible supports in the direction of measurement) tend to lie at the upper end of the range.

Figure 3.3: Typical values for the zone boundaries of the velocity RMS of non-rotating parts as proposed by ISO 20816-1 [ISO, 2016]

ISO 10816-21, however, shows different numbers for V_{RMS} and are shown in Figure 3.4. These numbers are proposed for onshore wind turbines with a nominal output less or equal to 3 MW.

Wind turbine component	Assessment velocity broad-band r.m.s. value in mm/s in the frequency band	
	Zone boundary B/C	Zone boundary C/D
Nacelle and tower	0,1 Hz to 10 Hz	
	60	100
Rotor with rolling element bearings	10 Hz to 1 000 Hz	
	2,0	3,2
Gearbox with rolling element bearings	10 Hz to 1 000 Hz	
	3,5	5,6
Generator with rolling element bearings	10 Hz to 1 000 Hz	
	6,0	10

Figure 3.4: Typical values for the zone boundaries of the velocity RMS of non-rotating parts as proposed by ISO 2018-21 [ISO, 2015]

Since Ghane and Nejad [Ghane et al., 2017, Nejad and Moan, 2017] both used the minimum zone boundaries of ISO 20816-1, these boundaries are applied in the following too. The RMS of the bearing velocity V_{RMS} is calculated with MATLAB [The MathWorks Inc., nd] using Equation 3.3.

$$V_{RMS} = \sqrt{\frac{1}{N} \sum_{n=1}^N |V_n|^2} \quad (3.3)$$

Peeters' Anomaly Detection Method

Peeters proposed in his PhD thesis [Peeters, 2019] a new fault detection method. Peeters had five years of data available for four wind turbines, which measured the vibration for 10 s at intermittent times of the day [Peeters, 2019]. Statistical indicators, like kurtosis and crest factor, are calculated for this time period and are averaged on approximately 20 data points per year per wind turbine. Each data point includes its statistical indicators. For every single statistical indicator, a predictive distribution of these approximately 400 data points is created. The predictive distribution has the properties as depicted in Equation 3.4. Here, $E\{\cdot\}$ is the expectation operator and $V\{\cdot\}$ the variance operator. σ_N is a noise parameter. $x(t)$ is the observed operational parameter, for example rotor speed or output power, and $f(x(t))$ is the time series of statistical indicators.

$$y(t) \sim N(E\{f(x(t))\}, V\{f(x(t))\} + \sigma_N^2) \quad (3.4)$$

Equation 3.5 compares a sample with the predictive distribution of that sample. The equation indicates the distance from $y(t)$ to the mean in a number of standard deviations $\beta(t)$. $x(t)$ and $y(t)$ are the observed operational parameters and constructed feature at time t respectively.

$$\beta(t) = \left| \frac{y(t) - E\{f(x(t))\}}{\sqrt{V\{f(x(t))\} + \sigma_N}} \right| \quad (3.5)$$

However, for this project there is not enough data available compared to the data available for Peeters' PhD thesis. It is known, though, which data represents a healthy gearbox and there is no noise in the data. A few modifications are proposed to make it possibly suitable for this project:

1. From the baseline and faulty data, small data sets are created of 10 s each. This size is in the latter referred to as fused period.
2. Statistical indicators $y(t)$ are calculated from data sets and are presented in the middle of the small time series. So for a fused period of 10 s, $y(t)$ is presented at $t = 5$ s, 15 s, 25 s,
3. For the time series of each statistical indicator $y(t)$ of the healthy data set, a predictive normal distribution is created using the Matlab function `fitdist(x, 'Normal')` [The MathWorks Inc., nd]. This returns $E\{f(x(t))\}$ and $V\{f(x(t))\}$ to create a normal distribution of the time series.
4. Now, for every fused time step, fault case and statistical indicator, the β parameter can be calculated using a modification of Equation 3.5, shown in Equation 3.6. Like that, a time series of alarm levels is created for every fault case. $E\{f(x(t))\}$ and $V\{f(x(t))\}$ are the values from the baseline case for the specific statistical indicator.

$$\beta(t) = \left| \frac{y(t) - E\{f(x(t))\}}{\sqrt{V\{f(x(t))\}}} \right| \quad (3.6)$$

The definition of a standard normal distribution is consulted, stating that for a data set, 4.6% of all data points lie outside the range of $\mu \pm 2\sigma$. Anything more than that will be considered as an anomaly; the introduced fault can be detected. In Table 3.7, one can see how Peeters defines the alarm level β in colors and the maximum allowed share of β 's in that range.

Table 3.7: Peeters' definition of alarm level β in colors and the maximum allowed share of β 's in that range [Peeters, 2019]

β [-]	Maximum share of β 's
<2	95.4%
2-4	4.5%
>4	0.1%

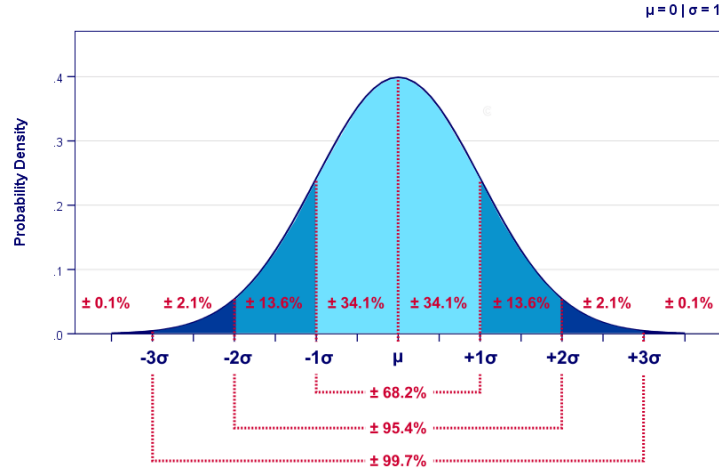


Figure 3.5: Standard normal distribution¹

The following statistical indicators are considered for the anomaly detection [Ghane, 2018, Guo et al., 2015]:

- **Mean.** Calculated with Equation 3.7 [The MathWorks Inc., nd].

$$\mu = \frac{1}{N} \sum_{n=1}^N x_n \quad (3.7)$$

- **Standard deviation.** Defined by Equation 3.8 [The MathWorks Inc., nd].

$$\sigma = \sqrt{\frac{1}{N-1} \sum_{n=1}^N |x_n - \mu|^2} \quad (3.8)$$

- **Root-mean-square.** Shown in Equation 3.9 [The MathWorks Inc., nd].

$$x_{RMS} = \sqrt{\frac{1}{N} \sum_{n=1}^N |x_n|^2} \quad (3.9)$$

- **Skewness.** Calculated with Equation 3.10 [The MathWorks Inc., nd].

$$s = \frac{E\{x - \mu\}^3}{\sigma^3} \quad (3.10)$$

- **Kurtosis.** Defined as in Equation 3.11 [The MathWorks Inc., nd].

$$K = \frac{E\{x - \mu\}^4}{\sigma^4} \quad (3.11)$$

- **Crest factor.** Defined as in Equation 3.12 [Guo et al., 2015] and found with Matlab function `peak2rms` [The MathWorks Inc., nd].

$$c = \frac{|x_p|}{x_{RMS}} \quad (3.12)$$

- **Peak.** Highest peak of the fused period. Found with the Matlab function `findpeaks` [The MathWorks Inc., nd].

¹<https://www.spss-tutorials.com/normal-distribution/> [Visited on 24th of July 2020]

3.5.2 Frequency Domain Analysis

For frequency domain analysis, the spectral analysis is performed. Spectra will be made of the motions of the drive train's (sub)components. The spectra show the power spectral density (PSD) φ over a range of frequencies. The PSD, describing the signal's power distribution into frequency components [Stoica and Moses, 2005], is defined as the discrete-time Fourier transform of the covariance sequence, shown in Equation 3.13 [Stoica and Moses, 2005].

$$\varphi(\omega) = \sum_{k=-\infty}^{\infty} r(k)e^{-i\omega k} \quad (3.13)$$

where $r(k) = E \{y(t)y^*(t-k)\}$

The maximum frequency in the spectral analysis is equal to the Nyquist frequency f_{Nyq} , which is half the sampling frequency f_s and is defined by Equation 3.14. The power density spectrum signal folds around this particular frequency [Grenander, 1959], meaning that $\varphi(Nf_{Nyq} - \Delta f) = \varphi(Nf_{Nyq} + \Delta f)$ (shown in Figure 3.6). An aliasing error causes the existence of power at frequencies higher than the Nyquist frequency.

$$f_{Nyq} = \frac{f_s}{2} \quad (3.14)$$

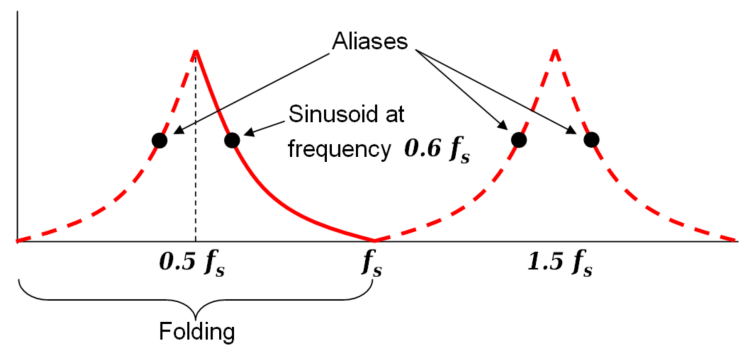


Figure 3.6: Spectrum folding around the Nyquist frequency²

Spectra are created with the WAFO toolbox [WAFO, 2017] using the function `dat2spec(x,L)`. Here, x is the data set consisting of a time series and the monitored parameter. L is the maximum lag size of the window function. The default value L is chosen by WAFO and is such that the lag size is equal to the lag where the auto correlation is less than two standard deviations [WAFO, 2017]. L is thus dependent on sampling frequency f_s and increases when f_s increases. In this work L is set to be equal to 400.

In the following, one non-traditional (Angular Velocity Error Energy Method) and two novel methods (Bearing Velocity Energy Method and Shaft Vibration Energy Method) are introduced.

²https://en.wikipedia.org/wiki/Nyquist_frequency [Visited on 26th of March 2020]

Angular Velocity Error Energy Method

In this work, the Angular Velocity Error Energy Method, as proposed by Nejad [Nejad et al., 2014c], is applied to the output data of Wang's 10 MW drive train model. The methodology used is adapted but similar. It is explained in the following.

Provided that the input velocity is steady and constant, gears with conjugate involute tooth profiles transfer motion with a constant ratio [Nejad et al., 2014c], inversely proportional to the number of teeth [Chen, 2011], shown in Equation 3.15. In this equation, n is the number of teeth. The angular position and velocity of a gear pair are represented by ϕ and ω , respectively.

$$\frac{\phi_{out}}{\phi_{in}} = \frac{\omega_{out}}{\omega_{in}} = \frac{n_{in}}{n_{out}} \quad (3.15)$$

However, Equation 3.15 is only valid in theory. due to variations from a true involute profile, assembly misalignment, and variation in the elastic deflection on the gear teeth, bearings and support structures [Nejad et al., 2014c]. Therefore, a transmission error (TE), shown in Equation 3.16, is introduced. This error shows the difference between the actual positions of the output and input gear [Nejad et al., 2014c, Litvin and Fuentes, 2004, Smith, 2003]. It has been proven that this is a good measure for geometrical deviations and to monitor gear performance [Boguski, 2010].

$$TE = \phi_{out} - \frac{n_{in}}{n_{out}} \phi_{in} \quad (3.16)$$

From this equation, the dynamic transmission error e , or angular velocity error function, can be derived, being the first time derivative of the TE. Its expression is shown in Equation 3.17. The dynamic transmission error is caused by elastic deformations, defects in bearings and gears and manufacturing errors [Nejad et al., 2014c]. The excitation frequency of both errors is often approximately equal to the mesh frequency, which is calculated like in Equation 3.1 in Section 3.4.2 [Nejad et al., 2014c].

$$e = \omega_{out} - \frac{n_{in}}{n_{out}} \omega_{in} \quad (3.17)$$

Similar to Nejad's fault detection method [Nejad et al., 2014c], three angular velocity error functions are defined and depicted in Table 3.8. Usually, the rotor and generator speed are already monitored [Nejad et al., 2014c]. Therefore, no extra effort is taken to compare the main and high speed shaft's rotational speed. This comparison is made when formulating e_{tot} for the baseline situation. The variation on this error function related to the applied damage MBR, MBX and HSBR are $e_{tot_{MBR}}$, $e_{tot_{MBX}}$ and $e_{tot_{HSBR}}$, respectively.

When the main bearing is damaged, it is expected that the gear in the first stage is affected, this means that the rotation of the low speed shaft could possibly be different. Therefore, the angular velocity error function e_{LSS} is introduced, which compares the main shaft's and low speed shaft's rotational velocity. When introducing the MBR and MBX faults, the according error functions are named e_{MBR} and e_{MBR} .

Finally, damage in the HS-B bearing could possibly mean that the third gear stage is affected. The error function for the baseline scenario e_{HSS} is consequently established. After introduction of HSBR damage, the corresponding function is named e_{HSBR} .

α_i is the gear ratio of the i^{th} stage, meaning $\alpha_i = \frac{n_{in_i}}{n_{out_i}}$ with $\alpha_1 = 4.423$, $\alpha_2 = 5.192$ and $\alpha_3 = 2.179$ [Wang et al., 2019].

Table 3.8: Angular velocity error functions for the different fault cases

Load case	Error function	Detection
Baseline	$e_{LSS}(\omega_{LSS}, \omega_{MS}) = \omega_{LSS} - \alpha_1 \omega_{MS} $ $e_{HSS}(\omega_{HSS}, \omega_{IMS}) = \omega_{HSS} - \alpha_3 \omega_{IMS} $ $e_{tot}(\omega_{HSS}, \omega_{MS}) = \omega_{HSS} - \alpha_1 \alpha_2 \alpha_3 \omega_{MS} $	Reference values
MBR	$e_{MBR}(\omega_{LSS}, \omega_{MS}) = \omega_{LSS} - \alpha_1 \omega_{MS} $ $e_{tot_{MBR}}(\omega_{HSS}, \omega_{MS}) = \omega_{HSS} - \alpha_1 \alpha_2 \alpha_3 \omega_{MS} $	Comparing e_{MBR} with e_{LSS} Comparing $e_{tot_{MBR}}$ with e_{tot}
MBX	$e_{MBX}(\omega_{LSS}, \omega_{MS}) = \omega_{LSS} - \alpha_1 \omega_{MS} $ $e_{tot_{MBX}}(\omega_{HSS}, \omega_{MS}) = \omega_{HSS} - \alpha_1 \alpha_2 \alpha_3 \omega_{MS} $	Comparing e_{MBX} with e_{LSS} Comparing $e_{tot_{MBX}}$ with e_{tot}
HSBR	$e_{HSBR}(\omega_{HSS}, \omega_{IMS}) = \omega_{HSS} - \alpha_3 \omega_{IMS} $ $e_{tot_{HSBR}}(\omega_{HSS}, \omega_{MS}) = \omega_{HSS} - \alpha_1 \alpha_2 \alpha_3 \omega_{MS} $	Comparing e_{HSBR} with e_{HSS} Comparing $e_{tot_{HSBR}}$ with e_{tot}

These equations are first analysed in the time domain and afterwards in the frequency domain. The spectra are created similar as in Section 3.5.2.

Afterwards, an interesting angular frequency interval (ω_l, ω_u] is determined, where subscript l indicates lower and u means upper. This interval is chosen following a manual process. The angular frequency intervals are selected there, where the spectral curves for the unhealthy cases are deviating the most from the healthy or baseline load case. The change in spectral curves in these frequency intervals means an increase or decrease in energy levels. Therefore, the energy of the spectrum for the chosen frequency range is calculated. This is equal to the area under the spectrum curve for the chosen interval. Equation 3.18 is used for its calculation.

$$E_{i_j}(\omega) = \int_{\omega_{l,i_jk}}^{\omega_{u,i_jk}} S_{i_jk}(\omega) d\omega$$

$$\text{where } i = MBR, MBR_{tot}, MBX, MBX_{tot}, HSBR, HSBR_{tot} \quad (3.18)$$

$$j = BL, FC1, FC2, FC3, FC4, FC5$$

$$\text{and } k = 1, 2, 3, \dots, n$$

The normalized energy E^* would then be calculated corresponding to Equation 3.19.

$$E^*(\omega) = \frac{E_{i_j}(\omega)}{E_{BL_j}(\omega)} \quad (3.19)$$

The normalized energy is compared with a threshold. This threshold tells whether and at what degradation level there is a noticeable fault. Nejad et al. found out, after consulting the wind industry, that a threshold of $E^* \geq 3$ [Nejad et al., 2014c]. For this matter, an extra threshold of $E^* \leq \frac{1}{3}$ is applied.

The Angular Velocity Error Energy Method is especially interesting since, for a normal wind turbine, the generator speed and rotor torque (of which the rotor speed can be derived) are already known [Nejad et al., 2014c]. Therefore, for detection of faults, a maximum of one extra sensor should be applied. For the energy comparison of the e_{tot} functions, no extra sensors should be applied to the wind turbine's drive train.

Bearing Velocity Energy Method

In this work, a novel method is introduced. It involves the energy calculated from the spectra of the velocities of bearings and is called the Bearing Velocity Energy Method. This method is based on the Angular Velocity Error Energy Method and is inspired by the Bearing Velocity RMS Threshold Method. Since ISO 10816-21 [ISO, 2015] and ISO 20816-1 [ISO, 2016] state that the vibration velocity root-mean-square V_{RMS} of bearings increase with its damage, it is also expected that this has an influence on the bearings' vibration energy.

For this method, however, no error functions are formulated. The to be analysed spectra come straight from the bearing velocities in the x -, y - and z -direction after data filtration. Afterwards, similar to the Angular Velocity Error Energy Method, interesting frequency intervals $(\omega_l, \omega_u]$ are selected. These intervals are characterized by a change in amplitude of the spectra. Then, the energy of the frequency interval is calculated similar to the Angular Velocity Error Energy Method, using Equation 3.18. Afterwards, this energy is normalized using Equation 3.19.

Finally, the normalized energy E^* is compared with the same threshold as the Angular Velocity Error Energy Method, depicted in Equation 3.20. This could very well have been a different threshold. However, the wind energy industry is not very willing to reveal their fault detection practices. Therefore, it was decided to stick to the threshold proposed by Nejad [Nejad et al., 2014c], although different motions and functions were analysed. If the normalized energy E^* of a bearing's vibration velocity satisfies the threshold, the vibration propagation on this bearing caused by the damage, which is introduced on one of the bearings (INP-A or HS-B), is detectable. It does not necessarily mean that the particular bearing is damaged, since this has not been proved yet.

$$E^*(\omega) \leq \frac{1}{3} \text{ or } E^*(\omega) \geq 3 \text{ or} \quad (3.20)$$

Shaft Vibration Energy Method

Another novel method is introduced in this work. It involves the energy calculated from the spectra created from the velocities and accelerations of shafts and it does not come as a surprise that this method is called the Shaft Vibration Energy Method. This method is again based on the Angular Velocity Error Energy Method. The reason why the shaft vibrations are investigated is due to the reduced stiffness of the bearings. It is expected that with a lower bearing stiffness and damping, vibrations increase.

Similar to the Angular Velocity Error Energy and Bearing Velocity Energy Methods, spectra are obtained from the filtered time series depicting the velocity and acceleration of the gearbox's shafts. Again, no error functions are formulated. Afterwards, searched is for the frequency intervals $(\omega_l, \omega_u]$ where the spectral curve of a fault case deviates significantly from the baseline response spectrum. Then, the normalized energy E^* of the frequency interval is calculated using Equations 3.18 and 3.19 and compared with the threshold, shown in Equation 3.20. If the threshold is satisfied, the damage applied on bearing INP-A or HS-B can be detected. Again, the threshold could be a different value. However, since the normalized energy threshold as proposed by Nejad et al [Nejad et al., 2014c], is (one of) the only threshold presented in literature, it is decided to stick with this threshold.

4 | Results

In this chapter, the results, obtained using the methodology of Chapter 3, are presented. This chapter is structured as follows: first, the drive train's natural frequencies are presented in Section 4.1, then the results of the five fault detection methods are presented. Starting with the results in the time domain in Section 4.2. Then, in Section 4.3, one can find the results of the frequency domain. Finally, in Section 4.4, the outcome of the five fault detection methods are compared with measurement locations as recommended by ISO 10816-21 [ISO, 2015].

4.1 Natural Frequencies

In the following, the natural frequencies of the system are presented. The natural frequencies of the DTU 10 MW wind turbine and the spar are shown in Sections 4.1.1 and 4.1.2, respectively. Then, the shaft rotational frequencies (in Section 4.1.3) and mesh frequencies (in Section 4.1.4) are obtained and compared with the minimum and maximum shaft rotational and mesh frequencies, which are documented and presented by Wang [Wang et al., 2019]. Finally, in Sections 4.1.5 and 4.1.6, one can find the shaft vibration and bearing natural frequencies, respectively.

4.1.1 DTU 10 MW Wind Turbine Natural Frequencies

The blade's natural frequencies are depicted in Table 4.1. The first tower bending natural frequency is 0.25 Hz.

Table 4.1: Natural frequencies of the isolated DTU 10 MW reference turbine blade [Dose et al., 2018, Pavese et al., 2015]

Mode	First flap	First edge	Second flap	Second edge	First torsion
ω [rad/s]	3.864	6.101	11.08	17.95	36.15
f [Hz]	0.615	0.971	1.764	2.857	5.753
ω [rpm]	36.90	58.26	105.84	171.42	345.18

4.1.2 Spar Natural Frequencies

It is crucial to know in which range the spar's natural frequencies lie. From decay tests the natural frequency is obtained and shown in Table 4.2.

Table 4.2: Spar natural frequencies obtained from decay tests [Hegseth and Bachynski, 2019]

Mode	Surge	Pitch	First bending
ω [rad/s]	0.0516-0.0538	0.1578-0.1641	3.396-3.510
f [Hz]	0.0082-0.0086	0.0251-0.0261	0.5405-0.5587
ω [rpm]	0.4931-0.5137	1.507-1.567	32.43-33.52

4.1.3 Shafts Rotational Frequencies

Wang presented in his work [Wang et al., 2019] minimum (at V_{cut-in}) and maximum (at $V_{cut-out}$) shaft rotational frequencies. These are presented in Tables 4.3 and 4.4.

Table 4.3: Drive train's minimum shaft rotational frequencies [Wang et al., 2019]

	MS	LS	IMS	HS
ω [rad/s]	0.628	2.765	14.45	31.42
f [Hz]	0.1	0.44	2.30	5.00
ω [rpm]	6.00	26.40	138.0	300.0

Table 4.4: Drive train's maximum shaft rotational frequencies [Wang et al., 2019]

	MS	LS	IMS	HS
ω [rad/s]	1.005	4.461	23.06	50.33
f [Hz]	0.16	0.71	3.67	8.01
ω [rpm]	9.600	42.60	220.2	480.6

The simulation is ran at a wind speed of 12 m/s. Therefore, using the method as explained in Section 3.4.2, the shaft rotational frequencies are obtained and are shown in Table 4.5. The minimum and maximum frequencies correspond with the obtained shaft rotational frequencies.

Table 4.5: Drive train's shaft rotational frequencies for a wind speed of 12 m/s

	MS	LS	IMS	HS
ω [rad/s]	0.9811	4.339	22.53	49.09
f [Hz]	0.1561	0.6906	3.586	7.812
ω [rpm]	9.369	41.44	215.2	468.7

4.1.4 Mesh Frequencies

The minimum and maximum mesh frequencies of the drive train are also presented in Wang's work [Wang et al., 2019]. The minimum and maximum mesh frequencies correspond to the minimum (cut-in) and maximum (cut-out) wind speed and are presented in Tables 4.6 and 4.7, respectively.

Table 4.6: Drive train's minimum mesh frequencies [Wang et al., 2019]

	1	2	3
ω [rad/s]	55.92	302.9	880.3
f [Hz]	8.90	48.21	140.11
ω [rpm]	534.0	2893	$8.407 \cdot 10^3$

Table 4.7: Drive train's maximum mesh frequencies [Wang et al., 2019]

	1	2	3
ω [rad/s]	89.47	484.7	1409
f [Hz]	14.24	77.14	224.2
ω [rpm]	854.4	4628	$1.345 \cdot 10^4$

Using the methodology as described in Section 3.4.2, mesh frequencies are found. They are depicted in Table 4.8. They match with the minimum and maximum mesh frequencies.

Table 4.8: Drive train's mesh frequencies for a wind speed of 12 m/s

	1	2	3
ω [rad/s]	87.31	473.0	1374
f [Hz]	13.90	75.28	218.7
ω [rpm]	833.8	4517	$1.312 \cdot 10^4$

4.1.5 Shafts Natural Frequencies

In Appendix B.1, one can find the figures showing the spectra of the translational accelerations of the main, low speed, intermediate speed and high speed shaft. The natural frequencies of these shafts are obtained by filtering the mesh and rotational frequencies. Its results are presented in Table 4.9. Some natural frequencies, however, could not be found using this method. Sometimes the natural frequencies were too close to the mesh and rotational frequency. The natural frequencies in the z -direction were also more difficult or sometimes impossible to find, since shafts are usually stiffer in this direction and thus are their corresponding peaks not presented in the spectra.

Table 4.9: Shaft natural frequencies

		MS		LS	IMS	HS
		1	2	1	1	1
x	ω [rad/s]	46	147		508	1809
	f [Hz]	7.32	23.40		80.85	287.9
	ω [rpm]	439.3	1404		4581	$1.727 \cdot 10^4$
y	ω [rad/s]	50			50	50
	f [Hz]	7.958			7.958	7.958
	ω [rpm]	477.5			477.5	477.5
z	ω [rad/s]					1835
	f [Hz]					292.0
	ω [rpm]					$1.752 \cdot 10^4$

4.1.6 Non-Rotating Bearings Natural Frequencies

The figures showing the spectra of the translational velocities of non-rotating bearings are presented in Appendix B.2. After filtration from mesh and rotational frequencies, the bearing frequencies are obtained and presented in the following. Sometimes the natural frequencies could not be found, possibly the bearing's natural frequencies are interfering with rotational and/or mesh frequencies. The bearings can also be too stiff to show its natural frequency in the spectra and therefore, using this methodology, the natural frequencies can not be obtained. In Table 4.10, one can find the natural frequencies of the main shaft bearings (INP-A and INP-B).

Table 4.10: Main shaft front and rear bearings natural frequencies

		INP-A				INP-B			
		1	2	3	4	1	2	3	4
x	ω [rad/s]	20	41	104	147	20	41	104	147
	f [Hz]	3.183	6.525	16.55	23.40	3.183	6.525	16.55	23.40
	ω [rpm]	191.0	391.5	993.1	1404	191.0	391.5	993.1	1404
y	ω [rad/s]	21	50			50			
	f [Hz]	3.342	7.958			7.958			
	ω [rpm]	200.5	477.5			477.5			

The natural frequencies of the low speed shaft planet carrier front and rear bearings (PLC-A and PLC-B) can be found in Table 4.11.

Table 4.11: Low speed shaft planet carrier front and rear bearings natural frequencies

		PLC-A			PLC-B		
		1	2	3	1	2	3
x	ω [rad/s]	50	510	711	50	510	711
	f [Hz]	7.958	81.17	113.2	7.958	81.17	113.2
	ω [rpm]	477.5	4870	6790	477.5	4870	6790
y	ω [rad/s]	50			50		
	f [Hz]	7.958			7.958		
	ω [rpm]	477.5			477.5		
z	ω [rad/s]	484					
	f [Hz]	77.03					
	ω [rpm]	4622					

Then, Table 4.12 depicts the natural frequencies of the intermediate speed shaft planet carrier front and rear bearings (IMS-PLC-A and IMS-PLC-B).

Table 4.12: Intermediate speed shaft planet carrier front and rear bearings natural frequencies

		IMS-PLC-A		IMS-PLC-B	
		1	2	1	2
x	ω [rad/s]	188	509	188	509
	f [Hz]	29.92	81.01	29.92	81.01
	ω [rpm]	1795	4861	1795	4861

In Table 4.13, one can find the natural frequencies of the intermediate speed shaft front and rear bearings (IMS-A and IMS-B).

Table 4.13: Intermediate speed shaft front and rear bearings natural frequencies

		IMS-A		IMS-B	
		1	2	1	2
x	ω [rad/s]	188	509	188	509
	f [Hz]	29.92	81.01	29.92	81.01
	ω [rpm]	1795	4861	1795	4861

Finally, the natural frequency of the high speed shaft front and rear bearings (HS-A and HS-B) are presented in Table B.4.

Table 4.14: High speed shaft front and rear bearings natural frequencies

		HS-A		HS-A	
		1	2	1	2
x	ω [rad/s]	50	711	50	711
	f [Hz]	7.96	113.2	7.96	113.2
	ω [rpm]	477.5	6790	477.5	6790
y	ω [rad/s]	50		50	
	f [Hz]	7.958		7.958	
	ω [rpm]	477		477	
z	ω [rad/s]	711		711	
	f [Hz]	113.1		113.1	
	ω [rpm]	6790		6790	

4.2 Time Series Analysis

In the following, one can find an explanations on why carefully analyzing time series is important. In Section 4.2.1, it is shown how data is filtered from transients and abnormal behaviour. Afterwards, results of the Velocity RMS Threshold Method are depicted in Section 4.2.2. At last, results of Peeters' Anomaly Detection Method are discussed in Section 4.2.3. Note that not all time series of all signals can be used. Some signals, for example, are discrete and can therefore not be compared. This data is discarded.

4.2.1 Filtering Transient & Abnormal Behaviour

In the following, the time series of the low speed shaft planet carrier front bearing (PLC-A) displaying velocity in the x -direction for the MBR fault case is used as an example. However, the methodology used is applied on every time series. The time series of the baseline case and the five fault cases are depicted in Figure 4.1.

In Figure 4.1a, one can see the complete time series. There is a high and abnormal peak at the beginning of the time series, making it difficult to analyse the bearing's response. This is a transient, a signal of which its Fourier expansion requires an infinite number of sinusoids [Smith, 2007]. The time series is filtered on its transient by removing the first 0.1 s, Figure 4.1b is then obtained.

Now it is to be expected that there is no abnormal behaviour present in the time series. However, for the response of the MBR fault cases three intervals with high peaks are still observed: the first 100 s for the baseline case, around 200 s for FC3 and around 600 s for FC2. These peaks do not seem to fit in the time series, especially since these responses are not followed by the fault cases of higher degradation levels. For the baseline case, FC2 and FC3, it is observed by inspecting a video of the gearbox response produced by SIMPACK, that some components lose contact with other components. As a result, the gearbox components' motions are not constrained during these time intervals. This is a SIMPACK software error and data in this interval may not be reliable. Therefore, the useful data is considered to be from the interval 250 s to 550 s. All other data are removed from the MBR time series. The resulting PLC-A x -velocity is displayed in Figure 4.1c.

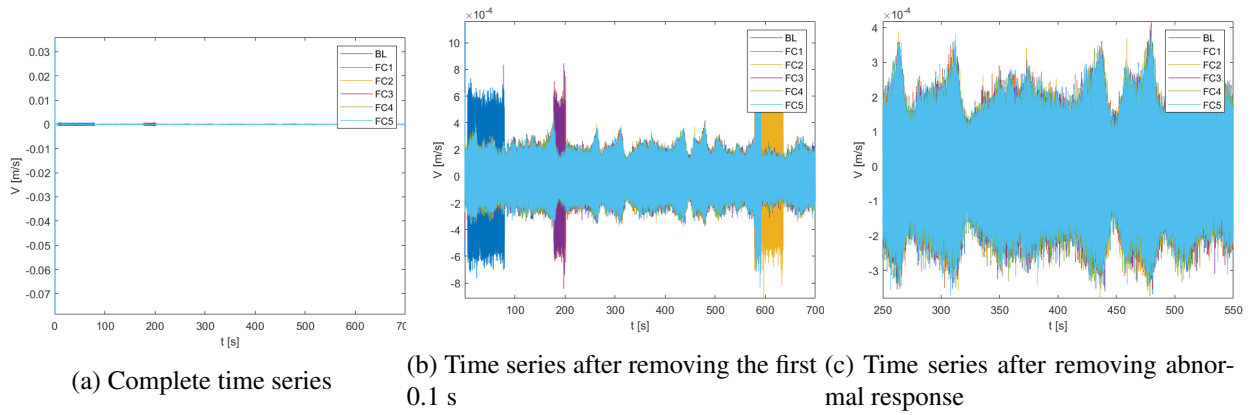


Figure 4.1: Time series of low speed shaft planet carrier front bearing (PLC-A) velocity in x -direction with MBR damage

Similarly, data filtration is performed for HSBR and MBR damage. The useful data for the HSBR time series is between 100 s and 700 s. For MBX damage, the useful time series is taken from the interval 250 s to 450 s. The filtered time series are also used for analysis in the frequency domain.

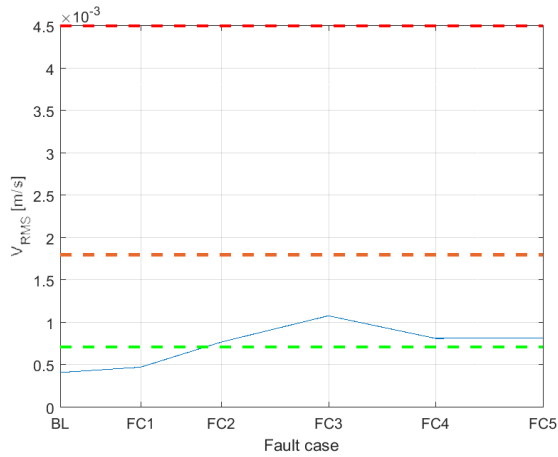
4.2.2 Velocity RMS Threshold Method

Using the methodology described in Section 3.5.1 and applying the thresholds as recommend by ISO 20816-1 [ISO, 2016], some noteworthy figures are produced with the Velocity Root-Mean-Square (RMS) Threshold Method. These are presented in the following. Afterwards, some doubtful results are presented and discussed.

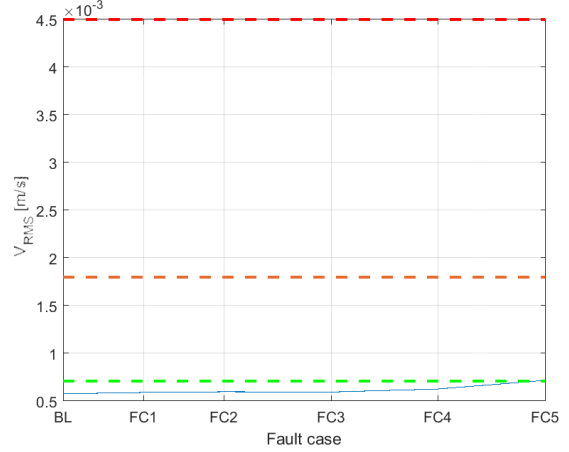
MBR

After applying radial damage in the main shaft front bearing (INP-A), which is in the latter referred to as MBR damage, the Velocity RMS Threshold Method is deployed. Since the stiffness of the bearing is reduced in the axial (y - and z -) direction, a change in response is expected in this direction. The stiffness indicates, in a way, the load carrying capacity of a component (in this case a bearing). If the bearing stiffness reduces, the load carrying capacity reduces. This implies that the extra load, which is not carried by the bearing anymore, needs to be carried by other surrounding bearings.

In Figure 4.2, one can see two noteworthy results from the Velocity RMS Threshold Method. In these Figures, it is shown that the vibration velocity in the z -direction of the main shaft rear bearing (INP-B) gets into Zone B from FC2 onwards. Also, the vibration in the same direction of the high speed shaft rear bearing (HS-B) gets into zone B at the highest degradation level (FC5). However, for both still acceptable vibration, it is assumed that this increase in motion is detectable and thus worth it to have a look at.



(a) z-direction of main shaft rear bearing (INP-B)



(b) z-direction of high speed shaft rear bearing (HS-B)

Figure 4.2: Velocity RMS development of critical bearings with MBR damage. The green line indicates the zone boundary between A and B, the orange one between B and C and the red line the zone boundary between C and D.

The two bearings are mapped in Figure 4.8. The map also shows from which fault case (or degradation level) detectable (or Zone B) vibrations are found.

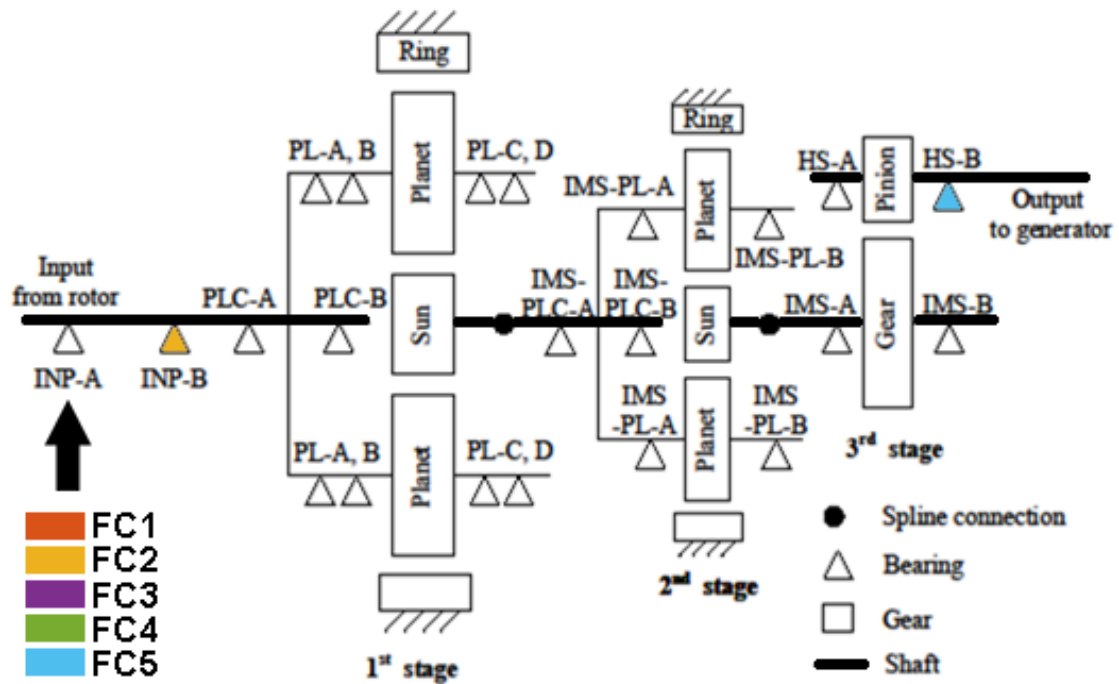


Figure 4.3: Map showing where MBR damage (indicated with an arrow) is detectable using the Velocity RMS Threshold Method. Indicated is which bearings' velocity should be monitored in order to detect the fault. The color indicates the lowest fault case from which the fault is detectable.

MBX

Using the same approach, results for MBX damage are produced. The stiffness of INP-A is reduced in the axial direction and thus was a change in bearing vibration in the x -direction expected, especially on the main shaft front and rear bearing (INP-A and INP-B). The velocity RMS value development of these bearings is presented in Figure 4.5. As one can see, the RMS value of the bearings' velocity in x -direction stays for all fault cases below the zone boundary between A and B and the curve is (almost) flat. Possibly, the bearing is too much constrained in the x -direction to allow for higher vibrations.

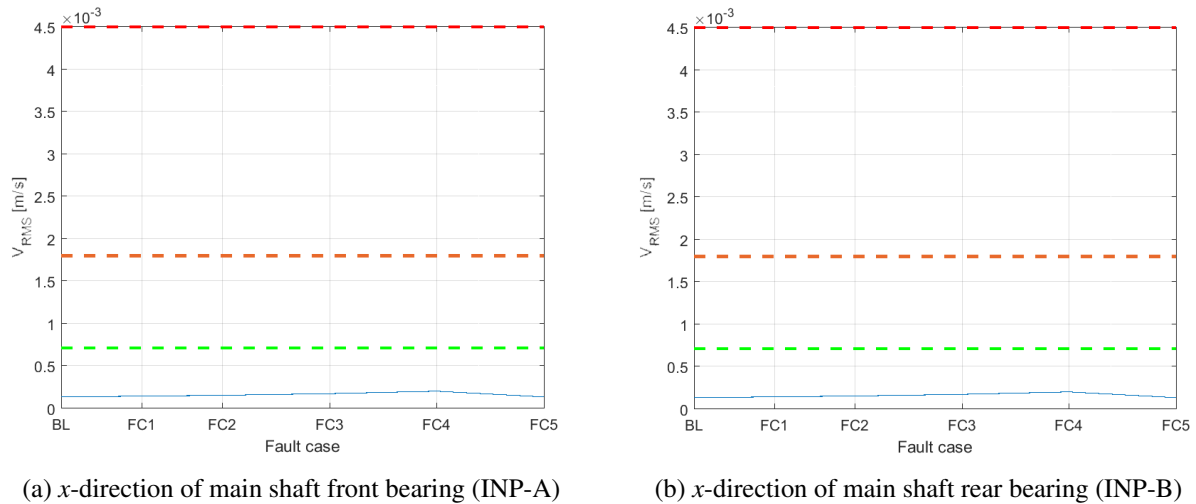
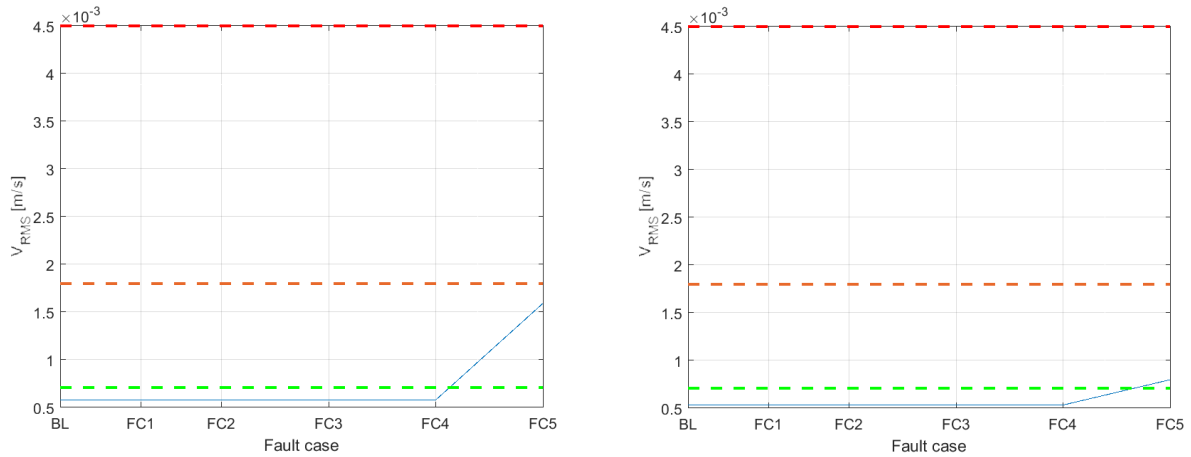


Figure 4.4: Velocity in x -direction root-mean-square development of main shaft front and rear bearings with MBX damage. The green line indicates the zone boundary between A and B, the orange one between B and C and the red line the zone boundary between C and D.

Only two interesting results are obtained after application of axial damage on INP-A (MBX). These results are shown in Figure 4.5. It is shown that at FC5 HS-B's vibration in the y - and z -direction is high enough to classify the vibration in Zone B (of which its zone boundary is indicated with the green line). The vibration in the y -direction is only a little away to reach Zone C. Higher and detectable vibration was for the MBX fault case not necessarily expected in the high speed shaft rear bearing, but more in the main shaft bearings (INP-A and INP-B) since damage is introduced there.

The vibration direction came out as a surprise. The stiffness of INP-A is reduced in the axial direction and thus was a change in vibration in this direction expected. Assumed is that in the gears the axial motion is converted into radial motion.



(a) y-direction of high speed shaft rear bearing (HS-B) (b) z-direction of high speed shaft rear bearing (HS-B)

Figure 4.5: Velocity RMS development of critical bearings with MBX damage. The green line indicates the zone boundary between A and B, the orange one between B and C and the red line the zone boundary between C and D.

The before mentioned findings are shown in Figure 4.6. It shows that MBX damage can be detected when the vibration gets into Zone B for a very high degradation.

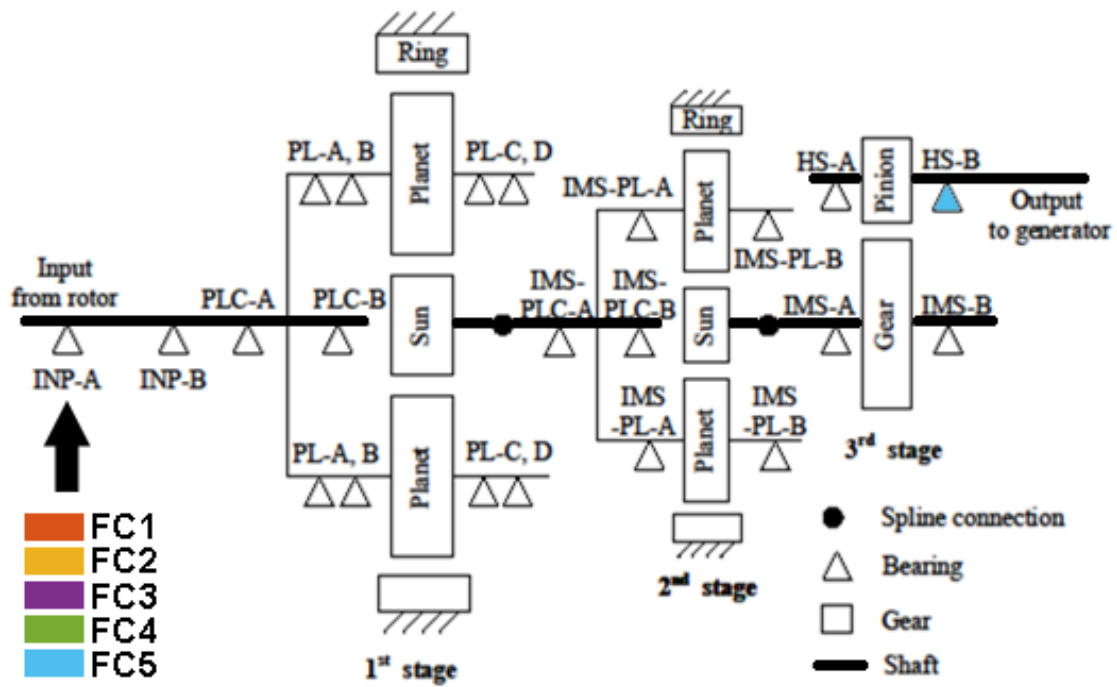
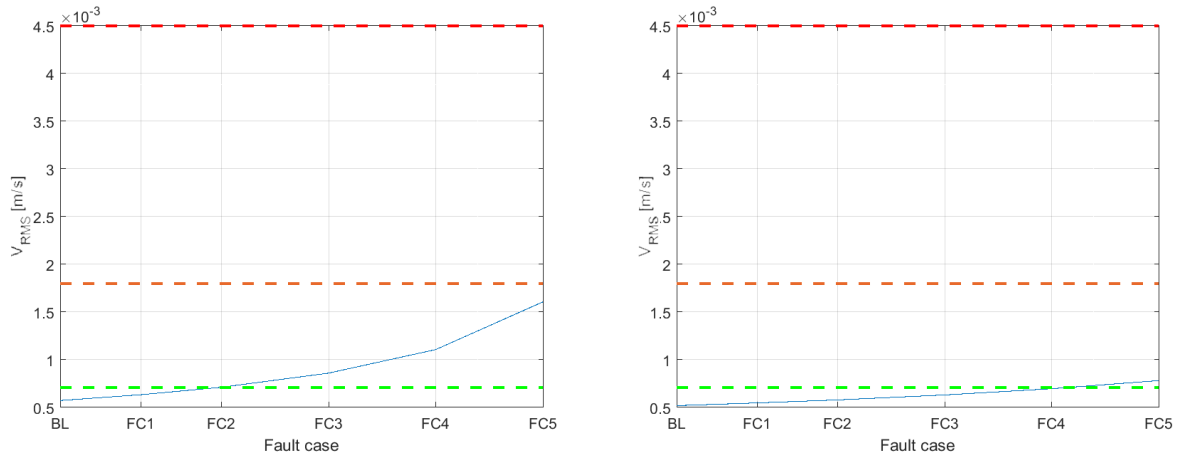


Figure 4.6: Map showing where MBX damage (indicated with an arrow) is detectable using the Velocity RMS Threshold Method. Indicated is which bearings' velocity should be monitored in order to detect the fault. The color indicates the lowest fault case from which the fault is detectable.

HSBR

Finally, HSBR damage (radial damage on the high speed shaft rear bearing (HS-B)) is applied and the Velocity RMS Threshold Method is executed. Applying the same Velocity RMS threshold, two interesting results are obtained and presented in Figure 4.7. It is shown that the bearing vibration

in the y -direction exceeds the boundary between zones A and B (marked with the green line) from FC2 onwards and gets close to the boundary between zones B and C. For the HS-B vibration velocity in the z -direction, on the contrary, vibration only exceeds the boundary between zone A and B at FC5. This difference can be explained since HS-B's stiffness in the y -direction is 23% less stiff than in the z -direction and thus it allows for more motion in this direction.



(a) y -direction of high speed shaft rear bearing (HS-B) (b) z -direction of high speed shaft rear bearing (HS-B)

Figure 4.7: Velocity RMS development of critical bearings with HSBR damage. The green line indicates the zone boundary between A and B, the orange one between B and C and the red line the zone boundary between C and D.

The findings are mapped in Figure 4.8.

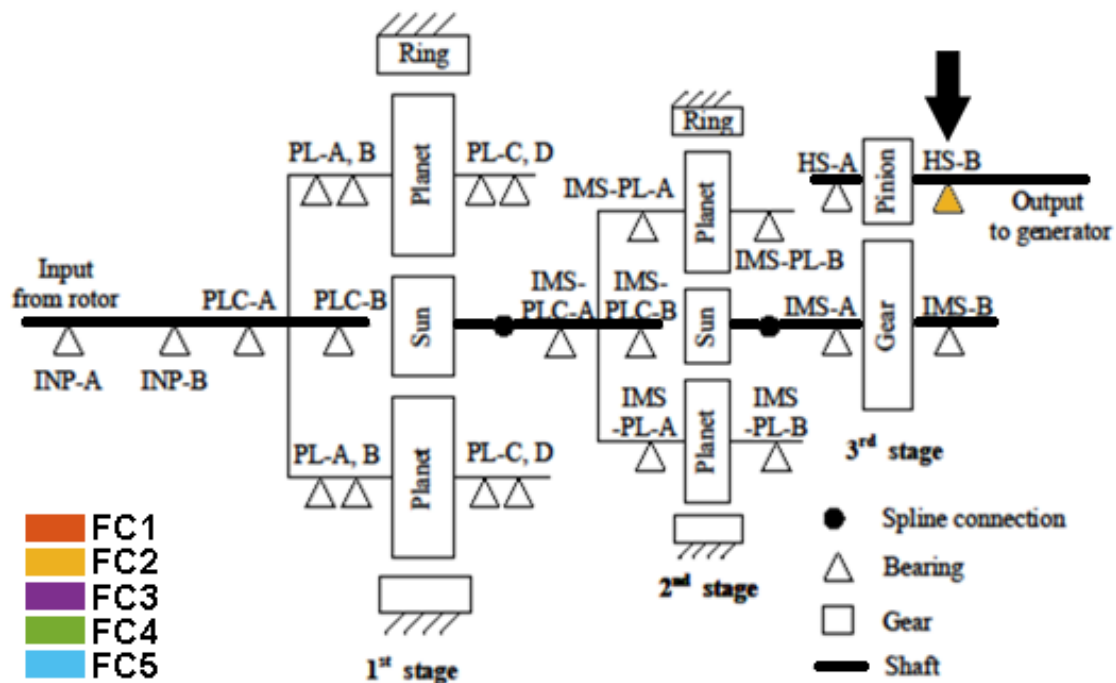


Figure 4.8: Map showing where HSBR damage (indicated with an arrow) is detectable using the Velocity RMS Threshold Method. Indicated is which bearings' velocity or acceleration should be monitored in order to detect the fault. The color indicates the lowest fault case from which the fault is detectable.

Doubtful Results

Next to the promising results presented before, some results were obtained which gave food for thought. These results are presented in the figures of Figure 4.9 for the MBR fault. Similar results are produced for the HSBR and MBX fault cases.

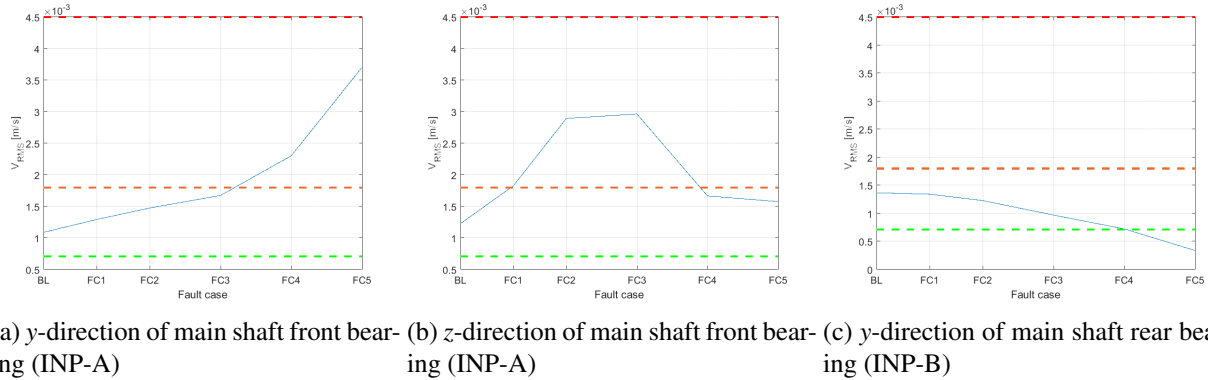


Figure 4.9: Doubtful velocity RMS development with MBR damage. The green line indicates the zone boundary between A and B, the orange one between B and C and the red line the zone boundary between C and D.

One can see that RMS vibration of the main shaft front and rear bearing (INP-A and INP-B) is already in zone B when it is fault free. Therefore, it is considered that the imposed minimum boundary values, as proposed by ISO 20816-1 [ISO, 2016], can not always be valid. Therefore, the boundary values should possibly be flexible and depend on both bearing and vibration direction. For the depicted vibrations, the higher end of the boundary values would be too high. A boundary value between the maximum and minimum values is proposed for the main shaft bearings' vibration and a lower value for the vibration of the high speed shaft bearings. In Figure 4.9b, however, nonlinear behaviour is observed. This could indicate that flexible boundaries might not even work.

Next to this, Nejad and Moan showed that vibration in zones A and B, does not necessarily result in no fatigue damage [Nejad and Moan, 2017]. Also, Igba stated that usage of RMS values is not suitable for early fault detection, since RMS values are not so much affected by short bursts of low intensity vibrations [Igba et al., 2016].

Moreover, bearing vibrations of Wang's model [Wang et al., 2019] are possibly not validated and/or verified. After all, the bearings are modelled as a set of springs and dampers. It is therefore possible that bearing vibrations are not matching the vibrations of real bearings in a gearbox.

Therefore, the Velocity RMS Threshold Method is considered to be useless for this study. The main lesson learned from this is: the higher the RMS of the bearing vibration velocity, the less feasible it is for the gearbox. An increase in V_{RMS} has been observed for most of the vibrations of different components. Therefore, in this work, a novel method is presented which is based on this finding. This method is called the Bearing Velocity Energy Method and is explained in Section 3.5.2 and its results are presented in Section 4.3.2.

4.2.3 Peeters' Anomaly Detection Method

In the following only data for the HSBR fault case is presented. Similar conclusions are drawn from the results of the MBR and MBX fault cases.

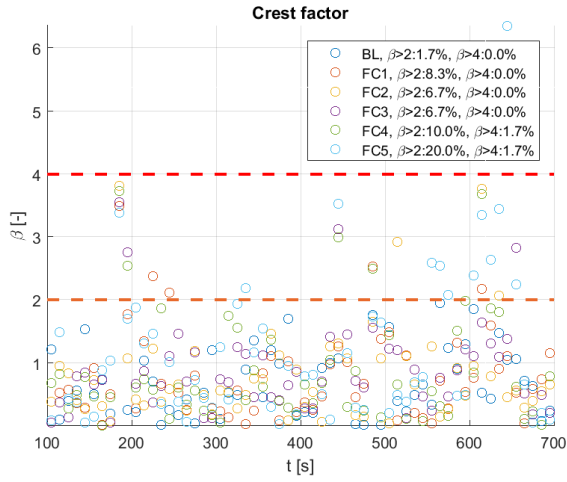
After following the methodology for the Peeters' Anomaly Detection Method, as described in Section 3.5.1, at first sight some promising results were obtained. In Figures 4.10 and 4.11, showing respectively the β time series of the drive train components' velocity and acceleration, one can see a selection of positive results. The figures are selected on the different statistical indicators and different affected gearbox components. The legend shows the share of β 's lying in the range 2-4 and the share of $\beta > 4$. When the share of $\beta > 2$ exceeds the 4.6%, the fault and its vibration propagation is considered to be detectable. Since there are only 60 data points, this threshold is rounded up to 5%.

Statistical indicators, like the crest factor (Figures 4.10a and 4.10f), skewness (see Figures 4.10b, 4.10d, 4.10e and 4.11c), kurtosis (see Figure 4.10c), standard deviation (in Figures 4.11a and 4.11e), RMS (Figures 4.11b and 4.11f) and peaks (Figure 4.11d), all have the potential to indicate faulty behaviour using the Peeters' Anomaly Detection Method. The mean was proven to be not a great statistical indicator to detect faults using the Peeters' Method.

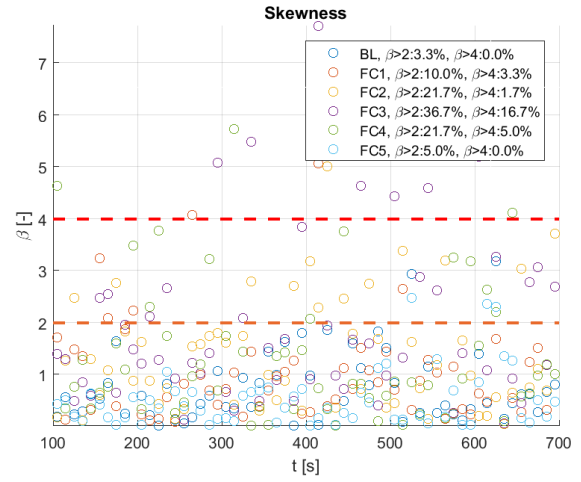
It is also shown that there are multiple components in the gearbox which behaved different than normal after introduction of the fault. Fault and vibration propagation after introduction of HSBR damage is detectable at, amongst others (but not limited to), the first stage planet carrier (Figures 4.10a, 4.11a and 4.11b), second stage first planet (in Figure 4.11c), the third spline (see Figures 4.10b and 4.10c) and high speed shaft (Figures 4.10d, 4.10e, 4.10f, 4.11d, 4.11e and 4.11f). It is obvious that there are more figures presented which show the statistical indicators of the high speed shaft's motion, since the high speed rear bearing (HS-B) is damaged and it is expected that vibration propagation is mainly local. Anomalies can already be detected from FC1 onwards, this is shown in Figures 4.10a, 4.10b, 4.10c, 4.11d, 4.11e and 4.11f.

Generally, one could see an increase in the share of $2 \leq \beta \leq 4$ and $\beta > 4$ when the degradation level increases, although this is not always the case. Highlighted are Figures 4.10b and 4.10c which show the skewness and kurtosis of the third's spline rotation. Here, one can see an increase in the share of $2 \leq \beta \leq 4$ and $\beta > 4$ until FC3, but from FC4 onwards there is a sudden drop in these shares. The skewness and kurtosis give information about the shape of the distribution of the monitoring data. The distribution gets more into the original (baseline) shape again; meaning that the distribution of the measured parameters is more normal. This could indicate that the system is not able to carry the excessive loads, induced by the decreasing load carrying capacity of HS-B.

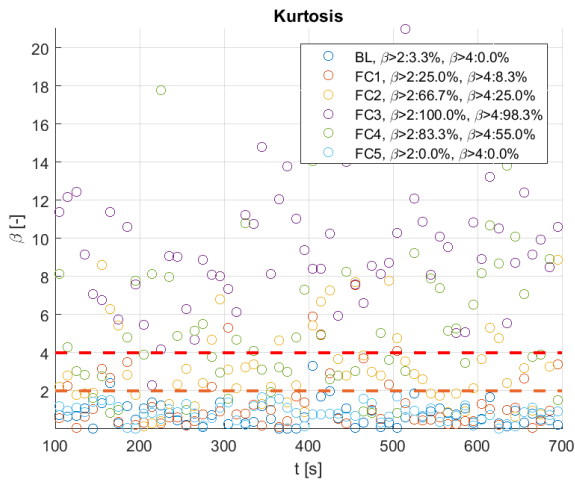
Interesting to observe is that also motion in the x -direction is affected by HSBR damage, as is observed in Figures 4.10a and 4.10d. As already explained, this was not to be expected. The stiffness and damping tell something about the load carrying capacity in that direction. When the stiffness and damping changes in a certain direction, it is expected that the load is divided over other components just in that direction. HSBR damage causes possibly problems in the third gear stage, which might affect the motion of the shafts in the x -direction.



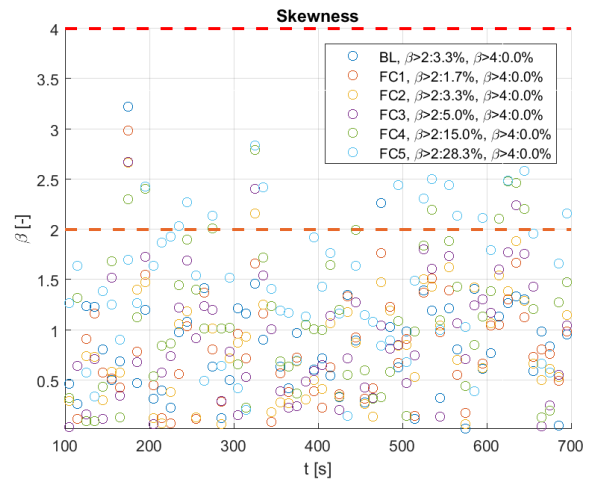
(a) Crest factor of first stage planet carrier in x -direction



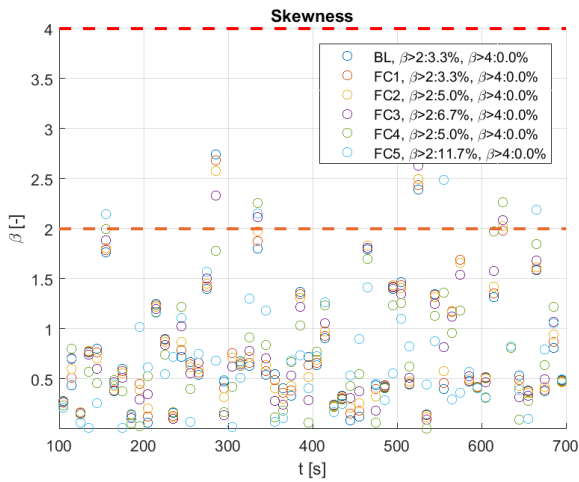
(b) Skewness of the third spline's rotation around the y -axis



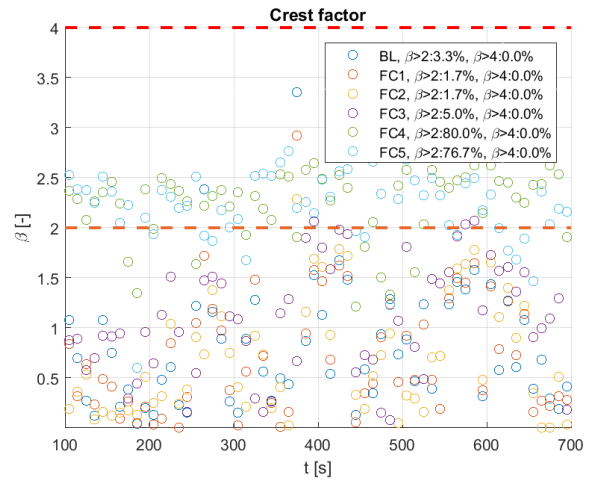
(c) Kurtosis of the third spline's rotation around the z -axis



(d) Skewness of the high speed shaft in x -direction

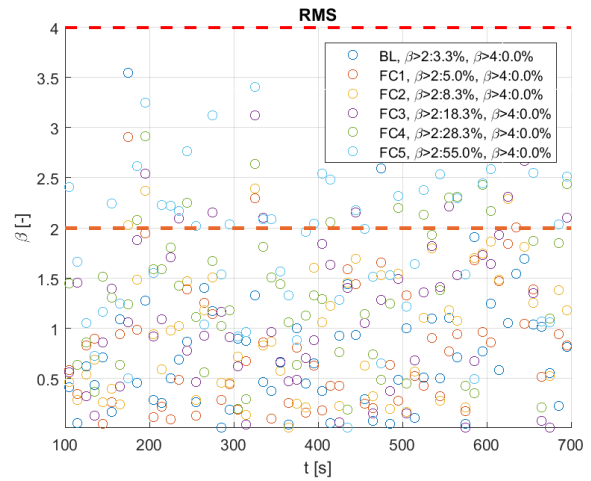
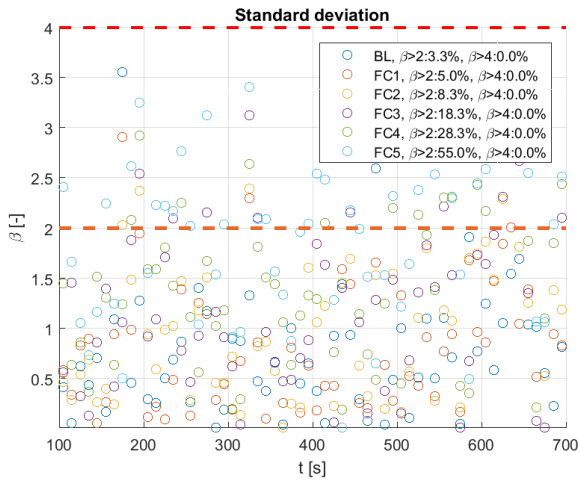


(e) Skewness of the high speed shaft's rotation around the z -axis

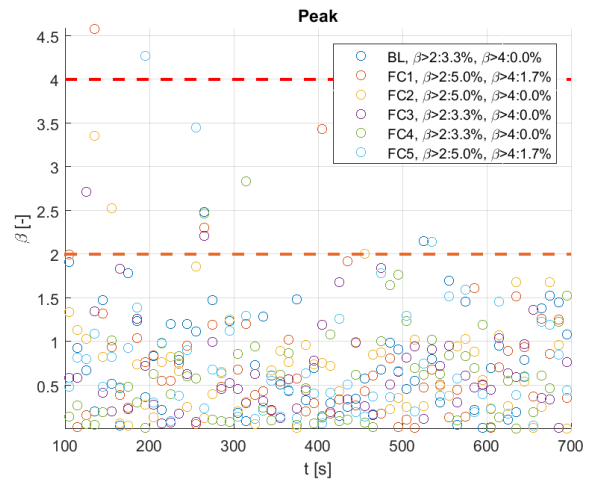
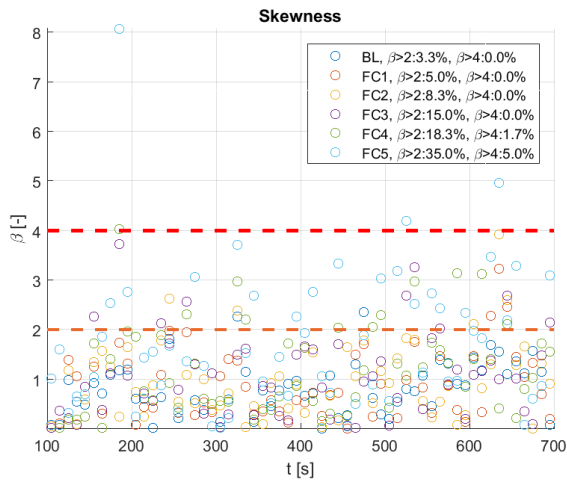


(f) Crest factor of the high speed shaft in z -direction

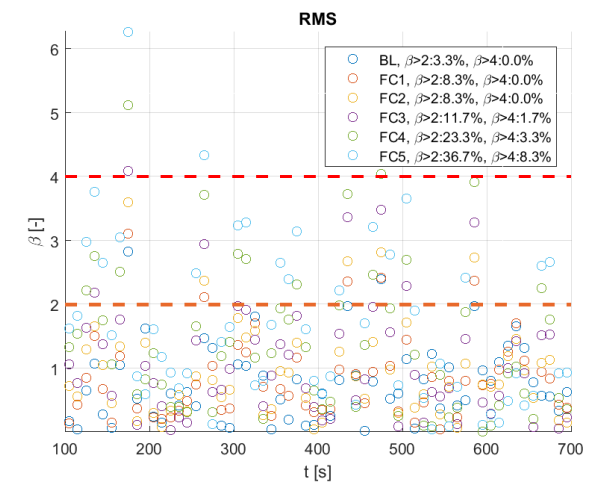
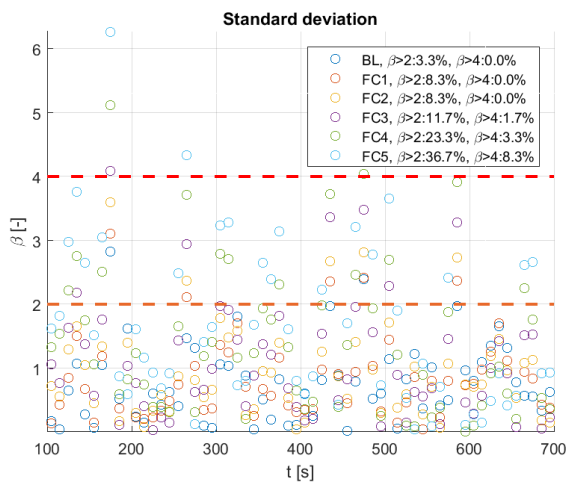
Figure 4.10: β time series of velocity with HSR damage



(a) Standard deviation of first stage planet carrier in z - (b) RMS of the first stage planet carrier's rotation around the y -axis



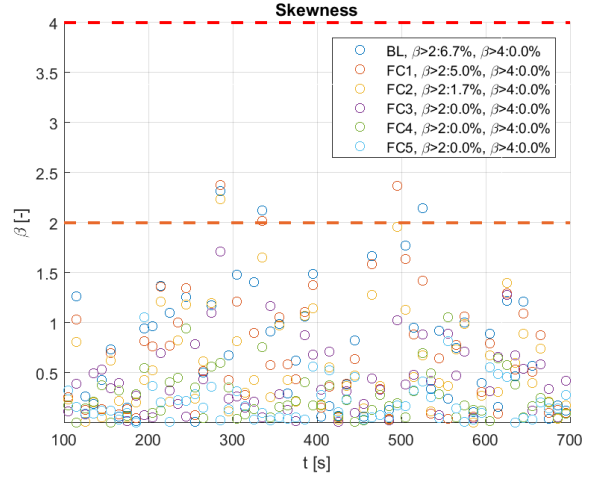
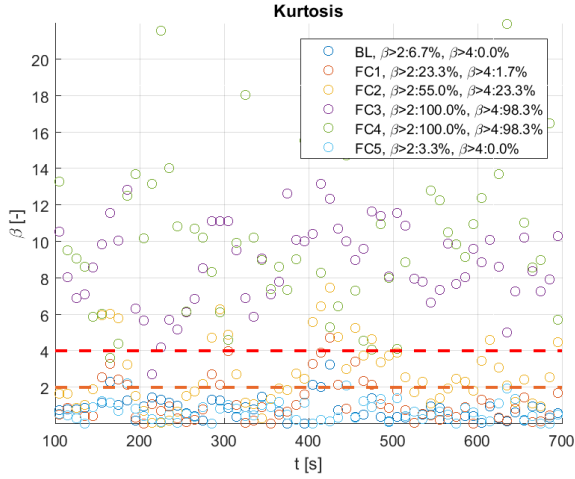
(c) Skewness of the second stage first planet in y -direction (d) Peak of the high speed shaft's rotation around the y -axis



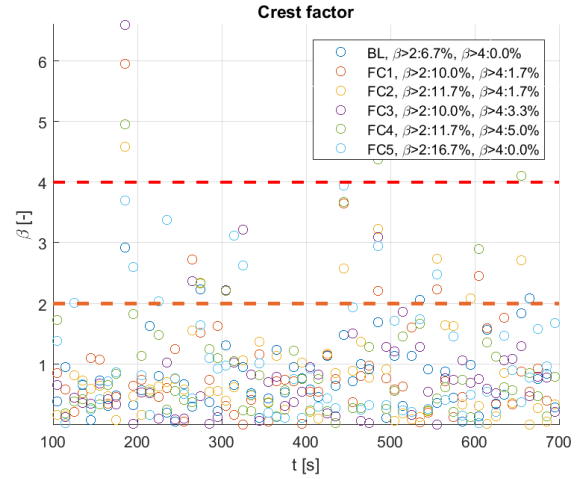
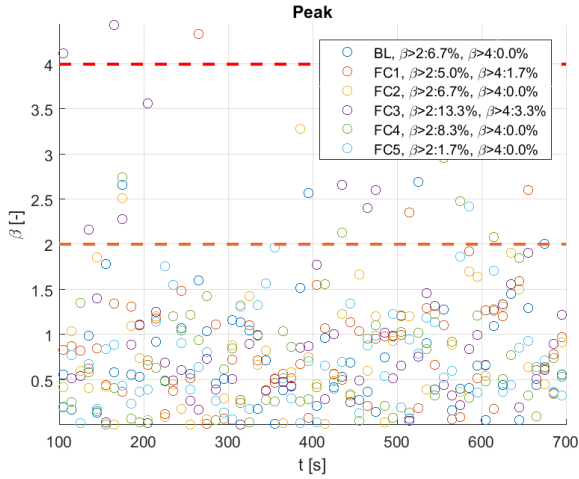
(e) Standard deviation of the high speed shaft in z -direction (f) RMS of the high speed shaft in z -direction

Figure 4.11: β time series of acceleration with HSRB damage

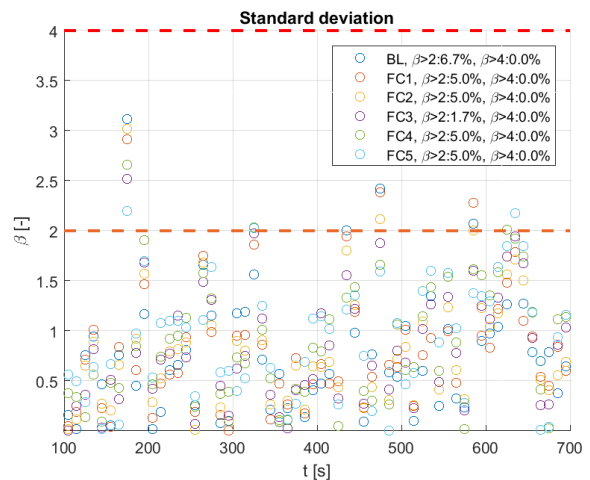
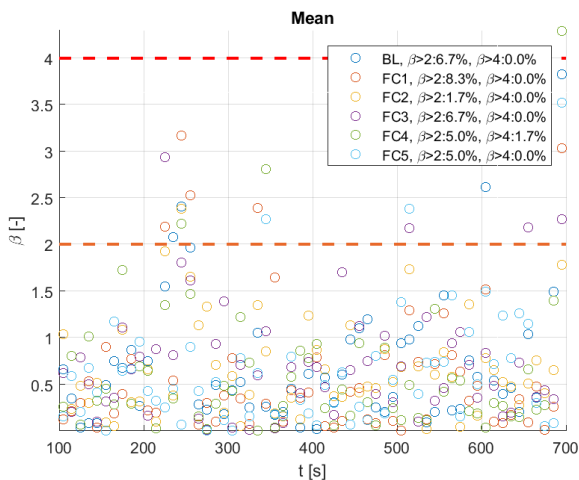
However, there is also an other side of the coin. Next to the promising results, a multitude of not expected results are produced. A selection of these results are presented in Figure 4.12. The selection is made such that different statistical indicators and gearbox components are presented.



(a) Kurtosis of second spline's rotational velocity around the z -axis (b) Skewness of high speed shaft's velocity in z -direction



(c) Peak of second stage planet carrier's acceleration in the y -direction (d) Crest factor of second stage third planet's acceleration in z -direction



(e) Mean of intermediate speed shaft's rotational acceleration around the z -axis (f) Standard deviation of high speed shaft's acceleration in y -direction

Figure 4.12: Doubtful β time series of velocity and acceleration with HSRB damage

One can clearly see fluctuations in the share of β 's which are higher than 2 between the baseline and different fault cases, which can be an indication of faults. One can, however, also see the common factor of the β time series in Figure 4.12. This is the higher than normal share exceeding the $\beta \geq 2$ threshold at the baseline fault case for six different statistical indicators. When this share is higher than this 4.6% (as shown in Figure 3.5), it was defined as faulty behaviour. There is obviously no faulty behaviour in the baseline situation. Although, the definition of a normal distribution is that 95.4% of all the observed parameters should lie in the range of $\mu - 2\sigma$ till $\mu + 2\sigma$. Possibly the Matlab function `fitdist(x, 'Normal')` is not able to fit a normal distribution from its data input. To confirm this, in Figure 4.14, the normal distributions are plotted for the same statistical indicators of the same gearbox components' motion as presented in Figure 4.12. Surprisingly, the probability density functions look like a perfect normal distribution. There should thus be another reason explaining the observed phenomenon.

There can be different reasons which can possibly explain the observation. Fundamental is the lack of data from healthy (or fault free) wind turbines. This directly influences the mean and variance of the normal distribution of a healthy wind turbine's data set. Also, the observed parameters are different. Peeters focused mainly on rotor rotational speed and power production and data is sampled above 25 kHz, whereas this work is more focused on monitoring data with a sampling rate of 600 Hz. It is possible that the statistical indicators are sensitive to the sampling rate and observed operational parameter and that they are therefore not able to capture enough information of this study's data. This might influence the results negatively.

Moreover, the size of the fused period (of 10 s) might be too big or too small. For a larger fused period, it would be easier to trespass the threshold of the 4.6% share of β 's exceeding 2. Also, a minimum of 30 data points is required to create a useful normal distribution [Mordkoff, 2016]. For smaller fused periods, it is possible that some statistical data can not be recorded, since indicators might need more data points. Therefore, a sensitivity analysis is performed to find a suitable fused period. For this, 7 statistical indicators are extracted from the acceleration time series of 16 gearbox components, having 6 degrees of freedom ($x, y, z, \alpha, \beta, \gamma$). Then the total number of baseline time series with a share of $\beta \geq 2$ higher than 4.6% is calculated and divided by 672 (= number of statistical indicators \times number of components \times degrees of freedom = $7 \times 16 \times 6$). This is performed for multiple fused periods. The outcome of this sensitivity analysis is shown in Figure 4.13.

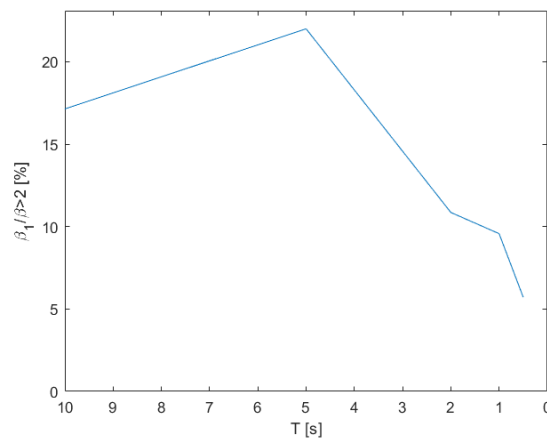
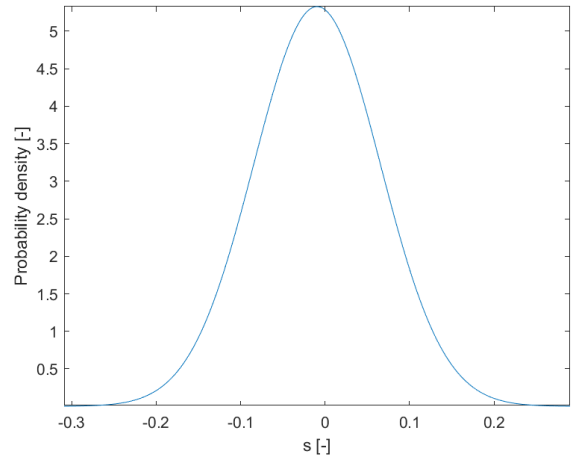
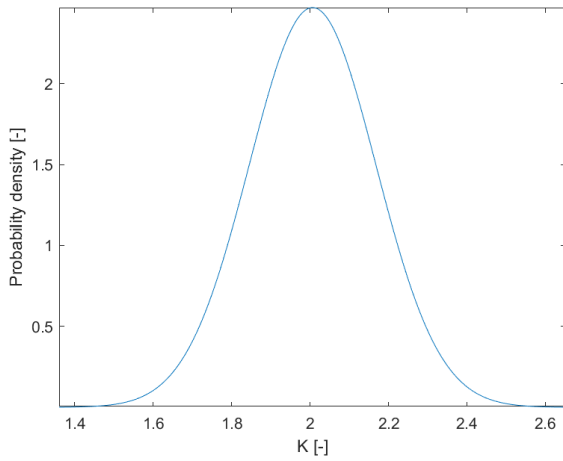
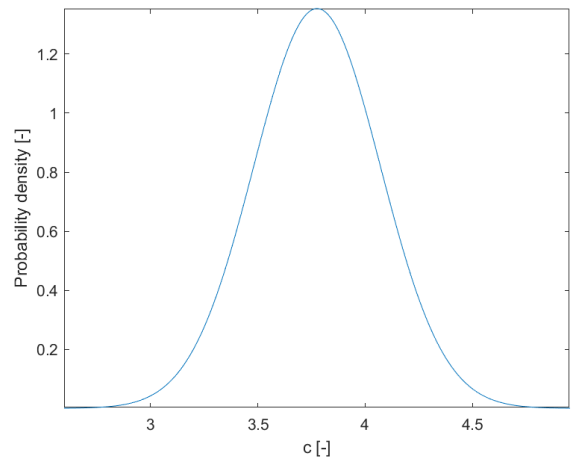
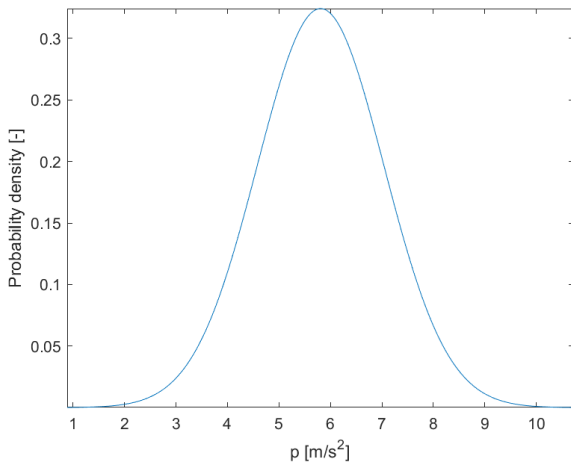


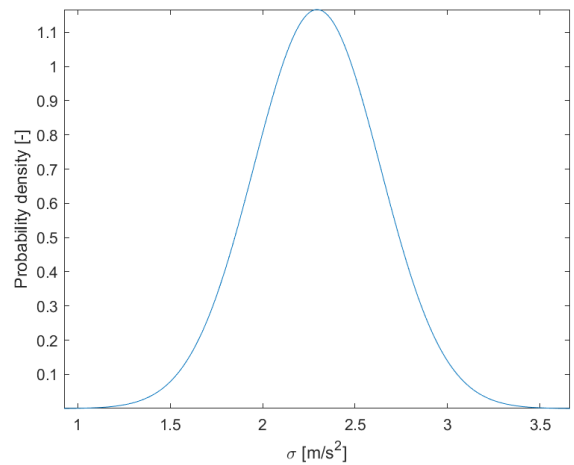
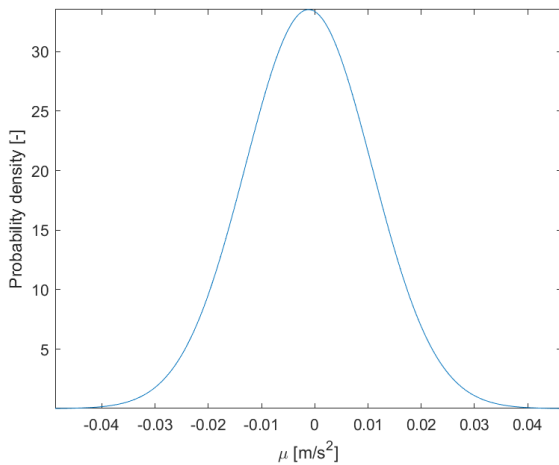
Figure 4.13: Sensitivity analysis of fused period versus total number of baseline time series with a share of $\beta \geq 2$ higher than 4.6% for gearbox components' acceleration



(a) Kurtosis of second spline's rotational velocity around the z-axis (b) Skewness of high speed shaft's velocity in z-direction



(c) Peak of second stage planet carrier's acceleration in the y-direction (d) Crest factor of second stage third planet's acceleration in z-direction



(e) Mean of intermediate speed shaft's rotational acceleration around the z-axis (f) Standard deviation of high speed shaft's acceleration in y-direction

Figure 4.14: Normal distributions of doubtful β time series of velocity and acceleration with HSBR damage

One can see that, generally, the total number of baseline time series with a share of $\beta \geq 2$ higher than 4.6% decreases when the fused period decreases. However, at a fused period of 0.5 s not a satisfactory result was reached. Still about 5% of all baseline time series have a share of $\beta \geq 2$ higher than 4.6%, there where 0% was desired. Smaller periods would lead to more computation time and statistical indicators are possibly not able to record features of the data set. It was decided to discard the option of reducing the fused period.

In order to make this method suitable for fault detection of similar data sets, the threshold of $\beta \geq 2$ could be flexible and differ per statistical indicator, parameter or component. It is possible that some statistical indicators or the response of components vary more than others, possibly not suitable for fitting a normal distribution. Tailor fitting the limits could then be possible. However, this strategy would require more knowledge on statistics and on the gearbox components, which is out of the scope of this work.

Of course, still the options remain that either the drive train model or the framework of Peeters' Anomaly Detection Method are not validated nor verified. This is for sure the case for this work's interpretation of Peeters' Method. Therefore, this method is discarded for this project.

4.3 Frequency Domain Analysis

In this section, the results of three fault detection methods in the frequency domain are presented and discussed. Starting off with the Angular Velocity Error Energy Method in Section 4.3.1. And concluding with the results of the two novel methods in Section 4.3.2 and 4.3.3, being the Bearing Velocity Energy Method and Shaft Vibration Energy Method, respectively.

4.3.1 Angular Velocity Error Energy Method

The spectra, obtained from the shafts' angular velocity error function time series, are shown in Appendix C. From these spectra, the angular frequency intervals of interest (ω_l, ω_u] are determined. These intervals are presented in Table 4.15. Here, ω_1 indicates the first frequency interval and ω_2 the second and so on. This notation will be used in the remainder of this study. In the following, only zooms of the obtained spectra are presented and discussed. All fault cases (MBR, MBX and HSBR) are analysed, however, for the MBX case no promising frequency intervals were found.

Table 4.15: Analysed angular frequency intervals for the Angular Velocity Error Energy Method

	e_{MBR}		e_{totMBR}		e_{HSBR}		e_{totHSBR}	
	ω_l	ω_u	ω_l	ω_u	ω_l	ω_u	ω_l	ω_u
ω_1 [rad/s]	80	100	75	105	1002	1023	220	302
ω_2 [rad/s]			755	770				

MBR

The zooms of the spectra of the interesting angular frequency intervals for the MBR faults are presented in Figure 4.15. In Figure 4.15a, one can find a zoom of the e_{MBR} spectrum, whereas Figures 4.15b and 4.15c show the zooms of the e_{totMBR} spectrum.

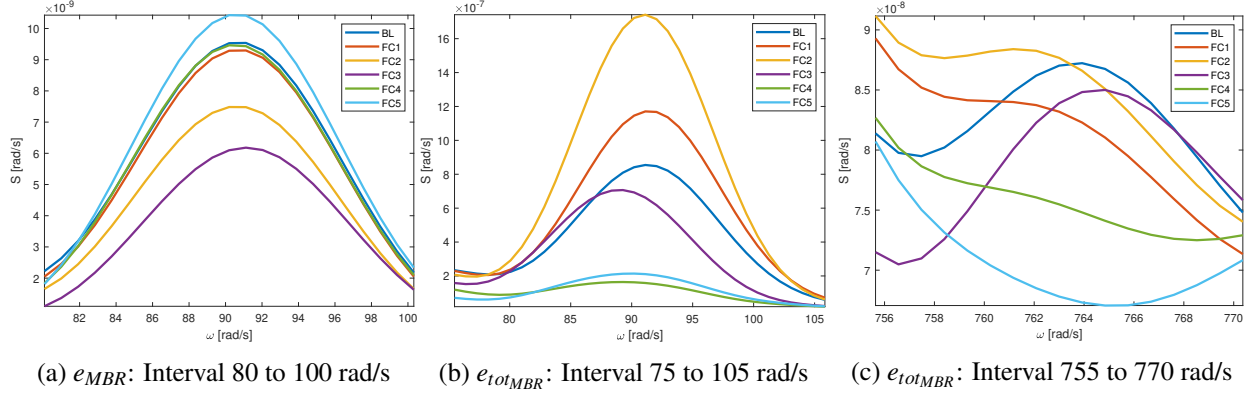


Figure 4.15: Zooms of spectra showing e_{MBR} and e_{totMBR} with MBR damage

Calculating the normalized energy E^* using Equations 3.18 and 3.19, results in the values as presented in Table 4.16. The results depicted in green meet the threshold and thus its fault can be detected. From this, it can be seen that the value of E_{totMBR}^* is below $\frac{1}{3}$ for FC4 and FC5 at frequency interval (75 rad/s,105 rad/s]. It can thus be concluded that high radial damage in the main bearing (INP-A) can be detected by monitoring the high speed and main shaft's angular velocity.

Table 4.16: Normalized energy E^* for e_{MBR} and e_{totMBR} frequency intervals

	E_{MBR}^*	E_{totMBR}^*	
	ω_{MBR1}	$\omega_{totMBR1}$	$\omega_{totMBR2}$
FC1	0.9680	1.320	0.9825
FC2	0.7806	1.836	1.0248
FC3	0.6406	0.7715	0.9554
FC4	0.9843	0.2278	0.9148
FC5	1.080	0.2636	0.8504

The frequency range where the MBR fault could be observed is around the first gear mesh frequency. This was to be expected and it can be explained. The loads induced by the wind enter the gearbox at the main shaft. When INP-A degrades, INP-B should compensate. This means that INP-B should carry more loads. Later, when INP-A degrades even more, INP-B can not cope with the increasing loads. The excessive loads are then propagated towards the first stage and can from this point influence the rotational velocity in other shafts..

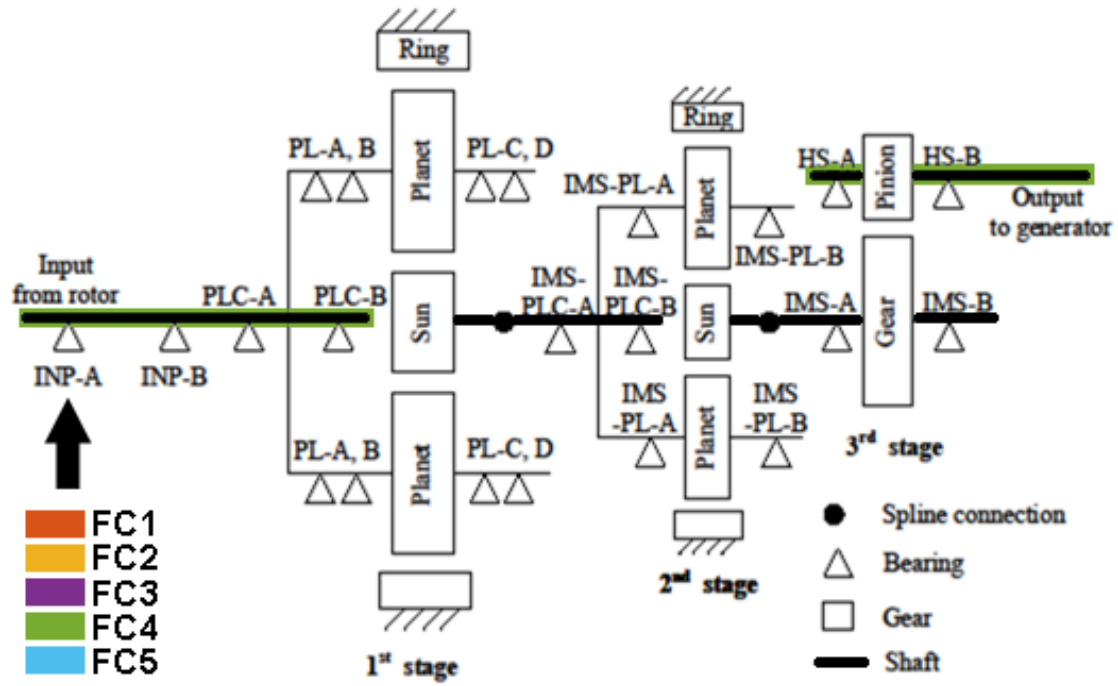


Figure 4.16: Map showing where MBR damage (indicated with an arrow) is detectable using the Angular Velocity Error Energy Method. Indicated is which shafts' angular velocity should be monitored in order to detect the fault. The color indicates the lowest fault case from which the fault is detectable.

HSBR

A similar analysis is performed for the case when the high speed shaft rear bearing is damaged in the radial direction (HSBR). The interesting frequency ranges are selected and depicted in Table 4.15. Figures 4.17a to 4.17b show the corresponding zooms of the spectra.

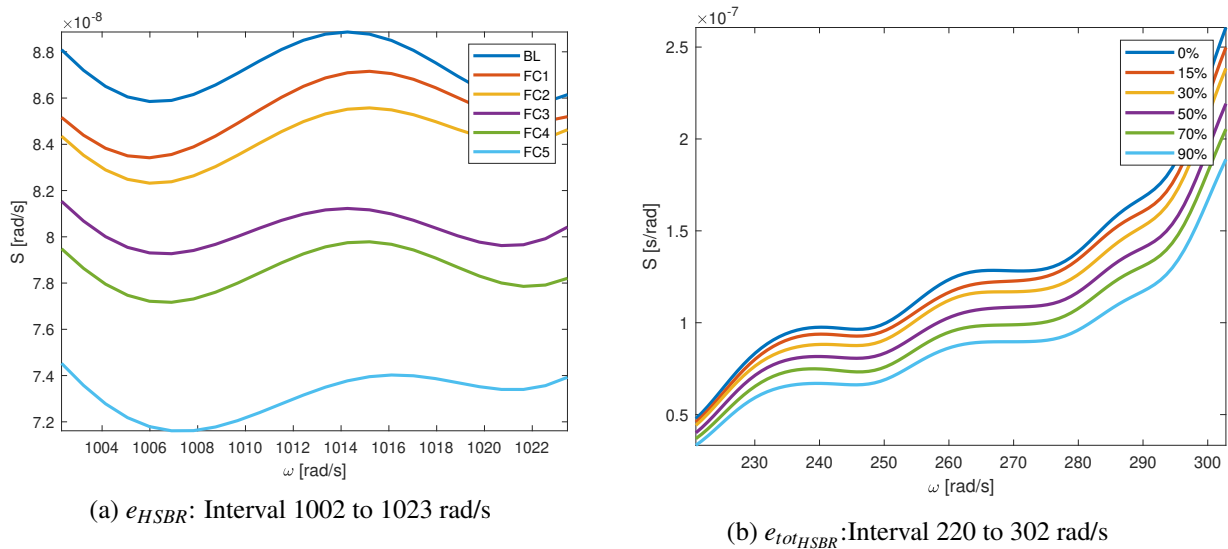


Figure 4.17: Zooms of spectra showing e_{HSBR} and $e_{totHSBR}$ with HSBR damage

The values of the normalized energy E^* are presented in Table 4.17. From this it can be concluded that none of the normalized energy values are smaller than $\frac{1}{3}$ or greater than 3. Therefore, it can be concluded that radial degradation of the high speed shaft rear bearing (HS-B) can not be detected for these angular frequency intervals using the Angular Velocity Error Energy Method considering the rotational velocities of the main, intermediate and high speed shaft.

Table 4.17: Normalized energy E^* for e_{HSBR} and $e_{totHSBR}$ frequency intervals

	E_{HSBR}^*	$E_{totHSBR}^*$
	ω_1	ω_1
FC1	0.9777	0.9580
FC2	0.9645	0.9104
FC3	0.9146	0.8397
FC4	0.8942	0.7744
FC5	0.8352	0.6998

This is surprising, since it was expected that the behaviour of the high speed end of the gearbox with a HSBR fault would be similar to the behaviour of the low speed end with a MBR fault. A reason could be the following. The high speed shaft rear bearing (HS-B) is a tapered roller bearings of the type 45T605729 from producer Koyo. This is a double-row tapered roller bearing¹ [Koyo, 2019]. This bearing should therefore be modelled as two sets of springs. Damaging this bearing would also mean that the stiffness and damping of two sets of springs should be decreased. Observing the behaviour of the drive train after HSBR damage, it is very likely that the damage is only applied on one of the two sets of springs. However, there is not enough insight in the model to verify this, since the fault is modelled by Wang and the model is not accessible.

4.3.2 Bearing Velocity Energy Method

The Bearing Velocity Energy Method, of which its methodology is described in Section 3.5.2, is executed for the MBR, MBX and HSBR fault cases. The relevant time series and complete spectra of bearing velocities are shown in Appendix D. In the following, the results of the determined relevant frequency intervals are discussed. However, for the MBX fault cases no promising results were obtained and are therefore not depicted.

MBR

After applying the MBR damage in five different degradation levels, the spectra of bearing velocity are obtained and depicted in Appendix D.2. It is found that multiple bearings are affected by the introduction of MBR damage. Therefore, all these interesting frequency intervals obtained from spectra of bearing velocity are discussed, starting from the low speed end and ending at the high speed end of the drive train. The relevant frequency intervals of the main shaft front and rear bearing (INP-A and INP-B), listed in Table 4.18, are discussed.

¹<http://eb-cat.ds-navi.co.jp/eb-eng/directory/index.asp> [Visited on 30th of July 2020]

Table 4.18: Frequency intervals for main shaft front and rear bearing (INP-A and INP-B) velocity with MBR damage

	INP-A				INP-B			
	y		z		y		z	
	ω_l	ω_u	ω_l	ω_u	ω_l	ω_u	ω_l	ω_u
ω_1 [rad/s]	15	30	15	25	12	32	15	30
ω_2 [rad/s]	32	56	45	64	38	59	78	101
ω_3 [rad/s]	80	101	78	102	70	106		

First, the front bearing is considered. The corresponding zooms of the spectra for the chosen intervals are displayed in Figures 4.18 and 4.19 for the bearing velocity in the y- and z- direction, respectively.

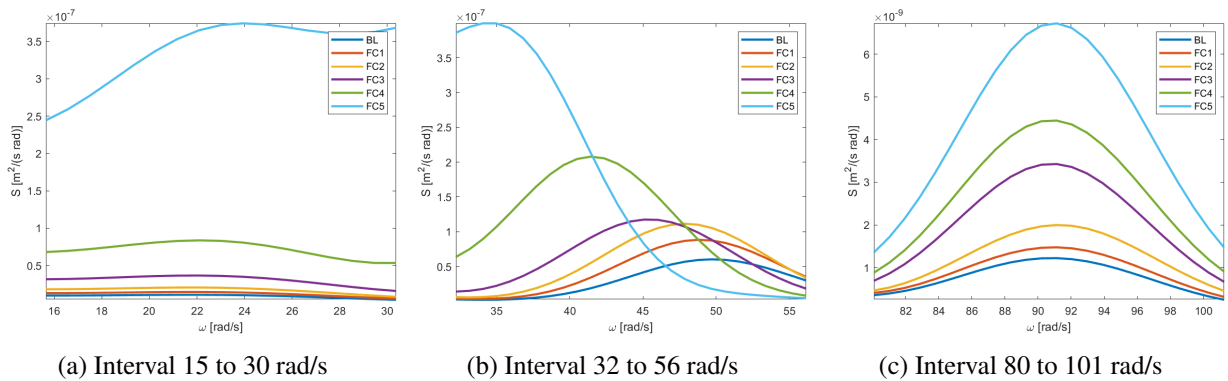


Figure 4.18: Zooms of spectrum showing main shaft front bearing (INP-A) velocity y-direction with MBR damage

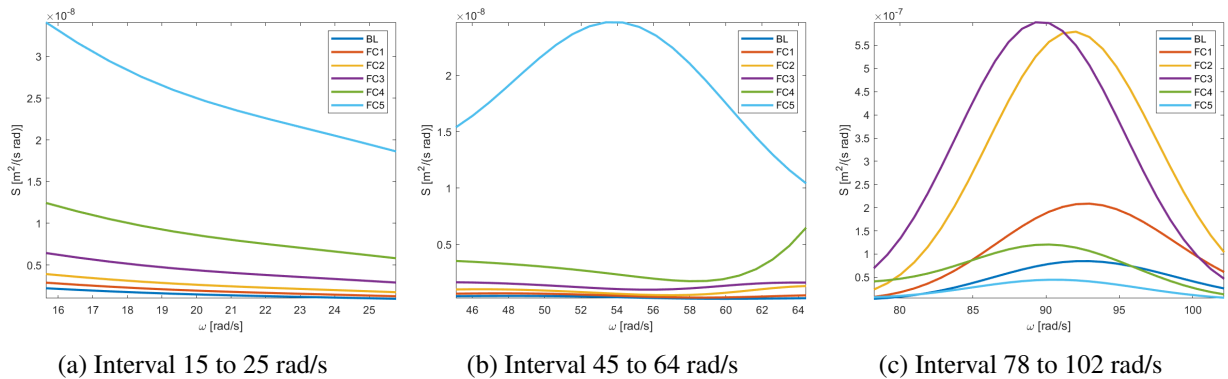


Figure 4.19: Zooms of spectrum showing main shaft front bearing (INP-A) velocity z-direction with MBR damage

The area below the curve is calculated with ω_l as lower and ω_u as upper limit and expressed as an energy E . After normalization, the normalized energies E_{INP-A}^* are calculated to be as depicted in Table 4.19. Results marked green are meeting the threshold. It can be concluded that, using the normalized energy method for bearing velocity, faulty behaviour can be observed for 30% radial degradation of the main shaft front bearing (INP-A) by monitoring the main shaft front bearing's (INP-A) velocity in the z-direction. Faulty behaviour can also be observed by monitoring INP-A's velocity in the y-direction, albeit for degradations from 50% and higher.

Table 4.19: Normalized energy E^* for main shaft front bearing (INP-A) velocity with MBR damage

	$E_{\text{INP-A}_y}^*$			$E_{\text{INP-A}_z}^*$		
	ω_1	ω_2	ω_3	ω_1	ω_2	ω_3
FC1	1.344	1.498	1.207	1.309	1.547	2.421
FC2	1.899	1.948	1.621	1.790	2.699	6.502
FC3	3.395	2.199	2.732	2.969	4.209	6.801
FC4	7.951	3.800	3.568	5.829	9.218	1.494
FC5	37.62	5.465	5.432	17.03	63.89	0.5259

Looking at the results, one can see an increase in energy and thus an increase in variance. This was to be expected and can be explained as follows. When the stiffness of a spring (in this case bearing INP-A) decreases, the amplitude of its response increases (and the period increases) [Inman, 2013, Turteltaub, 2015]. As a consequence, the variance of the response and thus the energy of the spectrum increases.

The relevant spectra intervals of the main shaft rear bearing's y - and z -velocity are displayed in Figures 4.20 and 4.21, respectively.

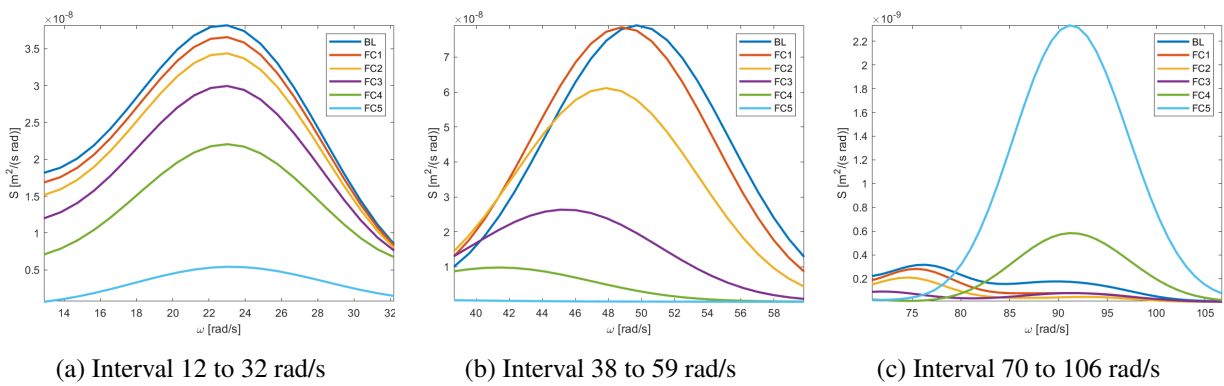


Figure 4.20: Zooms of spectrum showing main shaft rear bearing (INP-B) velocity y -direction with MBR damage

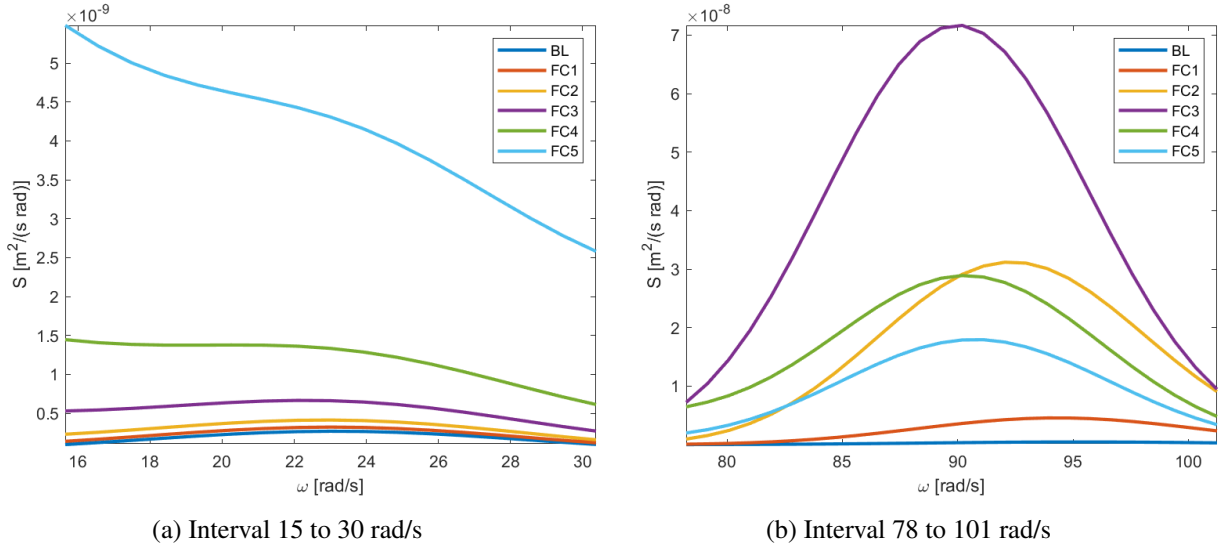


Figure 4.21: Zooms of spectrum showing main shaft rear bearing (INP-B) velocity z -direction with MBR damage

In Table 4.20, the normalized energy E^* is calculated for the relevant frequency intervals. It is shown that already for MBR damage with 15% degradation, the fault can be detected by measuring the velocity in z -direction. When monitoring the velocity in the y -direction, one could only detect damage when it is 50% degraded.

Table 4.20: Normalized energy E^* for main shaft rear bearing (INP-B) velocity with MBR damage

	$E_{\text{INP-B}_y}^*$			$E_{\text{INP-B}_z}^*$	
	ω_1	ω_2	ω_3	ω_1	ω_2
FC1	0.9543	0.9855	0.6664	1.218	9.470
FC2	0.8929	0.7631	0.4317	1.610	65.27
FC3	0.7714	0.3196	0.3174	2.734	153.7
FC4	0.5596	0.0923	1.489	5.911	65.39
FC5	0.1289	0.0029	5.929	20.39	39.28

The results can be explained as follows. With the decreased stiffness of the main shaft front bearing (INP-A), the rear bearing needs to carry more loads. This results in larger vibrations and thus an increase in energy. The non-monotonic behaviour at the third frequency interval can be explained. It is possible that the bearing, modelled as a spring, was not able to carry the increased loads anymore and could not transfer loads with this frequency interval.

The frequency intervals, where the damage on INP-A could be detected, are around the intermediate and high speed shaft rotational frequencies and the first mesh frequency. This could indicate that the rotation of these shafts is affected when INP-A gets damaged. Also, as explained earlier, excessive loads are propagated from the two main shaft bearings to the first stage of the gearbox and are probably affecting the gears.

The frequency intervals for the x - and z -velocity for the front and rear planet carrier bearings of the low speed shaft are depicted in Figure 4.21.

Table 4.21: Frequency intervals for low speed shaft planet carrier front and rear bearing (PLC-A and PLC-B) velocity with MBR damage

ω_1 [rad/s]	PLC-A				PLC-B			
	x		z		x		z	
	ω_l	ω_u	ω_l	ω_u	ω_l	ω_u	ω_l	ω_u
	12	32	77	105	13	31	80	103

The corresponding zooms of the spectra are shown in Figure 4.22 and 4.23 for the front (PLC-A) and rear (PLC-B) bearing, respectively.

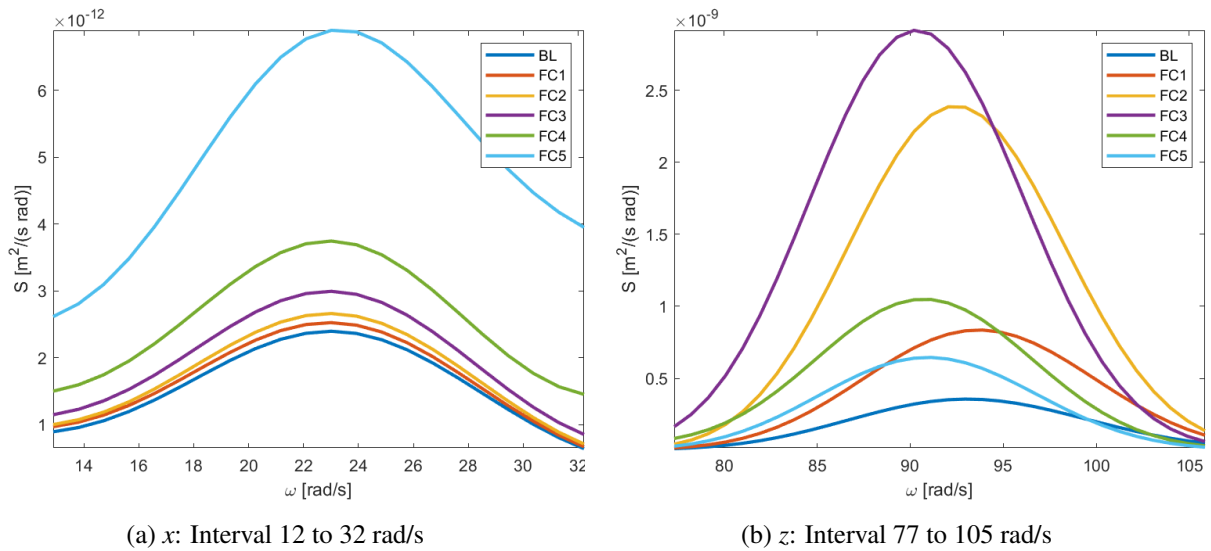


Figure 4.22: Zooms of spectra showing low speed shaft planet carrier front bearing (PLC-A) velocity x - and z -direction with MBR damage spectra

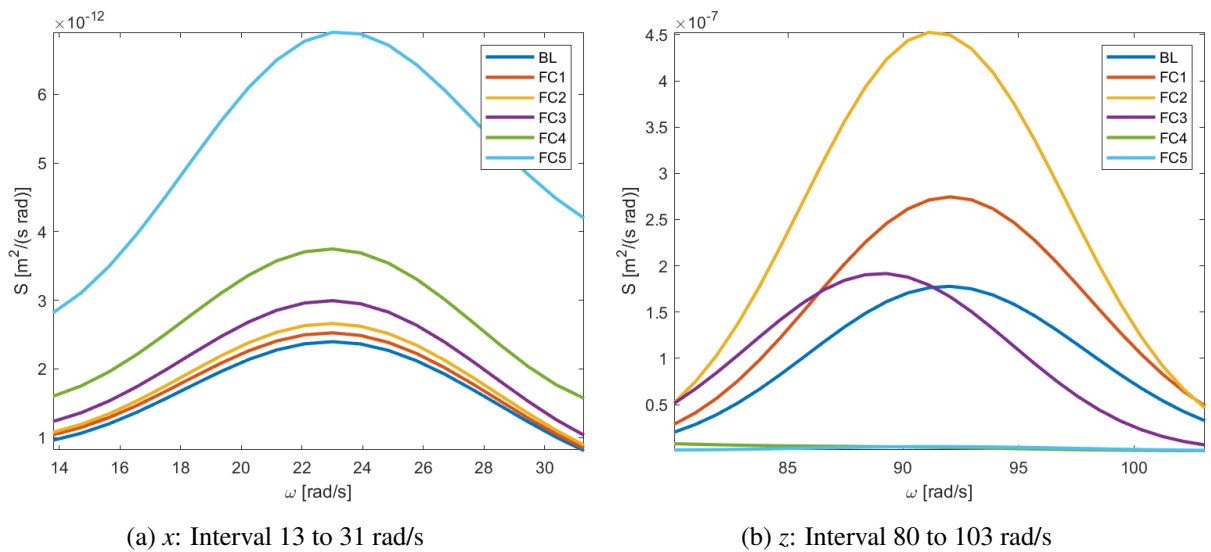


Figure 4.23: Zooms of spectra showing low speed shaft planet carrier rear bearing (PLC-B) velocity x - and z -direction with MBR damage

The resulting normalized energies are displayed in Table 4.25. It is shown that damage in the low speed shaft front bearing (PLC-A) can be detected from 30% degradation onwards by measuring its velocity in the z -direction. Detecting damage in PLC-B is possible from a degradation of 70%, when its z -velocity is monitored.

Table 4.22: Normalized energy E^* for low speed shaft planet carrier front and rear bearing (PLC-A and PLC-B) velocity with MBR damage

	$E_{\text{PLC-A}_x}^*$	$E_{\text{PLC-A}_z}^*$	$E_{\text{PLC-B}_x}^*$	$E_{\text{PLC-B}_z}^*$
	ω_1	ω_1	ω_1	ω_1
FC1	1.057	2.259	1.057	1.530
FC2	1.111	6.105	1.111	2.424
FC3	1.256	7.433	1.255	1.004
FC4	1.606	2.742	1.595	0.0327
FC5	3.123	1.671	3.081	0.0263

Damage can be detected around the first mesh frequency and rotational frequency of the intermediate speed shaft. When the main shaft front bearing is damaged it is to be expected that, next to the extra loads carried by the INP-B bearing, PLC-A also takes some extra loads. When this exceeds PLC-A's load carrying capacity, PLC-B will carry more and more loads. The non-monotonic behaviour is explained by the fact that higher loads could possibly not be carried by the bearing and are compensated for in the bearings behind PLC-A. That is why MBR damage can be detected at the PLC-B in a later stage. Interesting to see is that MBR damage could also be detected when monitoring the vibration velocity of PLC-A and PLC-B in the x -direction. As damage is introduced in the y - and z -direction of INP-A, it is expected that only motion in these directions are affected. Since MBR damage can only be detected at a very late stage (FC5) in the x -direction, it is expected that the system fails completely at this stage and that therefore all motion is affected.

In Table 4.23, one can see the interesting frequency interval for the intermediate speed shaft front bearing (IMS-A). This interval is depicted in Figure 4.24 and the corresponding E^* is calculated to be as in Table 4.24. It can be seen that damage can only be detected when the bearing is severely degraded. This makes sense, since IMS-A is quite far away from INP-A and changes in motion would probably only be noticeable when the fault is detected at PLC-B.

Table 4.23: Frequency intervals for intermediate speed shaft front bearing (IMS-A) velocity with MBR damage

IMS-A		
y		
	ω_1	ω_u
ω_1 [rad/s]	41	58

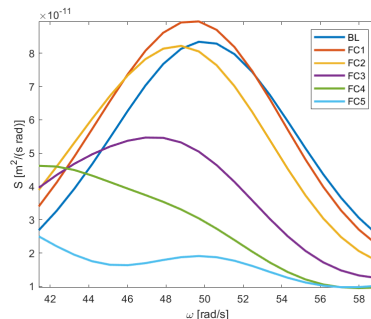


Figure 4.24: Zoom of spectrum showing intermediate speed shaft front bearing (IMS-A) velocity y -direction with MBR damage

Table 4.24: Normalized energy E^* for intermediate speed shaft front bearing (IMS-A) velocity with MBR damage

	$E_{\text{IMS-A}_y}^*$
	ω_1
FC1	1.068
FC2	0.9740
FC3	0.6626
FC4	0.4759
FC5	0.2746

In Table 4.25, one can see the frequency intervals of interest for the high speed shaft front and rear bearing. The corresponding zooms of the spectra are shown in Figures 4.25 and 4.26 for the front and rear bearing, respectively.

Table 4.25: Frequency intervals for high speed shaft front and rear bearing (HS-A and HS-B) velocity with MBR damage

ω_l [rad/s]	HS-A				HS-B			
	y		z		y		z	
	ω_l	ω_u	ω_l	ω_u	ω_l	ω_u	ω_l	ω_u
	13	31	35	62	13	31	35	62

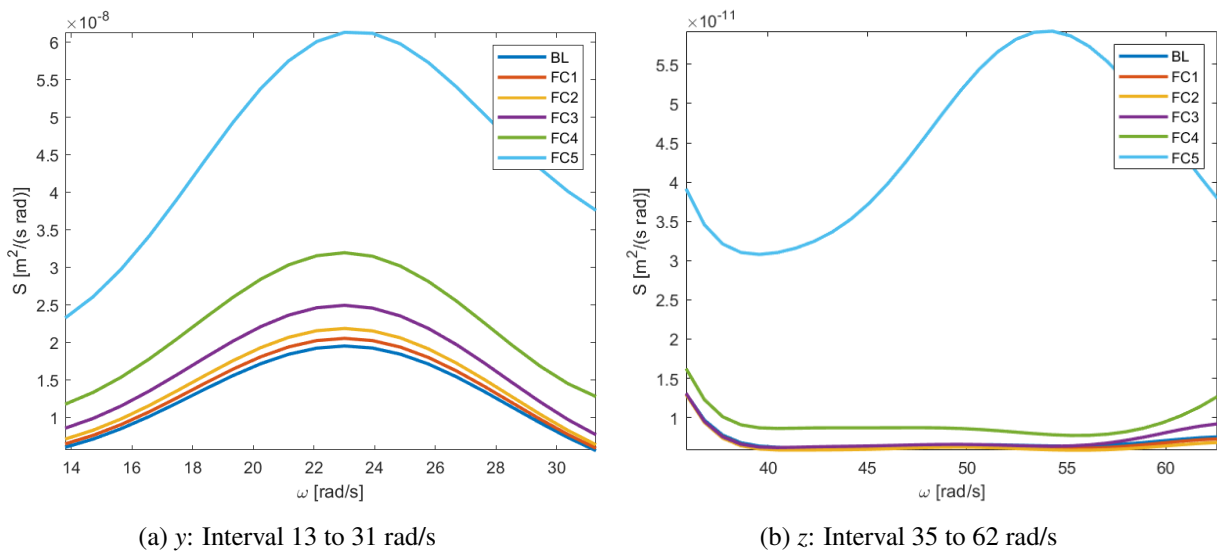


Figure 4.25: Zooms of spectrum showing high speed shaft front bearing (HS-A) velocity y- and z-direction with MBR damage

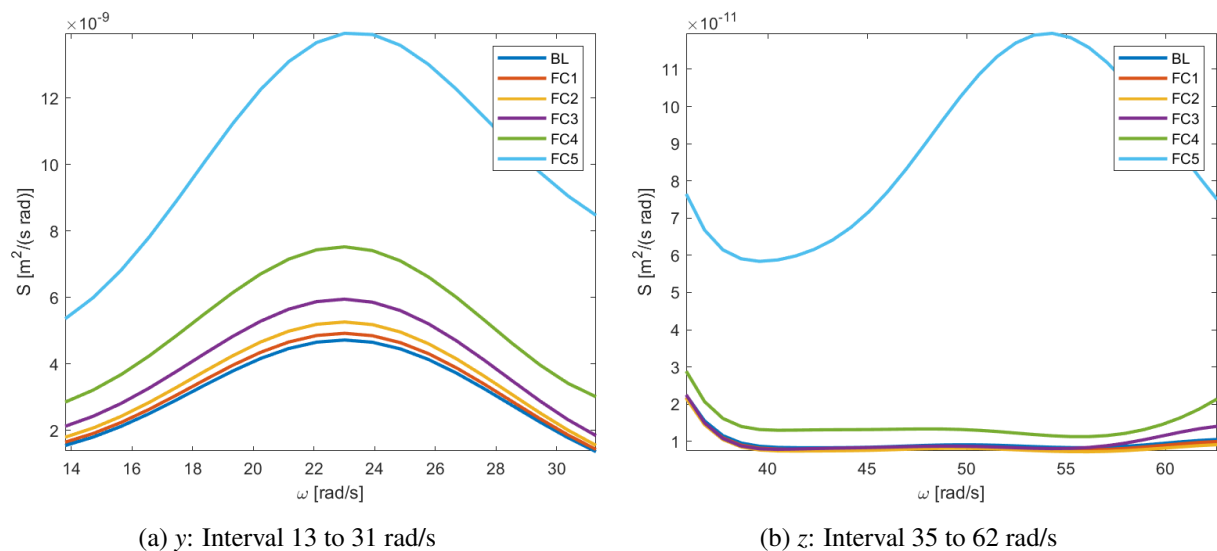


Figure 4.26: Zooms of spectra showing high speed shaft rear bearing (HS-B) velocity y- and z-direction with MBR damage

The resulting normalized energies E^* are calculated to be as depicted in Table 4.26. As one can see, only severe damage is detectable in both HS-A and HS-B when measuring the velocity in the y- or z-direction.

Table 4.26: Normalized energy E^* for high speed shaft front and rear bearing (HS-A and HS-B) velocity with MBR damage

	E_{HS-Ay}^*	E_{HS-Az}^*	E_{HS-By}^*	E_{HS-Bz}^*
	ω_1	ω_1	ω_1	ω_1
FC1	1.054	0.9708	1.045	0.9384
FC2	1.126	0.9391	1.121	0.8910
FC3	1.296	1.033	1.277	1.016
FC4	1.698	1.331	1.650	1.484
FC5	3.468	6.561	3.238	9.346

After damage on INP-A can be detected at PLC-A and PLC-B, the additional loads get transferred to the intermediate and high speed shaft bearings. The frequency intervals where damage can be detected is around the intermediate speed shaft rotational frequency and first mesh frequency. Because these frequency intervals were also critical for the before mentioned bearings, it is expected that additional damage occurs at the gearbox' first stage and the intermediate speed shaft. Although, this is not proven in this study.

As a summary of the outcomes presented in this section, a map is made to show where the MBR damage is detectable. This map is presented in Figure 4.27. It corresponds with the map shown in Figure 4.2, showing the detectability of vibration propagation using the Velocity RMS Threshold Method, on which the Bearing Velocity Energy Method is based. However, the one in Figure 4.27 shows more bearings where vibration propagation is detectable.

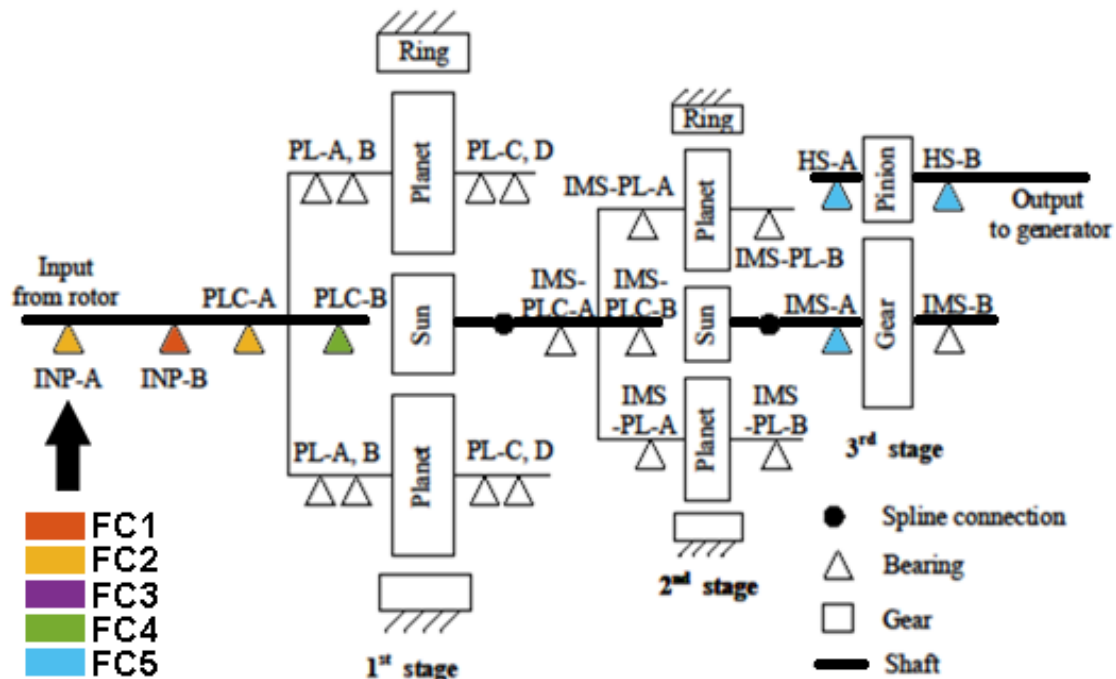


Figure 4.27: Map showing where MBR damage (indicated with an arrow) is detectable using the Bearing Velocity Energy Method. Indicated is which bearings' velocity or acceleration should be monitored in order to detect the fault. The color indicates the lowest fault case from which the fault is detectable.

HSBR

In Table 4.27, one can find the selected frequency intervals for the high speed shaft front and rear bearing's (HS-A and HS-B) velocity. This is based on the spectra of Figures D.17 and D.18.

Table 4.27: Frequency intervals for high speed shaft bearings (HS-A and HS-B) velocity with HSBR damage

	HS-A				HS-B			
	y		z		y		z	
	ω_1	ω_u	ω_1	ω_u	ω_1	ω_u	ω_1	ω_u
ω_1 [rad/s]	11	32	15	31	12	33	13	33
ω_2 [rad/s]	38	60	71	110	40	60	79	103
ω_3 [rad/s]	78	105			80	103	1350	1470
ω_4 [rad/s]					445	500		

Figures 4.28 and 4.29 show the zooms of the spectra obtained from HS-A's velocity in the y- and z-direction.

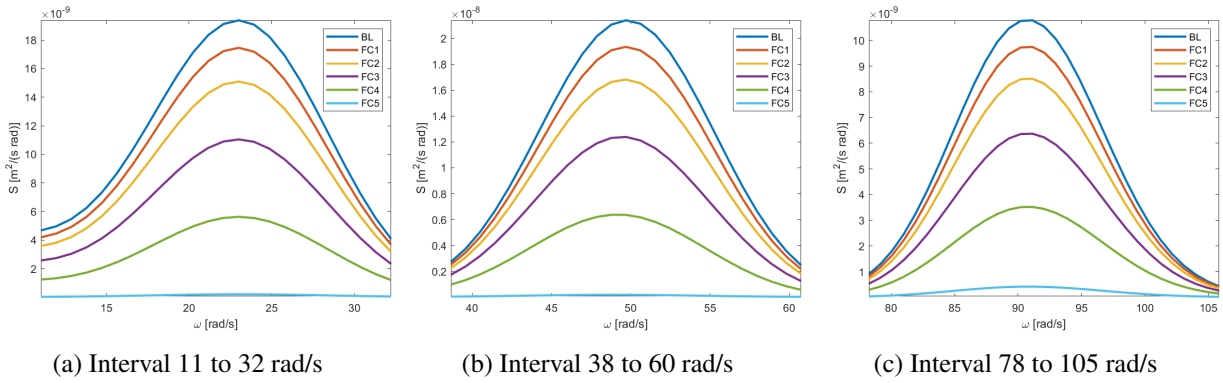


Figure 4.28: Zooms of spectrum showing high speed shaft front bearing (HS-A) velocity in y-direction with HSBR damage

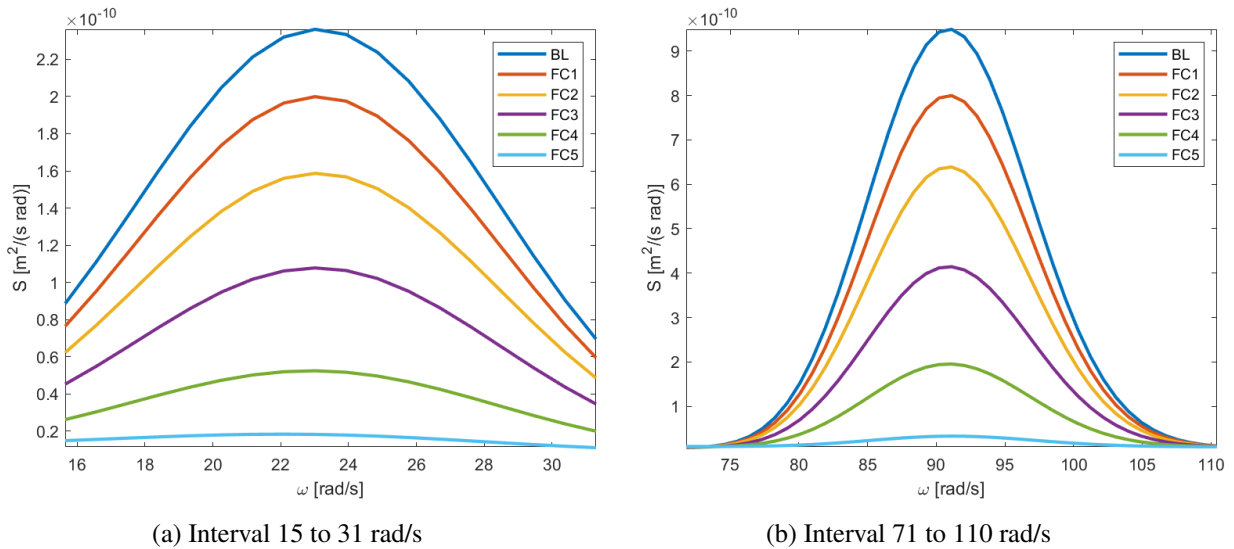


Figure 4.29: Zooms of spectrum showing high speed shaft front bearing (HS-A) velocity in z-direction with HSBR damage

Using Equations 3.18 and 3.19, the normalized energies are calculated for the zooms depicted in Figures 4.28 and 4.29. Afterwards, the results are compared to the threshold (depicted in Equation 3.20). Its outcome is depicted in Table 4.28, results which are indicated in green meet the threshold. From this, one can see that faults in HS-B with high degradation levels (FC4 and FC5) can be detected when monitoring the velocity in y - and z -direction.

Table 4.28: Normalized energy E^* for high speed shaft front bearing (HS-A) velocity with HSBR damage

	$E_{HS-A_y}^*$			$E_{HS-A_z}^*$	
	ω_1	ω_2	ω_3	ω_1	ω_2
FC1	0.9005	0.9038	0.9040	0.8489	0.8450
FC2	0.7778	0.7852	0.7893	0.6773	0.6781
FC3	0.5683	0.5777	0.5914	0.4653	0.4451
FC4	0.2884	0.2969	0.3278	0.2350	0.2180
FC5	0.0108	0.0090	0.0406	0.0934	0.0505

The outcome was partially expected. The radial stiffness and damping of HS-B is reduced and so does its load carrying capability. Therefore, HS-A needs to compensate for this. A change in motion of HS-A is its result. The frequency intervals of interest are around the intermediate speed and high speed shaft rotational frequencies and the first stage mesh frequency, which could possibly mean that faults are propagated to the high speed shaft and intermediate speed shaft (see Section 4.3.3) or the first gear stage.

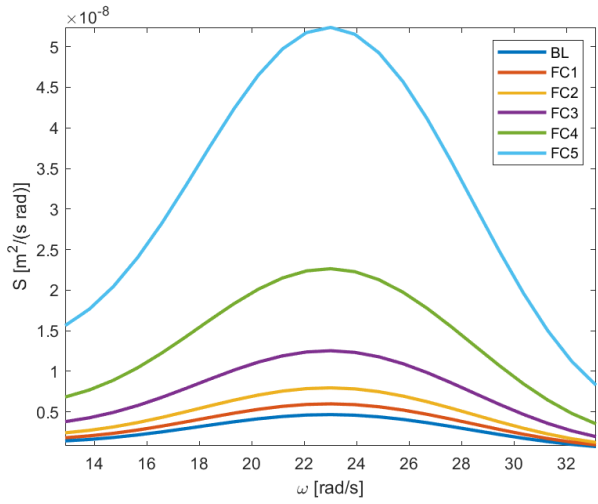
In Figures 4.30 and 4.31, one could see the zooms of the HS-B's y - and z -velocity, respectively, matching with the frequency intervals of Table 4.27.

The values of the normalized energy E^* are presented in Table 4.29. From this it can be concluded that a radial degradation of the high speed shaft bearing (HS-B) can be detected for the corresponding frequency intervals when monitoring the velocity in y - and z -direction of the high speed rear bearing (HS-B). Faults can be detected with a high degradation level of 70% and more.

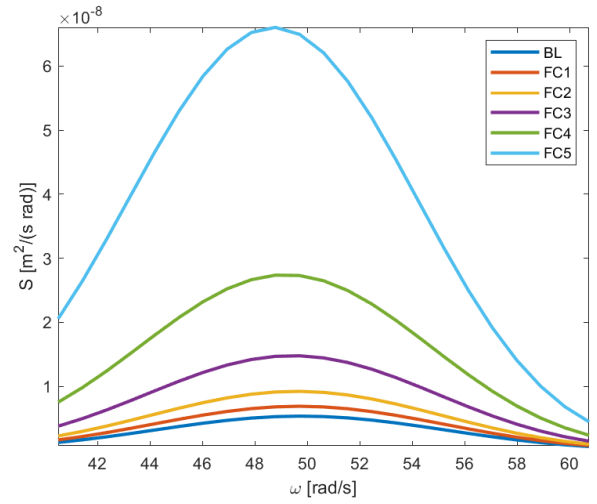
Table 4.29: Normalized energy E^* for high speed shaft rear bearing (HS-B) velocity with HSBR damage

	$E_{HS-B_y}^*$				$E_{HS-B_z}^*$		
	ω_1	ω_2	ω_3	ω_4	ω_1	ω_2	ω_3
FC1	1.282	1.284	1.270	1.208	1.282	1.270	1.209
FC2	1.706	1.713	1.659	1.509	1.706	1.658	1.422
FC3	2.684	2.735	2.545	2.146	2.684	2.544	1.967
FC4	4.847	5.039	4.425	3.428	4.848	4.423	2.982
FC5	11.21	11.98	9.432	6.747	11.21	9.429	6.591

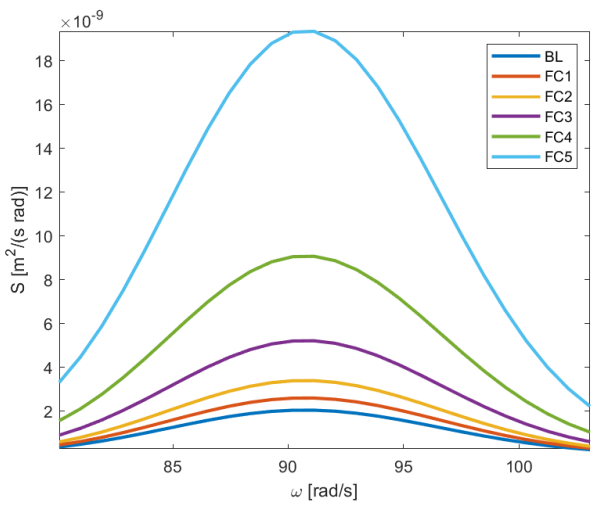
It does not need an explanation that this was to be expected. It is obvious that when a bearing gets damaged, it will behave differently. The late fault detection was surprising. In Section 4.3.3 one could read a possible explanation.



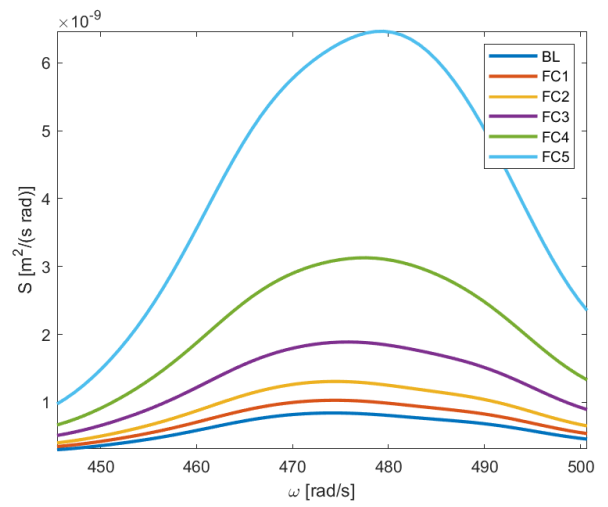
(a) Interval 12 to 33 rad/s



(b) Interval 40 to 60 rad/s

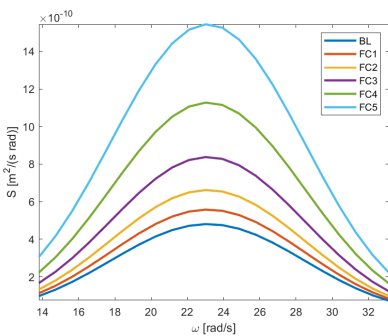


(c) Interval 80 to 103 rad/s

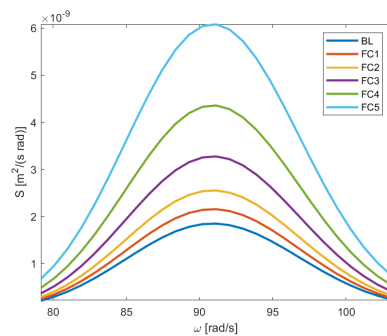


(d) Interval 445 to 500 rad/s

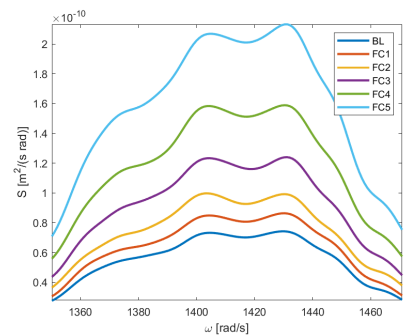
Figure 4.30: Zooms of spectrum showing high speed rear bearing (HS-B) velocity y-direction with HSBR damage



(a) Interval 13 to 33 rad/s



(b) Interval 79 to 103 rad/s



(c) Interval 1350 to 1470 rad/s

Figure 4.31: Zooms of spectrum showing high speed shaft rear bearing (HS-B) velocity z-direction with HSBR damage

The findings of this section are summarized and mapped in Figure 4.32.

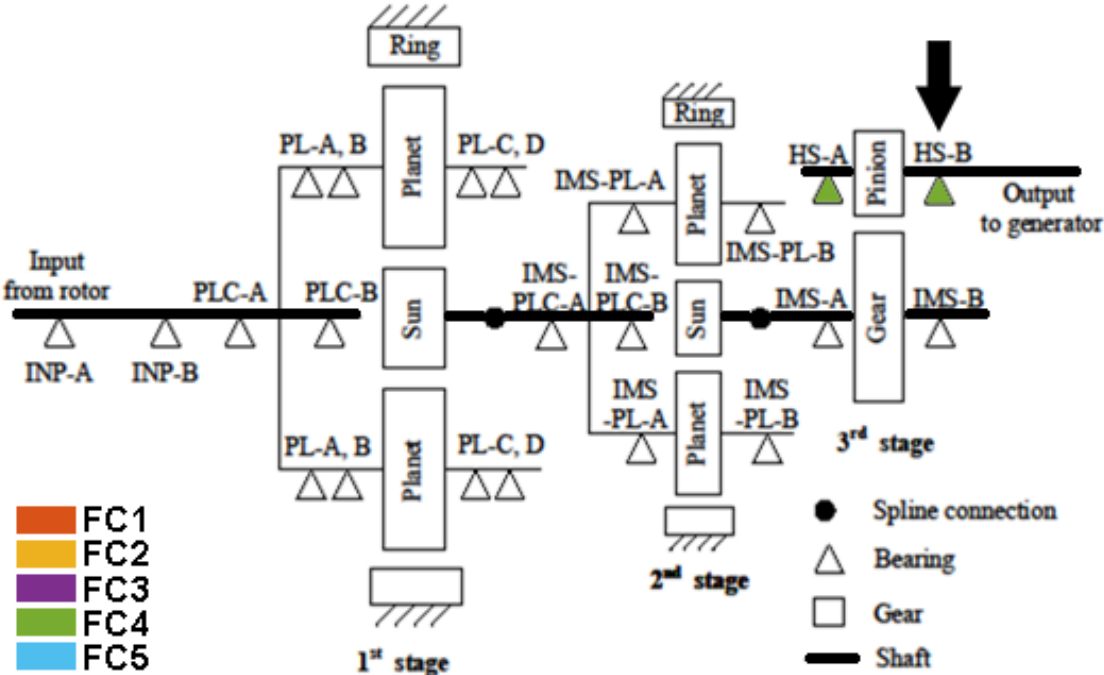


Figure 4.32: Map showing where HSRB damage (indicated with an arrow) is detectable using the Bearing Velocity Energy Method. Indicated is which bearings’ velocity should be monitored in order to detect the fault. The color indicates the lowest fault case from which the fault is detectable.

4.3.3 Shaft Vibration Energy Method

Using the methodology as is explained in Section 3.5.2, the Shaft Vibration Energy Method is executed for the MBR, MBX and HSRB fault cases and presented in the following. The interesting frequency intervals are based on the complete vibration spectra presented in Appendix E.

MBR

In Table 4.34, one can see the interesting frequency intervals for main shaft vibration (velocity and acceleration) based on the spectra of Figures E.7 and E.8.

Table 4.30: Frequency intervals for main shaft vibration with MBR damage

	Velocity		Acceleration	
	y	z	y	z
ω_1 [rad/s]	35	55	82	100
ω_2 [rad/s]	82	100	82	100

The corresponding zooms of the spectra are depicted in Figures 4.33 and 4.34, showing velocity and acceleration respectively.

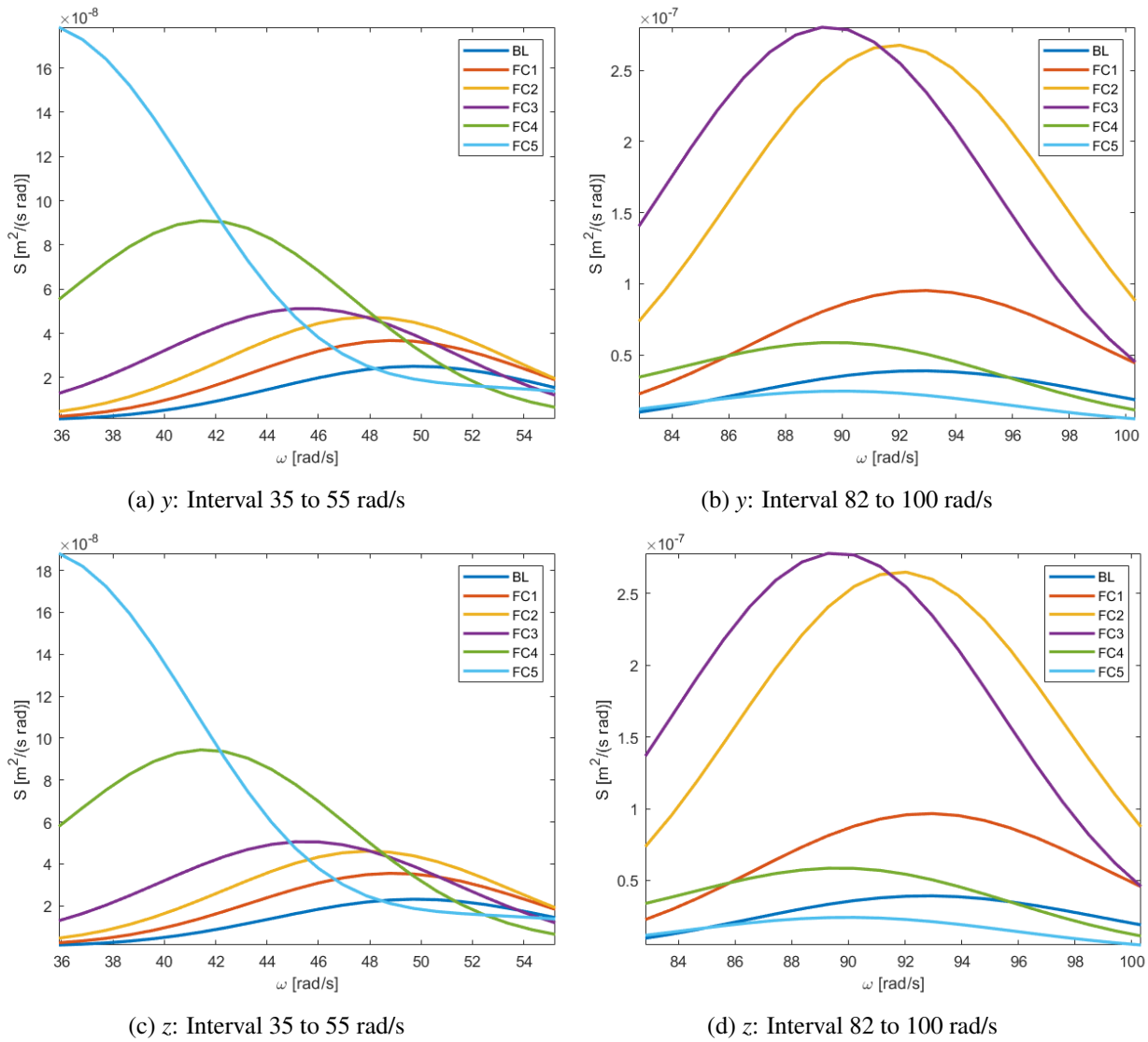


Figure 4.33: Zooms of spectra showing main shaft velocity in y- and z-direction with MBR damage

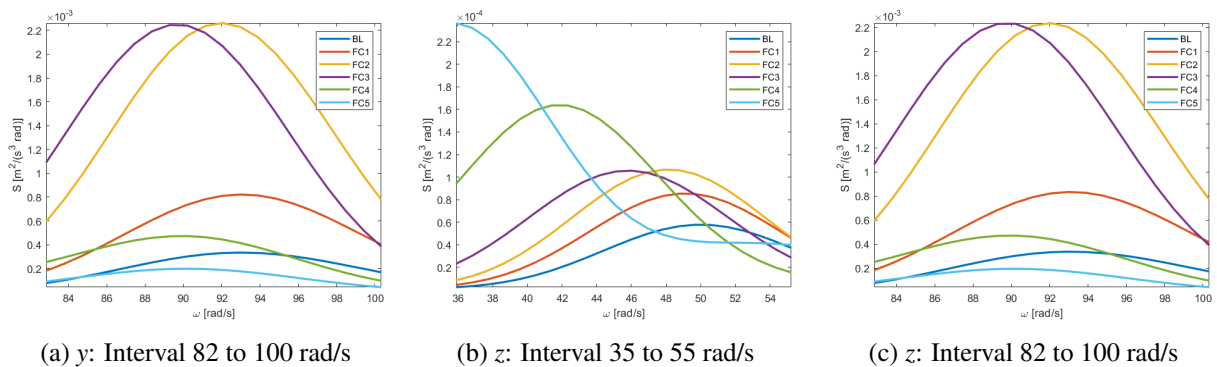


Figure 4.34: Zooms of spectra showing main shaft acceleration in y- and z-direction with MBR damage

The normalized energy is calculated using Equations 3.18 and 3.19 and the result for every frequency interval is presented in Table 4.31. The results are compared with the threshold, which is shown in Equation 3.20. The results meeting the threshold are indicated in green.

Table 4.31: Normalized energy E^* for main shaft vibration velocity and acceleration with MBR damage

	$E_{MS_{vel,y}}^*$		$E_{MS_{vel,z}}^*$		$E_{MS_{acc,y}}^*$		$E_{MS_{acc,z}}^*$	
	ω_1	ω_2	ω_1	ω_2	ω_1	ω_1	ω_2	
FC1	1.511	2.434	1.578	2.441	2.436	2.436	1.530	
FC2	2.015	6.713	2.115	6.566	6.595	6.595	1.979	
FC3	2.309	6.849	2.463	6.717	6.425	6.425	2.095	
FC4	3.768	1.485	4.181	1.4637	1.394	1.394	3.037	
FC5	4.547	0.6136	5.053	0.5996	0.5795	0.5795	3.032	

From Table 4.31 it can be concluded that MBR damage can be detected by monitoring the main shaft's velocity and acceleration in the y - and z -direction. The damage is already detectable from FC2 onwards. That MBR damage is noticeable on the main shaft is expected, since a decrease in stiffness in INP-A would directly result in more shaft motion. Since the stiffness is decreased in radial (y - and z -) direction, the change in motion would be more likely to happen in these directions.

For the second frequency interval of $E_{MS_{vel,y}}^*$ and $E_{MS_{vel,z}}^*$ and the first interval of $E_{MS_{acc,y}}^*$ and $E_{MS_{acc,z}}^*$, one could see a sudden drop in normalized energy. This could indicate that the excessive load, induced by the decrease in load carrying capacity of the main bearing, could not be carried anymore by the system and thus the system would partially collapse or vibrations on this frequency interval reduce. This does not indicate that the fault is not detectable anymore, since the fault certainly is detectable but only for other frequency intervals.

The frequencies of interest are around the mesh frequency of the first stage and the high speed shaft rotational frequency. This could possibly indicate that the fault propagates to the first gear stage and influences the high speed shaft's rotation.

The same approach is followed by finding the frequency intervals of interest for the low speed shaft. These intervals are presented in Table 4.32 and are based on the spectra of Figure E.9. It was found that the shaft's acceleration was not influenced that much.

Table 4.32: Frequency intervals for low speed shaft vibration velocity with MBR damage

ω_1 [rad/s]	y		z	
	82	100	82	100

The corresponding zooms of the spectra are shown in Figure 4.35.

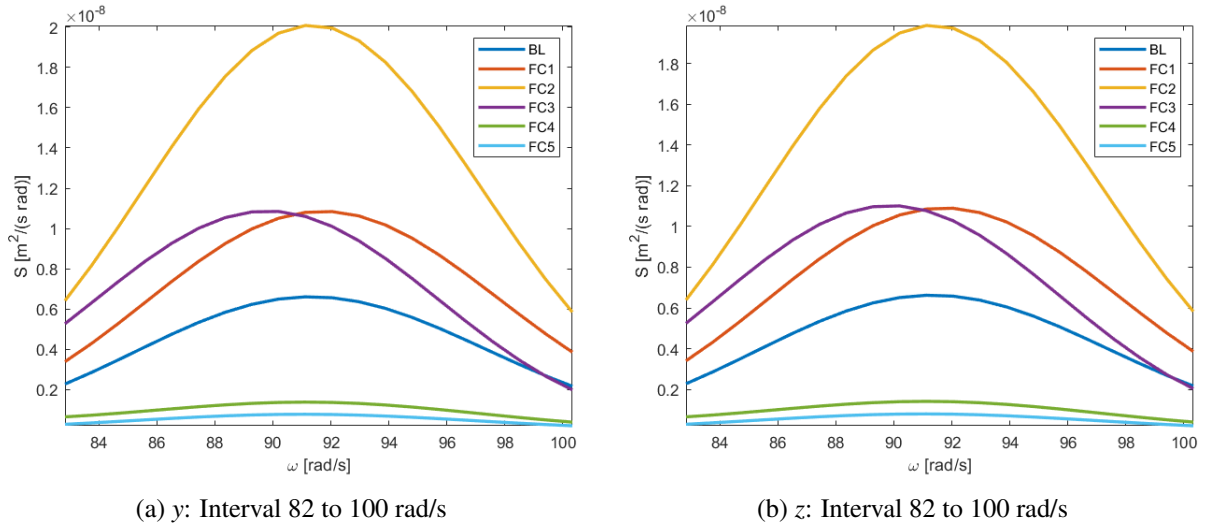


Figure 4.35: Zooms of spectra showing low speed shaft velocity in y- and z-direction with MBR damage

The normalized energy is calculated and its results are presented in Table 4.33. Again, the results which are marked green meet the threshold.

Table 4.33: Normalized energy E^* for low speed shaft velocity with MBR damage

	$E_{LSS_{vel,y}}^*$	$E_{LSS_{vel,z}}^*$
	ω_1	ω_1
FC1	1.641	1.646
FC2	2.973	2.943
FC3	1.586	1.606
FC4	0.2113	0.2145
FC5	0.1160	0.1177

One could see that a MBR fault is detectable while monitoring the low speed shaft's vibration velocity in y- and z-direction from for high degradation levels (FC4 and FC5). It was to be expected that the MBR fault is detectable with vibration monitoring of the low speed shaft, since the frequency interval of interest for vibration monitoring of the main shaft was around the first stage mesh frequency. As a consequence of possible damage in the first gear stage, the vibration of the low speed shaft could possibly be different.

The frequency interval of interest is around the first stage mesh frequency too. This possibly means that the MBR fault is propagated to the first gear stage, influencing the vibration of the main and low speed shaft.

The findings in this section are summarized in the map of Figure 4.36. One could see that a MBR fault, which is radial damage in the main shaft front bearing, is detectable by monitoring the vibration of the main and low speed shaft. Early fault detection (from FC2 onwards) is possible while monitoring the main shaft. Detection of faults with higher degradation levels (FC4 and FC5) is possible when monitoring the low speed shaft.

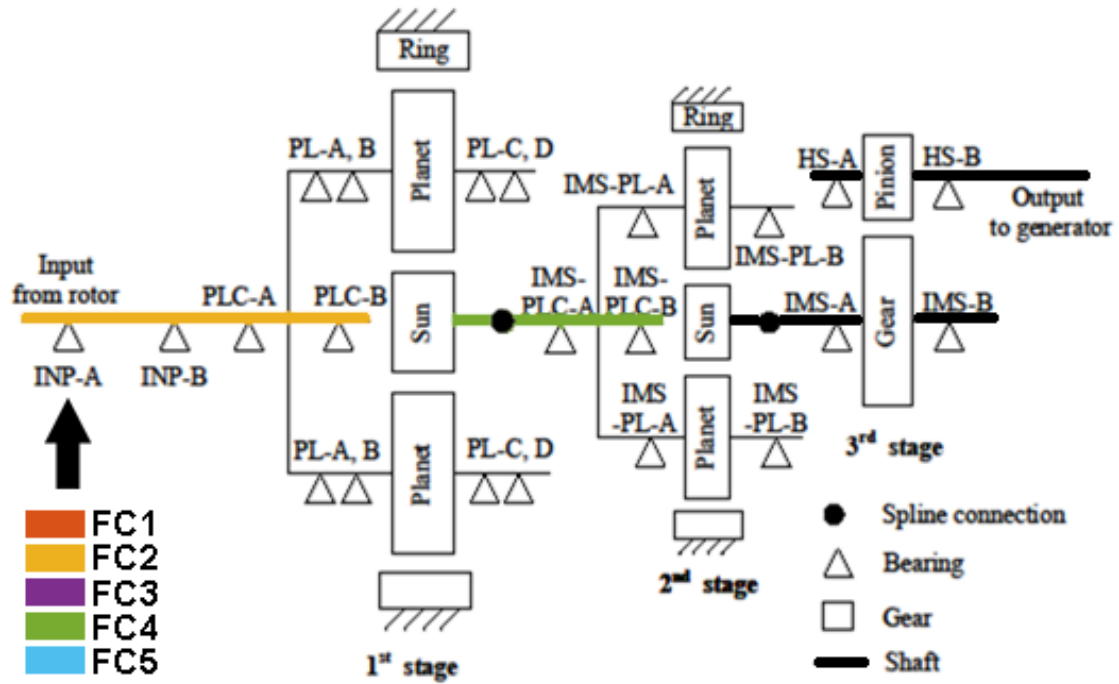


Figure 4.36: Map showing where MBR damage (indicated with an arrow) is detectable using the Shaft Vibration Energy Method. Indicated is which shafts' velocity or acceleration should be monitored in order to detect the fault. The color indicates the lowest fault case from which the fault is detectable.

MBX

Based on Figures E.10 and E.11, two frequency intervals for both acceleration and velocity are selected.

Table 4.34: Frequency intervals for main shaft vibration with MBR damage

	Velocity		Acceleration	
	x	x	x	x
ω_1 [rad/s]	95	115	95	115
ω_2 [rad/s]	138	155	138	155

One can find the corresponding zooms of the frequency intervals for velocity and acceleration in Figures 4.37 and 4.38, respectively.

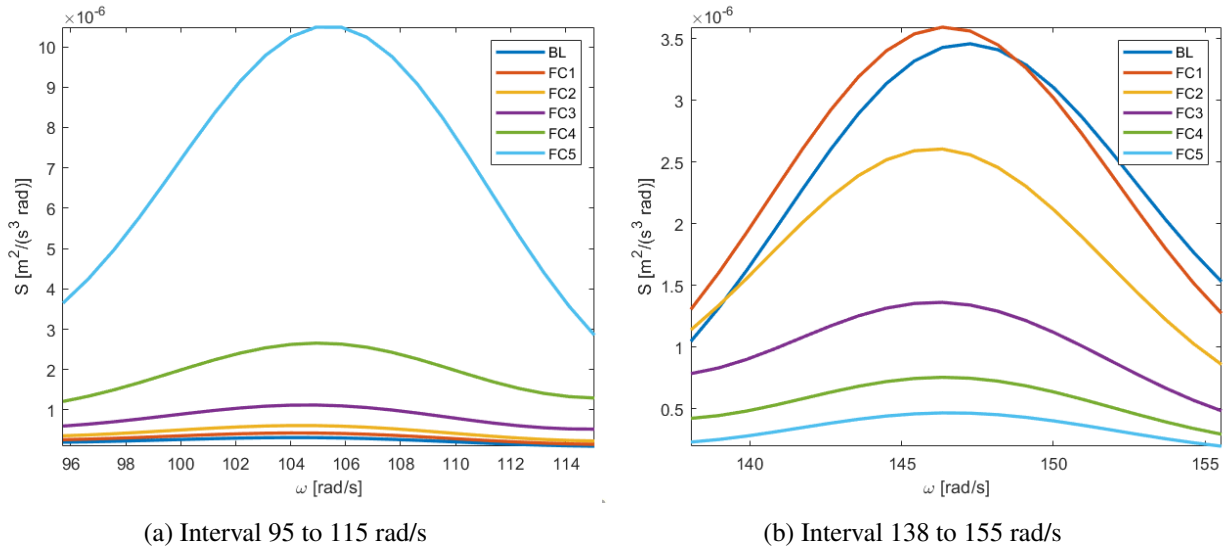


Figure 4.38: Zooms of spectrum showing main shaft acceleration in x -direction with MBX damage

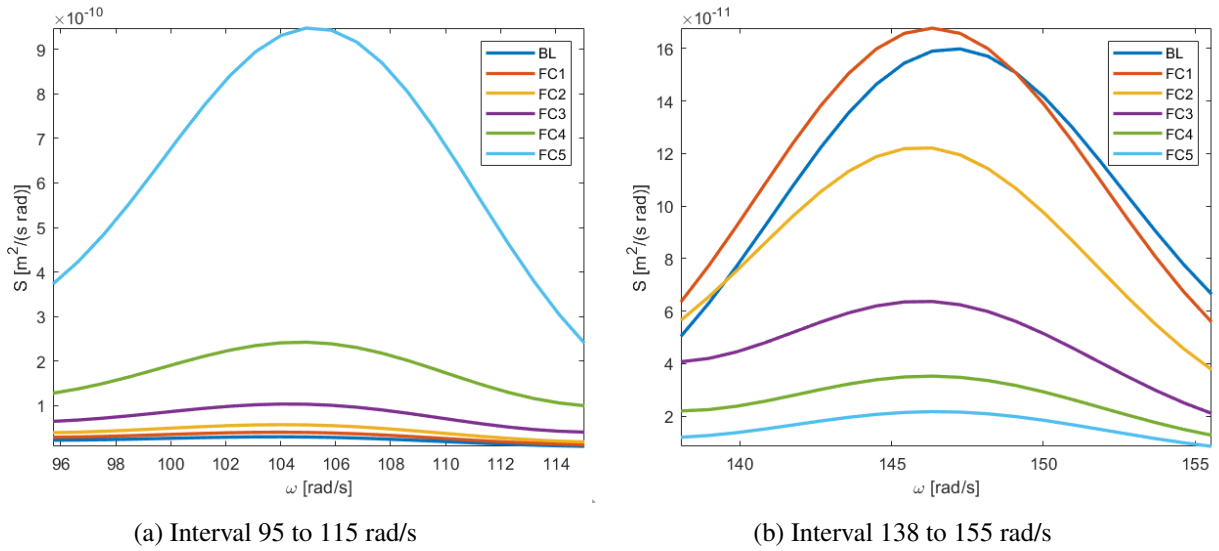


Figure 4.37: Zooms of spectrum showing main shaft velocity in x -direction with MBX damage

The normalized energy E^* is calculated, compared with the threshold and presented in Table 4.35. It is shown that the MBX fault (INP-A is damaged in the axial direction) can be detected by monitoring the main shaft's vibration velocity in the x -direction from FC3 onwards.

Table 4.35: Normalized energy E^* for main shaft velocity and acceleration with MBX damage

	$E_{MS_{vel,x}}^*$		$E_{MS_{acc,x}}^*$	
	ω_1	ω_2	ω_1	ω_2
FC1	1.351	1.041	1.361	1.031
FC2	1.928	0.7655	1.947	0.7538
FC3	3.525	0.4134	3.592	0.4060
FC4	8.205	0.2298	8.432	0.2260
FC5	30.26	0.1412	31.16	0.1393

It was to be expected that an axial fault in the main bearing would influence the main shaft's axial vibration (velocity and acceleration). When the stiffness of the bearing in axial direction decreases, it allows for more motion of the shaft while applying the same forcing. The frequency intervals of interest are around the main bearing frequencies (see Section 4.1.6), which is confirming the expectations, since INP-A is the damaged bearing. The map depicted in Figure 4.39 is summarizing this section.

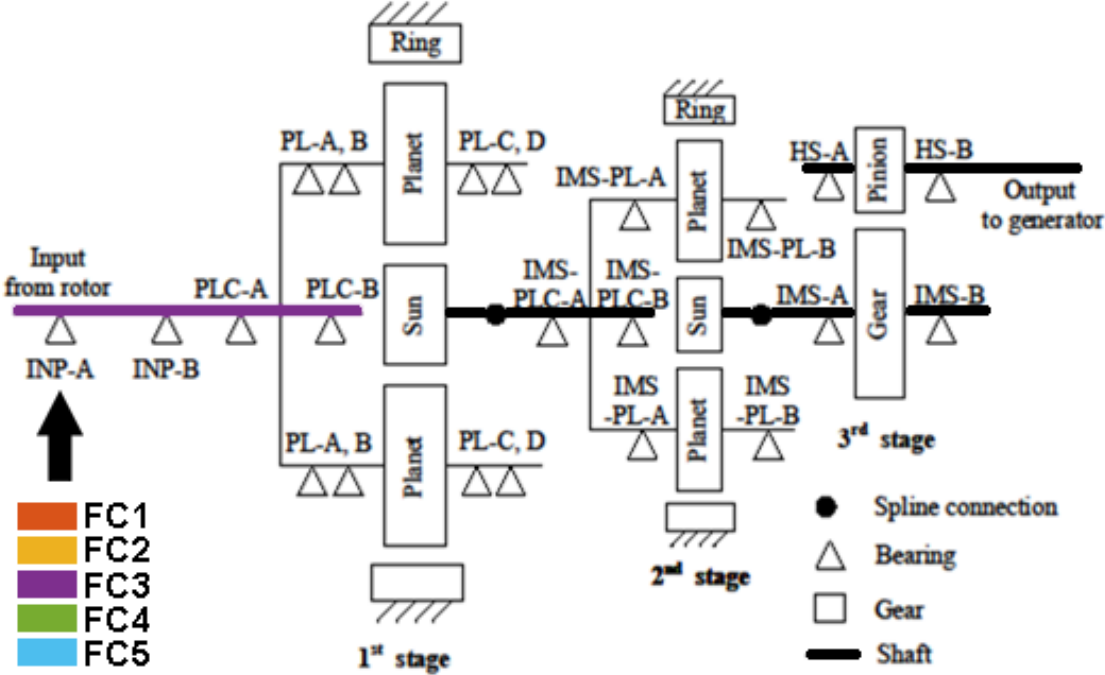


Figure 4.39: Map showing where MBX damage (indicated with an arrow) is detectable using the Shaft Vibration Energy Method. Indicated is which shafts' velocity or acceleration should be monitored in order to detect the fault. The color indicates the lowest fault case from which the fault is detectable.

HSBR

Finally, the interesting frequency intervals, based on the spectra in Figure E.12, are selected and presented in Table 4.36.

Table 4.36: Frequency intervals for high speed shaft vibration velocity with HSBR damage

	y		z	
ω_1 [rad/s]	90	110	90	110
ω_2 [rad/s]	130	152	130	152

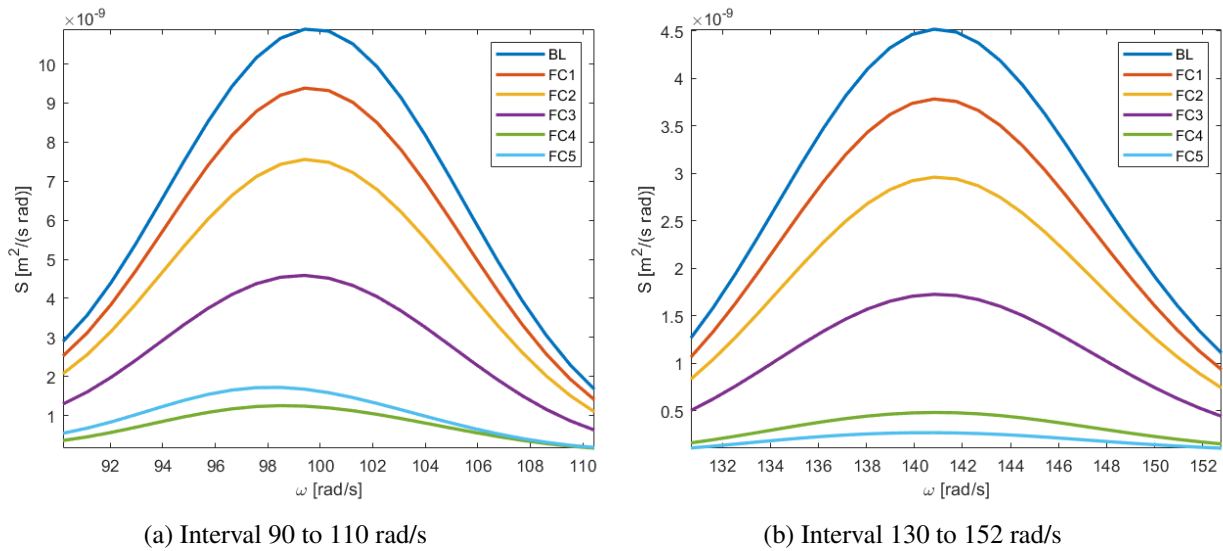


Figure 4.41: Zooms of spectrum showing high speed shaft z -velocity with HSR damage

The corresponding zooms of the spectra are shown in Figures 4.40 and 4.41 for the velocity in y - and z -direction, respectively.

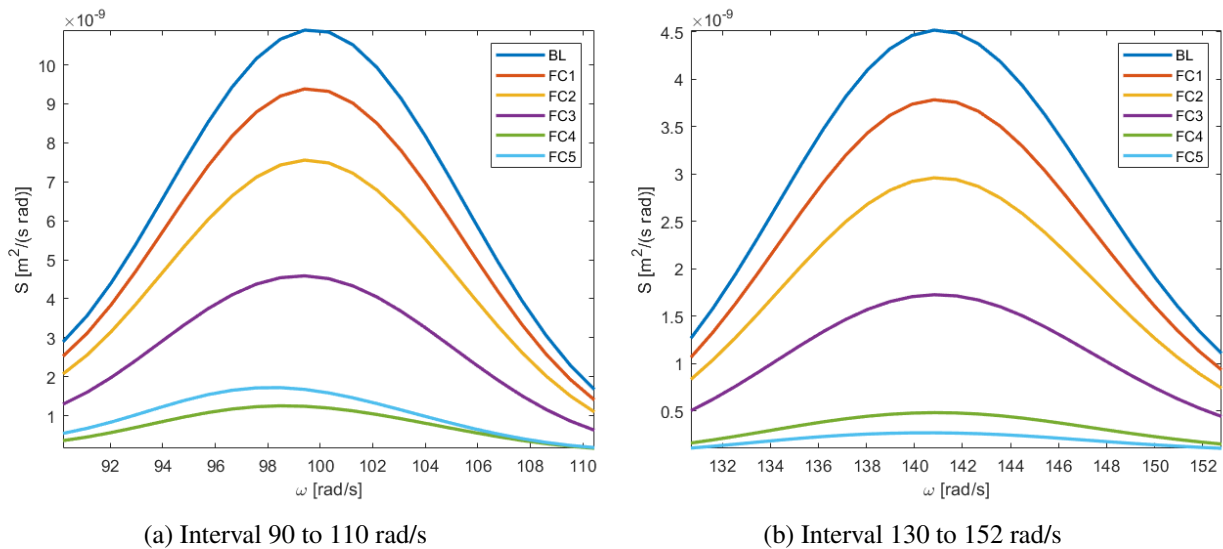


Figure 4.40: Zooms of spectrum showing high speed shaft y -velocity with HSR damage

For the before mentioned frequency intervals, the resulting normalized energies E^* are calculated and compared with the threshold. The results indicated in green show that the damage is detectable. It is shown that HSR damage is detectable when monitoring the high speed shaft velocity either in y - or z -direction. The damage is only detectable for high degradation levels (FC4 and FC5). Vibration propagation to the high speed shaft, stemmed from HSR damage, was to be expected. A decrease in bearing stiffness and damping, obviously results in a change in motion of the mass attached to it (in this case the shaft).

Table 4.37: Normalized energy E^* for high speed shaft velocity with HSBR damage

	$E_{HSS_{vel,y}}^*$		$E_{HSS_{vel,z}}^*$	
	ω_1	ω_2	ω_1	ω_2
FC1	0.8600	0.8379	0.8600	0.8379
FC2	0.6914	0.6564	0.6914	0.6564
FC3	0.4180	0.3845	0.4180	0.3845
FC4	0.1120	0.1110	0.1120	0.1110
FC5	0.1496	0.0650	0.1496	0.0650

This section is summarized with Figure 4.42.

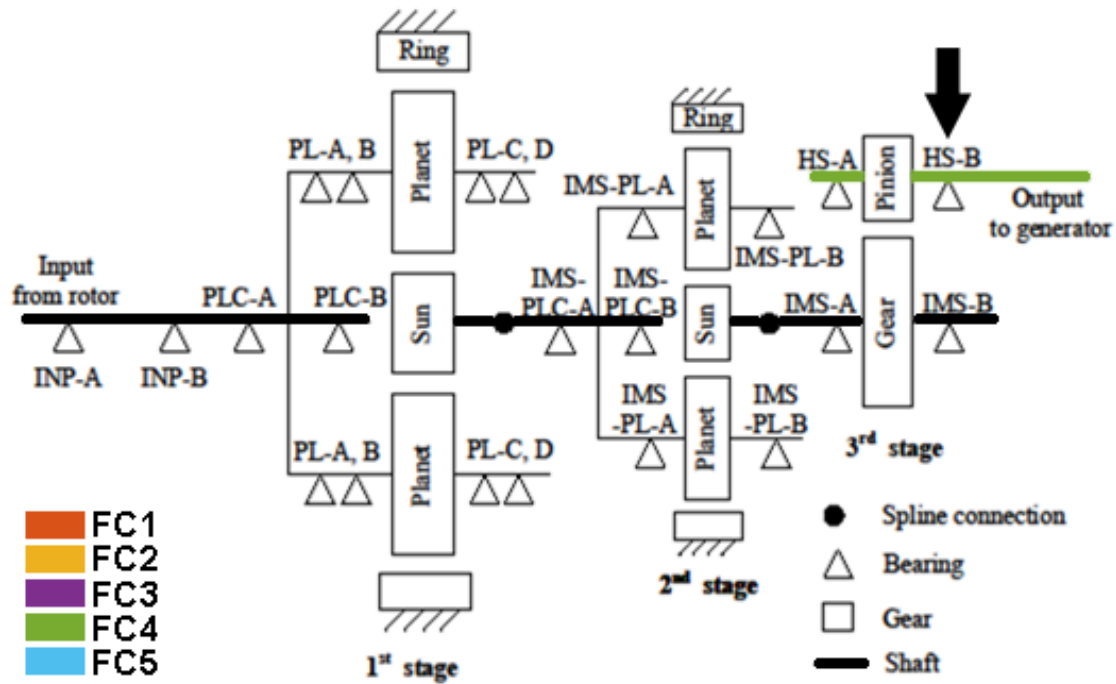


Figure 4.42: Map showing where HSBR damage (indicated with an arrow) is detectable using the Bearing Velocity Energy Method. Indicated is which shafts' velocity or acceleration should be monitored in order to detect the fault. The color indicates the lowest fault case from which the fault is detectable.

Questions are raised, however, by the late fault detection, not only using the Shaft Vibration Energy Method, but also by using the Bearing Velocity Energy Method (where faults could also only be detected from FC4 and onwards) and Angular Velocity Error Energy Method (where the HSBR fault could not be detected at all). It was expected that the high speed end of the shaft, after applying the HSBR fault, would behave similarly as the low speed end of the drive train after applying MBR damage. A possible reason could be that the drive train model is not validated nor verified. After all, Wang's model is built and ran in multibody simulation software, which only serves as an estimation of the reality.

4.4 Comparison Measurement Locations with ISO Standard

In this chapter, one could find the results of fault detection methods in the time (see Section 4.2) and frequency domain (read Section 4.3) applied on data sets resulting from MBR, MBX and HSBR damage. The time domain analysis results were not so promising and were therefore discarded. The other outcomes are summarized in the following and are compared to the measurement locations as proposed by ISO 10816-21 [ISO, 2015].

MBR damage could be detected using three fault detection methods: Angular Velocity Error Energy Method, Bearing Velocity Error Energy Method and Shaft Vibration Energy Method. By using the Angular Velocity Error Energy Method, it was found that MBR damage was detectable from FC4 onwards by monitoring the main and high speed shaft's rotational velocity simultaneously. The Bearing Velocity Energy Method was able to detect the same damage by monitoring the velocity of INP-A (from FC2), INP-B (from FC1), PLC-A (from FC2), PLC-B (from FC4) and IMS-A, HS-A and HS-B (only for FC5). Finally, using the Shaft Vibration Energy Method, MBR damage was detectable when monitoring the main shaft's vibration velocity and acceleration and low speed shaft's vibration velocity. Faults are then detectable from FC2 and FC4 onwards, respectively. This is all mapped in Figure 4.43.

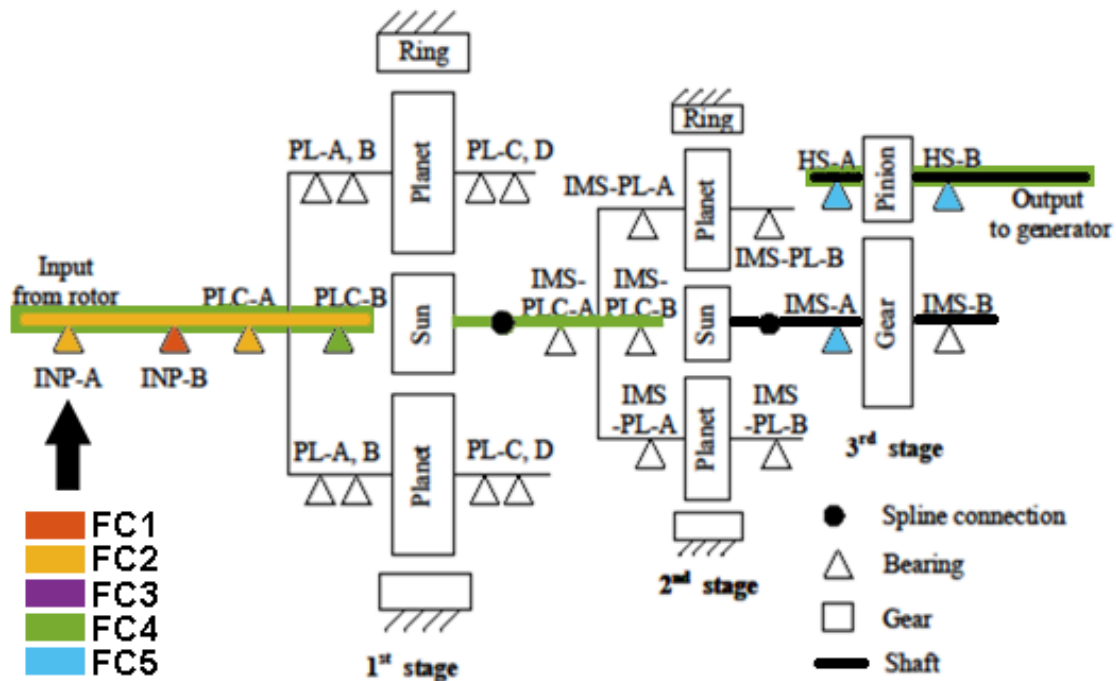


Figure 4.43: Concluding map showing where MBR damage (indicated with an arrow) is detectable using the Angular Velocity Error Energy, Shaft Vibration Energy and Bearing Velocity Energy Methods. The color indicates the degradation level from which MBR damage is possible.

MBX damage could only be detected using one of the three fault detection methods: the Shaft Vibration Energy Method. It was shown that MBX damage was detectable when measuring the main shaft's vibration velocity and acceleration in x -direction. Damage could be detected from FC3 and higher. This is shown in Figure 4.44.

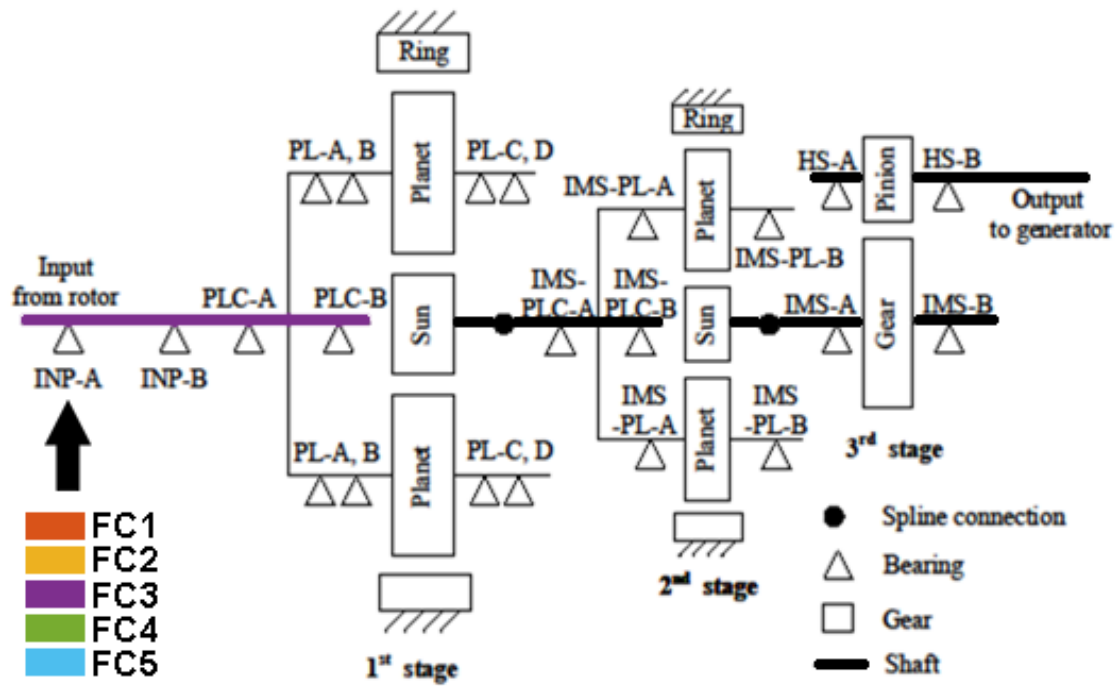


Figure 4.44: Concluding map showing where MBX damage (indicated with an arrow) is detectable using the Angular Velocity Error Energy, Shaft Vibration Energy and Bearing Velocity Energy Methods. The color indicates the degradation level from which MBX damage is possible.

HSBR damage could be detected using two fault detection methods: the Bearing Velocity Error Energy Method and Shaft Vibration Energy Method. It was shown that when monitoring the velocity in y - and z -direction of the high speed shaft and its front and rear bearing, damage was detectable only for FC4 and FC5. This is mapped in Figure 4.45.

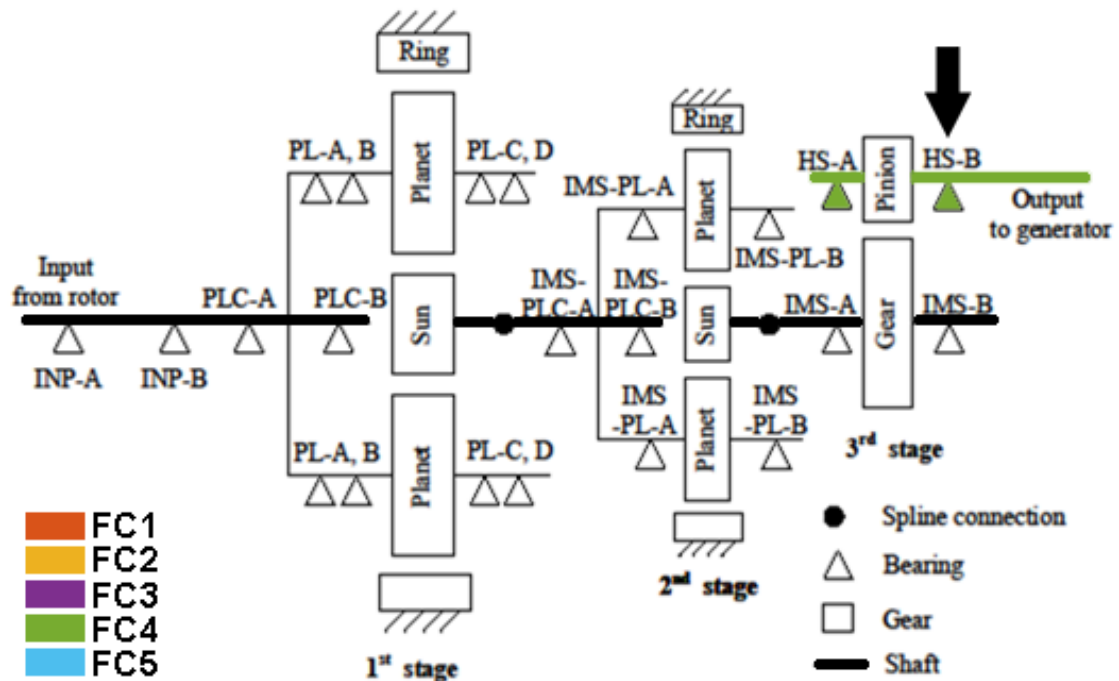


Figure 4.45: Concluding map showing where HSBR damage (indicated with an arrow) is detectable using the Angular Velocity Error Energy, Shaft Vibration Energy and Bearing Velocity Energy Methods. The color indicates the degradation level from which HSBR damage is possible.

According to ISO 10816-21 [ISO, 2015], measurements should be taken on the bearing support housings or structural parts which respond significantly to the environmental loads. ISO 10816-21 also recommends to perform triaxial measurements to fully define the machine's vibration. Though, this may not always be necessary. The vibration velocity and acceleration should be measured and the wind speed, load and its variation should be documented [ISO, 2015].

ISO [ISO, 2015] also recommends a few measurement locations in its standard 10816-21, these typical locations for a wind turbine with two main bearings were already shown in Figure 2.10. ISO recommends measurement locations for the nacelle and tower, but in this work focus is put on the monitoring of the rotor bearing, gearbox and generator. For this purpose, sensors need to be put on both main shaft bearing housings, on the housing of the generator outer bearing and on the gearbox housing in the region of the main shaft, high speed shaft and halfway. Measurement directions should be axial (x -direction, in the direction of the rotor shaft), horizontal (y -direction, transversely to the rotor shaft) and vertical (z -direction) [ISO, 2015].

As an outcome of the frequency domain fault detection studies in this work, it is recommended to also place sensors measuring velocity on the PLC-A, PLC-B and IMS-A bearing housings and on the low speed shaft. This all is provided that placing sensors on the bearings and shaft inside the gearbox is reasonably possible, the rotational velocity of the main shaft and high speed shaft are already monitored and that the sensors placed on the housings of the main and high speed shaft bearings are able to precisely measure the vibration of the shaft and front and rear bearings.

5 | Discussion, Conclusion & Recommendations

In this research work, damage is introduced on the main shaft front bearing and high speed shaft rear bearing in a drive train of a 10 MW floating offshore wind turbine. Model simulations resulted in vibration monitoring data, which were analysed. The goal was to detect the introduced faults and their vibration propagation through the system. One common, two non-traditional and two novel fault detection methods are deployed.

In this chapter, first the outcome of this work is discussed in Section 5.1. Then, conclusions are drawn in Section 5.2. In Section 5.3, finally, recommendations are given for future research work.

5.1 Discussion

In this study, a non-traditional fault detection method, being the Angular Velocity Error Energy Method, is again applied on vibration monitoring data and it is shown that this method is able to detect faults. Two novel methods, namely the Bearing Velocity Energy Method and Shaft Vibration Energy Method (which were both based on a non-traditional fault detection method), were introduced in this work and could possibly be applied in the future during maintenance of offshore wind turbines. These three fault detection methods were deployed in the frequency domain. However, changes in the results of the time domain were observable, it was decided that fault detection in this domain was not feasible, using the applied fault detection methods. These two methods were named the Velocity RMS Threshold Method and Peeters' Anomaly Detection Method. This confirms the findings of Igba [Igba et al., 2016].

Questioned is how useful the results of this project are. Even though, it has been proven that faults and its propagation are detectable in the frequency domain, the results were generated using models for only one set of environmental conditions, load conditions and one operating regime. It is expected that for different environmental conditions (like different wind speed or turbulence intensity) and load conditions (like asymmetric loading), the response of the wind turbine and, more importantly, the response of the drive train changes [Peeters et al., 2006, Igba et al., 2016]. For example, an increase in turbulence intensity, results in different loads on shafts and bearings [Brand et al., 2011]¹, probably resulting in a different response. As a result, the considered fault detection methods would probably not be able to detect faults anymore.

Additionally, thresholds for the novel fault detection methods were rather arbitrary. The same threshold was applied as the one of the non-traditional Angular Velocity Error Energy Method, which compares the same quantity, namely normalized energy. However, this normalized energy was calculated from a rotational velocity error function instead of acceleration and velocity. Changing the threshold, could possibly lead to an earlier fault detection, but also later or no fault detection. The latter would make the novel fault detection methods less useful or not meaningful at all. A threshold of $E^*(\omega) \geq \frac{5}{4}$ or $E^*(\omega) \leq \frac{4}{5}$ for the Angular Velocity Error Energy Method would have resulted in an earlier (from FC2 onwards) detected fault for MBR damage and in a detectable fault (for FC4 and FC5) for HSBR damage. For the Bearing Velocity Energy Method a threshold $E^*(\omega) \geq 2$ or $E^*(\omega) \leq \frac{1}{2}$ is proposed to make faults earlier detectable and to make its vibration

¹<https://www.windpowerengineering.com/how-turbulent-wind-abuse-wind-turbine-drivetrains/> [Visited on 17th of August 2020]

propagation detectable in more bearings. For the Shaft Vibration Energy Method, earlier detection is possible when applying a threshold of $E^*(\omega) \geq \frac{3}{2}$ or $E^*(\omega) \leq \frac{2}{3}$, also the change in vibration could then be detected at more shafts. Possibly, since the Matlab function `dat2spec(x,L)` from WAFO [WAFO, 2017], with $L=400$, is used for generation of the spectra, the proposed thresholds might be different with a different lag size L .

Since the bearings are modelled as a set of springs, some bearing characteristics are not visible in the vibration monitoring data. For example, ball passing and ball spinning frequencies could not be covered in the frequency domain analysis. Therefore, some typical bearing faults can not be detected.

Some results were not in line with the expectations and possibly implies that the drive train is not behaving as it should. This thought was triggered by analyzing the results produced by the Velocity RMS Threshold Method. The figures showed that the velocity of the high speed shaft rear bearing (HS-B) was affected in the y - and z -direction after applying MBX damage. It was expected, though, that only vibration in the x -direction would have been affected.

It could also be possible that the introduction of the fault happened incorrectly. This was observed after applying the fault detection methods for HSBR damage. It was expected that similar results would have been produced as for MBR damage. However, the vibration propagation was rather local, whereas MBR damage spread through the whole drive train. Moreover, HSBR damage could only be detected in a late stage (FC4 and FC5), which was in contrast with the early fault detection (FC1 and onwards) of MBR damage. It does not need explanation, that, if the drive train model's behaviour and the implementation of the HSBR fault are incorrect, consequences would be severe, potentially leading to useless results.

Also, in contrast to actual measurements, the data produced by the model does not contain noise, measurement errors or missing data. Also, there are no bad measurements performed. In other words, the data is much more reliable (and possibly more useful) than data produced by actual wind turbines, provided that the wind turbine and drive train models perform accurately. This could affect the measurement results which might be very sensitive to these kind of changes. It is possible that thresholds should be changed and methods adapted.

5.2 Conclusion

The intention of this thesis was to get an insight about the effect of faults on the vibration monitoring data of a drive train. Simulated faults in Wang's 10 MW drive train model [Wang et al., 2019] resulted in this monitoring data. The faulty data was compared to data of a healthy drive train. This gave the opportunity to detect faults and their vibration propagation in an offshore wind turbine's drive train.

It was proven to be possible to detect drive train bearing faults. Faults were detected using one common and one non-traditional fault detection methods in the time domain and one non-traditional and two novel frequency domain fault detection methods. These are respectively the Velocity Root-Mean-Square Threshold Method, the Peeters' Anomaly Detection Method, the Angular Velocity Error Energy Method, the Bearing Velocity Energy Method and the Shaft Vibration Energy Method.

The two methods in the time domain were able to detect the faults, but also produced results which gave reasons to doubt on its outcome. The Velocity Root-Mean-Square Threshold Method showed that after introduction of the fault cases, the RMS of the vibration velocity generally increased and crossed zone boundaries which were proposed by ISO 10816-21 [ISO, 2015]. However, it was

shown that for the baseline case, vibration sometimes was already higher than acceptable for new machines. The Peeters' method showed a change in behaviour for the different fault cases. However, a normal distribution which would always fit the baseline series of statistical indicators could not be found. Therefore, both fault detection methods in the time domain were discarded.

Nejad's Angular Velocity Error Energy Method [Nejad et al., 2014c] is a fault detection method in the frequency domain and relies on the relative rotation of shafts. It was able to detect radial damage in the main shaft front bearing (MBR). Shown was that by measuring the rotational velocity of both the main shaft and the high speed shaft, the fault could be detected for the higher degradation levels FC4 and FC5.

The novel Bearing Velocity Energy Method, a frequency domain fault detection method based on the Velocity RMS Threshold Method and the Angular Velocity Error Energy Method, was able to detect radial damage in the main shaft front bearing (MBR) and radial damage in the rear high speed shaft bearing (HSBR). Next to the successful fault detection on the main shaft front bearing, the MBR fault's vibration propagation was detectable at the main shaft rear bearing (INP-B), first stage planet carrier front and rear bearing (PLC-A and PLC-B), intermediate speed shaft front bearing (IMS-A) and high speed shaft front and rear bearing (HS-A and HS-B). MBR damage could be detected as early as FC1 using this method. The HSBR vibration propagation was detectable at HS-A and could be detected from FC4, where also the fault was detected by monitoring HS-A.

Another novel fault detection method in the frequency domain was the Shaft Vibration Energy Method, also based on the Angular Velocity Error Energy Method. It was able to detect propagation of the MBR fault to the main and low speed shaft by monitoring its vibration. The fault and its propagation were detectable at an early stage, from FC2 onwards. Axial damage in the main shaft front bearing (MBX) damage was also detectable using this method. Its propagation was detected by measuring the main shaft's vibration and was detectable from FC3 onwards. Finally, HSBR vibration propagation was detectable in the high speed shaft for high degradation levels (FC4 and FC5).

ISO 10816-21 [ISO, 2015] proposes measurement locations. As an outcome of this work, it is recommended to place extra sensors measuring velocity on the PLC-A, PLC-B and IMS-A bearing housings and on the low speed shaft, provided that this is reasonably possible.

It is shown that an effect of main shaft front bearing radial damage propagates through the whole system, whereas similar damage in the high speed shaft rear bearing only has an effect on the bearings and shaft on the high speed end of the drive train. Axial damage in the main shaft front bearing, however, propagates very local and only has an effect on the vibration of the main shaft, of course limited by the fault detection methods discussed in this thesis. To detect a MBX fault it is thus important to monitor the main shaft's vibration.

The outcome contributes to the understanding of vibration propagation and its detection in a drive train. In this work, it is shown how an implemented fault somewhere in the system, would result in a difference in vibration of other drive train's components. This change in vibration does not indicate that the other component is damaged, but it could very well be the case. The methods presented in this study can be implemented in monitoring and maintenance methods. Additionally, due to the detected propagation of vibrations, maintenance engineers can check the affected gear-box components and replace them before they fail. This can lead to lower maintenance costs and thus a lower levelized cost of wind energy, making (offshore) wind energy more feasible compared to cheap fossil energy.

5.3 Recommendations

This study has shown how an implemented fault causes a different vibration response in a 10 MW drive train of an offshore wind turbine. It showed that a fault could be detectable in different components of the gearbox, however, it did not show that these components got damaged as well after the fault introduction. This, however, is to be expected. Further research need to be carried out on the effects of the fault on these components, e.g. by means of a fatigue study.

The study is performed with one environmental condition and one foundation. In order to make the methodology useful for general purposes, a number of similar studies should be performed with different conditions (like foundations, wind speed, turbulence, wave height, etcetera) to normalize the project.

The drive train response after fault introduction were not always as expected. Therefore it is recommended to perform (another) verification and validation round to confirm whether the drive train and fault introduction are matching reality. Vibration monitoring of multiple 10 MW offshore wind turbines is proposed to compare these results with the vibration data of the drive train model [Igba et al., 2016, Peeters et al., 2006, Wilkinson et al., 2014].

One common and one non-traditional fault detection method were deployed in the time domain, being the the Velocity Root-Mean-Square Threshold Method and Peeters' Anomaly Detection Method. The first method needs further research in imposing flexible zone boundary limits, depending on vibration velocity direction and gearbox component. The detection method introduced by Peeters (which was slightly adapted in this work) needs more data of fault-free wind turbines and more research on which data to use and the size of the fused period.

Two novel methods are introduced in this study: the Bearing Velocity Energy Method and the Shaft Vibration Energy Method. Although they are both based on the Angular Velocity Error Energy Method as developed by Nejad [Nejad et al., 2014c] (and the first one is also based on the Velocity RMS Threshold Method), those methods are not validated yet. It is proven that there is a difference in motion of the drive train's components. However, it is not sure whether the fault (and its vibration propagation) is detectable since the threshold comparing normalized energy is not completely justified. Validation of the methods is recommended to apply this method for maintenance of offshore wind turbines.

Finally, it was considered to be difficult to find currently used fault detection techniques and their thresholds or limits, practised in the offshore wind energy industry. There was especially not much available for fault detection in the time domain, this heavily influenced the outcome of this study. Also, the request to access databases regarding fault statistics of drive trains were rejected. It is recommended that the wind energy industry reveals its practices. Only together, the wind industry can fight against global warming. Like that, the industry can make wind energy more feasible to reduce the levelized cost of wind energy.

6 | List of References

- [AGMA, 2006] AGMA (2006). *Design manual for enclosed epicyclic gear drives*. American National Standards Institute (AGMA), Alexandria, Virginia, US.
- [Andersen and Sorensen, 2018] Andersen, S. and Sorensen, J. N. (2018). *Offshore Wind Energy - Aerodynamics for Offshore Wind Farms*. DTU Wind, Lyngby, Denmark.
- [Bachynski, 2014] Bachynski, E. E. (2014). *Design and Dynamic Analysis of Tension Leg Platform Wind Turbines*. Norwegian University of Science and Technology, Engineering Science and Technology, Marine Technology, Trondheim, Norway.
- [Bak, 2015] Bak, C. (2015). *Experimental Study of the Dynamic Response of the DTU 10 MW Wind turbine on a Tension Leg Platform - Proceedings of the EWEA Annual Event and Exhibition 2015*. DTU Wind Energy.
- [Bak et al., 2013] Bak, C., Zahle, F., Bitsche, R., Kim, T., Yde, A., Henriksen, L. C., Hansen, M. H., Blasques, J. P. A. A., Gaunaa, M., and Natarajan, A. (2013). *Description of the DTU 10 MW Reference Wind Turbine*. Technical University of Denmark, Roskilde, Denmark.
- [Bauer, 2016] Bauer, S. (2016). *Basics of Multibody Systems: Presented by Practical Simulation Examples of Spine Models, Numerical Simulation*. Brain Imaging to Turbulent Flows, Ricardo Lopez-Ruiz, IntechOpen.
- [Blodt et al., 2008] Blodt, M., Granjon, P., Raison, B., and Rostaing, G. (2008). *Models for Bearing Damage Detection in Induction Motors Using Stator Current Monitoring*, volume 55.
- [Boguski, 2010] Boguski, B. (2010). *An experimental investigation of the system-level behaviour of planetary gear sets*. MSc. thesis, Department of Mechanical Engineering, Ohio State University.
- [Boyce, 2012] Boyce, M. P. (2012). *19 - Control Systems and Instrumentation*. Butterworth-Heinemann, Oxford, fourth edition.
- [Brand et al., 2011] Brand, A., Peinke, J., and Mann, J. (2011). Turbulence and wind turbines. *Journal of Physics: Conference Series*, 318.
- [Bredmose, 2018] Bredmose, H. (2018). *Offshore Wind Energy - Rainflow counting & Lifetime fatigue*. DTU Wind, Lyngby, Denmark.
- [Burton et al., 2011] Burton, T., Jenkins, N., Sharpe, D., and Bossanyi, E. (2011). *Wind Energy Handbook*. Wiley.
- [Castro, 2017] Castro, I. D. R. (2017). *Design of a 10MW Wind Turbine Rotor Blade for Testing of a Scaled-down Floating Offshore Support Structure*. Delft University of Technology, Delft, The Netherlands.
- [Chaaban et al., 2014] Chaaban, R., Ginsberg, D., and Fritzen, C.-P. (2014). *Structural load analysis of floating wind turbines under blade pitch system faults*. In *Wind Turbine Control and Monitoring*. Springer.

- [Chae and Kim, 2003] Chae, Y. and Kim, J. (2003). *Implementation of configuration dependent stiffness proportional damping for the dynamics of rigid multi-block systems*. Earthquake Engineering and Engineering Vibration 2.
- [Chen, 2011] Chen, Z. (2011). *Wind turbine drive train systems*. Aalborg University, Aalborg, Denmark.
- [Cho, 2019] Cho, S. (2019). *Model-based fault detection and diagnosis of a blade pitch system in floating wind turbines*. Department of Marine Technology, NTNU, Trondheim, Norway.
- [Chopra, 1995] Chopra, A. K. (1995). *Dynamics of Structures: Theory and Applications to Earthquake Engineering*. Prentice Hall, 1st edition.
- [Cook et al., 2002] Cook, R., Malkus, D., Plesha, M., and Witt, R. (2002). *Concepts and Applications of Finite Element Analysis*. John Wiley & Sons, fourth edition.
- [Coronado and Fischer, 2015] Coronado, D. and Fischer, K. (2015). *Condition monitoring of wind turbines: state of the art, user experience and recommendations*. Fraunhofer Institute for Wind Energy and Energy System Technology IWES Northwest, Bremerhaven, Germany.
- [de Beer, 1982] de Beer, F. (1982). *WINDBOUWWERK. Dl. 1. Werktekeningen voor beproefde windmolens voor electriciteits-opwekking: rotordiameter van 3 en 5 meter*. Organisatie voor Duurzame Energie.
- [Dose et al., 2018] Dose, B., Rahimi, H., Stoevesandt, B., Peinke, J., and Schepers, J. (2018). *On the effect of blade deformations on the aerodynamic performance of wind turbine rotors subjected to yawed inflow*, volume 1037.
- [Evans, 2011] Evans, R. D. (2011). *Classic Bearing Damage Modes*. Wind Turbine Tribology Seminar, Broomfield, Colorado, USA.
- [Faulstich et al., 2011] Faulstich, S., Hahn, B., and Tavner, P. (2011). *Wind turbine downtime and its importance for offshore deployment*. Wind Energy.
- [Gao, 2019] Gao, Z. (2019). *Marine Operations Related to Installation of Offshore Wind Turbines*. Department of Marine Technology, NTNU, Trondheim, Norway.
- [Gawarkiewicz et al., 2015] Gawarkiewicz, R., Wasilczuk, M., and Wasilczuk, F. (2015). *Drivetrain of a Wind Turbine*. Politechnika Gdańska, Środowiskowe Studium Doktoranckie przy Wydz. Mechanicznym Politechniki Gdańskiej, Gdansk, Poland.
- [Ghane, 2018] Ghane, M. (2018). *Fault Diagnosis of Floating Wind Turbine Drivetrain - Methodologies and Applications*. Norwegian University of Science and Technology, Engineering Science and Technology, Marine Technology, Trondheim, Norway.
- [Ghane et al., 2016] Ghane, M., Nejad, A. R., Blanke, M., Gao, Z., and Moan, T. (2016). *Statistical fault diagnosis of wind turbine drivetrain applied to a 5 MW floating wind turbine*. Journal of Physics: Conference Series.
- [Ghane et al., 2017] Ghane, M., Nejad, A. R., Blanke, M., Gao, Z., and Moan, T. (2017). *Diagnostic monitoring of drivetrain in a 5 MW spar-type floating wind turbine using Hilbert spectral analysis*, volume 137. 14th Deep Sea Offshore Wind RD Conference, EERA DeepWind 2017.
- [Ghane et al., 2018] Ghane, M., Nejad, A. R., Blanke, M., Gao, Z., and Moan, T. (2018). *Condition monitoring of spar-type floating wind turbine drivetrain using statistical fault diagnosis*. Wind Energy.

- [Giurgiutiu, 2007] Giurgiutiu, V. (2007). *Structural Health Monitoring with Piezoelectric Wafer Active Sensors*. Academic Press.
- [González-González and Galar, 2018] González-González, A. and Galar, D. (2018). *Condition monitoring of wind turbine pitch controller: A maintenance approach*. Measurement.
- [Grenander, 1959] Grenander, U. (1959). *Probability and Statistics: The Harald Cramér Volume*. Wiley Publications in Statistics. Almqvist & Wiksell.
- [Guo et al., 2015] Guo, Y., Keller, J., Cava, W. L., Austin, J., Nejad, A., Halse, C., Bastard, L., and Helsen, J. (2015). *Recommendations on model fidelity for wind turbine gearbox simulations*. National Renewable Energy Lab (NREL), Golden, Colorado, USA.
- [Hameed et al., 2007] Hameed, Z., Hong, Y., Cho, Y., Ahn, S., and Song, C. (2007). *Condition monitoring and fault detection of wind turbines and related algorithms: A review*. Elsevier, Seoul, Republic of Korea.
- [Hansen et al., 2010] Hansen, J., Ruedy, R., Sato, M., and Lo, K. (2010). *Global Surface Temperature Change*. Wiley.
- [Hansen, 2008] Hansen, M. O. L. (2008). *Aerodynamics of Wind Turbines*. Earthscan, London, UK, second edition.
- [Harris, 2001] Harris, T. A. (2001). *Rolling bearing analysis*. John Wiley and sons.
- [Hasselmann et al., 1973] Hasselmann, K., Barnett, T., Bouws, E., Carlson, H., Cartwright, D., Enke, K., Ewing, J., Gienapp, H., Hasselmann, D., Kruseman, P., Meerburg, A., Muller, P., Olbers, D., Richter, K., Sell, W., and Walden, H. (1973). *Measurements of wind-wave growth and swell decay during the Joint North Sea Wave Project (JONSWAP)*, volume 8.
- [Hau, 2008] Hau, E. (2008). *Windkraftanlagen*. Springer.
- [Hegseth and Bachynski, 2019] Hegseth, J. M. and Bachynski, E. E. (2019). *A semi-analytical frequency domain model for efficient design evaluation of spar floating wind turbines*, volume 64.
- [Hill, 1963] Hill, R. (1963). *Elastic properties of reinforced solids: Some theoretical principles*, volume 11.
- [IEC, 2005] IEC (2005). *IEC61400-1. Wind turbines, part 1: Design requirements*. International Electrotechnical Commission (IEC), Geneva, Switzerland.
- [Igba et al., 2016] Igba, J., Alemzadeh, K., Durugbo, C., and Eiriksson, E. T. (2016). *Analysing RMS and peak values of vibration signals for condition monitoring of wind turbine gearboxes*, volume 91.
- [Inman, 2013] Inman, D. J. (2013). *Engineering Vibrations*. Pearson, 4th, intern. edition.
- [IRENA, 2016] IRENA (2016). *Floating Foundations: A Game Changer for Offshore Wind Power*.
- [IRENA, 2019a] IRENA (2019a). *FUTURE OF WIND - Deployment, investment, technology, grid integration and socio-economic aspects*. International Renewable Energy Agency, Abu Dhabi.
- [IRENA, 2019b] IRENA (2019b). *Renewable Power Generation Costs in 2018*. International Renewable Energy Agency, Abu Dhabi.

- [ISO, 2015] ISO (2015). *ISO 10816-21. Mechanical vibration — Evaluation of machine vibration by measurements on non-rotating parts — Part 21: Horizontal axis wind turbines with gearbox*. International Organization for Standardization (ISO), Geneva, Switzerland.
- [ISO, 2016] ISO (2016). *ISO 20816-1. Mechanical vibration - Measurement and evaluation of machine vibration - Part 1: General guidelines*. International Organization for Standardization (ISO), Geneva, Switzerland.
- [Jonkman et al., 2009] Jonkman, J., Butterfield, S., Musial, W., and Scott, G. (2009). *Definition of a 5-MW Reference Wind Turbine for Offshore System Development*. National Renewable Energy Lab (NREL), Golden, Colorado, USA.
- [Juchem, 2009] Juchem, S. (2009). *Development of a computer model of the lumbar spine for the determination of mechanical loads*. University Koblenz-Landau, Koblenz, Germany.
- [Kaimal et al., 1972] Kaimal, J., Wyngaard, J., Izumi, Y., and Coté, O. (1972). *Spectral characteristics of surface-layer turbulence*. Quarterly Journal of the Royal Meteorological Society.
- [Koyo, 2019] Koyo (2019). *Large Size Ball & Roller Bearings - General Bearings - Cat. No. BS008EN-0DS*. JTEKT Corporation, Japan.
- [Kursat Yalcin, nd] Kursat Yalcin, M. (n.d.). *Velocity and Motion sensors*. Nigde University, Nigde, Turkey.
- [Lee et al., 2020] Lee, J., Zhao, F., Dutton, A., Backwell, B., Fiestas, R., Qiao, L., Balachandran, N., Lim, S., Liang, W., Clarke, E., and Lathigaralead, A. (2020). *Global Wind Report 2019*. Global Wind Energy Council (GWEC), Brussels, Belgium.
- [Lehner, 2007] Lehner, S. (2007). *Development and validation of biomechanical computer models and their use in sports science*. University Koblenz-Landau, Koblenz, Germany.
- [Lemaitre, 1996] Lemaitre, J. (1996). *A Course on Damage Mechanics*. Springer-Verlag Berlin Heidelberg, 2nd edition.
- [Li et al., 2015] Li, L., Gao, Z., and Moan, T. (2015). *Joint Distribution of Environmental Condition at Five European Offshore Sites for Design of Combined Wind and Wave Energy Devices*, volume 137.
- [Lin et al., 2016] Lin, Y., Tu, L., Liu, H., and Li, W. (2016). *Fault analysis of wind turbines in China*. Renewable and Sustainable Energy Reviews, China.
- [Litvin and Fuentes, 2004] Litvin, F. L. and Fuentes, A. (2004). *Gear Geometry and Applied Theory*. Cambridge University Press, Cambridge, UK, 2nd edition.
- [Long et al., 2011] Long, H., Wu, J., Matthew, F., and Tavner, P. (2011). *Fatigue analysis of wind turbine gearbox bearings using SCADA data and miner's rule*. Conference: European Wind Energy Association Conference.
- [Manwell et al., 1999] Manwell, J., Rogers, A., Abdulwahid, U., Ellis, A., and Mcniff, B. (1999). *Wind turbine gearbox evaluation*.
- [Metrikine, 2010] Metrikine, A. (2010). *Dynamics, Slender Structures and an Introduction to Continuum Mechanics (CT 4145) Module - Dynamics of Mechanical Systems and Slender Structures*. Faculty of Civil Engineering and Geosciences - Section of Structural Mechanics, Delft University of Technology.

- [Miao and Zhou, 2015] Miao, Q. and Zhou, Q. (2015). *Planetary Gearbox Vibration Signal Characteristics Analysis and Fault Diagnosis*. Fault Diagnosis and Prognosis of Critical Components.
- [Mordkoff, 2016] Mordkoff, J. T. (2016). The assumption(s) of normality.
- [Morison, 1950] Morison, J. (1950). *The force exerted by surface waves on piles*. Petroleum Transactions, American Institute of Mining Engineers.
- [Nejad et al., 2015a] Nejad, A., Bachynski, E., Gao, Z., and Moan, T. (2015a). *Fatigue Damage Comparison of Mechanical Components in a Land-based and a Spar Floating Wind Turbine*, volume 101.
- [Nejad et al., 2012] Nejad, A., Xing, Y., and Moan, T. (2012). *Gear Train Internal Dynamics in Large Offshore Wind Turbines - Volume 3: Advanced Composite Materials and Processing; Robotics; Information Management and PLM; Design Engineering*. Engineering Systems Design and Analysis.
- [Nejad, 2018] Nejad, A. R. (2018). *Modelling and Analysis of Drivetrains in Offshore Wind Turbines*. John Wiley & Sons, Ltd.
- [Nejad et al., 2015b] Nejad, A. R., Bachynski, E. E., Kvittem, M. I., Luan, C., Gao, Z., and Moan, T. (2015b). *Stochastic dynamic load effect and fatigue damage analysis of drivetrains*. Marine Structures, Trondheim, Norway.
- [Nejad et al., 2014a] Nejad, A. R., Gao, Z., and Moan, T. (2014a). *Fatigue reliability-based inspection and maintenance planning of gearbox components in wind turbine drivetrains*. Energy Procedia, Trondheim, Norway.
- [Nejad et al., 2016b] Nejad, A. R., Gao, Z., Moan, T., and Guo, Y. (2016b). *Development of a 5-MW reference gearbox for offshore wind turbines*. Wind Energy, Trondheim, Norway.
- [Nejad and Moan, 2017] Nejad, A. R. and Moan, T. (2017). *On model-based system approach for health monitoring of drivetrains in floating wind turbines*. Elsevier, Trondheim, Norway.
- [Nejad et al., 2014c] Nejad, A. R., Odgaard, P. F., Gao, Z., and Moan, T. (2014c). *A prognostic method for fault detection in wind turbine drivetrains*, volume 42.
- [Newmark, 1959] Newmark, N. M. (1959). *A Method of Computation for Structural Dynamics*, volume 85.
- [Ohlenforst et al., 2018] Ohlenforst, K., Sawyer, S., Dutton, A., Backwell, B., Fiestas, R., Lee, J., Qiao, L., Zhao, F., and Balachandran, N. (2018). *Global Wind Report 2018*. Global Wind Energy Council (GWEC), Brussels, Belgium.
- [Pavese et al., 2015] Pavese, C., Wang, Q., Kim, T., Jonkman, J., and Sprague, M. (2015). *Proceedings of the EWEA Annual Event and Exhibition 2015*. European Wind Energy Association (EWEA).
- [Peeters, 2019] Peeters, C. (2019). *Advanced signal processing for the identification and diagnosis of the condition of rotating machinery - Doctoral Thesis*. Vrije Universiteit Brussel & INSA Lyon.
- [Peeters et al., 2006] Peeters, J., Vandepitte, D., and Sas, P. (2006). *Analysis of internal drive train dynamics in a wind turbine*. Wind Energy, Belgium.

- [Pierson Jr. and Moskowitz, 1964] Pierson Jr., W. J. and Moskowitz, L. (1964). *A proposed spectral form for fully developed wind seas based on the similarity theory of S. A. Kitaigorodskii*, volume 69.
- [Poore and Walford, 2008] Poore, R. and Walford, C. (2008). *Development of an Operations and Maintenance Cost Model to Identify Cost of Energy Savings for Low Wind Speed Turbines*. Global Energy Concepts, LLC (NREL), Seattle, Washington, US.
- [Qiu et al., 2002] Qiu, J., Seth, B. B., Liang, S. Y., and Zhang, C. (2002). *Damage Mechanics Approach for Bearing Lifetime Prognostics*, volume 16.
- [Rademakers et al., 2011] Rademakers, L., Braam, H., and Obdam, T. (2011). *Operation and maintenance of offshore wind energy systems*. Energy Research Centre of The Netherlands (ECN), The Netherlands.
- [Ramírez et al., 2020] Ramírez, L., Fraile, D., and Brindley, G. (2020). *Offshore Wind in Europe - Key trends and statistics 2019*. WindEurope, Brussels, Belgium.
- [Ritchie and Roser, 2018] Ritchie, H. and Roser, M. (2018). *CO₂ and Greenhouse Gas Emissions*. Our World in Data.
- [Rockmann et al., 2017] Rockmann, C., Lagerveld, S., and Stavenuiter, J. (2017). *Operation and maintenance costs of offshore wind farms and potential multi-use platforms in the Dutch North Sea*, pages 97–113. Springer.
- [Ryabkova et al., 2019] Ryabkova, M., Karaev, V., Guo, J., and Titchenko, Y. (2019). *A Review of Wave Spectrum Models as Applied to the Problem of Radar Probing of the Sea Surface*, volume 124.
- [Rychlik, 1987] Rychlik, I. (1987). *A new definition of the rainflow cycle counting method*. International Journal of Fatigue.
- [Rytter, 1993] Rytter, A. (1993). *Vibrational Based Inspection of Civil Engineering Structures*. Aalborg University, Aalborg, Denmark.
- [Schwertassek and Wallrapp, 1999] Schwertassek, R. and Wallrapp, O. (1999). *Dynamics of flexible multibody systems. Methods of Mechanics for computer-aided design and analysis of mechatronic systems*. Vieweg+Teubner, Wiesbaden, Germany.
- [Sheng, 2016] Sheng, S. (2016). *Wind Turbine Gearbox Damage Distribution Statistics 2016*. National Renewable Energy Lab (NREL). <https://grd.nrel.gov/#/stats>.
- [SIMA, 2019] SIMA (2019). *SESAM Release Note - SIMA*. DNV GL – Digital Solutions.
- [SIMPACT, 2020] SIMPACK (2020). *Multi body system software*. <http://www.simpack.com>. Accessed on February 24, 2020.
- [Smith, 2003] Smith, J. D. (2003). *Gear noise and vibration*. CRC Press.
- [Smith, 2007] Smith, J. O. (2007). *Introduction to Digital Filters with Audio Applications*. W3K Publishing.
- [Stoica and Moses, 2005] Stoica, P. and Moses, R. (2005). *Spectral Analysis of Signals*. Pearson Prentice Hall.
- [Taghipour et al., 2008] Taghipour, R., Perez, T., and Moan, T. (2008). *Hybrid frequency-time domain models for dynamic response analysis of marine structures*. Ocean Engineering.

- [Tautz-Weinert and Watson, 2016] Tautz-Weinert, J. and Watson, S. J. (2016). *Using SCADA data for wind turbine condition monitoring – a review*. The Institution of Engineering and Technology (IET) Journals, Loughborough, UK.
- [Tavner, 2012] Tavner, P. (2012). *Offshore Wind Turbines-Reliability, Availability and Maintenance*. The Institution of Engineering and Technology, Stevenage, UK.
- [The MathWorks Inc., nd] The MathWorks Inc. (n.d.). *MATLAB*. Natick, Massachusetts, USA. www.mathworks.com.
- [Thornblad, 1978] Thornblad, P. (1978). *Gears for wind power plants*. Second International Symposium on Wind Energy Systems, Amsterdam, The Netherlands.
- [Timken, 2011] Timken (2011). *Timken® cylindrical roller bearing catalog*. The Timken Company, USA.
- [Turteltaub, 2015] Turteltaub, S. (2015). *AE2135-II Vibrations - Lecture Slides*. Faculty of Aerospace Engineering - Delft University of Technology.
- [WAFO, 2017] WAFO (2017). *Wafover 2017*. Faculty of Engineering - Centre for Mathematical Sciences - Lund University, Lund, Sweden.
- [Wang et al., 2019] Wang, S., Nejad, A. R., and Moan, T. (2019). *On design, modelling, and analysis of a 10-MW medium-speed drivetrain for offshore wind turbines*. Department of Marine Technology, NTNU, Trondheim, Norway.
- [Wenyi et al., 2013] Wenyi, L., Zhenfeng, W., Jiguang, H., and Guangfeng, W. (2013). *Wind turbine fault diagnosis method based on diagonal spectrum and clustering binary tree svm*. Renewable Energy.
- [Wilkinson et al., 2014] Wilkinson, M., Darnell, B., Delft, T. V., and Harman, K. (2014). *Comparison of methods for wind turbine condition monitoring with SCADA data*, volume 8.
- [Wilkinson and Hendriks, 2010] Wilkinson, M. and Hendriks, B. (2010). *Reliability-focused research on optimizing Wind Energy system design, operation and maintenance: Tools, proof of concepts, guidelines & methodologies for a new generation*. Collaborative Project: Large Scale Integrated Project.
- [Xu and Xu, 2017] Xu, J. and Xu, L. (2017). *Integrated System Health Management - Perspectives on Systems Engineering Techniques*. Academic Press, China.
- [Yang et al., 2018b] Yang, L., Xu, T., Xu, H., and Wu, Y. (2018b). *Mechanical behavior of double-row tapered roller bearing under combined external loads and angular misalignment*, volume 142-143.
- [Yang et al., 2013] Yang, W., Court, R., and Jiang, J. (2013). *Wind turbine condition monitoring by the approach of SCADA data analysis*, volume 53.
- [Yang et al., 2014] Yang, W., Tavner, P. J., Crabtree, C. J., Feng, Y., and Qiu, Y. (2014). *Wind turbine condition monitoring: technical and commercial challenges*, volume 17.

7 | Bibliography

- [Agarwal et al., 2010] Agarwal, V., Aggarwal, R. K., Patidar, P., and Patki, C. (2010). *A novel scheme for rapid tracking of maximum power point in wind energy generation systems*. IEEE Transactions on Energy Conversion.
- [Bachynski, 2012] Bachynski, E. (2012). *Basic aerodynamics for wind turbines*.
- [Bachynski, 2019] Bachynski, E. E. (2019). *Multidisciplinary Design Optimization - Lecture slides*. Department of Marine Technology, NTNU, Trondheim, Norway.
- [Berg et al., 2017] Berg, J., Mann, J., Kelly, M., and Nielsen, M. (2017). *Micro meteorology for Wind Energy*. DTU, Roskilde, Denmark.
- [Bijl and Timmer, 2014] Bijl, H. and Timmer, N. (2014). *Introduction to Aerospace Engineering - Aerodynamics*. Delft University of Technology, Delft, The Netherlands.
- [Blanchard and Fabrycky, 2013] Blanchard, B. and Fabrycky, W. (2013). *Systems Engineering and Analysis Pearson New International Edition (5th Edition)*. Prentice Hall International Series in Industrial & Systems Engineering. Pearson Education Limited (Verlag), 5th edition.
- [Box et al., 2015] Box, G. E., Jenkins, G. M., Reinsel, G. C., and Ljung, G. M. (2015). *Time series analysis: forecasting and control*. John Wiley & Sons.
- [Brockwell and Davis, 2013] Brockwell, P. J. and Davis, R. A. (2013). *Time series: theory and methods*. Springer Science & Business Media.
- [Carroll et al., 2016] Carroll, J., McDonald, A., and McMillan, D. (2016). *Failure rate, repair time and unscheduled O&M cost analysis of offshore wind turbine*. Wind Energy.
- [Cho et al., 2019] Cho, S., Bachynski, E. E., Nejad, A. R., Gao, Z., and Moan, T. (2019). *Numerical modeling of the hydraulic blade pitch actuator in a spar-type floating wind turbine considering fault conditions and their effects on global dynamic responses*. Department of Marine Technology, NTNU, Trondheim, Norway.
- [Cohen, 1989] Cohen, L. (1989). *Time-frequency distributions-a review*. Proceedings of the IEEE.
- [Dean and Dalrymple, 1991] Dean, R. and Dalrymple, R. (1991). *Water Wave Mechanics for Engineers and Scientists*. World Scientific.
- [Ding, 2008] Ding, S. (2008). *Model-based fault diagnosis techniques: design schemes, algorithms, and tools*. Springer Science & Business Media.
- [DNV-GL, 2016] DNV-GL (2016). *DNVGL-ST-0361. Machinery for wind turbines*. Det Norske Veritas Germanischer Lloyd (DNV-GL).
- [Doolan, 2019] Doolan, C. (2019). *Taller, faster, better, stronger: wind towers are only getting bigger*. The Conversation. <http://theconversation.com/taller-faster-better-stronger-wind-towers-are-only-getting-bigger-120492>.

- [Dutton et al., 1997] Dutton, K., Thompson, S., and Barraclough, B. (1997). *The art of control engineering*. Harlow: Addison Wesley.
- [Ebrahimi and Eberhard, 2007] Ebrahimi, S. and Eberhard, P. (2007). *Aspects of contact problems in computational multibody dynamics*. in *Multibody Dynamics, Computational Methods in Applied Sciences*, Vol. 4. Springer, Dordrecht, The Netherlands.
- [Eggleston and Stoddard, 1987] Eggleston, D. and Stoddard, F. (1987). *Wind Turbine Engineering Design*. Van Nostrand Reinhold Company.
- [Esbensen and Sloth, 2009] Esbensen, T. and Sloth, C. (2009). *Fault diagnosis and fault-tolerant control of wind turbines*. Aalborg University, Aalborg, Denmark.
- [Faltinsen, 1990] Faltinsen, O. (1990). *Sea Loads on Ships and Offshore Structures*. Cambridge University Press.
- [Galar and Kumar, 2017] Galar, D. and Kumar, U. (2017). *eMaintenance - Chapter 5: Diagnosis*. Academic Press.
- [Garlick et al., 2009] Garlick, W., Dixon, R., and Watson, S. (2009). *A model-based approach to wind turbine condition monitoring using SCADA data*. 20th Int. Conf. System Engineering.
- [GIZ, nd] GIZ (n.d.). *The Structure of a Modern Wind Turbine – An Overview*. GIZ Energy, Vietnam. http://gizenergy.org.vn/media/app/media/PDF-Docs/Technical-Documents/The_Structure_of_a_Modern_Wind_Turbine.pdf.
- [Gray and Watson, 2010] Gray, C. and Watson, S. (2010). *Physics of Failure approach to wind turbine condition based maintenance*. Wind Energy.
- [Hansen et al., 2006] Hansen, M., Sorensen, J., Voutsinas, S., Sorensen, N., and H.Aa.Madsen (2006). *State of the art in wind turbine aerodynamics and aeroelasticity*. Progress in Aerospace Sciences, Denmark.
- [Harty, 2015] Harty, M. B. D. (2015). *The multibody systems approach to vehicle dynamics*. Butterworth-Heinemann, Elsevier Ltd, 2nd edition.
- [He, 1989] He, C. (1989). *Development and Application of a Generalized Dynamic Wake Theory for Lifting Rotors*. Georgia Institute of Technology.
- [IEC, 2009] IEC (2009). *IEC61400-3: Wind turbines, part 3: Design requirements for offshore wind turbines*. International Electrotechnical Commission (IEC), Geneva, Switzerland.
- [IEC, 2012] IEC (2012). *IEC61400-4. Wind turbines, part 4: Standard for design and specification of gearboxes*. International Electrotechnical Commission (IEC), Geneva, Switzerland.
- [Isermann, 2006] Isermann, R. (2006). *Fault-diagnosis systems: an introduction from fault detection to fault tolerance*. Springer Science & Business Media.
- [Isermann and Ballé, 2015] Isermann, R. and Ballé, P. (2015). *Trends in the application of model-based fault detection and diagnosis of technical processes*. Control engineering practice.
- [ISO, 2006] ISO (2006). *ISO 6336-1. Calculation of load capacity of spur and helical gears, part 6: basic principles, introduction and general influence factors*. International Organization for Standardization (ISO), Geneva, Switzerland.
- [Jian, 2011] Jian, K. (2011). *Wind turbine pitch system*. China electrical equipment industry, China.

- [Jiang et al., 2015] Jiang, Z., Xing, Y., Moan, T., and Gao, Z. (2015). *Long-term contact fatigue analysis of a planetary bearing in a land-based wind turbine drivetrain*. Wind Energy, Trondheim, Norway.
- [Johannessen, 2001] Johannessen, K. (2001). *Joint distribution for wind and waves in the northern North Sea*. Eleventh International Offshore and Polar Engineering Conference & Exhibition, Stavanger, Norway.
- [Jonasson, 2001] Jonasson, K. (2001). *Tillståndsövervakning av vindkraftverk—Utvärdering av system utfört av SKF Nova*. Elforsk.
- [Jonkman and Buhl, 2007] Jonkman, J. and Buhl, M. (2007). Development and verification of a fully coupled simulator for offshore wind turbines. volume 4.
- [Karpenko and Sepehri, 2005] Karpenko, M. and Sepehri, N. (2005). *Fault-tolerant control of a servohydraulic positioning system with crossport leakage*. IEEE Transactions on Control Systems Technology.
- [Kim and Dalhoff, 2014] Kim, M. and Dalhoff, P. (2014). *Yaw Systems for wind turbines - Overview of concepts, current challenges and design methods*. Department of Mechanical Engineering & Production Management, Hamburg University of Applied Sciences, Hamburg, Germany.
- [Kinner, 1937] Kinner, W. (1937). *Die kreisförmige Tragfläche auf potentialtheoretischer Grundlage*. Ing. Arch.
- [Koizumi et al., 2000] Koizumi, T., Tsujiuchi, N., and Matsumura, Y. (2000). *Diagnosis with the correlation integral in time domain*. Mechanical Systems and Signal Processing.
- [Li et al., 2009] Li, H., Chen, Z., and Polinder, H. (2009). *Optimization of multibrid permanent magnet wind generator systems*. IEEE Transactions on Energy Conversion.
- [Li et al., 2003] Li, W., Zhang, G., Shi, T., and Yang, S. (2003). *Gear crack early diagnosis using bispectrum diagonal slice*. Chinese Journal of Mechanical Engineering (English Edition).
- [Liangcai et al., 2002] Liangcai, X., Tielin, S., Shuzi, Y., and Rao, R. B. (2002). *A novel application of wavelet-based bispectrum analysis to diagnose faults in gears*. International Journal of COMADEM.
- [Lourens, 2019a] Lourens, E.-M. (2019a). *OE44120 Offshore Wind Farm Design - Course Introduction*. Delft University of Technology, Delft, The Netherlands.
- [Lourens, 2019b] Lourens, E.-M. (2019b). *OE44120 Offshore Wind Farm Design - Lecture Slides*. Delft University of Technology, Delft, The Netherlands.
- [Lu et al., 2009] Lu, B., Li, Y., Wu, X., and Yang, Z. (2009). *A review of recent advances in wind turbine condition monitoring and fault diagnosis*. Proceedings of the 2005 IEEE International Conference on Robotics and Automation (ICRA).
- [Lundberg and Palmgren, 1952] Lundberg, G. and Palmgren, A. (1952). *Dynamic capacity of roller bearings*. Acta Polytechnica Mechanical Engineering Series.
- [Maeda et al., 2008] Maeda, T., Kamada, Y., Suzuki, J., and Fujioka, H. (2008). *Rotor Blade Sectional Performance Under Yawed Inflow Conditions*. Journal of Solar Energy Engineering.
- [Manwell et al., 2009] Manwell, J., McGowan, J., and Rogers, A. (2009). *Wind Energy Explained*. John Wiley & Sons, Ltd.

- [Martins and Lambe, 2013] Martins, J. R. R. A. and Lambe, A. B. (2013). *Multidisciplinary Design Optimization: A Survey of Architectures*. American Institute of Aeronautics and Astronautics.
- [McKenna et al., 2015] McKenna, R., v.d. Leye, P. O., and Fichtner, W. (2015). *Key challenges and prospects for large wind turbines*. Elsevier, Karlsruhe, Germany.
- [Merritt, 1967] Merritt, H. (1967). *Hydraulic control systems*. John Wiley & Sons.
- [Mertz, 2015] Mertz, T. (2015). *Logical Operators*. Kansas State University. <http://faculty.salina.k-state.edu/tmertz/Java/041datatypesandoperators/13logicaloperators.pdf>.
- [Moriarty and Hansen, 2005] Moriarty, P. and Hansen, A. (2005). *AeroDyn theory manual*. National Renewable Energy Lab (NREL).
- [Namik and Stol, 2020] Namik, H. and Stol, K. (2020). *Control Methods for Reducing Platform Pitching Motion of Floating Wind Turbines*.
- [Nejad et al., 2016a] Nejad, A. R., Bachynski, E. E., Li, L., and Moan, T. (2016a). *Correlation between Acceleration and Drivetrain Load Effects for Monopile Offshore Wind Turbines*, volume 94. 13th Deep Sea Offshore Wind R&D Conference, EERA DeepWind'2016.
- [Nejad et al., 2014b] Nejad, A. R., Gao, Z., and Moan, T. (2014b). *On long-term fatigue damage and reliability analysis of gears under wind loads in offshore wind turbine drivetrains*. International Journal of Fatigue, Trondheim, Norway.
- [Niemann and Winter, 1983] Niemann, G. and Winter, H. (1983). *Maschinenelemente Band II: Getriebe allgemein, Zahnradgetriebe, Grundlagen, Stirnradgetriebe*. Springer-Verlag.
- [Opie, 2018] Opie, R. (2018). *Pitch Control Critical for Wind Power*. Energies, Beijing, China.
- [Parker et al., 2000] Parker, B. E., Ware, H., Wipf, D., Tompkins, W., Clark, B., Larson, E., and Poor, H. V. (2000). *Fault Diagnostics Using Statistical Change Detection in the Bispectral Domain*, volume 14.
- [Qu and Shi, 1998] Qu, L. and Shi, D. (1998). *Holospectrum during the past decade: Review & prospect*. Journal of Vibration, Measurement & Diagnosis.
- [Rokach, 2012] Rokach, L. (2012). *Introduction to Machine Learning*. Department of Information Systems Engineering, Ben-Gurion University of the Negev. <https://www.slideshare.net/liorrokach/introduction-to-machine-learning-13809045>.
- [Romax, nd] Romax (n.d.). *Romaxwind software*. <https://romaxtech.com>. Accessed on February 24, 2020.
- [Ronold and Larsen, 1999] Ronold, K. and Larsen, G. (1999). *Variability of Extreme Flap Loads during Turbine Operation*.
- [Schepers, 2007] Schepers, J. (2007). *IEA Annex XX: dynamic inflow effects at fast pitching steps on a wind turbine placed in the NASA-Ames wind tunnel*. ECN.
- [Schmidt and Vath, 2012] Schmidt, S. and Vath, A. (2012). *Comparison of existing medium-speed drive train concepts with a differential gearbox approach*. Euro Wind Energy Association, Copenhagen, Denmark.

- [Selot et al., 2019] Selot, F., Fraile, D., and Brindley, G. (2019). *Offshore Wind in Europe - Key trends and statistics 2018*. WindEurope, Brussels, Belgium.
- [Silva, 2005] Silva, C. W. D. (2005). *Vibration and shock handbook*. CRC Press.
- [Slootweg et al., 2003] Slootweg, J., de Haan, S., Polinder, H., and Kling, W. (2003). *General model for representing variable speed wind turbines in power system dynamics simulations*. IEEE Transactions on Power Systems.
- [Statkraft, 2014] Statkraft (2014). *Wind turbine technicians carrying out maintenance work at Sheringham Shoal offshore wind farm*. Offshore Wind. Retrieved from <https://www.offshorewind.biz/2014/06/06/photo-of-the-day-maintenance-at-sheringham-shoal-offshore-wind-farm/>.
- [Stiltz, 1961] Stiltz, H. (1961). *Aerospace telemetry*. Number v. 1 in Prentice-Hall space technology series. Prentice-Hall.
- [Terrell et al., 2012] Terrell, E. J., Needelman, W. M., and Kyle, J. P. (2012). *Wind Turbine Tribology*. In: Green Tribology: Biomimetics, Energy Conservation and Sustainability. Springer.
- [Torsvik et al., 2018] Torsvik, J., Nejad, A., and Pedersen, E. (2018). *Main bearings in large offshore wind turbines: development trends, design and analysis requirements*. Journal of Physics: Conference Series.
- [Tveiten et al., 2011] Tveiten, C. K., Albrechtsen, E., Heggset, J., Hofmann, M., Jersin, E., and Leira, B. J. (2011). *HSE challenges related to offshore renewable energy A study of HSE issues related to current and future offshore wind power concepts*. SINTEF, Norway.
- [Viré, nd] Viré, A. (n.d.). *Rotor Aerodynamics - Reader*. Delft University of Technology, Delft, The Netherlands.
- [WAFO, 2011] WAFO (2011). *Tutorial for WAFO version 2.5*. Faculty of Engineering - Centre for Mathematical Sciences - Lund University, Lund, Sweden.
- [Wagenaar et al., 2012] Wagenaar, W., Machielse, L., and Schepers, J. (2012). *Controlling wind in ECN's scaled wind farm*. EWEA Annual Event 2012.
- [Wang et al., 2017] Wang, S., Zhu, C., Song, C., Liu, H., Tan, J., and Bai, H. (2017). *Effects of gear modifications on the dynamic characteristics of wind turbine gearbox considering elastic support of the gearbox*. Journal of Mechanical Science and Technology.
- [Wang et al., 2001] Wang, W., Chen, J., Wu, X., and Wu, Z. (2001). *The application of some non-linear methods in rotating machinery fault diagnosis*. Mechanical Systems and Signal Processing.
- [Wang and Lin, 2003] Wang, W. and Lin, R. (2003). *The application of pseudo-phase portrait in machine condition monitoring*. Journal of Sound and Vibration.
- [Wehrmann, 2018] Wehrmann, B. (2018). *Power production at sea re-emerges as Energiewende cornerstone*. Clean Energy Wire, Germany.
- [Wei et al., 2018] Wei, L., Qian, Z., Yang, C., and Pei, Y. (2018). *Wind turbine pitch system condition monitoring based on performance curves in multiple states*. 2018 9th International Renewable Energy Congress (IREC).
- [Wilson and Lissaman, 1974] Wilson, R. and Lissaman, P. (1974). *Applied aerodynamics of wind-power machine*. Oregon State University, USA.

- [Wriggers and Zavarise, 2004] Wriggers, P. and Zavarise, G. (2004). *Computational Contact Mechanics. Encyclopedia of Computational Mechanics*. John Wiley & Sons Ltd, Chichester, UK.
- [Xing and Moan, 2013] Xing, Y. and Moan, T. (2013). *Multibody modelling and analysis of a planet carrier in a wind turbine gearbox*. Department of Marine Technology, NTNU, Trondheim, Norway.
- [Yang et al., 2018a] Yang, C., Qian, Z., Pei, Y., and Wei, L. (2018a). *A Data-Driven Approach for Condition Monitoring of Wind Turbine Pitch Systems*. Machine Design. <https://www.machinedesign.com/mechanical-motion-systems/article/21836463/pitch-control-critical-for-wind-power>.
- [Yang et al., 2002] Yang, D.-M., Stronach, A., MacConnell, P., and Penman, J. (2002). *Third-order spectral techniques for the diagnosis of motor bearing condition using artificial neural networks*. Mechanical systems and signal processing.
- [Yilmaz Balaman, 2019] Yilmaz Balaman, (2019). *Chapter 5 - Uncertainty Issues in Biomass-Based Production Chains*. Academic Press.
- [Young and Squire, 1938] Young, A. and Squire, H. (1938). *R&M No. 1838*.
- [Zutter et al., 2017] Zutter, S. D., Kooning, J. D., Samani, A. E., and Vandeveld, L. (2017). *Modeling of active yaw systems for small and medium wind turbines*. Ghent University (Belgium), Electrical Energy Laboratory (EELAB), Ghent, Belgium.

A | Model Specifications

In this chapter, one can find the specifications of the models used during this research project. For the global response analysis, the DTU 10 MW Reference Wind Turbine, of which its characteristics are listed in Section A.1, and a spar (find its specifications in A.2) are used. Then, for the local response analysis Wang's 10 MW drive train model is deployed. In Section A.3, one can find the drive train's characteristics.

A.1 DTU 10 MW Reference Wind Turbine Specifications

The Danmarks Tekniske Universitet (DTU) 10 MW wind turbine [Bak et al., 2013] was designed by upscaling the National Renewable Energy Laboratory (NREL) 5 MW wind turbine [Jonkman et al., 2009]. The three-bladed, clockwise rotating, variable speed 10 MW offshore wind turbine is designed for a International Electrotechnical Commission (IEC) class 1A wind climate. The wind turbine is equipped with a variable-speed collective pitch power control system [Bak et al., 2013, Wang et al., 2019]. In Table A.1 the properties of the DTU 10 MW are listed.

Parameter	Value
Wind Regime	IEC Class 1A
Cut-in wind speed [m/s]	4
Cut-out wind speed [m/s]	25
Rated wind speed [m/s]	11.4
Rated power [MW]	10
Number of blades [-]	3
Rotor diameter [m]	178.3
Hub diameter [m]	5.6
Hub height [m]	119.0
Drive train	Medium speed, multiple-stage gearbox
Minimum rotor speed [rpm]	6.0
Maximum rotor speed [rpm]	9.6
Maximum generator speed [rpm]	480.0
Gearbox ratio [-]	50
First tower bending natural frequency [Hz]	0.25
Maximum tip speed [m/s]	90.0
Hub overhang [m]	7.1
Shaft tilt angle [°]	5.0
Rotor precone angle [°]	-2.5
Blade prebend [m]	3.332
Rotor mass [kg]	227962
Nacelle mass [kg]	446036
Tower mass [kg]	628442

Table A.1: DTU 10 MW reference wind turbine properties [Castro, 2017, Bak et al., 2013, Bak, 2015]

The drive train of the wind turbine is simplified for the global analysis to a torsional model with a single DOF [Bak et al., 2013, Wang et al., 2019]. Its properties are listed in Table A.2.

Table A.2: Properties of DTU 10 MW wind turbine's drive train [Bak et al., 2013]

Parameter	Value
Rated rotor speed [rpm]	9.6
Rated generator speed [rpm]	480
Gearbox ratio [-]	50:1
Electrical generator efficiency [%]	94
Generator inertia about high-speed shaft [kg m²]	1500.5
Equivalent drive-shaft torsional-spring constant [Nm/rad]	2317025352
Equivalent drive-shaft torsional-damping constant [Nm/(rad/s)]	9240560
Fully-deployed high-speed shaft brake torque [Nm]	28116.2
High speed shaft brake time constant [s]	0.6

A.2 Spar Specifications

The spar designed by Hegseth and Bachynski [Hegseth and Bachynski, 2019] is used to obtain the global response. Its specifications are shown in Table A.3.

Parameter	Value
Draft [m]	90.0
Elevation to tower base above SWL [m]	10.0
Depth to top of taper below SWL [m]	4.0
Depth to bottom of taper below SWL [m]	12.0
Diameter above taper [m]	8.3
Diameter below taper [m]	15.0
Mass including ballast [kg]	$1.33 \cdot 10^7$
Displacement [m³]	$1.49 \cdot 10^4$
Moment of inertia about COG [kg m²]	$3.42 \cdot 10^9$
Vertical COG below SWL [m]	72.3
Vertical COB below SWL [m]	47.8

Table A.3: Spar's platform properties. COG = Center of gravity, COB = Center of buoyancy and SWL = Still water level [Hegseth and Bachynski, 2019]

The mooring line characteristics can be found in Table A.4

Parameter	Value
Radius to anchors [m]	855.2
Unstretched mooring line length [m]	902.2
Equivalent mooring line mass density [kg/m]	155.4
Equivalent mooring line axial stiffness [MN]	$3.84 \cdot 10^8$
Fairlead depth below SWL [m]	56.3
Yaw spring stiffness [Nm/rad]	$1.48 \cdot 10^8$

Table A.4: Spar's mooring system properties. SWL = Still water level [Hegseth and Bachynski, 2019]

A.3 Drive Train Specifications

Wang's 10 MW drive train model [Wang et al., 2019] is used for the local response analysis. The monitoring data from this model is used to produce the results of this research work. Therefore, it is crucial to know how the model looks like and which properties it has. To start off, in Figure A.1 one can find the topological diagram of the drive train model.

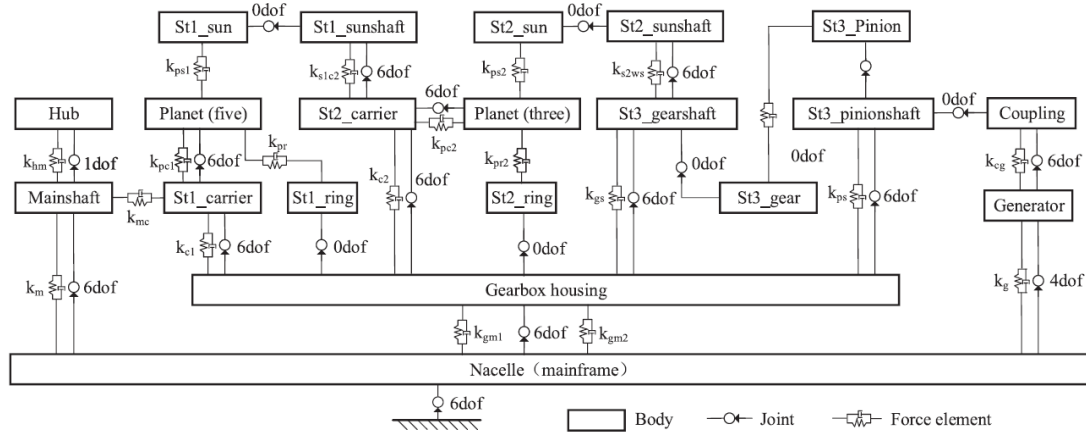


Figure A.1: Topological diagram of the 10 MW wind turbine drive train model [Wang et al., 2019]

The drive train specifications are depicted in Table A.5.

Table A.5: Specifications of 10 MW wind turbine drive train model [Wang et al., 2019]

Parameter	Value
Drive train type	Four-point support
Gearbox type	Two planetary + one parallel
First stage ratio [-]	4.423
Second stage ratio [-]	5.192
Third stage ratio [-]	2.179
Total ratio	50.039
Designed power [MW]	10
Rated input shaft speed [rpm]	9.6
Rated generator shaft speed [rpm]	480.4
Rated input shaft torque [KNm]	9947.9
Rated generator shaft torque [KNm]	198.8
Drive train dry mass [tonnes]	141.54
Gearbox dry mass [tonnes]	60.43
Gearbox maximum outer diameter [m]	3.098
Designed service life [yrs]	20

The shafts' material properties are listed in Table A.6.

Table A.6: Main components' material properties [Wang et al., 2019]

Component	Material	Density ρ [kg/m ³]	Young's Modulus E [GPa]	Poisson's ratio ν [-]
Hub	QT400	7010	161	0.274
Planet carrier	QT700	7090	169	0.305
Planet/Sun gears	18CrNiMo7-6	7800	207	0.300
Ring gears	42CrMo4	7800	207	0.300
Shafts	18CrNiMo7-6	7800	207	0.300

The geometry of the gears in three stages are displayed in Table A.7.

Table A.7: Gear geometrical specifications [Wang et al., 2019]

Parameter	First stage	Second stage	Third stage
Type	Planetary	Planetary	Parallel
Ratio [-]	1:4.423	1:5.192	1:2.179
Number of planets [-]	5	3	–
Normal module [mm]	30	20	18
Normal pressure angle [°]	20	20	20
Helix angle [°]	8	8	12
Face width [mm]	800	520	500
Center distance [mm]	877.033	684.273	825.885
Sun/Pinion number of teeth [-]	26	26	28
Planet/Gear number of teeth [-]	31	41	61
Ring gear number of teeth [-]	89	109	–
Sun/Pinion profile shift coefficient [-]	0.2702	0.2787	0.2976
Planet/Gear profile shift coefficient [-]	0.2093	0.1213	0.1024
Ring gear profile shift coefficient [-]	–0.1591	–0.0024	–
Sun/Pinion pitch diameter [mm]	787.666	525.110	515.260
Planet/Gear pitch diameter [mm]	939.140	828.059	1122.530
Ring gear pitch diameter [mm]	2696.240	2201.424	–
Sun/Pinion tip diameter [mm]	863.878	576.258	561.973
Planet/Gear tip diameter [mm]	1011.698	872.911	1162.216
Ring gear tip diameter [mm]	2645.786	2161.52	–
Sun/Pinion root diameter [mm]	719.878	480.258	475.573
Planet/Gear root diameter [mm]	867.689	776.911	1075.816
Ring gear root diameter [mm]	2780.786	2251.520	–

The bearing designs can be found in Table A.8.

Table A.8: Bearings designation and geometrical specifications. TRB = Tapered roller bearing and CRB = Cylindrical roller bearing [Wang et al., 2019]

Name	Type	Designation	Provider	Outer diameter [mm]	Inner diameter [mm]	Bearing thickness [mm]
INP-A	TRB	2TR1450	Koyo	1770	1450	145
INP-B	TRB	2TR950B	Koyo	1250	950	136
PLC-A	TRB	LL889049/ LL889010D	Koyo	1435	1270	146
PLC-B	CRB	NNU49/ 1120-S-M-C3	FAG	1460	1120	335
PL-A,B,C,D	TRB	45T806520D	Koyo	650	400	200
IMS-PLC-A	TRB	2TR950B	Koyo	1250	950	136
IMS-PLC-B	TRB	452/900	Koyo	1280	900	140
IMS-PL-A,B	TRB	45368	Koyo	580	340	190
IMS-A	TRB	2TR600J	Koyo	870	600	134.5
IMS-B	TRB	452/500	Koyo	720	500	83.5
HS-A	CRB	NNCF4980BV	SKF	540	400	140
HS-B	TRB	45T605729	Koyo	570	300	290

The bearings are modelled as a set of springs, their stiffness is depicted in Table A.9.

Table A.9: Dynamic model parameters of bearings [Wang et al., 2019]

Name	K_x [GN/m]	K_y [GN/m]	K_z [GN/m]	K_β [MNm/rad]	K_γ [MNm/rad]
INP-A	4.1442	10.231	14.984	1450.6	989.37
INP-B	4.0095	6.8461	9.9126	669.1	669.1
PLC-A	7.7772	22.339	31.137	2642	1894.6
PLC-B	0	13.445	20.185	146.78	96.695
PL-A,B,C,D	6.2541	8.0297	10.761	101.16	74.871
IMS-PLC-A	2.1546	0.92936	8.0765	526.67	59.859
IMS-PLC-B	3.1836	23.904	23.694	418.21	422.83
IMS-PL-A,B	0.76453	7.3226	9.6458	2.7065	1.5687
IMS-A	0.95783	6.3441	9.1733	59.894	41.182
IMS-B	1.5269	11.778	11.051	60.533	64.727
HS-A	0	2.5422	11.793	163.31	33.156
HS-B	1.3427	8.6946	10.694	166.77	130.47

B | Natural Frequencies of Shafts & Non-Rotating Bearings

In this appendix, one can find the spectra and the lists with their peaks, created for the determination of the natural frequencies of the shafts and the non-rotating bearings. One can find the natural frequencies of the shafts in Section B.1. The natural frequencies of the non-rotating bearings are depicted in Section B.2. The natural frequencies are obtained by finding the peaks in the velocity spectra. The frequencies indicated in red are most likely gear mesh frequencies, harmonics and sidebands. The natural frequencies in the y - and z -direction can not always be found, since the natural frequencies are usually higher than 1885 rad/s due to the high bearing stiffness in these directions.

B.1 Shafts Natural Frequencies

The spectra for the main, low speed, intermediate speed and high speed shafts' translational accelerations are created and presented in Figures B.1 to B.4. The spectra do not show the frequency interval 0-20 rad/s, since in approximately this frequency range the excitation frequencies are located.

In some figures, one can see next to the peaks, a noisy signal. For determination of the natural frequency, an impulse test is preferred. However, this data was not available. The noisy signal is caused by the multi-frequency excitation by the wind and waves.

In Figure B.1 one can find the spectra of the main shaft's acceleration in x -, y - and z -direction. The corresponding natural frequencies can be found in Table B.1.

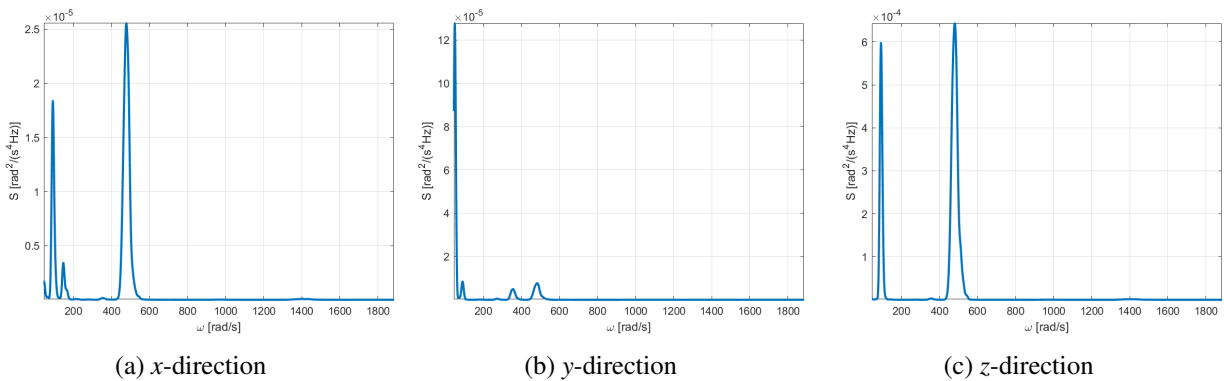


Figure B.1: Spectra of main shaft's acceleration

Table B.1: Main shaft natural frequencies

		1	2	3	4
x	ω [rad/s]	46	92	147	480
	f [Hz]	7.32	14.64	23.40	76.39
	ω [rpm]	439.3	878.5	1404	4583
y	ω [rad/s]	50	92	480	
	f [Hz]	7.958	14.64	76.39	
	ω [rpm]	477.5	878.5	4583	
z	ω [rad/s]	92	480		
	f [Hz]	14.64	76.39		
	ω [rpm]	878.5	4583		

One can see the spectra of the acceleration of the low speed shaft in three directions in Figure B.2. In every spectrum, only one peak is observable. This is around the second mesh frequency and thus the natural frequency of the shaft can not be determined as is shown in Table B.2.

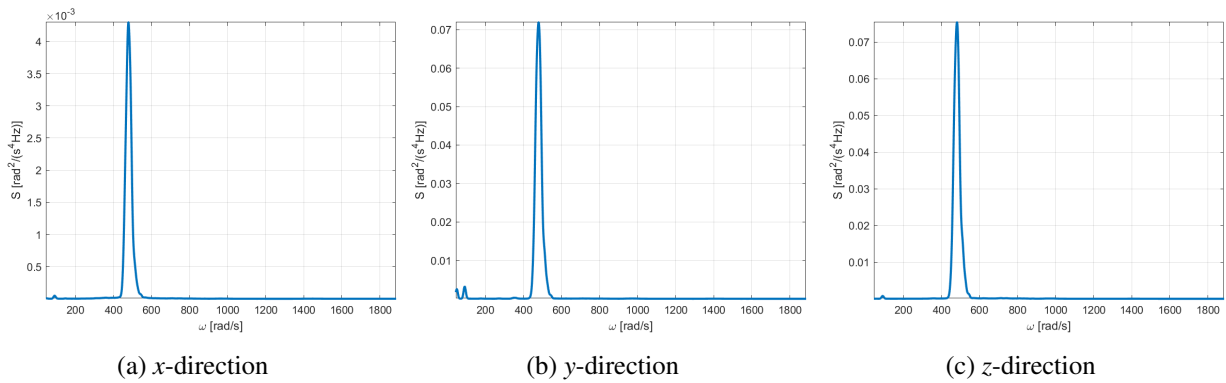


Figure B.2: Spectra of low speed shaft's acceleration

Table B.2: Low speed shaft natural frequencies

		1
x	ω [rad/s]	480
	f [Hz]	76.39
	ω [rpm]	4584
y	ω [rad/s]	480
	f [Hz]	76.39
	ω [rpm]	4584
z	ω [rad/s]	480
	f [Hz]	76.39
	ω [rpm]	4584

The spectra, representing acceleration of the intermediate speed shaft in the x-, y- and z-direction, are shown in Figure B.3. The natural frequencies are shown in Table B.3.

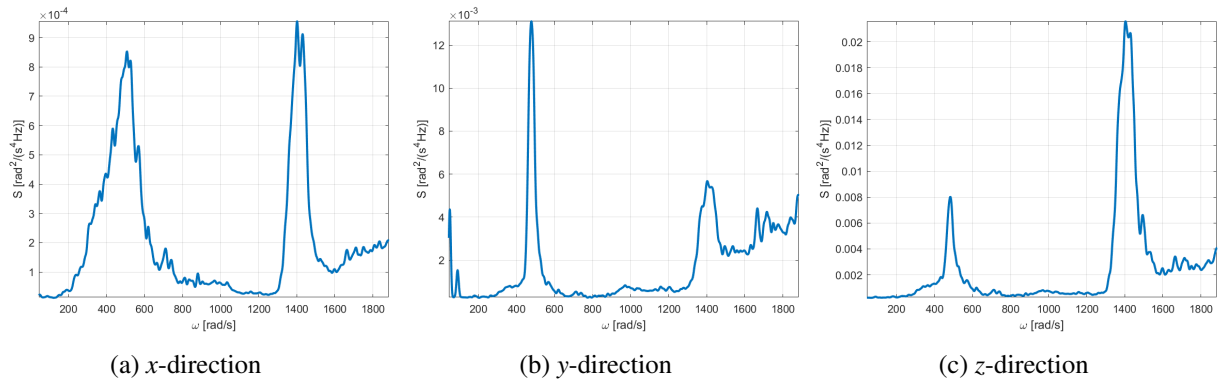


Figure B.3: Spectra of intermediate speed shaft's acceleration

Table B.3: Intermediate speed shaft natural frequencies

		1	2	3	4
x	ω [rad/s]	508	1402		
	f [Hz]	80.85	223.1		
	ω [rpm]	4581	$1.339 \cdot 10^4$		
y	ω [rad/s]	50	91	480	1403
	f [Hz]	7.958	14.48	76.39	223.3
	ω [rpm]	477.5	869.0	4584	$1.340 \cdot 10^4$
z	ω [rad/s]	483	1404		
	f [Hz]	76.87	223.5		
	ω [rpm]	4612	$1.341 \cdot 10^4$		

Finally, the high speed shaft acceleration spectra are depicted in Figure B.4, the peak locations are displayed in Table B.4.

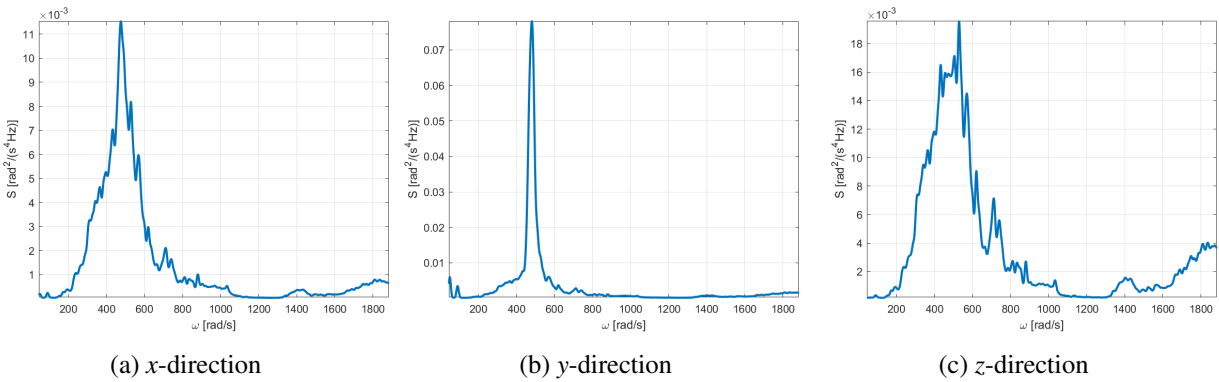


Figure B.4: Spectra of high speed shaft's acceleration

Table B.4: High speed shaft natural frequencies

		1	2	3
x	ω [rad/s]	476	1809	
	f [Hz]	75.76	287.9	
	ω [rpm]	4545	$1.727 \cdot 10^4$	
y	ω [rad/s]	50	481	1403
	f [Hz]	7.958	76.55	223.3
	ω [rpm]	477.5	4593	$1.340 \cdot 10^4$
z	ω [rad/s]	529	1404	1835
	f [Hz]	84.19	223.5	292.0
	ω [rpm]	5051	$1.341 \cdot 10^4$	$1.752 \cdot 10^4$

B.2 Non-Rotating Bearings Natural Frequencies

The natural frequencies of the non-rotating bearings are found in the following. Starting with the main shaft front bearing (INP-A), its velocity spectra are depicted in Figure B.5 and its natural frequencies are listed in Table B.5.

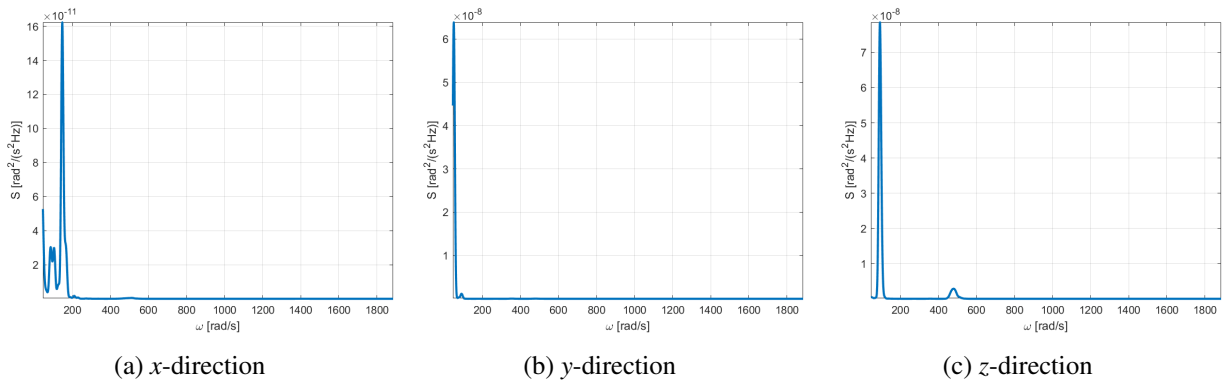


Figure B.5: Spectra of main shaft front bearing's velocity

Table B.5: Main shaft front bearing natural frequencies

		1	2	3	4	5
x	ω [rad/s]	20	41	86	104	147
	f [Hz]	3.183	6.525	13.69	16.55	23.40
	ω [rpm]	191.0	391.5	821.2	993.1	1404
y	ω [rad/s]	21	50			
	f [Hz]	3.342	7.958			
	ω [rpm]	200.5	477.5			
z	ω [rad/s]	93				
	f [Hz]	14.80				
	ω [rpm]	888.1				

The main shaft rear bearing's (INP-B) velocity spectra are depicted in Figure B.6, its corresponding natural frequencies are presented in Figure B.6.

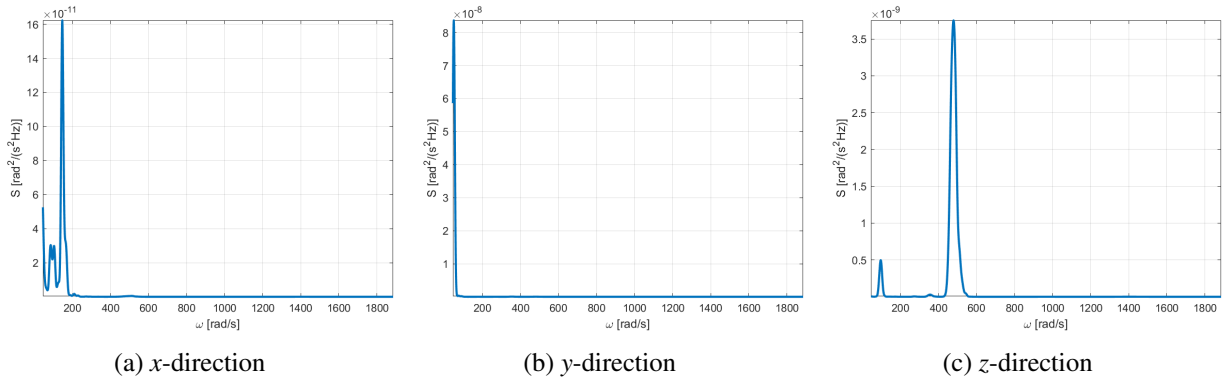


Figure B.6: Spectra of main shaft rear bearing's velocity

Table B.6: Main shaft rear bearing natural frequencies

		1	2	3	4	5
x	ω [rad/s]	20	41	86	104	147
	f [Hz]	3.183	6.525	13.69	16.55	23.40
	ω [rpm]	191.0	391.5	821.2	993.1	1404
y	ω [rad/s]	23	50			
	f [Hz]	3.661	7.958			
	ω [rpm]	219.6	477.5			
z	ω [rad/s]	23	96	480		
	f [Hz]	3.661	15.28	76.39		
	ω [rpm]	219.6	916.7	4584		

The velocity spectra of PLC-A are depicted in Figure B.7. The peaks of the spectra are located on the frequencies shown in Table B.7.

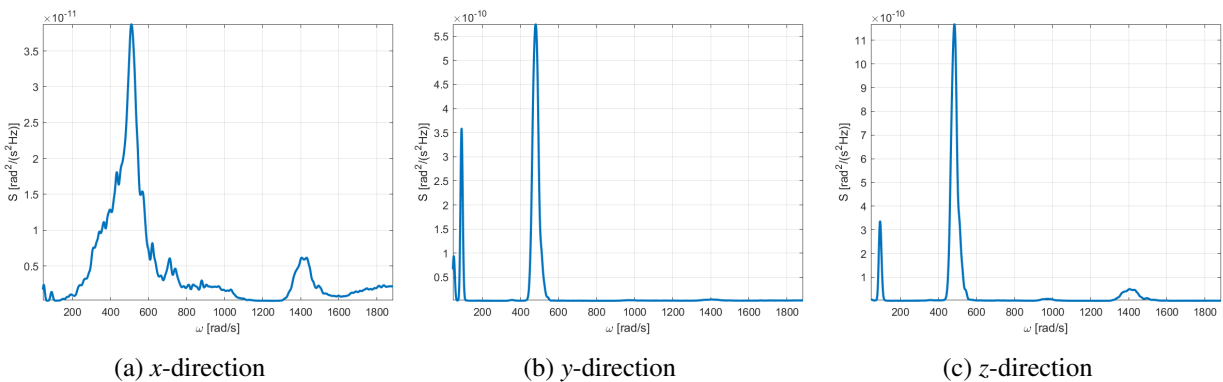


Figure B.7: Spectra of the low speed shaft planet carrier front bearing's velocity

Table B.7: Low speed shaft planet carrier front bearing natural frequencies

		1	2	3	4	5
x	ω [rad/s]	23	50	510	711	1430
	f [Hz]	3.661	7.958	81.17	113.2	227.6
	ω [rpm]	219.6	477.5	4870	6790	$1.366 \cdot 10^4$
y	ω [rad/s]	50	91	480		
	f [Hz]	7.958	14.48	76.39		
	ω [rpm]	477.5	869.0	4584		
z	ω [rad/s]	23	94	484		
	f [Hz]	3.661	14.96	77.03		
	ω [rpm]	219.6	897.6	4622		

In Figure B.8 one can find the velocity spectra of PLC-B. The corresponding natural frequencies are depicted in Table B.8.

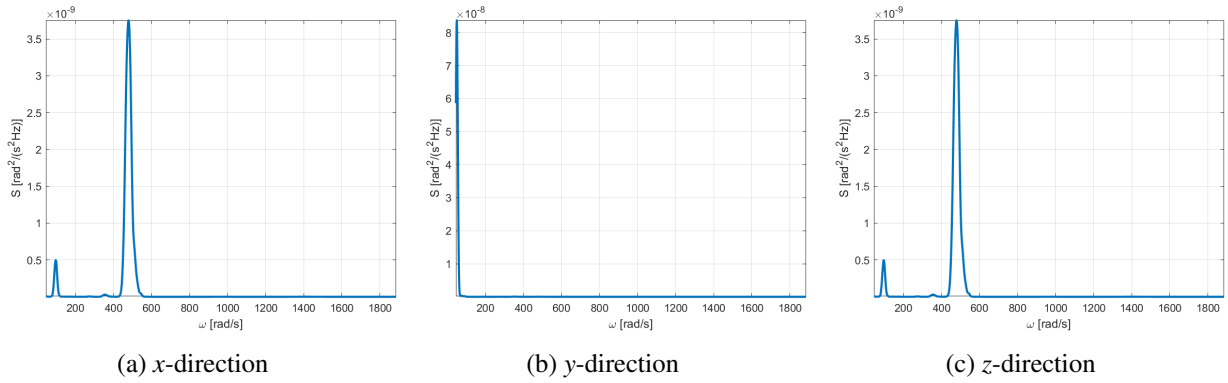


Figure B.8: Spectra of the low speed shaft planet carrier rear bearing's velocity

Table B.8: Low speed shaft planet carrier rear bearing natural frequencies

		1	2	3	4
x	ω [rad/s]	23	50	510	711
	f [Hz]	3.661	7.958	81.17	113.2
	ω [rpm]	219.6	477.5	4870	6790
y	ω [rad/s]	50	91	479	
	f [Hz]	7.958	14.48	76.24	
	ω [rpm]	477.5	869.0	4574	
z	ω [rad/s]	92			
	f [Hz]	14.64			
	ω [rpm]	878.5			

Figure B.9 shows the velocity spectra in the x -, y and z -direction of IMS-PLC-A. Table B.9 lists its natural frequencies.

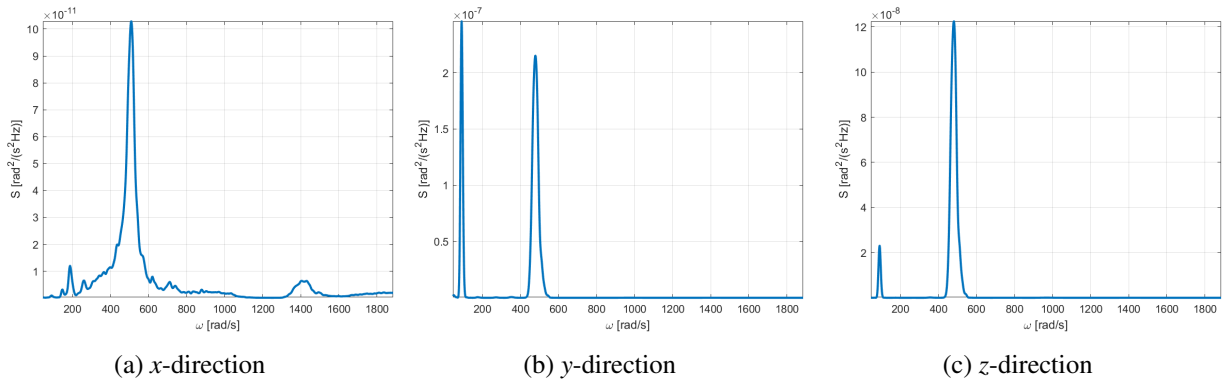


Figure B.9: Spectra of the intermediate speed shaft planet carrier front bearing's velocity

Table B.9: Intermediate speed shaft planet carrier front bearing natural frequencies

		1	2	3
x	ω [rad/s]	188	509	1405
	f [Hz]	29.92	81.01	223.5
	ω [rpm]	1795	4861	$1.342 \cdot 10^4$
y	ω [rad/s]	91	479	
	f [Hz]	14.48	76.24	
	ω [rpm]	869.0	4574	
z	ω [rad/s]	91	481	
	f [Hz]	14.48	76.55	
	ω [rpm]	869.0	4593	

Then, the velocity spectra of IMS-PLC-B are shown in Figure B.10. One can find the corresponding natural frequencies in Table B.10.

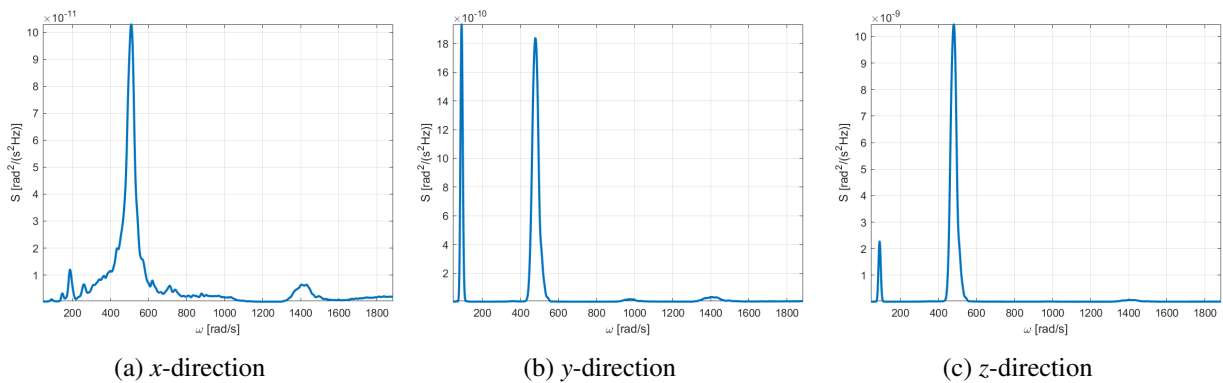


Figure B.10: Spectra of the intermediate speed shaft rear bearing's velocity

Table B.10: Intermediate speed shaft rear bearing natural frequencies

		1	2	3
x	ω [rad/s]	188	509	1405
	f [Hz]	29.92	81.01	223.5
	ω [rpm]	1795	4861	$1.342 \cdot 10^4$
y	ω [rad/s]	91	479	
	f [Hz]	14.48	76.24	
	ω [rpm]	869.0	4574	
z	ω [rad/s]	91	480	
	f [Hz]	14.48	76.39	
	ω [rpm]	869.0	4584	

HS-A's velocity spectra and natural frequencies in x -, y - and z -directions are depicted in Figure B.11 and Table B.11, respectively.

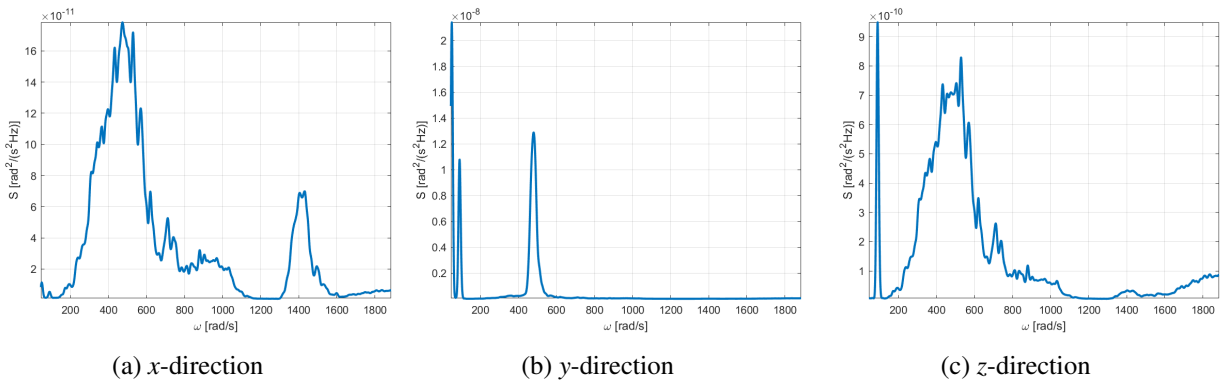


Figure B.11: Spectra of the high speed shaft front bearing's velocity

Table B.11: High speed shaft front bearing natural frequencies

		1	2	3	4
x	ω [rad/s]	50	474	711	1430
	f [Hz]	7.958	75.44	113.2	227.6
	ω [rpm]	477.5	4526	6790	$1.366 \cdot 10^4$
y	ω [rad/s]	23	50	91	480
	f [Hz]	3.661	7.958	14.48	76.39
	ω [rpm]	219.6	477	869.0	4583
z	ω [rad/s]	91	529	711	
	f [Hz]	14.48	84.19	113.1	
	ω [rpm]	869.0	5052	6790	

Concluding with the velocity spectra and natural frequencies of HS-B in Figure B.12 and Table B.12.

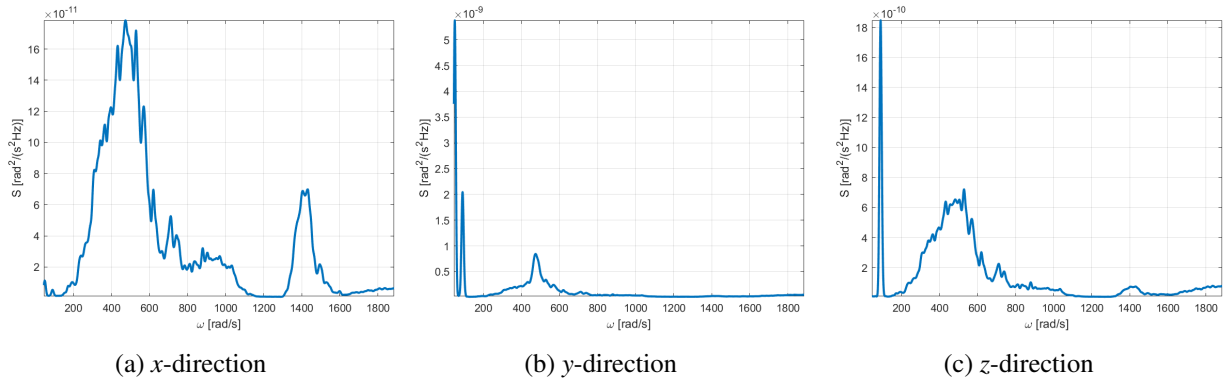


Figure B.12: Spectra of the high speed shaft rear bearing's velocity

Table B.12: High speed shaft rear bearing natural frequencies

	1	2	3	4	
x	ω [rad/s]	50	474	711	1430
	f [Hz]	7.958	75.44	113.2	227.6
	ω [rpm]	477.5	4526	6790	$1.366 \cdot 10^4$
y	ω [rad/s]	23	50	91	474
	f [Hz]	3.661	7.958	14.48	75.44
	ω [rpm]	219.6	477	869.0	4526
z	ω [rad/s]	23	91	529	711
	f [Hz]	3.661	14.48	84.19	113.1
	ω [rpm]	219.6	869.0	5052	6790

C | Angular Velocity Error Energy Method Figures

For the Angular Velocity Error Energy Method, error functions e and e_{tot} are defined as in Table 3.8. The complete time series and spectra are presented in Sections C.1 and C.2, respectively.

C.1 Angular Velocity Error Function Time Series

The time series of the error functions for MBR, MBX and HSBR damage are depicted in Sections C.1.1, C.1.2 and C.1.3, respectively.

C.1.1 MBR

The times series of the error functions e_{MBR} and $e_{tot_{MBR}}$ are shown in Figure C.1.

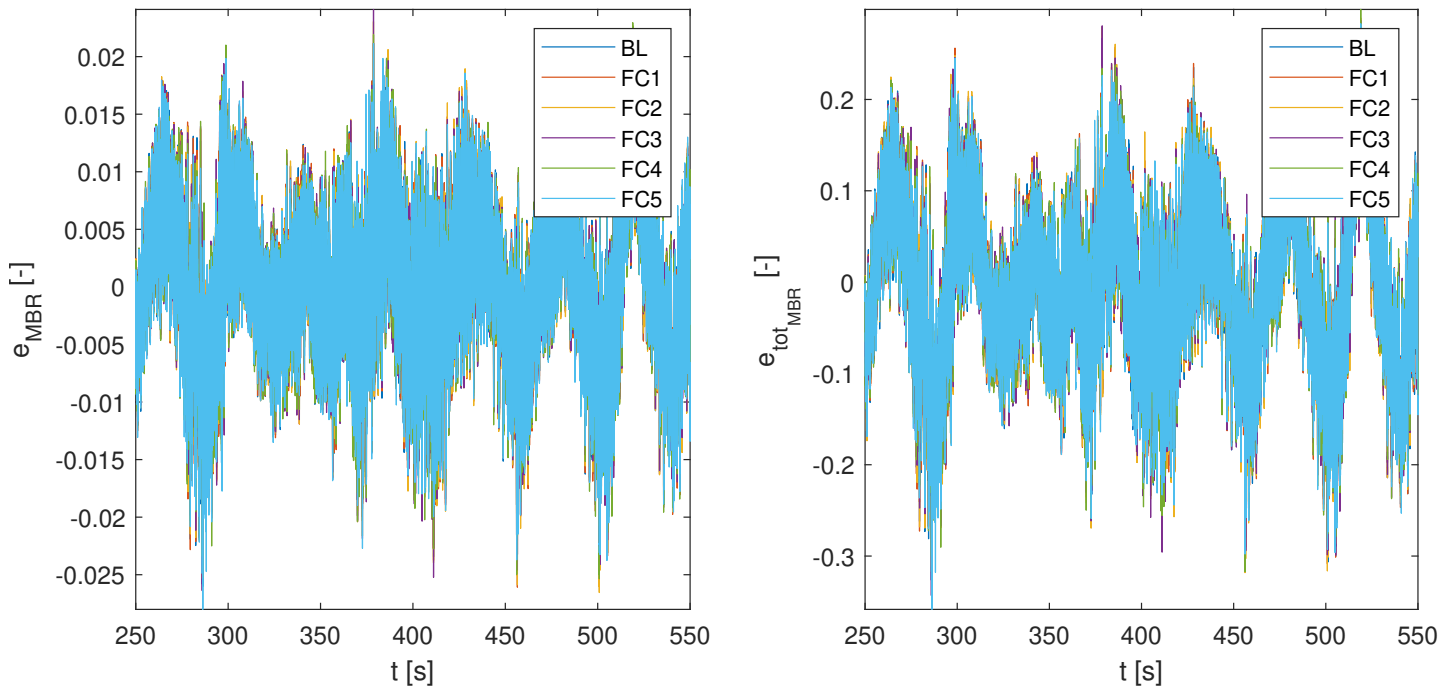


Figure C.1: Angular velocity error functions e_{MBR} (left) and $e_{tot_{MBR}}$ (right)

C.1.2 MBX

In Figure C.2, one can see the time series of e_{MBX} and $e_{tot_{MBX}}$.

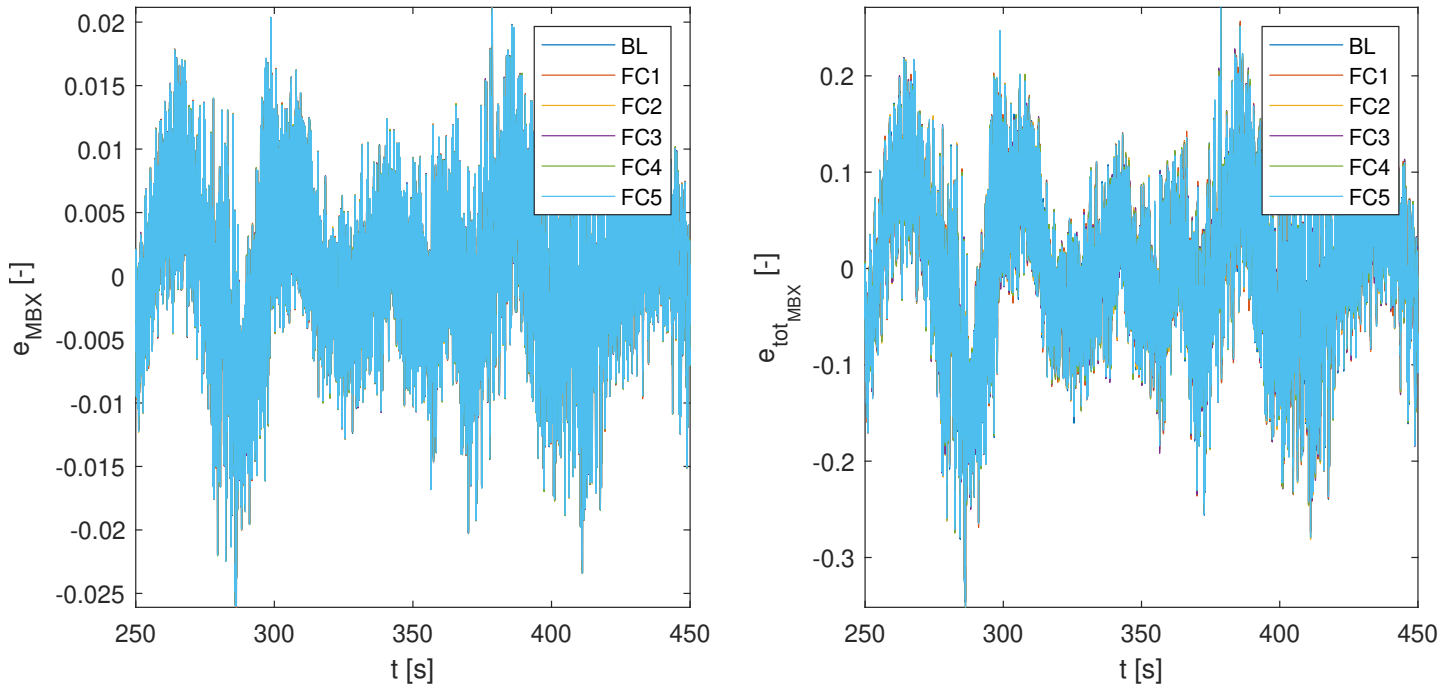


Figure C.2: Angular velocity error functions e_{MBX} (left) and $e_{tot_{MBX}}$ (right)

C.1.3 HSBR

Figure C.3 shows the time series of error functions e_{HSBR} and $e_{tot_{HSBR}}$.

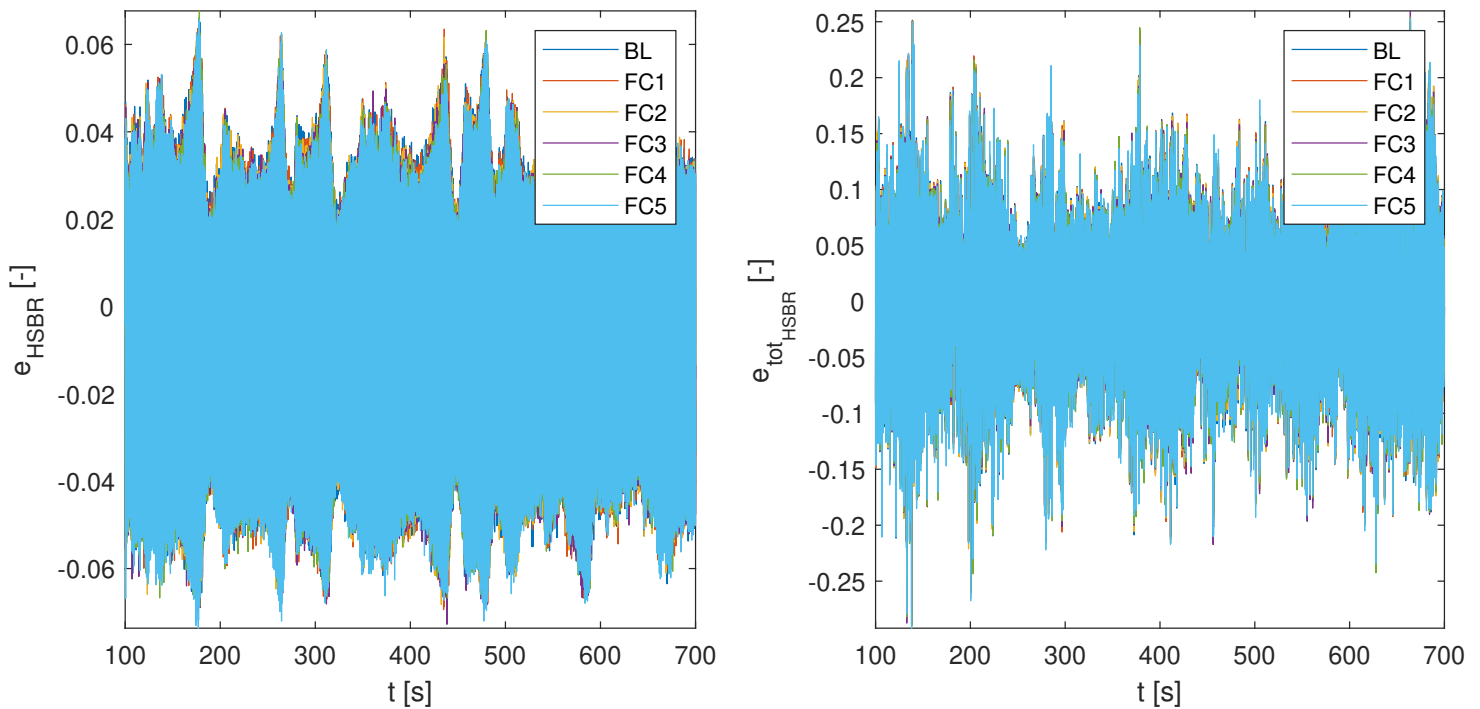


Figure C.3: Angular velocity error functions e_{HSBR} (left) and $e_{tot_{HSBR}}$ (right)

C.2 Angular Velocity Error Function Spectra

The angular velocity error spectra, created from the time series of Section C.1, are depicted in the following sections.

C.2.1 MBR

In Figure C.4, one can see the spectra of e_{MBR} and $e_{tot_{MBR}}$.

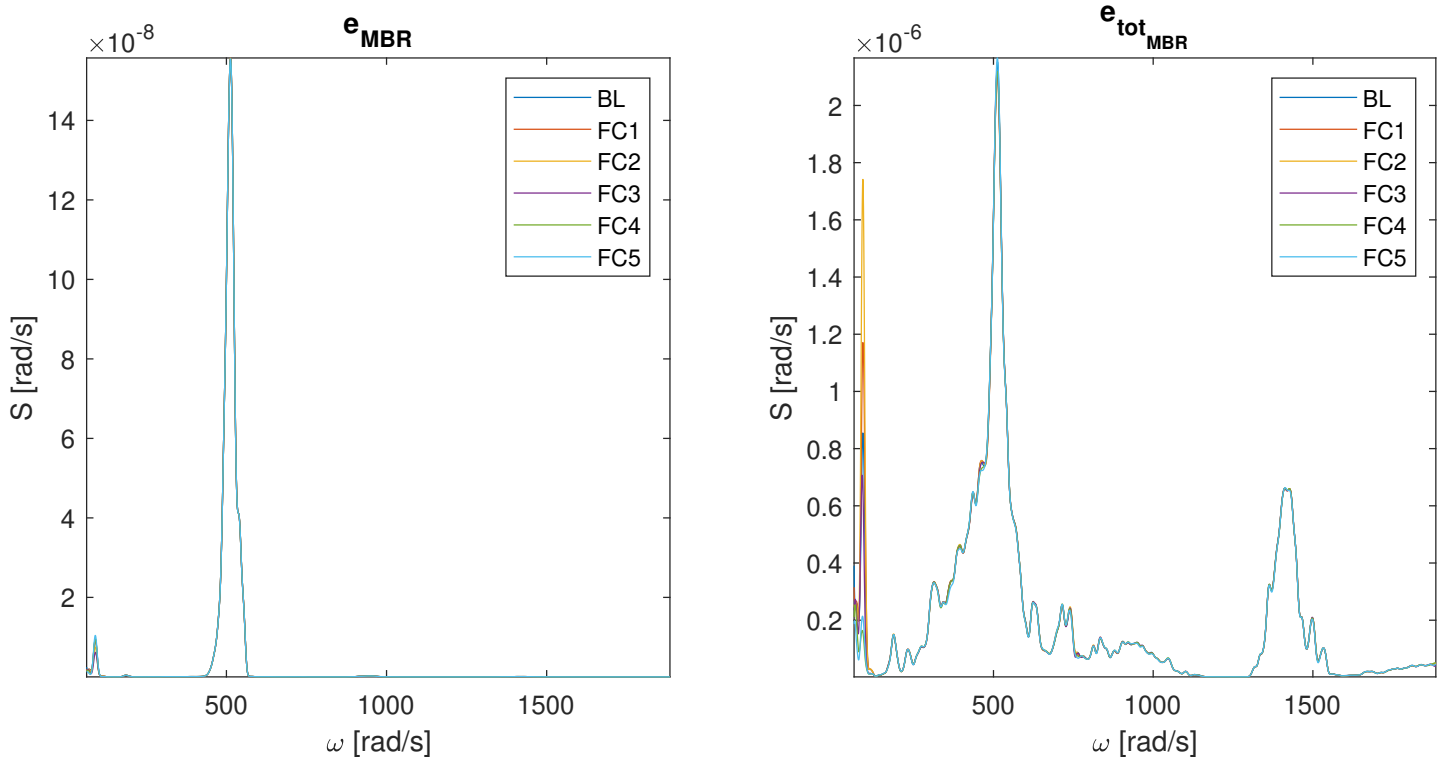


Figure C.4: Angular velocity error spectra e_{MBR} (left) and $e_{tot_{MBR}}$ (right)

C.2.2 MBX

Figure C.5 shows the spectra of e_{MBX} and $e_{tot_{MBX}}$. One can see (almost) no difference between the baseline and fault cases.

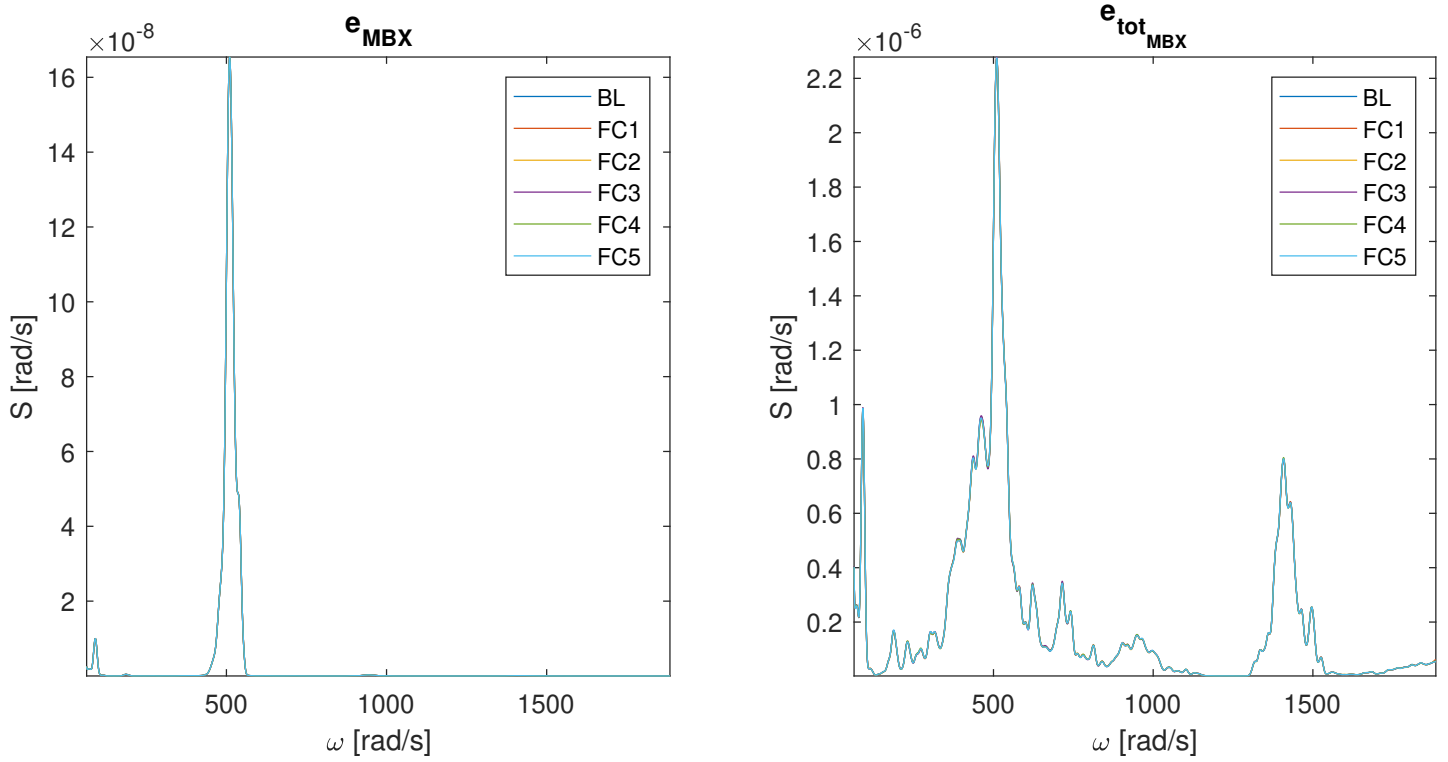


Figure C.5: Angular velocity error spectra e_{MBX} (left) and $e_{tot_{MBX}}$ (right)

C.2.3 HSBR

The spectra of e_{HSBR} and $e_{tot_{HSBR}}$ are depicted in Figure C.6.

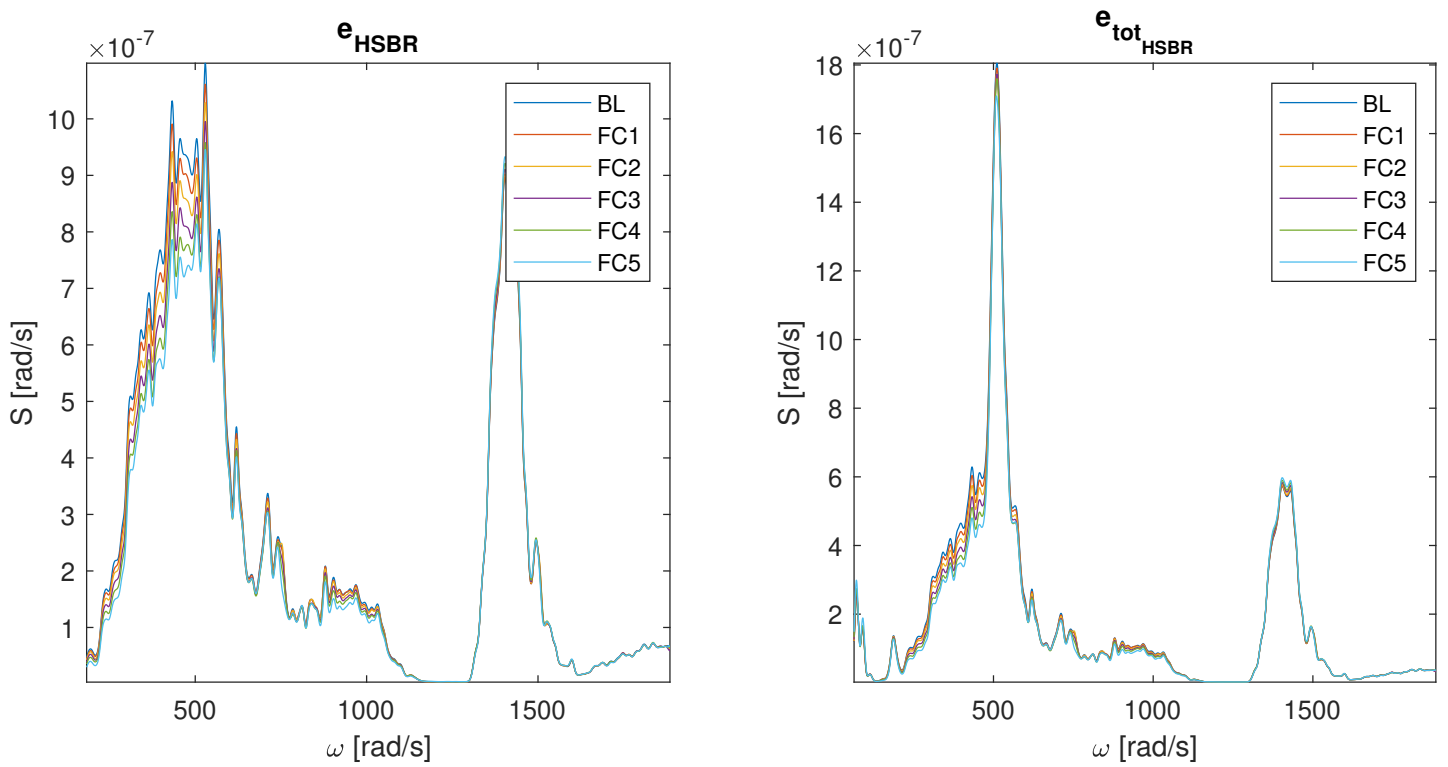


Figure C.6: Angular velocity error spectra e_{HSBR} (left) and $e_{tot_{HSBR}}$ (right)

D | Bearing Velocity Energy Method Figures

The Bearing Velocity Energy Method produced bearing velocity time series and spectra. These can be found in Sections D.1 and D.2, respectively. After analysis of bearing velocity time series and spectra with MBX damage, no change was observed. Therefore, these time series and spectra are not presented in the following.

D.1 Bearing Velocity Time Series

The bearing velocity of relevant time series are displayed in Sections D.1.1 and D.1.2 of MBR and HSBR damage, respectively.

D.1.1 MBR

In Figures D.1 and D.2, one can see the velocity of main shaft front and rear bearing (INP-A and INP-B) after applied MBR damage, respectively.

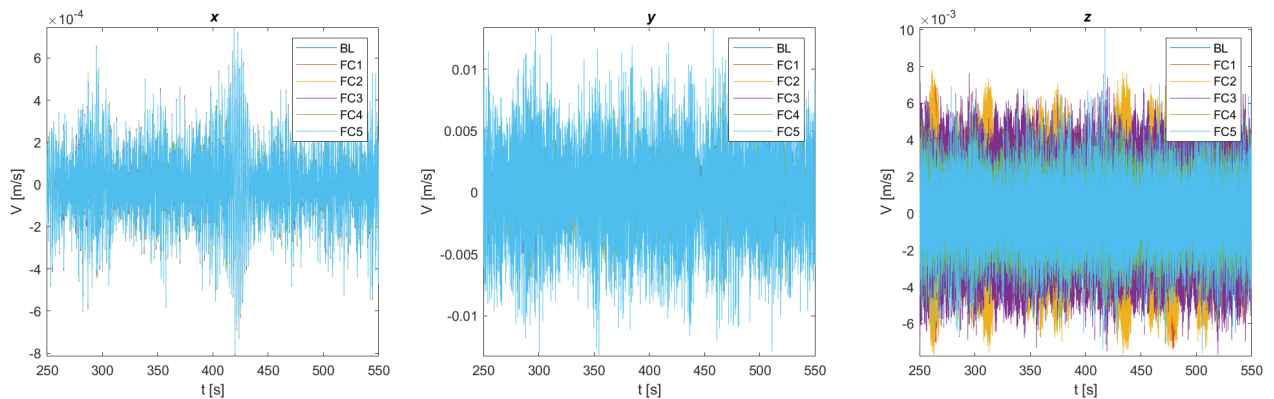


Figure D.1: Main shaft front bearing (INP-A) velocity with MBR damage time series x -direction (left), y -direction (center) and z -direction (right)

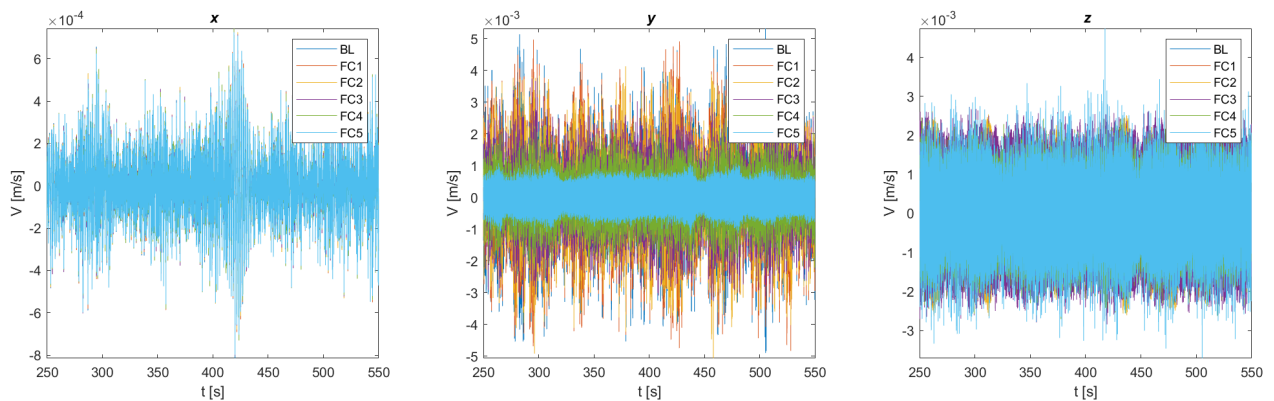


Figure D.2: Main shaft rear bearing (INP-B) velocity with MBR damage time series x -direction (left), y -direction (center) and z -direction (right)

The vibration velocity of the low speed shaft front and rear bearing (PLC-A) and (PLC-B) after introduction of MBR damage is shown in Figures D.3 and D.4, respectively.

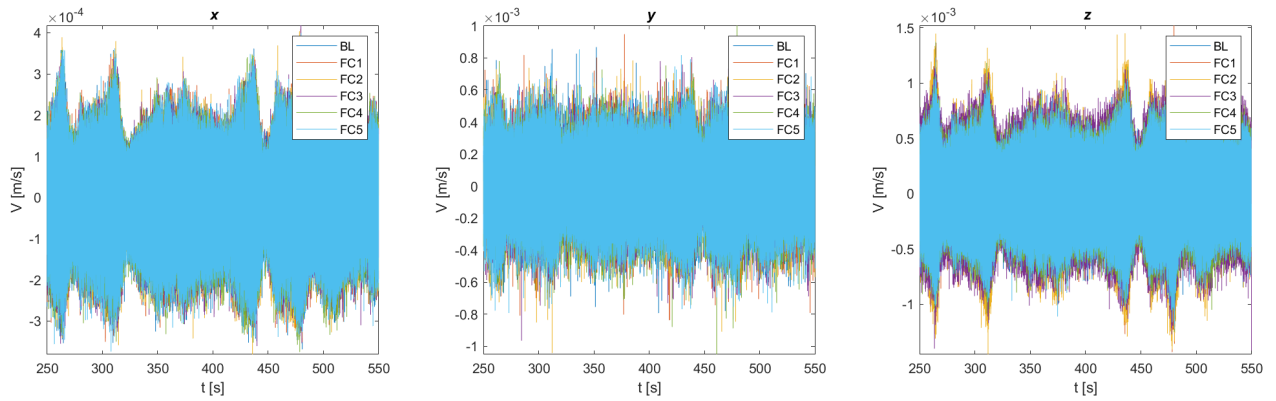


Figure D.3: Low speed front bearing (PLC-A) velocity with MBR damage time series x -direction (left), y -direction (center) and z -direction (right)

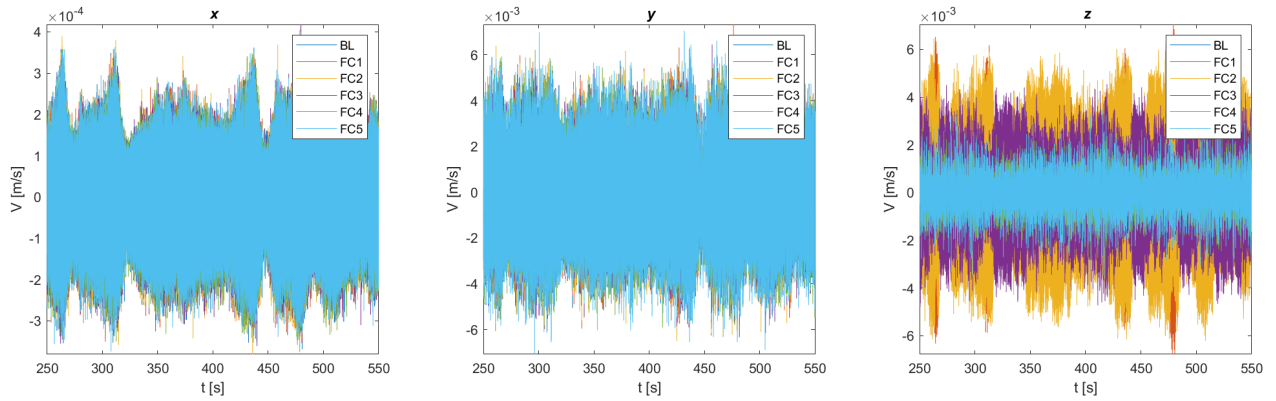


Figure D.4: Low speed rear bearing (PLC-B) velocity with MBR damage time series x -direction (left), y -direction (center) and z -direction (right)

One can see the vibration velocity of IMS-A in Figure D.5.

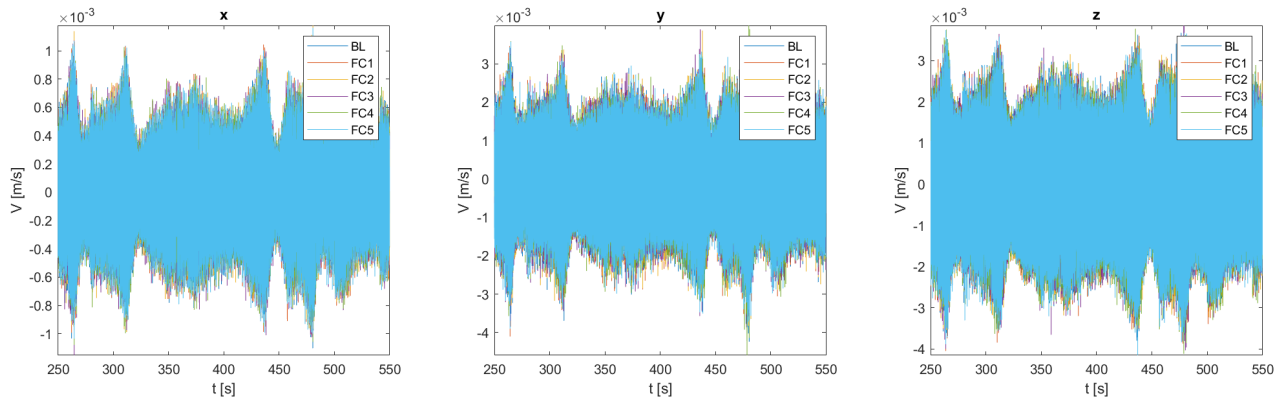


Figure D.5: Intermediate speed front bearing (IMS-A) velocity MBR x -direction (left), y -direction (center) and z -direction (right)

Finally, the vibration velocity of HS-A and HS-B is depicted in Figures D.6 and D.7.

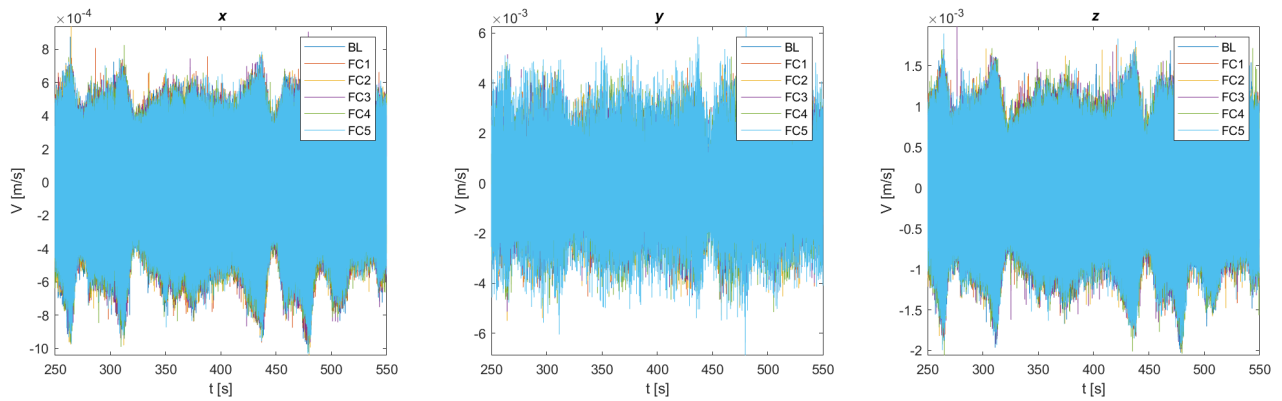


Figure D.6: High speed shaft front bearing (HS-A) velocity with MBR damage time series x -direction (left), y -direction (center) and z -direction (right)

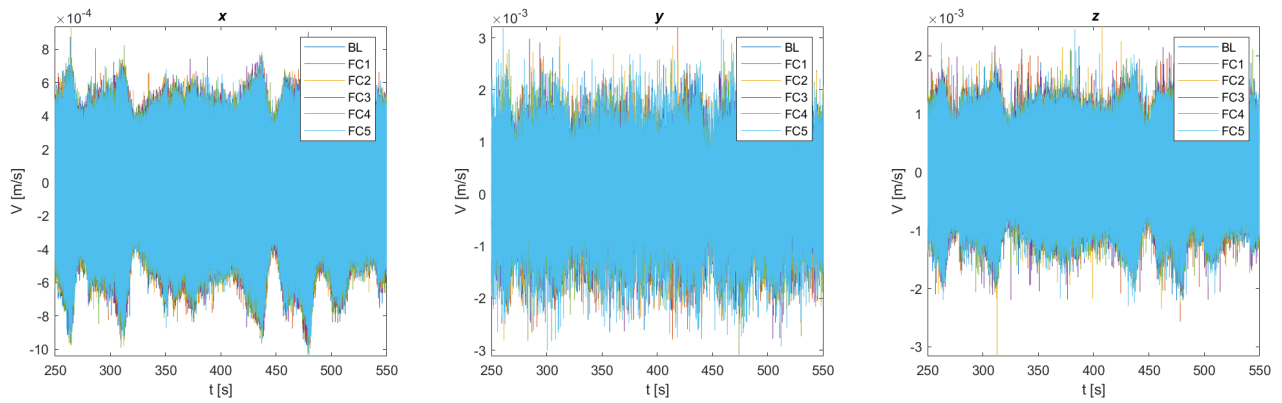


Figure D.7: High speed shaft rear bearing (HS-B) velocity with MBR damage time series x -direction (left), y -direction (center) and z -direction (right)

D.1.2 HSBR

After applying HSBR damage, the interesting time series showing bearing vibration velocities, which are only the vibration of HS-A and HS-B, are presented in Figures D.8 and D.9.

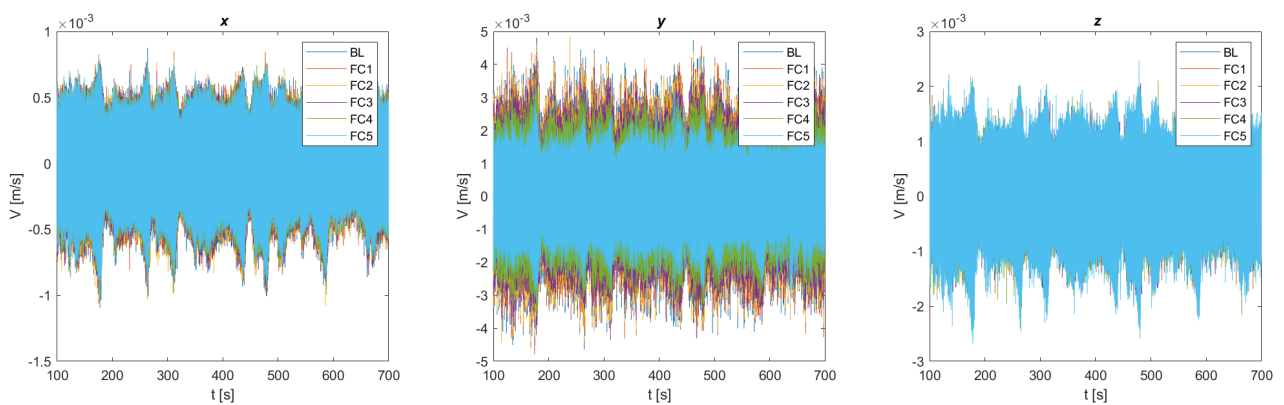


Figure D.8: High speed shaft front bearing (HS-A) velocity with HSBR damage time series x -direction (left), y -direction (center) and z -direction (right)

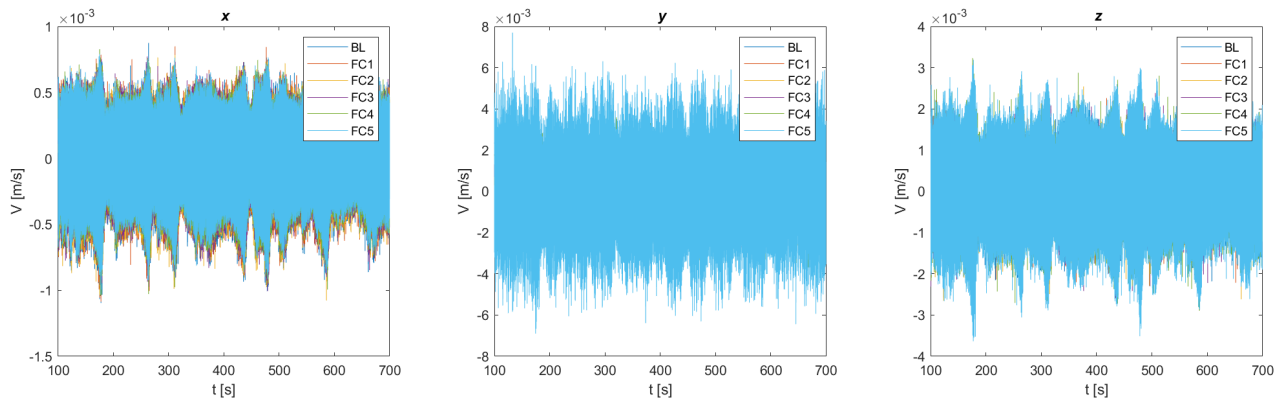


Figure D.9: High speed shaft rear bearing (HS-B) velocity with HSBR damage time series x -direction (left), y -direction (center) and z -direction (right)

D.2 Bearing Velocity Spectra

The spectra of the bearing vibration velocity are displayed in Sections D.2.1 and D.2.2 for MBR and HSBR damage, respectively.

D.2.1 MBR

After application of MBR damage, the spectra of the vibration velocity of INP-A and INP-B are displayed in Figures D.10, respectively.

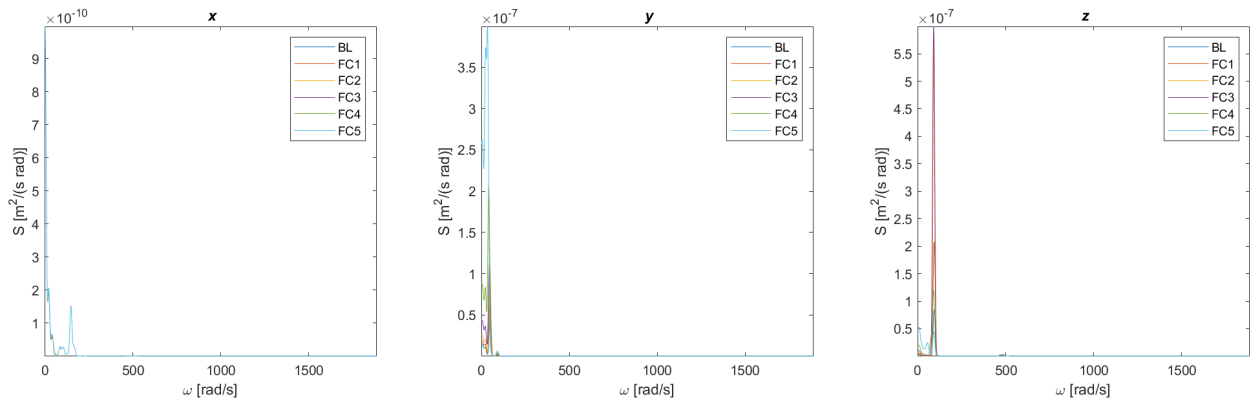


Figure D.10: Main shaft front bearing (INP-A) velocity with MBR damage spectra x -direction (left), y -direction (center) and z -direction (right)

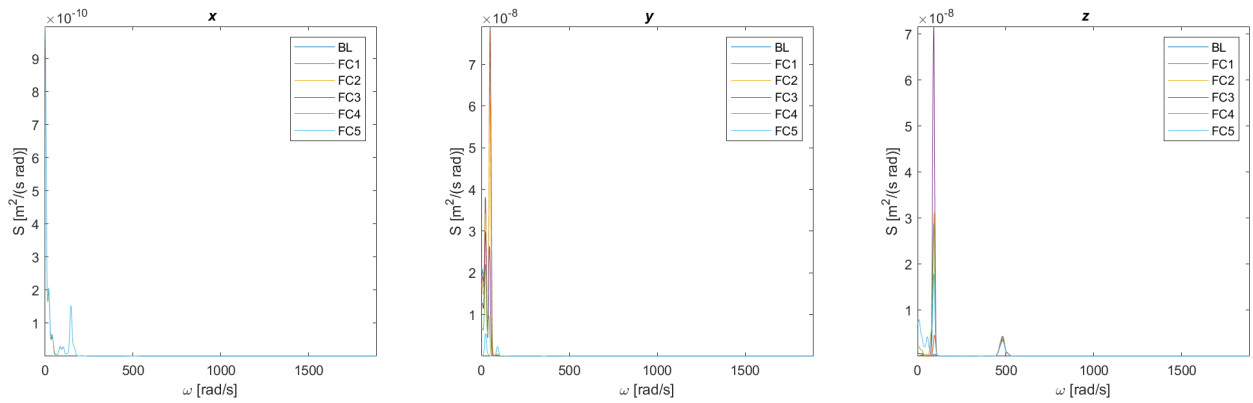


Figure D.11: Main shaft rear bearing (INP-B) velocity with MBR damage spectra x -direction (left), y -direction (center) and z -direction (right)

The spectra of the vibration velocity of PLC-A and PLC-B are shown in Figures D.12 and D.13, respectively.

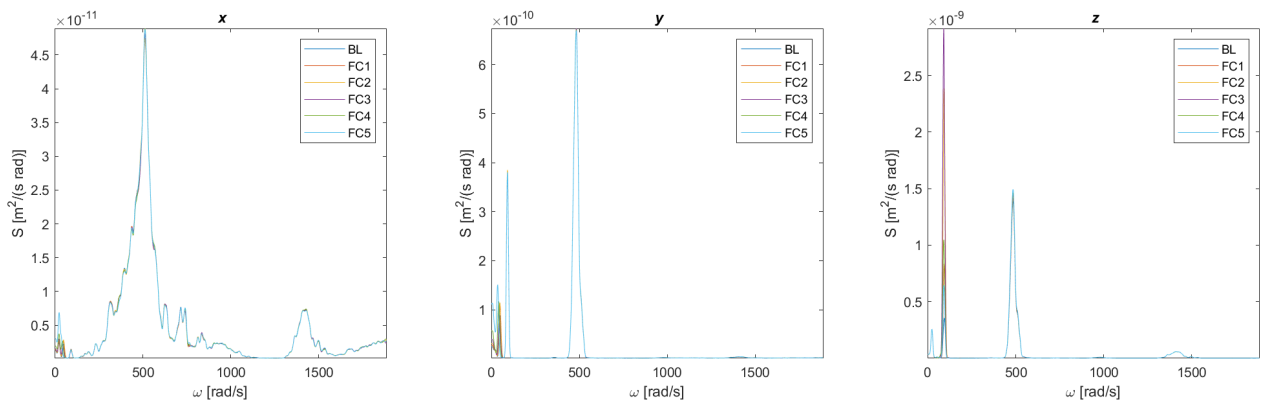


Figure D.12: Low speed shaft planet carrier front bearing (PLC-A) velocity with MBR damage spectra x -direction (left), y -direction (center) and z -direction (right)

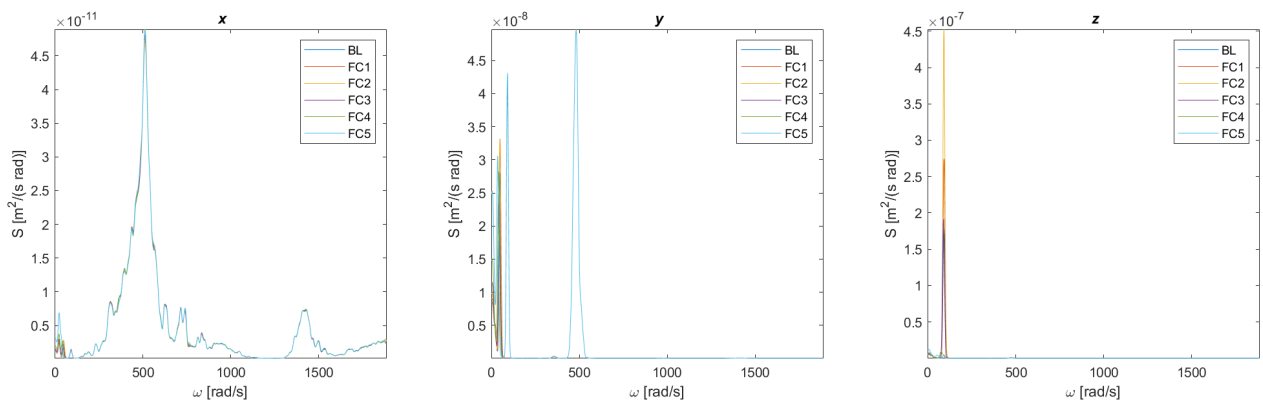


Figure D.13: Low speed shaft planet carrier rear bearing (PLC-B) velocity with MBR damage spectra x -direction (left), y -direction (center) and z -direction (right)

One can see the vibration velocity spectra of IMS-A in Figure D.14.

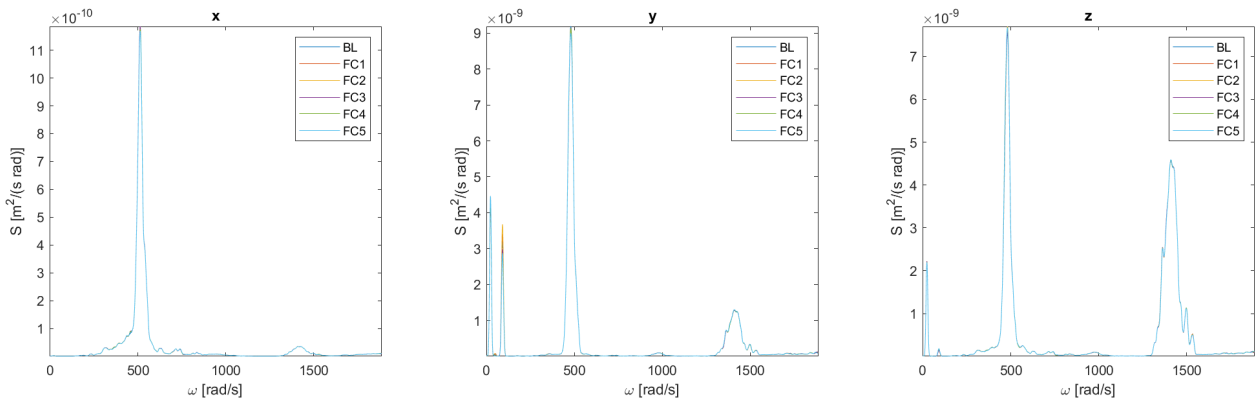


Figure D.14: Intermediate speed front bearing (IMS-A) velocity with MBR damage spectra x -direction (left), y -direction (center) and z -direction (right)

Finally, one can find HS-A's and HS-B's vibration velocity spectra in Figures D.15 and D.16, respectively.

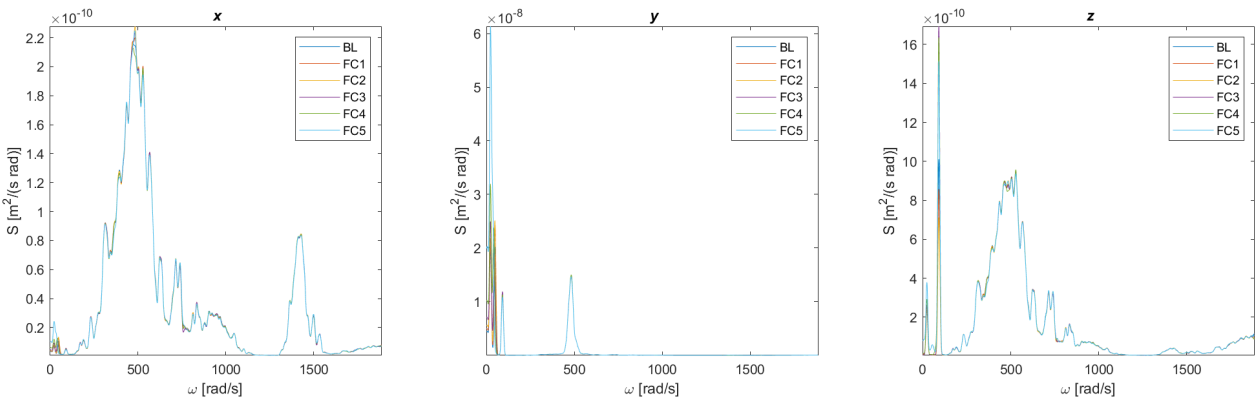


Figure D.15: High speed shaft front bearing (HS-A) velocity with MBR damage spectra x -direction (left), y -direction (center) and z -direction (right)

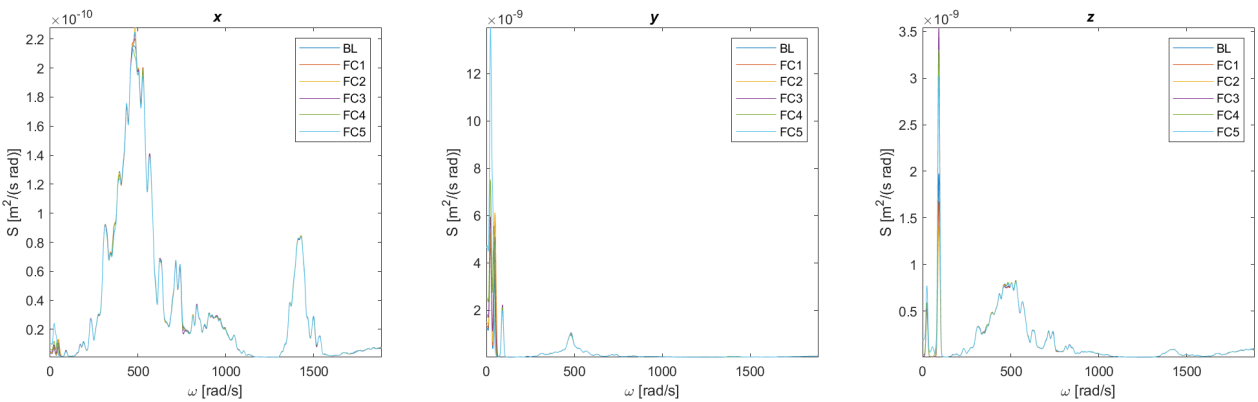


Figure D.16: High speed shaft rear bearing (HS-B) velocity with MBR damage spectra x -direction (left), y -direction (center) and z -direction (right)

D.2.2 HSBR

Concluded is with the vibration velocity spectra of HS-A and HS-B after application of HSBR damage, which are shown in Figures D.17 and D.18, respectively.

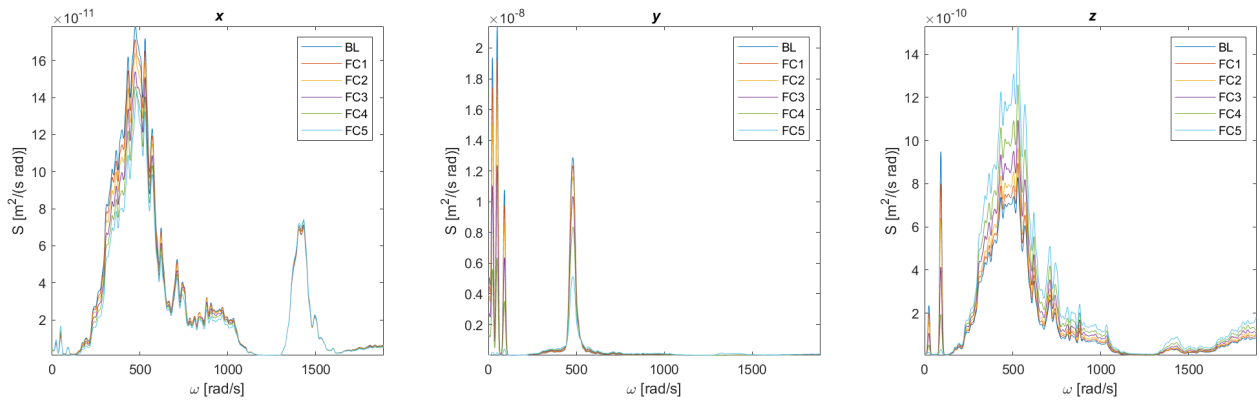


Figure D.17: High speed shaft front bearing (HS-A) velocity with HSBR damage spectra x -direction (left), y -direction (center) and z -direction (right)

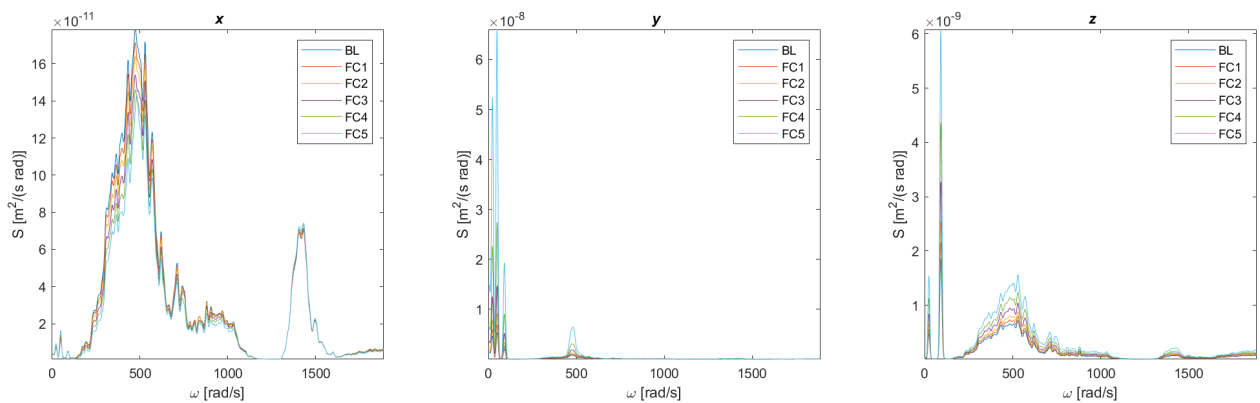


Figure D.18: High speed shaft rear bearing (HS-B) velocity with HSBR damage spectra x -direction (left), y -direction (center) and z -direction (right)

E | Shaft Vibration Energy Method Figures

In this chapter, one can find the figures obtained for the Shaft Vibration Energy Method. The time series of the shaft vibration velocities and accelerations can be found in Section E.1 and its spectra in Section E.2.

E.1 Shaft Vibration Time Series

The shaft vibration time series can be found in Sections E.1.1, E.1.2 and E.1.3 for MBR, MBX and HSBR damage, respectively.

E.1.1 MBR

In Figure E.1, one can see the main shaft vibration velocity time series in the x -, y - and z -direction.

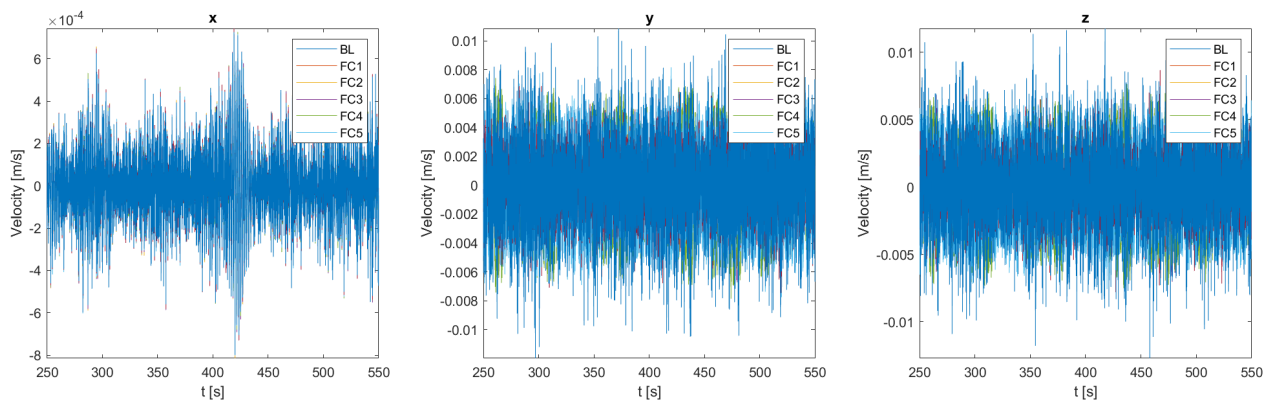


Figure E.1: Main shaft velocity with MBR damage time series x -direction (left), y -direction (center) and z -direction (right)

The time series of the main shaft vibration acceleration in the x -, y - and z -direction is found in Figure E.2.

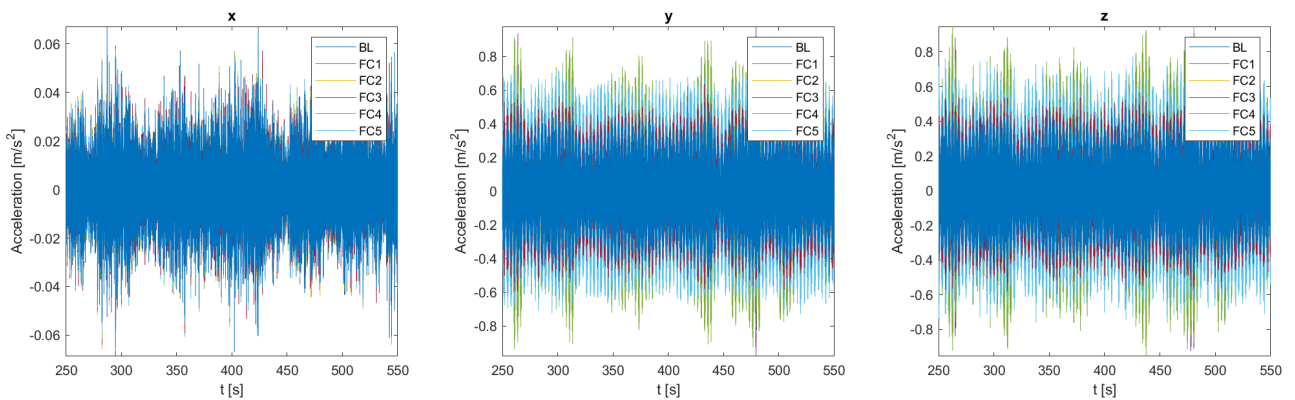


Figure E.2: Main shaft acceleration with MBR damage time series x -direction (left), y -direction (center) and z -direction (right)

One can find the low speed shaft vibration velocity time series in Figure E.3.

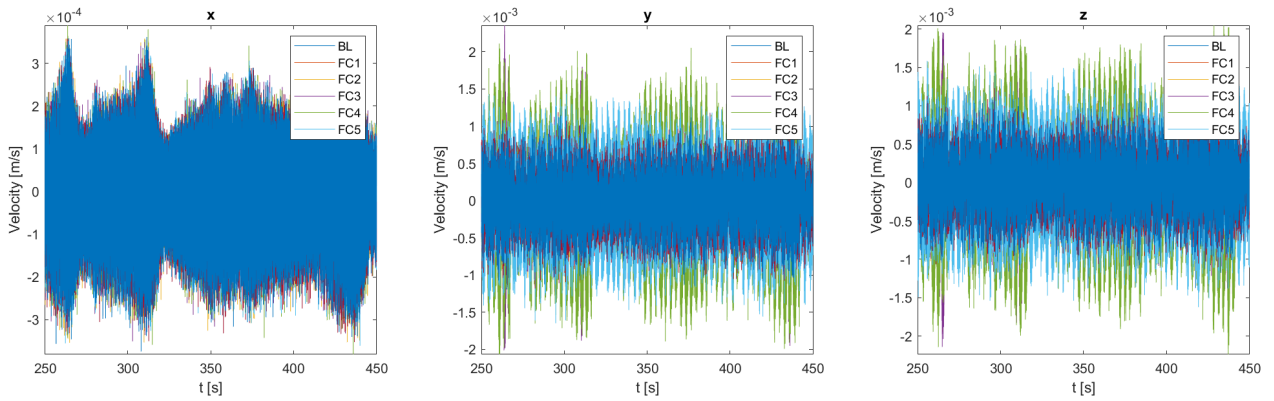


Figure E.3: Low speed shaft velocity with MBR damage time series x -direction (left), y -direction (center) and z -direction (right)

E.1.2 MBX

Only the main shaft vibration showed a different response for the different fault cases with MBX damage. Therefore, one can find the main shaft vibration velocity and acceleration in Figures E.4 and E.5, respectively.

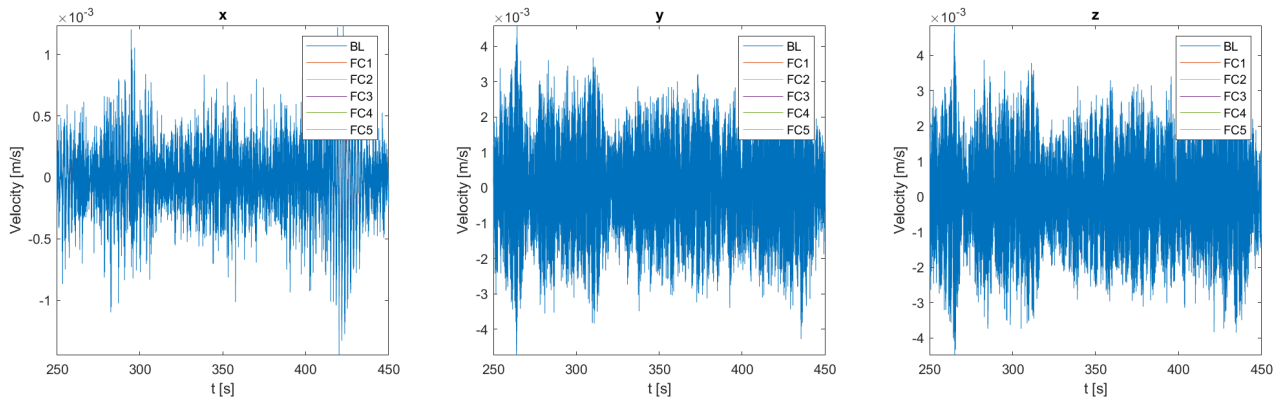


Figure E.4: Main shaft velocity with MBX damage time series x -direction (left), y -direction (center) and z -direction (right)

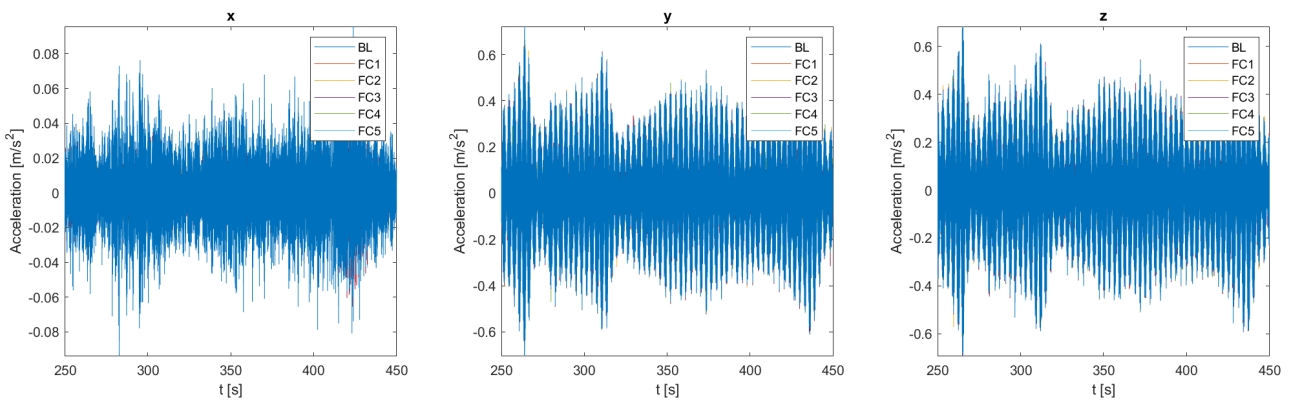


Figure E.5: Main shaft acceleration with MBX damage time series x -direction (left), y -direction (center) and z -direction (right)

E.1.3 HSBR

It appeared that only the high speed shaft vibration was affected by HSBR damage. Therefore, one can find its vibration velocity in Figure E.6.

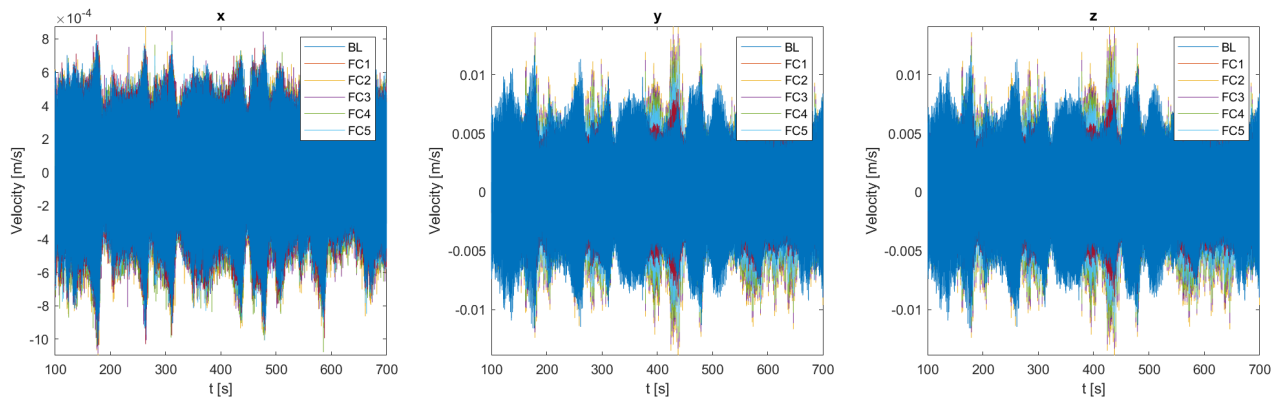


Figure E.6: High speed shaft front bearing velocity with HSBR damage time series x -direction (left), y -direction (center) and z -direction (right)

E.2 Shaft Vibration Spectra

Spectra are created from the time series displayed in Section E.1. These are displayed in the following. Sections E.2.1, E.2.2 and E.2.3 display the spectra for MBR, MBX and HSBR damage, respectively.

E.2.1 MBR

In Figures E.7 and E.8, one can see the spectra of main shaft vibration velocity and acceleration, respectively.

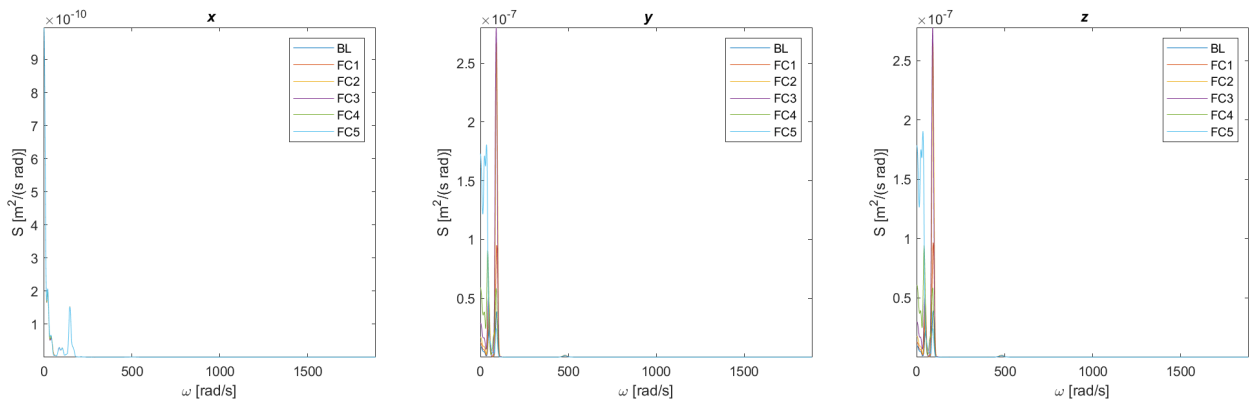


Figure E.7: Main shaft velocity with MBR damage spectra x -direction (left), y -direction (center) and z -direction (right)

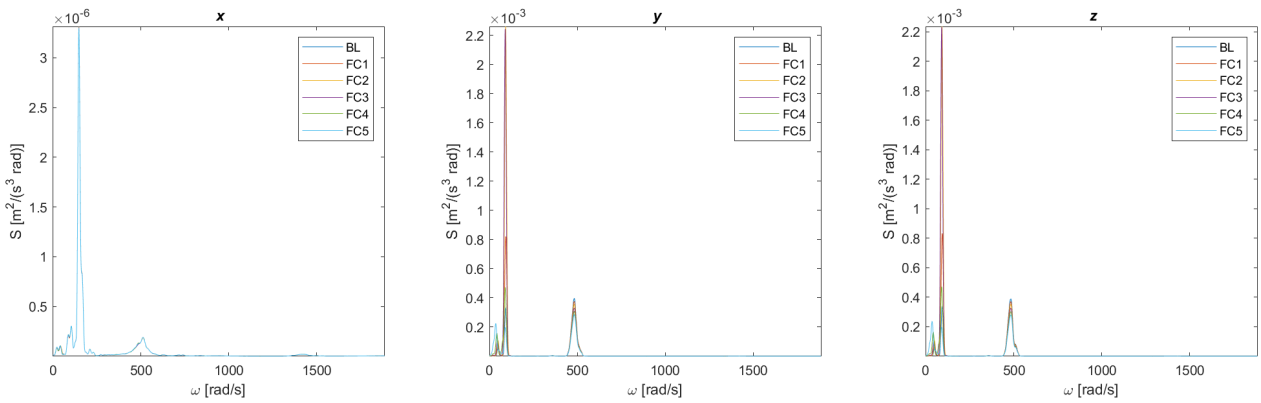


Figure E.8: Main shaft acceleration with MBR damage spectra x -direction (left), y -direction (center) and z -direction (right)

The low speed shaft vibration velocity spectra are depicted in Figure E.9.

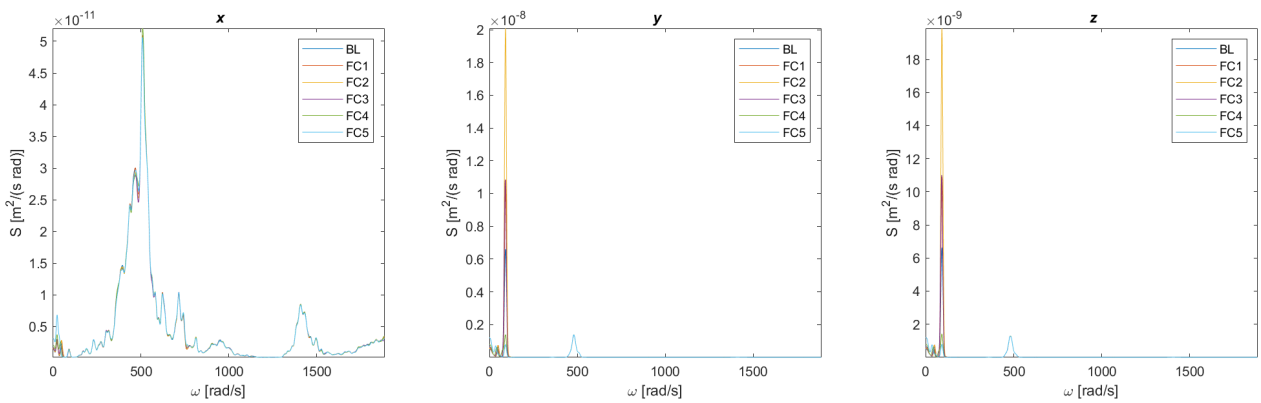


Figure E.9: Low speed shaft velocity with MBR damage spectra x -direction (left), y -direction (center) and z -direction (right)

E.2.2 MBX

The spectra of main shaft vibration velocity and acceleration after introduction of MBX damage is depicted in Figures E.10 and E.11, respectively.

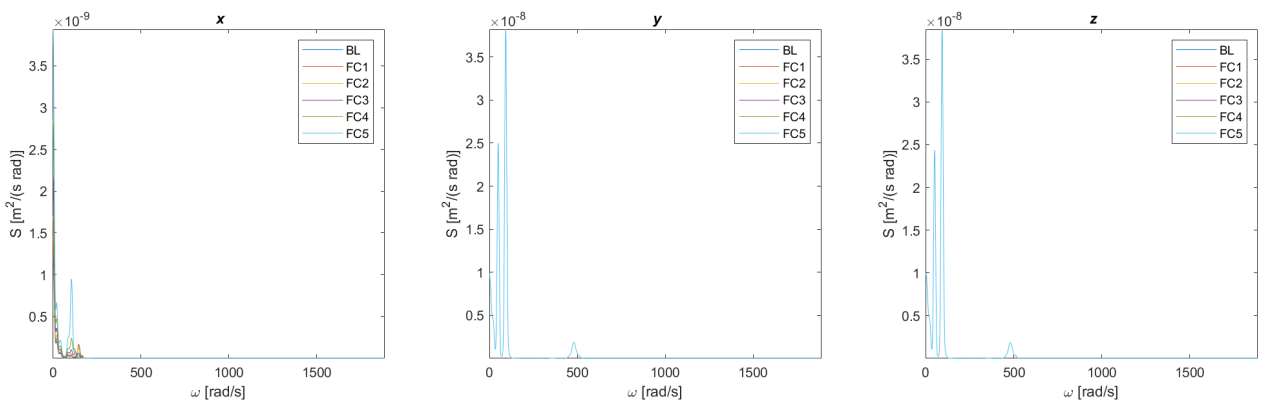


Figure E.10: Main shaft velocity with MBX damage spectra x -direction (left), y -direction (center) and z -direction (right)

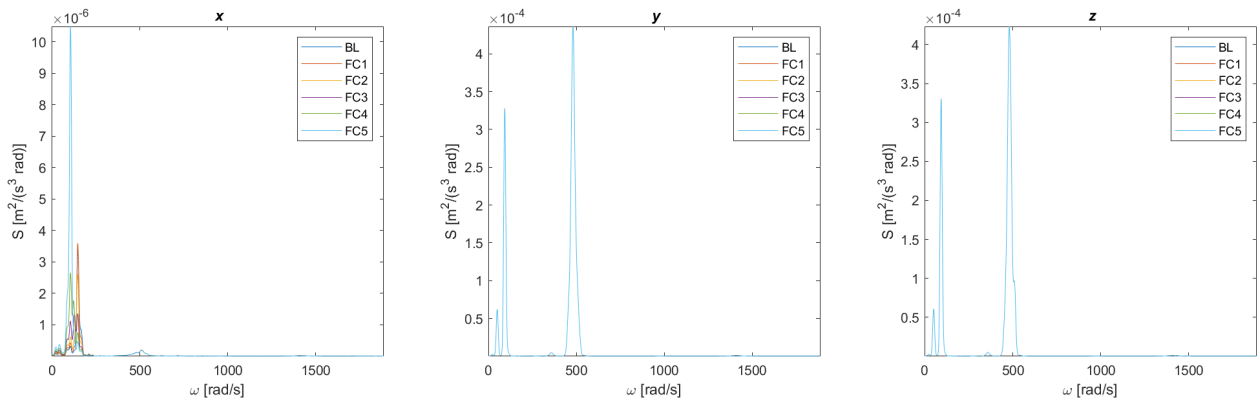


Figure E.11: Main shaft acceleration with MBX damage spectra x -direction (left), y -direction (center) and z -direction (right)

E.2.3 HSBR

Finally, the spectra, obtained from the time series of high speed shaft vibration velocity after applied HSBR damage, are displayed in Figure E.12.

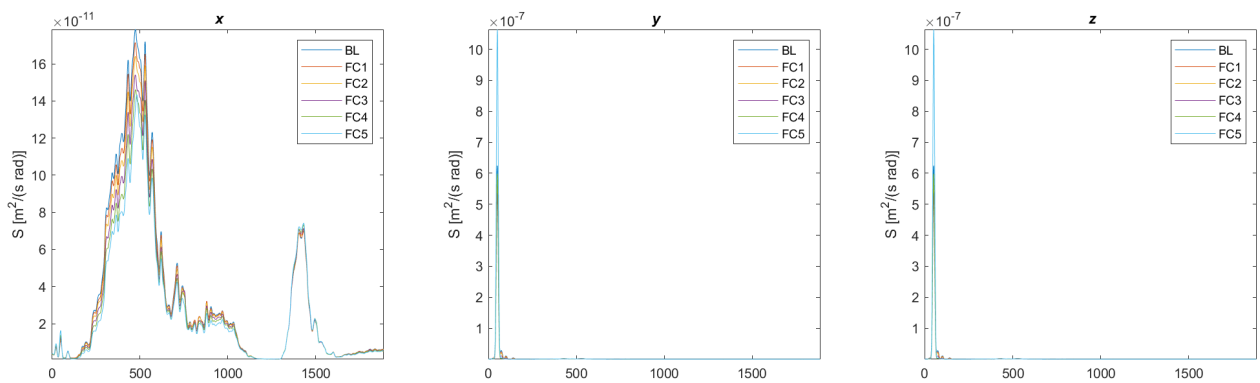


Figure E.12: High speed shaft velocity with HSBR damage spectra x -direction (left), y -direction (center) and z -direction (right)